Development of site-specific elastic design spectra for *future* building codes: an updated classification of empirical amplification functions (sub-project 1)

Paolo Bergamo and Donat Fäh,
Swiss Seismological Service
ETH Zürich

Technical Report
SED/2017/12
ETH Zürich

Citation

Bergamo P. and Fäh D. (2017) Development of site-specific elastic design spectra for future building codes, Part 1: an updated classification of empirical amplification functions, Technical Report SED 2017/12, Swiss Seismological Service, ETH Zurich. DOI: 10.3929/ethz-b-000262165

Disclaimer

Executive summary

This report illustrates the data collection, processing and elaborations carried out in the framework of strategy 1 ("An updated classification of empirical amplification functions") of the project "Development of site-specific elastic design spectra for future building codes".
This strategy aims at reconstructing a set of site-specific uniform hazard spectra (UHS), based on seismic hazard inputs representative of the Swiss hazard scenario and comprehensive of local amplification effects. We consider site amplification for a variety of subsurface soil configurations. These site-specific UHSs are sorted according to the characteristics of the corresponding subsoil, and collated with the elastic design spectra from the present building codes.
The input empirical data set is constituted by the recordings of the Japanese KiK-net strong motion network, including approximately 700 sites, each instrumented with a downhole reference seismometer (generally encased within the seismic bedrock) coupled with a receiver placed at the soil surface. This instrumental configuration is ideal for the study of site amplification phenomena.
Earthquake waveforms from KiK-net stations were processed to derive Fourier amplification functions at each site of the network; these functions are then referred to a common seismic bedrock condition (the same as in the Swiss hazard maps) and finally translated to the response spectral domain, so to express the site amplification in terms of spectral acceleration. In this process, the relevance of non-linear soil behavior is also discussed.
At the last processing step, the empirically derived response spectral amplification functions are finally superimposed to seismic hazard inputs characteristic for the Swiss hazard scenario, yielding site-specific UHSs, which are compared with elastic design spectra from the present building code.
The obtained results have evidenced the need for an improved site-condition classification and changes in the definition of normative spectra that would take into consideration site-amplification effects, in particular resonances. Conservative and simplified solutions are proposed for the case when only indirect or poor information is available for the considered site; vice versa, in case of well-constrained site characterization, a more specific and complex approach should be preferred.

TABLE OF CONTENTS

1.0 Introduction

It is widely recognized that seismic waves can be locally amplified due to soil layering and basin geometry (Bard et al., 1988; Yamanaka et al., 1989; Wald and Graves 1998); such amplification and resonance phenomena are key elements in the architecture of a seismic building normative. Site effects can be empirically evaluated by collating simultaneous earthquake recordings collected on sediments and at a nearby rock site (Borcherdt, 1970). As reliable reference (rock) sites close to the site of interest are not always available, vertical arrays of accelerometers (i.e. borehole stations), with a downhole reference site coupled to a surface instrument, can overcome the difficulty (e.g. Bonilla et al., 2002, Régnier et al., 2013).

In this study, we analyze the impact of local amplification and resonance phenomena on the seismic hazard levels to be expected at a given site. We determine response spectral amplification functions (based on empirically-derived Fourier amplification functions) for approximately 700 sites of the Japanese Kiban-Kyoshin (KiK-net) strong motion network; this is presently the largest network of borehole stations, with nearly 700 sites spanning a considerable variety of subsoil conditions (Aoi et al., 2004). We combine the response spectral amplification functions with probabilistic seismic hazard inputs representative of the Swiss hazard scenario (uniform hazard spectra on Swiss reference rock condition), so to obtain site-dependent hazard curves. These are finally sorted according to the subsoil conditions of the corresponding stations (soil classes) and collated with the elastic design spectra of the present SIA 261 2014 normative.

Sections 2 and 3 present the database used for this study. It is constituted by recordings from the Japanese network of borehole stations KiK-net. We then describe the quality-control operations we performed for these data. Sections 4 and 5 illustrate the strategy we followed to obtain, from triggered waveforms, two types of estimates of the Fourier amplification functions for each site of the KiK-net network. The first estimate is based on the collation of data acquired by surface and borehole receivers (surface to borehole ratios), while for the second one we apply a method based on empirical spectral modeling inverting the surface waveforms - cleared from source and path components - to reconstruct site amplification effects. In chapter 6, these two sets of Fourier amplification functions are brought to a common reference, which is the Swiss reference rock. Section 7 details how the obtained Fourier amplification functions were translated to the domain of response spectra, to yield response spectral amplification curves. Chapter 8 discusses the relevance of nonlinear soil behaviour. In section 9, the dataset of the response spectral amplification functions is combined with a seismic hazard input, considered representative of the hazard scenario in Switzerland (the uniform hazard spectra for the city of Sion). Site-specific UHSs are hence obtained, sorted by soil type and then compared with the elastic design spectra of the current SIA 261 2014 normative (chapter 10); both sets of spectra are normalized to a common reference. A proposal for the amendment of this norm is also formulated. In chapter 11, the normalization criterion adopted in section 9 and 10 is put aside and the absolute values from site-specific and design spectra are compared for ten Swiss cities (Basel, Bern, Chur, Geneva, Lausanne, Luzern, Lugano, St. Gallen, Sion, Zurich), belonging to all different seismic zones (1-3b) in the present Swiss normative. In section 12, we discuss the consequences of a different grouping of site-specific UHSs by soil type arising from a potential ambiguity in the definition of class E based on the sole Vs30 proxy. In particular, we focus on the changes affecting the comparison with normative design spectra. In Appendix A, we retrace in detail, step by step, the workflow illustrated in sections 4-10, assuming this alternative soil type classification scheme. Appendix B re-elaborates the results of the analogous study of Poggi and Fäh (2015) for the Swiss Federal Office of Energy (SFOE) and compares them with the outcome of this work.
Finally, section 13 collects discussions and conclusions regarding the main aspects arisen while implementing and finalizing this work.

This manuscript is accompanied by a companion report illustrating the alternative strategy ("Seismic Hazard Compatible Ground Motion Selection") followed within the framework of the same research project ("Development of site-specific elastic design spectra for future building codes").

2.0 The Japanese data set

For the strategy illustrated in this report, we use the Japanese Kiban-Kyoshin network (henceforth referred to as KiK-net). This is a network of almost 700 stations that uniformly covers the territory of Japan (Aoi et al. 2004; Figure 1). It is operating since 1995. Every KiK-net station is made up of a pair of high-quality digital accelerometers: one placed at the soil surface, the other one located at the bottom of an underlying borehole whose depth is 100 m or greater (generally up to 200 m for most of the stations). Although KiK-net sites were preferentially installed at rock or thin sediments sites (Fujiwara 2004), around two out of three sites exhibit a Vs30 smaller than 550 m/s (see Figure 2 for a complete overview of Vs30 distribution).

The KiK-net network provides waveforms of triggered events: the event trigger system of the data recorder is controlled using the signal of the downhole seismometer. Recording is started at a threshold level of 0.2 cm/sec^2 and ended 30 s after the last occurrence of 0.1 cm/sec^2. The sampling frequency of acquisition is 200 Hz; the overall frequency response of the KiK-net instruments is flat from zero frequency to about 30 Hz.

For most of the sites, P- and S-wave velocity profiles are available, obtained from seismic downhole measurements performed at the installation of the borehole seismometer.

Unfortunately, these velocity profiles are not necessarily reliable, or rather they depict a simplified subsurface structure (involving few average layers) that is often not sufficiently detailed to model the soil amplification at high frequency. Therefore, to assess the reliability of the KiK-net velocity profiles, Poggi et al. (2015, 2017) performed a comparison between the f_0 empirically measured in H/V spectral ratios, and the fundamental frequency obtained from synthetic amplification functions based on the downhole velocity models (see Figure 3 for an example). From this comparison, a selection of 289 sites with sufficiently trustworthy velocity profiles was obtained; in this report, this subset of KiK-net stations is henceforth referred to as “selection A”.

On the occasion of this research project, the list of reliable KiK-net sites was further re-assessed, thanks to the cooperation of prof. Hiroshi Kawase who provided information mostly regarding the recording accuracy of the various stations (proper installation, reliable equipment, flawless functioning of seismometers; Kawase, 2016, personal communications). Consequently, the subset of reliable KiK-net sites was further reduced to 144 stations, labeled “selection B”, mostly a subgroup of selection A.

In Figure 2, the distribution of Vs30 for the stations falling in selection A and B is shown; although the total number of sites is significantly reduced, the global trend of the Vs30 distribution and hence the representativeness of various soil conditions is somehow preserved (compare the center and bottom panel with the top one in Figure 2).

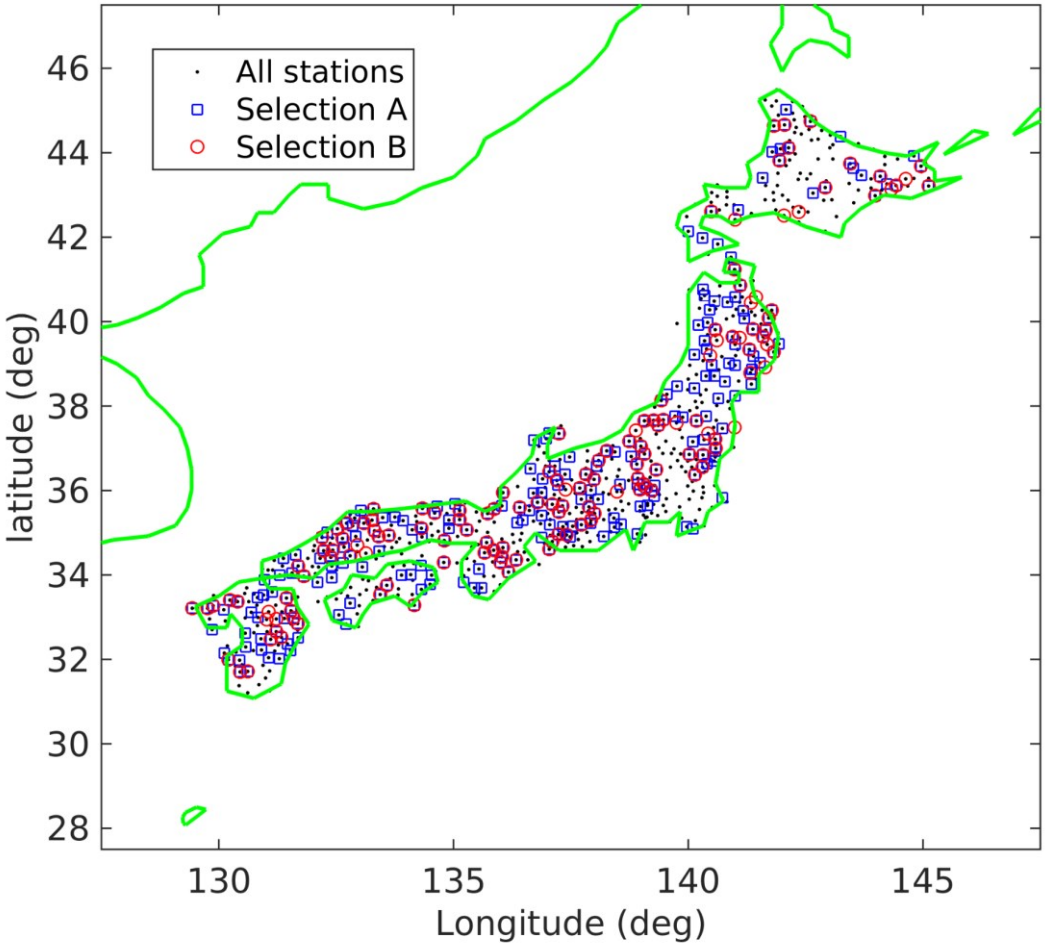

Figure 1 – Geographical distribution of KiK-net stations over the territory of Japan. The whole set of ~700 stations is represented with black dots. Stations falling in the subsets of reliable stations of selection A or B (see text) are circled with blue squares or red circles, respectively.

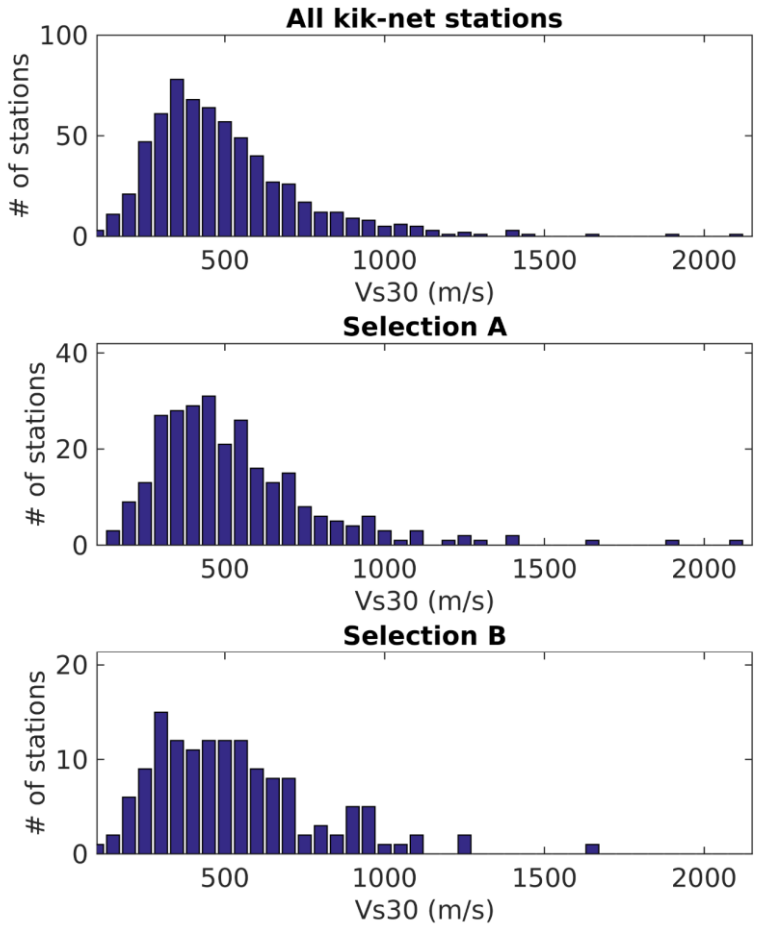

Figure 2 – Vs30 values for the KiK-net stations. From top to bottom: the entire dataset (~700 stations), subsets of reliable stations A (289 sites) and B (144 sites).

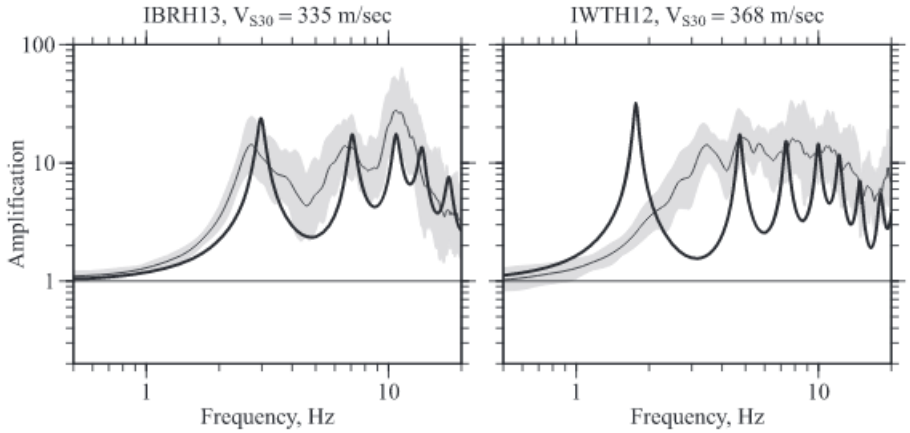

Figure 3 - Comparison between empirical amplification functions from spectral inversion (grey line plus/minus one standard deviation indicated in grey) and modeled SH transfer function (black line) for two sites of the Japanese KiK-Net network. Station IBRH13 (left panel) falls in the subset "selection A" of reliable sites; IWTH12 (right panel) is excluded.

3.0 SIA soil classification scheme

To account for the variability of ground motion amplification on different soil conditions, the classification scheme from SIA 261 normative (revision 2014) has been used to group sites of expected similar seismic response (Table 1). The SIA 261 normative describes six separated soil classes (A to F) of progressively decreasing stiffness. However, special class F could not be exploited within this study, due to lack of calibration data, and is therefore neglected from further analyses.

The SIA 261 classification scheme is based on direct geological/geotechnical description of the surface geology and on the use of indirect geotechnical and geophysical proxies. The most relevant proxy for our purposes is the travel-time average S-wave velocity over the first 30 m (Vs30), which is considered in literature a parameter highly correlated with site amplification (e.g. Cadet et al., 2010). In this study, we use the Vs30 at each analyzed site to discriminate between classes A to D (see Table 1 for class specific velocity boundaries). Class E requires a further analysis of the velocity profiles, accounting for the presence of stiff formations (V_S > 800 m/s) at shallow depths (5 to 20 m).

Table 1: Description of seismic soil conditions (classes A-E) of the SIA 261 normative (2014).

Klasse	Beschreibung SIA 261	Vs30 (m/s)
A	Fels oder andere felsähnliche geologische Formation mit höchstens 5 m Lockergestein an der Oberfläche	> 800
B	Ablagerungen von sehr dichtem Sand und Kies oder sehr steifem Ton mit einer Mächtigkeit von mindestens einigen zehn Metern, gekennzeichnet durch einen allmählichen Anstieg der mechanischen Eigenschaften mit der Tiefe	500 – 800
C	Ablagerungen von dichtem oder mitteldichtem Sand, Kies oder steifem Ton mit einer Mächtigkeit von einigen zehn bis mehreren hundert Metern	300 – 500
D	Ablagerungen von lockerem bis mitteldichtem kohäsionslosen Lockergestein (mit oder ohne einige weiche kohäsive Schichten) oder von vorwiegend weichem bis steifem kohäsivem Lockergestein	< 300
E	Oberflächliche Schicht von Lockerge steinmit Vs-Werten nach C oder D und veränderlicher Dicke zwischen 5 m und 20 m über steiferem Bodenmaterial mit Vs > 800 m/s	

As far as class E is concerned, the present version of SIA 261 normative contains a partly ambiguous definition, when this is based on the sole proxy of Vs30. In fact, the description for this particular soil category is more a geological one, rather than a geophysical one. In few words, the key point is whether the "weathering layer of soft soil with Vs values corresponding to class C or D" (see Table 1, bottom row) should be translated, in terms average-Vs proxy, as a constraint of either Vs30<500 m/s or Vs_{z800} < 500 m/s (where Vs_{z800} is the average S-wave velocity down to a depth *z800* where a stiff formation with Vs>800 m/s is encountered, with 5<*z800*<20 m). This potential ambiguity is relevant to our study as the classification of the set of KiK-net stations is based exclusively on the provided S-wave velocity profile; the geological information regarding the weathering formations is in fact unavailable in terms of univocal correlation with European soil types.
For the core part of our study (sections 3 – 11) we assumed as definition for class E the first one of the two presented above (Vs30<500 m/s and obviously 5<*z800*<20 m), consistently with the previous work of Poggi and Fäh (2015); the resulting distribution of KiK-net sites among classes A-E is shown in Figure 4. For the sake of completeness, in Appendix A we repeat the processing stages of sections 3-11 adopting the alternative criterion for E type soils (Vs_{z800}<500 m/s and 5<*z800*<20 m), and compare the two sets of results; we remark that this criterion is closer to the approach that appears to be currently followed for soil type designation in the revision of Eurocode 8 (Paolucci, 2017).

As anticipated, in Figure 4 we show the distribution of the KiK-net sites among classes A-E of SIA normative. The classification is based on the V_S profile provided for each KiK-net station and based on the interpretation of the seismic downhole test carried out at the installation of the downhole receiver (see previous paragraph). As previously observed for Figure 2, moving from the entire KiK-net dataset to subsets A and B, although the total number of sites is significantly reduced, the relative proportions among the different soil classes, and hence the representativeness of the variety of soil conditions, is somehow preserved (compare the center and bottom panel with the top one in Figure 4).

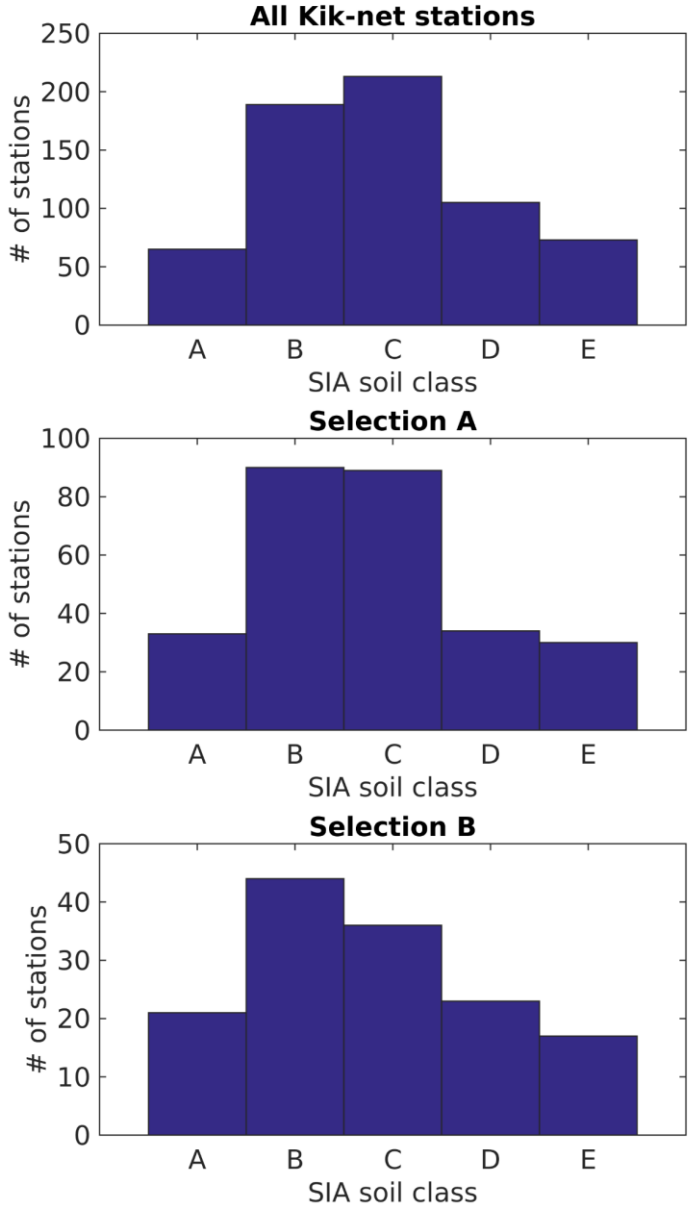

Figure 4 – Distribution of KiK-net stations among soil classes A-E of SIA 2014 normative. From top to bottom: the entire dataset (~700 stations), subsets of reliable stations A (289 sites) and B (144 sites).

4.0 Calculating surface to borehole ratios for KiK-net sites

The configuration of KiK-net stations, with a buried seismometer generally encased in the seismic bedrock and coupled with a surface receiver, makes them ideal for the study of soil amplification phenomena. The borehole seismometer in fact records seismic waveforms that can be considered less (or marginally) affected by site amplification, while this significantly influences the response of the surface receiver; a comparison between the recordings of the buried and surficial sensors provides therefore information on the seismic amplification properties of the soil formations interposing between the two seismometers.
A common method to employ the data from surface-borehole receivers is to collate the Fourier spectra of recordings from the sensors' pair to obtain so called "surface to borehole (SB) ratios", that are estimates of the subsurface amplification function (e.g., among others, Bonilla et al., 2002, Régnier et al., 2013). We follow this approach to compute the horizontal component SB ratios of the entire set of KiK-net stations; for this purpose, we use the accelerometric data recorded in the period 1997-2010 and produced by shallow events (hypocentral depth $\leq$ 25 km). The selected waveforms undergo a series of pre-processing operations: after baseline correction, the signal analysis window is first defined considering the peak of the signal as anchor reference. In a second refinement stage, the signal window is shrunk down assuming the 5^{th} and 75^{th} percentile of amplitude intensity as boundaries. The minimum and maximum frequencies considered are 0.05 to 30 Hz, although the included bandwidth of the individual spectra depends on the relative level of noise. To ensure that the ground motion signal is correct up to a period of at least 5 s, only components corrected by using a high-pass frequency less than or equal to 0.2 Hz are selected. This issue may be important when the soil column undergoes cyclic degradation including a consequent decrease of the effective vibration frequency. The noise estimate, taken from the pre-trigger waveform portion, is artificially increased until it intersects the signal spectrum at the lowest and highest frequencies. Finally, the maximum bandwidth over which the signal is at least three times greater than the level of noise is selected; these are the bandwidths employed for the collation (i.e. ratio computation) of borehole and surface Fourier spectra. From each event, an individual SB ratio is obtained; this is then added to the population of ratios referring to the same KiK-net station, and these are finally averaged.

It is understood that the material where the borehole sensors are encased is not the same for all stations; in fact, the properties of the "bedrocks" differ significantly. Therefore, once the "raw" ratios are obtained, they are then brought to a common reference, so to represent the amplification function with respect to such benchmark; this operation ensures the comparability among different KiK-net stations. The chosen reference is the Japanese reference rock Vs profile as defined in Poggi et al. (2013); the referencing operation is possible because the S-wave velocity at the borehole bottom for each KiK-net station is known, provided by downhole surveys (see section 2).
The obtained horizontal component SB ratios are displayed in Figures 5-7, referring to the complete KiK-net dataset (Figure 5), and to the subsets of stations selection A (Figure 6) and selection B (Figure 7). It is important to specify that here and in the following sections, the horizontal component is defined as the geometric mean of N-S and E-W components, unless differently indicated.
In Figures 5-7, the ratio functions are grouped by SIA soil class (A-E); in the lower right panel, we show the graphs of the number of events used for each frequency component of the average SB ratios.

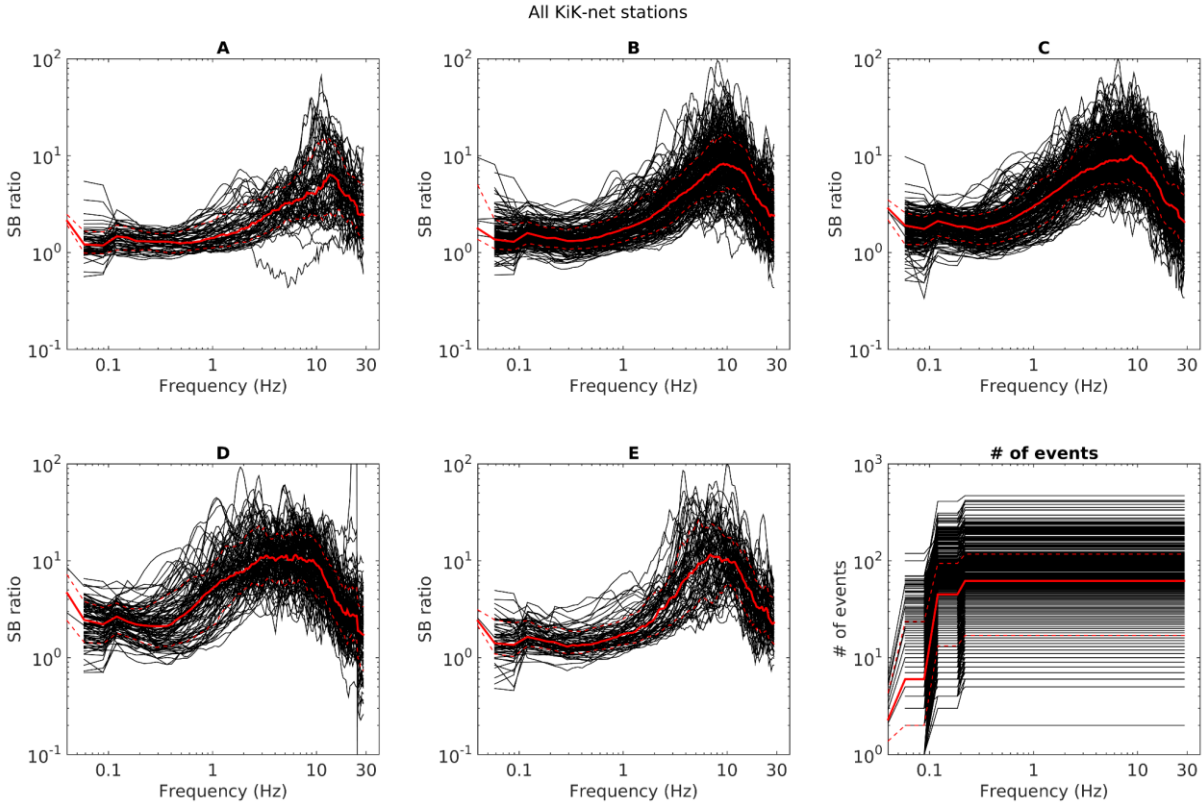

Figure 5 – surface to borehole ratios (black lines) for all the available KiK-net stations, referred to the Japanese reference Vs profile. Subpanels 1-5 collect the surface to borehole ratios for soil classes A-E according to SIA normative. The median for each group is represented with a red line; the 15th and 85th percentile with red dashed line. The panel in the lower right corner indicates the number of events employed for the estimation of the frequency components of each single surface to borehole ratio.

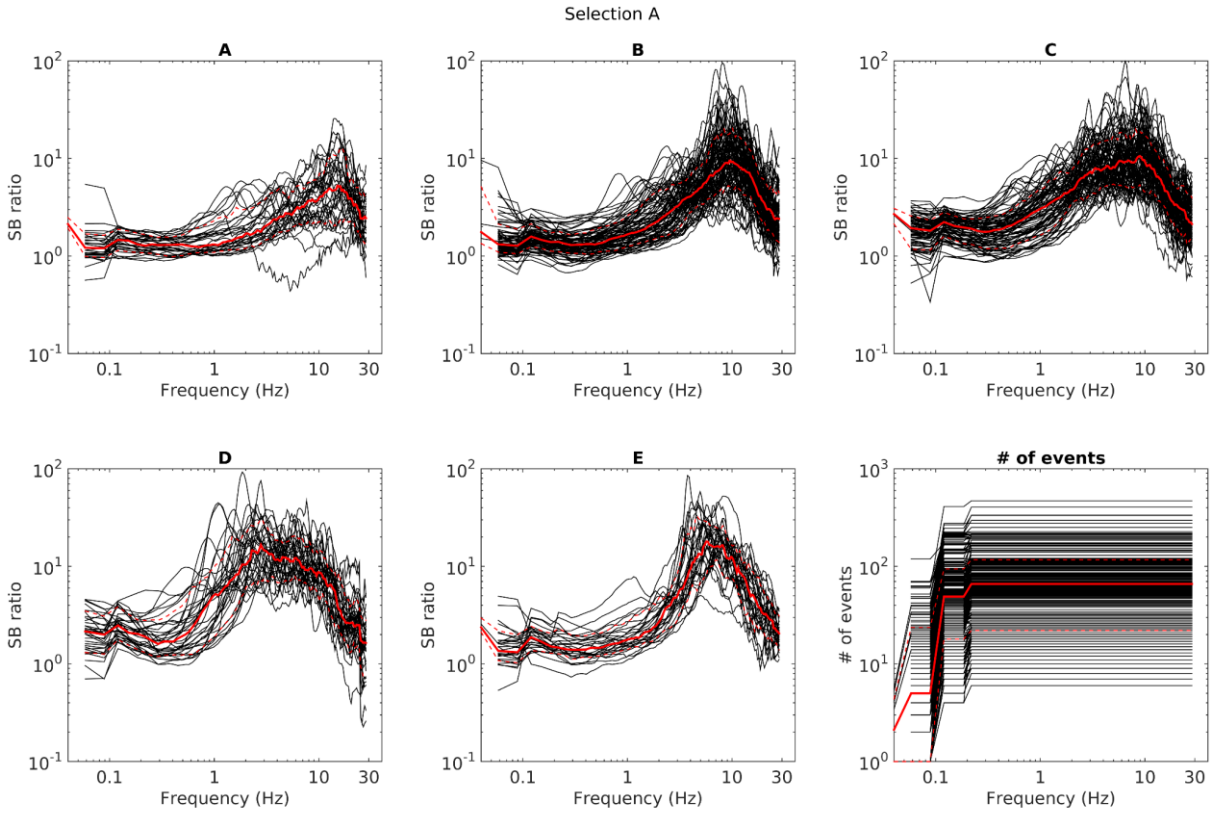

Figure 6 – surface to borehole ratios (black lines) for the KiK-net stations belonging to selection A, referred to the Japanese reference Vs profile. Subpanels 1-5 collect the surface to borehole ratios for soil classes A-E according to SIA normative. The median for each group is represented with a red line; the 15th and 85th percentile with red dashed line. The panel in the lower right corner indicates the number of events employed for the estimation of the frequency components of each single surface to borehole ratio.

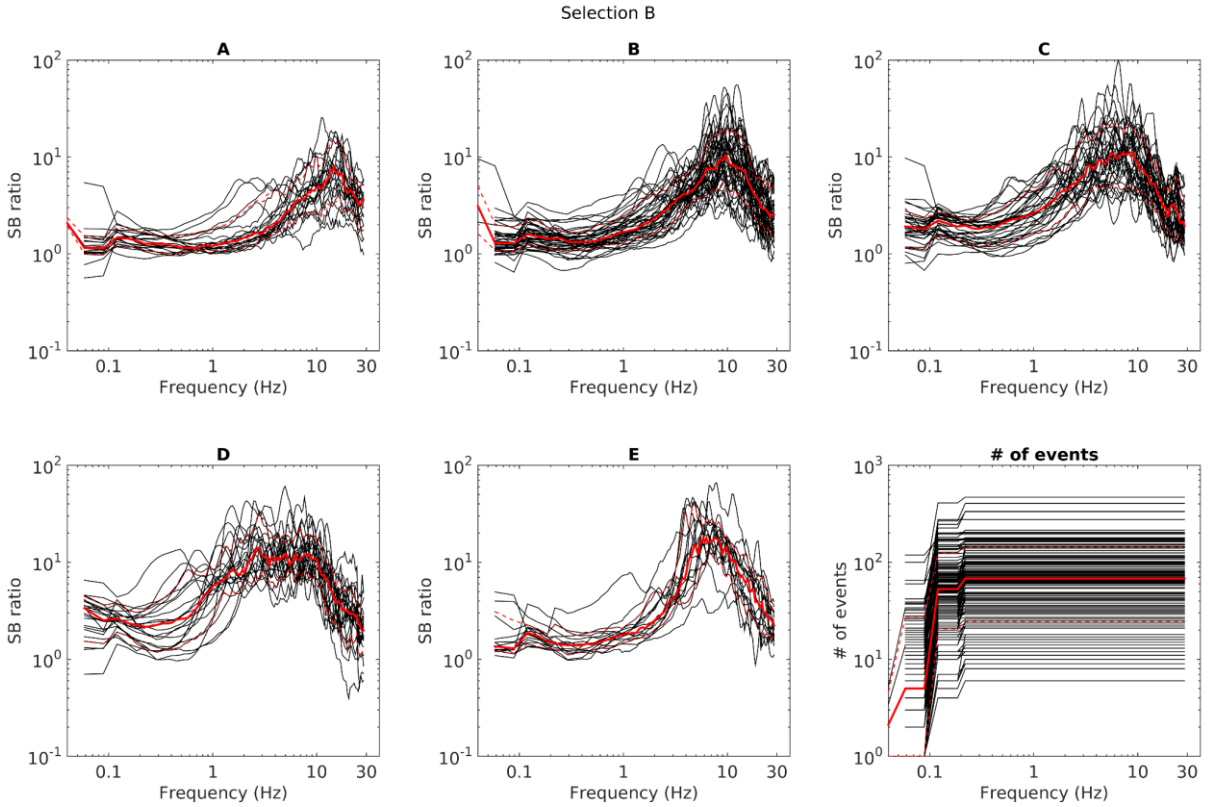

Figure 7 – surface to borehole ratios (black lines) for the KiK-net stations belonging to selection B, referred to the Japanese reference Vs profile. Subpanels 1-5 collect the surface to borehole ratios for soil classes A-E according to SIA normative. The median for each group is represented with a red line; the 15th and 85th percentile with red dashed line. The panel in the lower right corner indicates the number of events employed for the estimation of the frequency components of each single surface to borehole ratio.

As expected, going from soil class A through B, C, and finally to D, the median fundamental frequency peak moves progressively from higher (~15 Hz for class A) to lower values (~5 Hz for class D), as the soil material becomes on average softer and softer (decreasing Vs30). A different case is represented by class E, that gathers sites with thin (5-20 m thick) surficial soft sediments, underlain by stiffer (Vs>800 m/s) material; this shallow impedance contrast produces again relatively high values of f_0 (around 8 Hz). The considerations illustrated here are globally valid for all the three sets of KiK-net sites: the entire network (Figure 5), and the subsets selection A and B (Figures 6-7).

5.0 Calculating empirical amplification functions for KiK-net sites

A second, more complex procedure for the reconstruction of amplification function for KiK-net sites from recorded waveforms was followed as well. For each KiK-net site, the estimation of the empirical amplification function for the horizontal component at the soil surface was attempted, according to the spectral modeling method of Edwards et al. (2013, 2017).
This method can be considered as the analysis of site-specific ground motion residuals relative to spectral modeling of a large number of earthquakes. For each recorded event *i*, the accelerograms are processed following the procedure of Boore and Bommer (2005) to integrate to reliable velocity time histories. The corresponding Fourier velocity spectrum Ω_{ij} observed at station *j* is then given by

$$\Omega_{ij}(f,r) = 2\pi f\, E_i(f, M_{0i}, f_{ci})\, B_{ij}\left(f, t_{ij}^*\right) S_{ij}(r, r_{0\ldots n-1}, \lambda_{1\ldots n})\, T_j(f, A_j, \kappa_j) \qquad (1)$$

in which *f* is the frequency, *r* is the hypocentral distance, $E_i(f,M_{0i},f_{ci})$ is the source model, $B_{ij}(f, t_{ij}^*)$ is the intrinsic attenuation along the ray path, $S_{ij}(r,r_{0\ldots n-1},\lambda_{1\ldots n})$ is the frequency independent amplitude decay

with distance, and $T_j(f,A_j,\kappa_j)$ is the site-response function at station j. The source spectrum E_i is considered to be a Brune (1970, 1971) ω^2-spectrum with an event-specific corner frequency f_c and a long-period spectral plateau defined by the seismic moment M_{0i}. Oth et al. (2010) showed that for KiK-net data the source spectra can be well explained using the ω^2-model, and both crustal and subcrustal earthquakes show self-similar scaling characteristics over the entire magnitude range, with stress drops higher by one order of magnitude for subcrustal events (on the order of 10 MPa) as compared with crustal events (on the order of 1 MPa). We further assume path-specific intrinsic attenuation, and the geometric spreading function S_{ij} is described as a decay function with a constant, frequency independent exponential decay in the form $r^{-\lambda}$. An initial spherical decay, i.e. $\lambda = 1.0$, is followed by attenuation slightly slower than spherical with $\lambda = 0.9$ for $r > 150$ km (Kawase 2006).
Finally, local site amplification is given by

$$T_j(f, A_j, \kappa_j) = A_j a_j(f) e^{-\pi f \kappa_j} \quad (2)$$

in which A_j is the average site amplification relative to a given regional reference, $a_j(f)$ is the normalized frequency-dependent elastic site amplification function and κ_j is the site dependent local attenuation parameter.

A nonlinear, two-stage regression is used to separate the different contributions of equation (1) for obtaining $T_j(f, A_j, \kappa_j)$. In this way, we first determine the combined path attenuation ($t_{ij}^* + \kappa_j$) at each site, the event-common source corner frequency f_c, and a spectral amplitude parameter termed the signal moment for each spectrum. A regional attenuation model is not used to predetermine $t_{ij}^* + \kappa_j$ because this requires simultaneous inversion of the full dataset (rather than the event-by-event application) and may bias the results due to model simplification. The misfit of the spectral model to the data is minimized in the log-log space using the $L2$ norm. Using the resulting minimum misfit model, the residuals are then assumed to be an estimate of the normalized frequency-dependent elastic component of the site function $a_j(f)$. Consequently, by correcting for the geometric decay function S_{ij}, the frequency independent component of the modeled spectra – the signal moments – can be split into a single seismic moment M_0 and a site amplification term A_j relative to a common reference. However, a strong trade-off does exist between the moment and the average amplification. In order to decouple the site effect from the magnitude determination, M_{JMA} values determined by the Japan Meteorological Agency are fixed when available. No significant differences between M_{JMA} and M_w were found for shallow and strong events (Katsumata 1996) which are mostly encountered in this study.

For the reconstruction of the empirical amplification for the KiK-net sites, all the waveforms recorded by KiK-net network (surface seismometers only) in the period 1997-2010, and corresponding to events with hypocentral depth ≤ 25 km, were exploited. As result, we obtained an estimate for the terms concurring to local site amplification (A_j, $a_j(f)$ and κ_j, see equation 2) for each of the 689 KiK-net sites, although a simultaneous robust reconstruction of all three contributions was possible only at 477 stations (70% of the total). It is important to mention that, in the presented case, the regional reference assumed to define A_j is the reference Japanese V_S profile as defined in Poggi et al. (2013).

In Figures 8-10 we show the local site amplifications (equation 2) for the entire set of KiK-net stations, and selections A and B, respectively. In each case, the site amplifications are subdivided by SIA soil class, and the number of events constraining each frequency component of the amplifications functions are reported in the lower right panel.

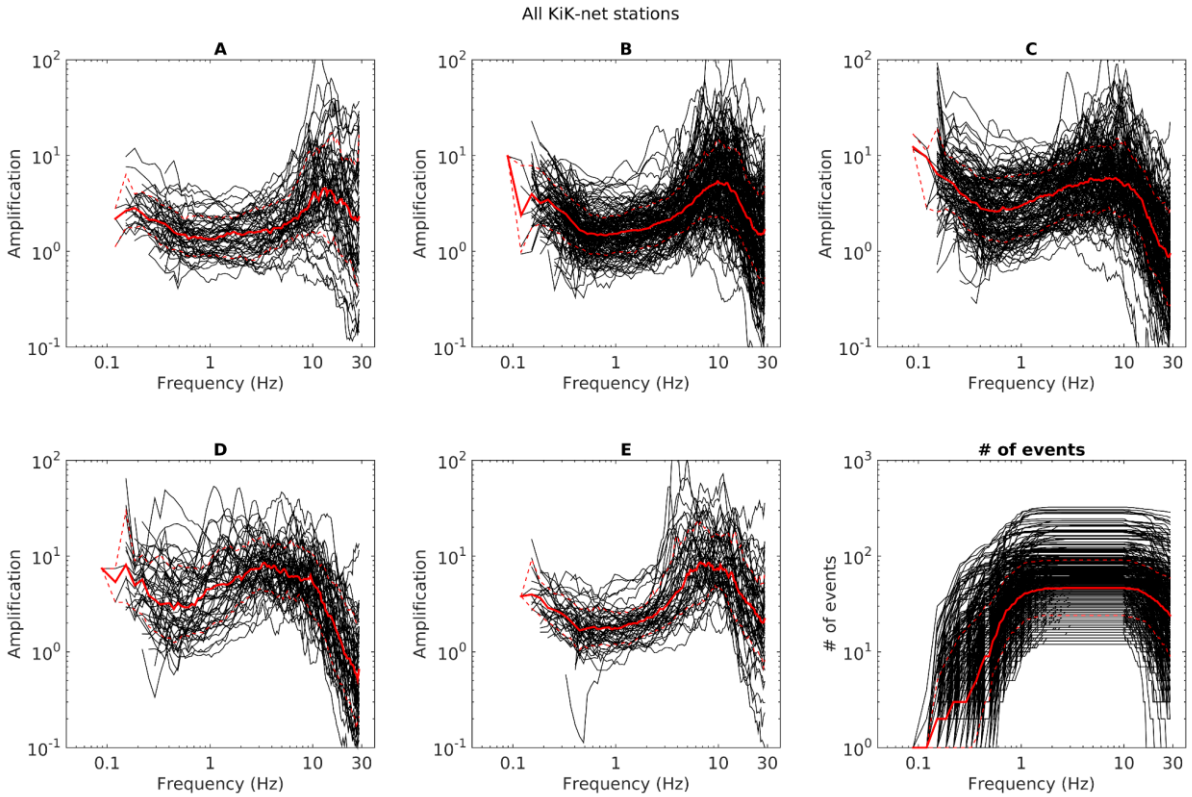

Figure 8 – Site amplification functions (black lines) for all the available KiK-net stations, referred to the Japanese reference Vs profile. Subpanels 1-5 collect the amplification functions for soil classes A-E according to SIA normative. The median for each group is represented with a red line; the 15th and 85th percentile with red dashed line. The panel in the lower right corner indicates the number of events concurring to the estimation of each single amplification function, with no distinction for soil class.

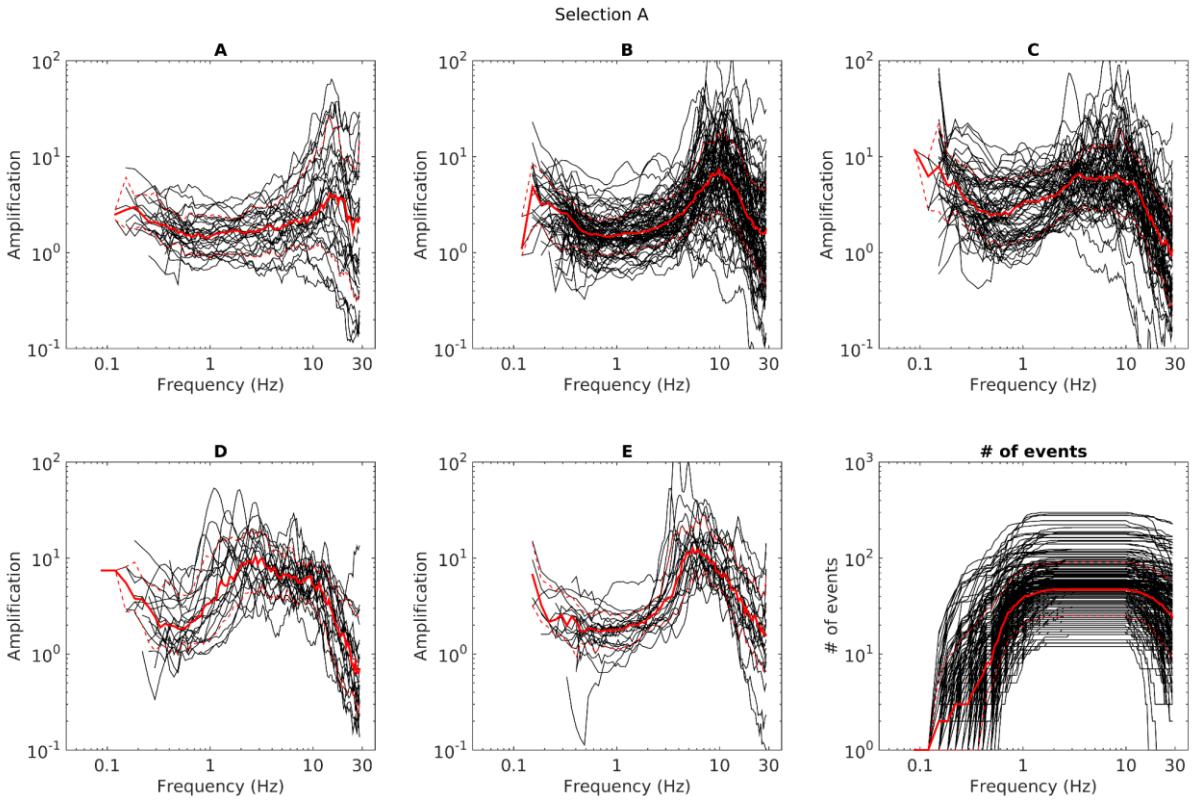

Figure 9 – Site amplification functions (black lines) for the KiK-net stations belonging to selection A, referred to the Japanese reference Vs profile. Subpanels 1-5 collect the amplification functions for soil classes A-E according to SIA normative. The median for each group is represented with a red line; the 15th and 85th percentile with red dashed line. The panel in the lower right corner indicates the number of events concurring to the estimation of each single amplification function, with no distinction for soil class.

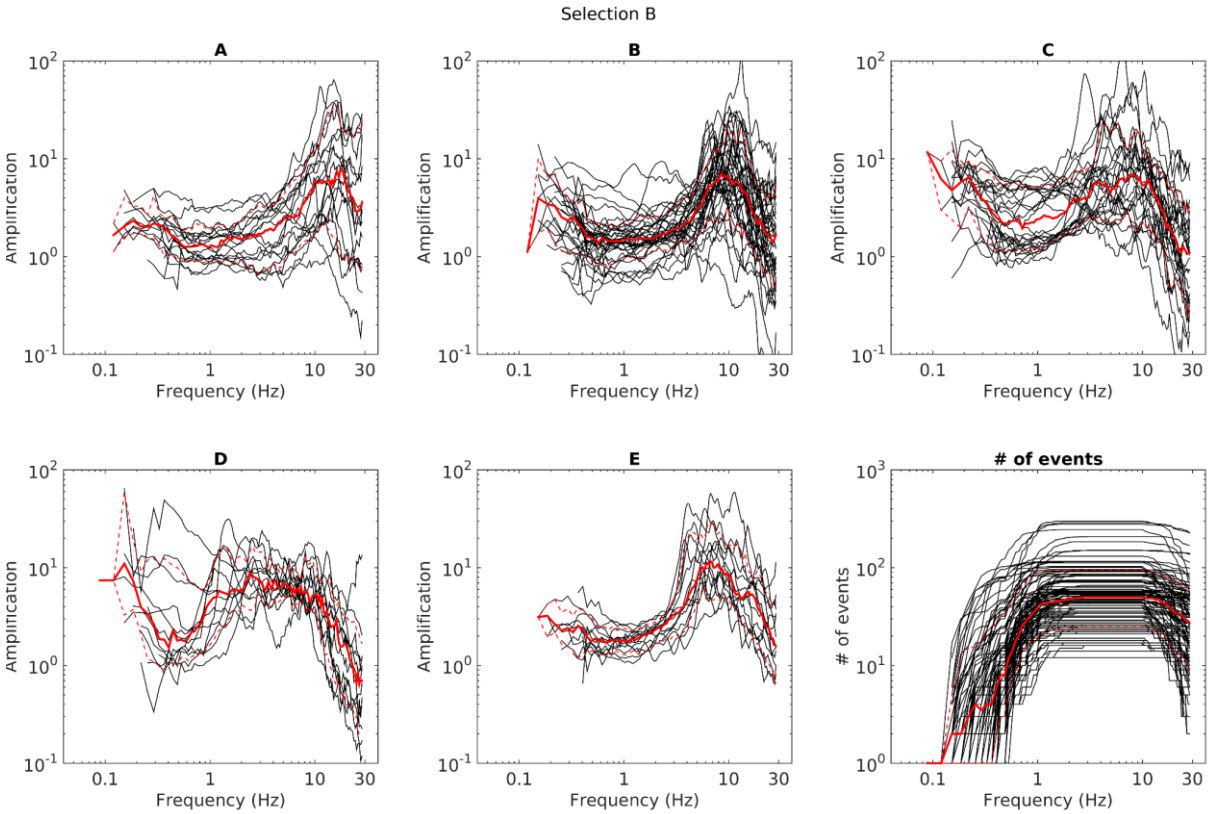

Figure 10 – Site amplification functions (black lines) for the KiK-net stations belonging to selection B, referred to the Japanese reference Vs profile. Subpanels 1-5 collect the amplification functions for soil classes A-E according to SIA normative. The median for each group is represented with a red line; the 15th and 85th percentile with red dashed line. The panel in the lower right corner indicates the number of events concurring to the estimation of each single amplification function, with no distinction for soil class.

As expected, going from soil class A through B, C, and finally to D, the median fundamental frequency peak moves progressively from higher (~15 Hz for class A) to lower values (~4 Hz for class D), as the soil material becomes on average softer and softer. A different case is represented by class E, that gathers sites with thin (5-20 m thick) surficial soft sediments, underlain by stiffer (Vs>800 m/s) material; this shallow impedance contrast produces again relatively high values of f_0 (around 8 Hz). The considerations illustrated here are globally valid for all the three considered sets of KiK-net sites: the entire network (Figure 8), and the subsets selection A and B (Figures 9-10); it is also worth remarking the similarity between the trend observed in Figures 8-10 and in Figures 5-7 (referring to surface to borehole ratios).

The agreement between computed empirical amplification functions and surface to borehole ratios was assessed. Globally, the consistency between the two estimates is good, and confirms the reliability of the procedure followed to obtain the site amplification functions from spectral modeling; as shown in Figure 11, the ratios between corresponding empirical amplifications and SB ratios converge on average around ratio = 1, in particular within the frequency band of reliable data 0.5-20 Hz. As an example, in Figure 12 the comparison for some sample KiK-net stations bearing very good agreement is displayed. To quantify this conformity over the entire KiK-net dataset, the misfit between the empirical amplification function and the corresponding SB ratio was obtained as RMS of the differences between the two functions in log scale (in the 0.5 – 20 Hz interval). Obviously, the pairs of SB ratios and empirical amplification functions are referred to the same condition (Japanese reference Vs profile). The population of misfits (Figure 13) follows a gradual distribution for low RMS values (0.05 - 0.4); then, at the 85th percentile, the RMS suddenly increases abruptly. This threshold was reasonably selected to define the unreliable empirical amplification functions; these were hence discarded, and excluded from the subsequent processing steps (see following sections).

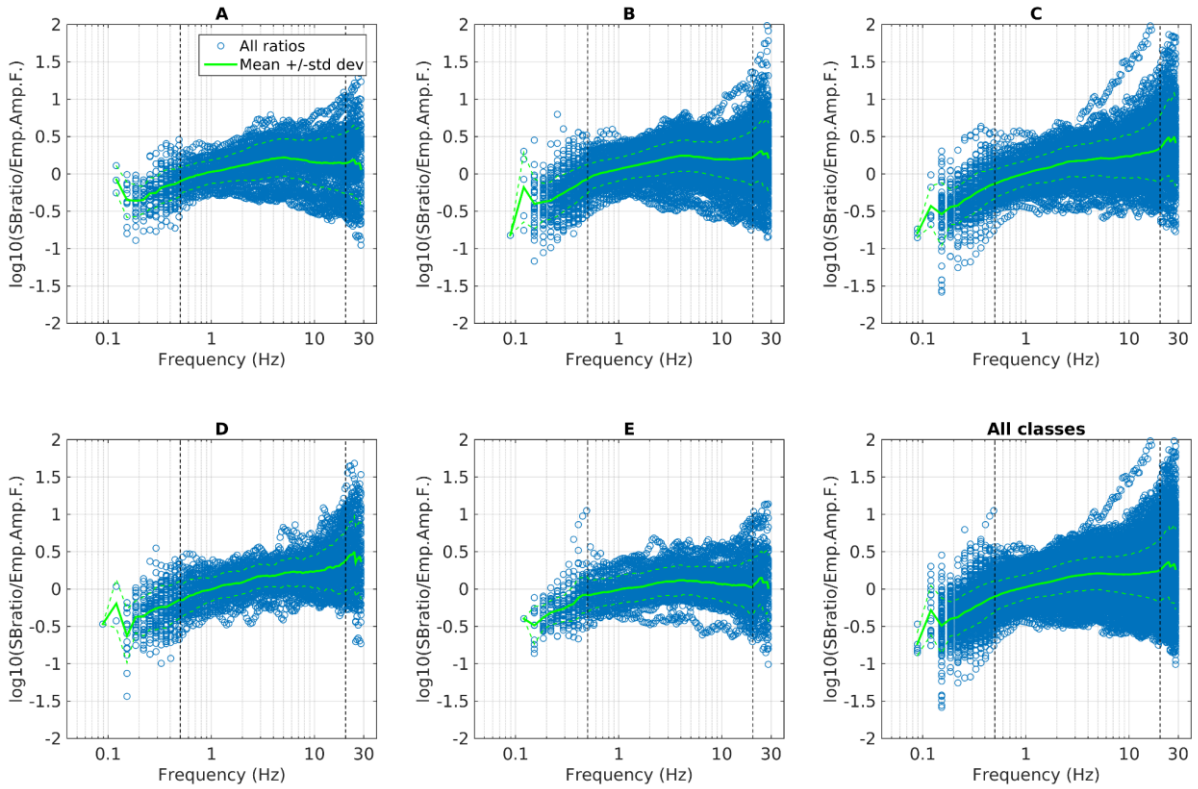

Figure 11 – ratios between corresponding surface to borehole ratios and empirical amplification functions. All available KiK-net stations were included in this representation. The vertical black dashed lines indicate the frequency band of valid comparison between the two datasets (0.5 – 20 Hz).

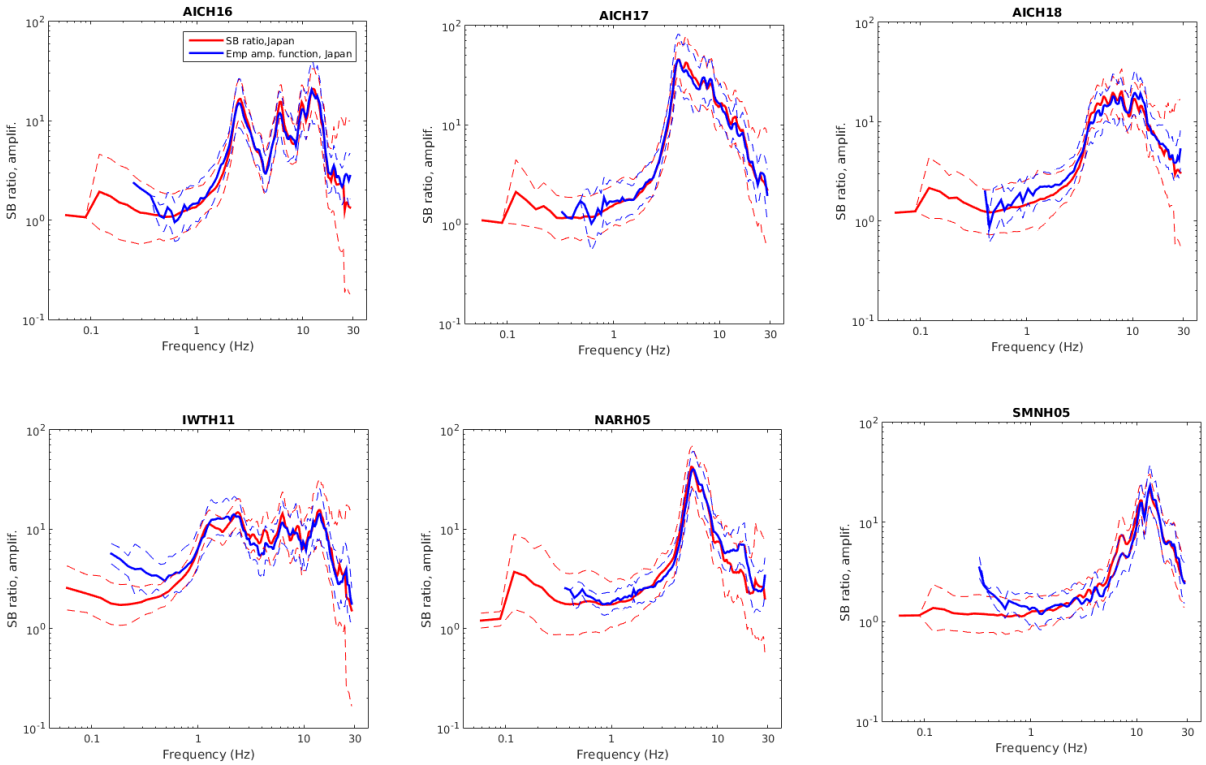

Figure 12 – example of comparison between empirical amplification function and surface to borehole ratio (both referred to the Japanese reference profile) for six KiK-net stations (the RMS between the two functions is below 0.1 in all cases). All presented stations belong to selection A; AICH16, AICH18, NARH05 and SMNH05 belong to selection B as well.

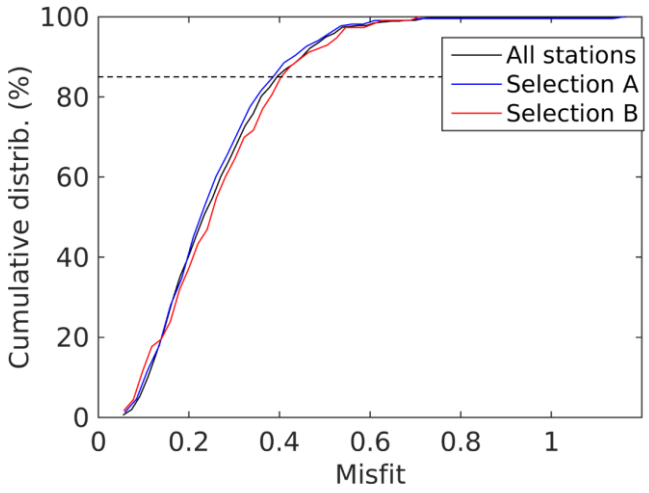

Figure 13 – cumulative distribution of misfit between corresponding surface to borehole ratios and empirical amplification functions. The dashed black line indicates the threshold (85th percentile) beyond which the distance between the two functions is considered as excessive and therefore the corresponding empirical amplification functions are discarded.

6.0 Translating to the Swiss reference conditions

In section 4 and 5 we have illustrated the procedures we followed to obtain, possibly at each KiK-net site, two parallel estimates of the soil amplification function (empirical amplification function from spectral modeling, section 5, and SB ratios, section 4). To ensure comparability within each dataset and between the two, these functions are brought to a common reference, i.e. the reference rock Vs profile for Japan (Poggi et al., 2013).

To use these amplification functions in a study of seismic hazard assessment for the Swiss territory, a further step is needed; SB ratios and empirical amplification functions have to be translated to the national Swiss rock reference conditions (Poggi et al., 2011) in terms of both average amplification level and anelastic attenuation (Edwards and Fäh, 2013).

Figure 14 shows the computed SB ratios and empirical functions for the same KiK-net sites of Figure 12, after being referred to the Swiss reference condition. Only the frequency band considered to carry reliable information (0.5 – 20 Hz) is included in the representation; this is the amplification function interval that will be passed on to the following processing steps (see next sections).

A comparison between Figure 12 and 14 evidences the lower level of amplifications determined by the referencing to the Swiss condition; this change is related to the difference in stiffness between the Japanese and Swiss rock reference, the latter being “softer”.

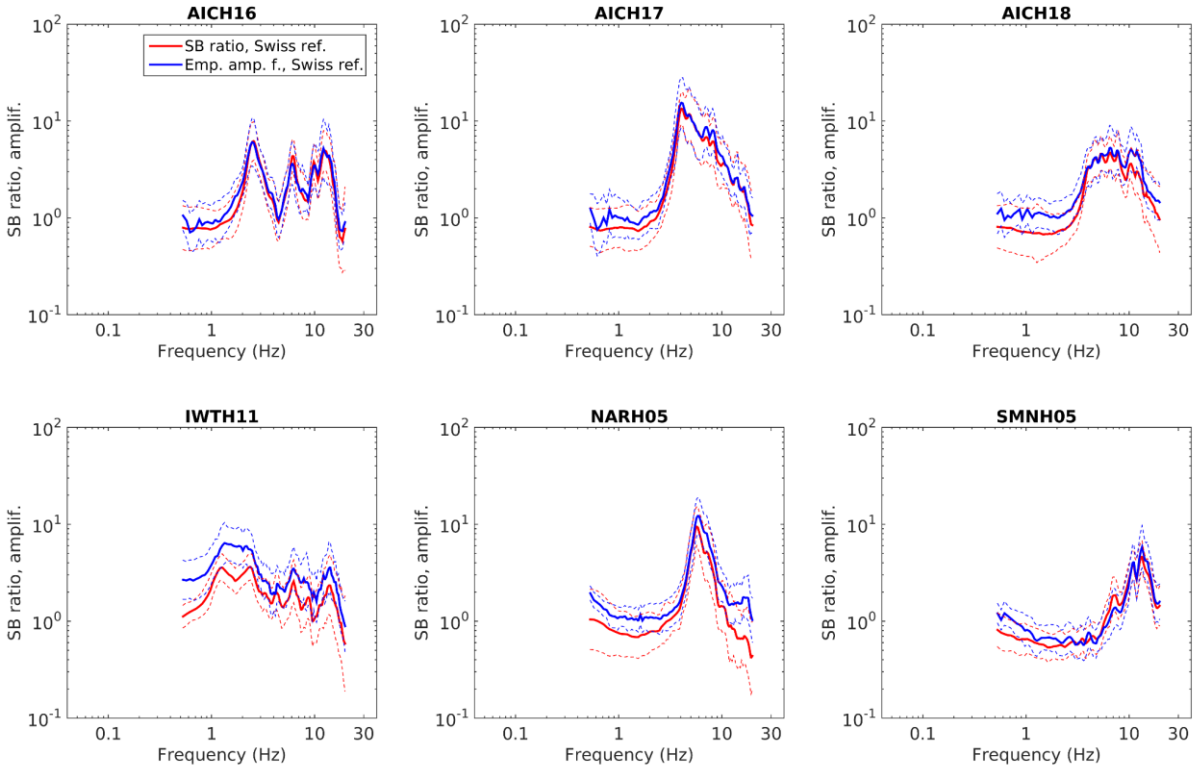

Figure 14 – SB ratios and empirical amplification functions from six sample KiK-net sites (same of Figure 12) after being translated to the Swiss reference conditions. Only the frequency band of reliable data (0.5-20 Hz) is represented.

7.0 Response spectral amplification

The population of Fourier amplification functions, estimated from either spectral modeling (5) or computation of surface to borehole ratio (4), once brought to the Swiss reference conditions (6), was then transformed into a dataset of response spectra. For this operation, a stochastic approach based on random vibration theory (RVT, Cartwright and Longuet-Higgins, 1956), as implemented by Boore (2003), was followed. According to this approach, the input earthquake spectrum is first analytically modeled, based on a variety of selected parameters that refer to the scenario (e.g. magnitude, distance, stress drop) and to the propagation model (attenuation, duration, site amplification). In a second step, the response spectrum is directly derived resorting to random vibration theory.

The chosen reference ground motion is compliant with the Swiss spectral model as defined in Edwards and Fäh (2013) for the alpine region. It is worth highlighting the consistency between the selected ground motion model and the Swiss reference rock condition (Poggi et al., 2011) assumed for the referencing of Fourier amplification functions to a common condition (paragraph 6).

In terms of scenario, we considered a single combination of magnitude (M_w = 6.5), stress drop (SD = 6.3 MPa) and distance (rupture distance Rrup = 10 km). The reasoning is twofold; on one side, this scenario is in fact significant with respect to the disaggregation analysis evaluated for the city of Sion (SED, 2016), itself considered in this study as representative of the hazard scenario in Switzerland in zone 3b, that is the zone where the highest levels of ground motion are to be expected (SIA 261, 2014). On the other hand, it has been shown that response spectra, when normalized to the rock reference ground motion, i.e. transformed to response spectral amplification functions, bear little sensitivity towards the chosen input scenario (see later in this paragraph, Figure 23 in particular; Poggi and Fäh 2015, Poggi et al., 2017).

In fact, for the purposes of our study, it is not crucial to estimate the absolute value of spectral acceleration at a variety of sites; rather, it is meaningful to estimate the amplification, in terms of spectral acceleration, determined by a variety of local site (soil) configurations. Therefore, once the response spectra are computed (using alternatively empirical amplification functions or SB ratios as input site-specific Fourier amplifications), these are then normalized to the response spectra at the rock reference model (in our case, the Swiss reference rock conditions). The obtained ratios are here referred to as response spectral amplification functions (see Figure 15 for an example of computed response spectra).

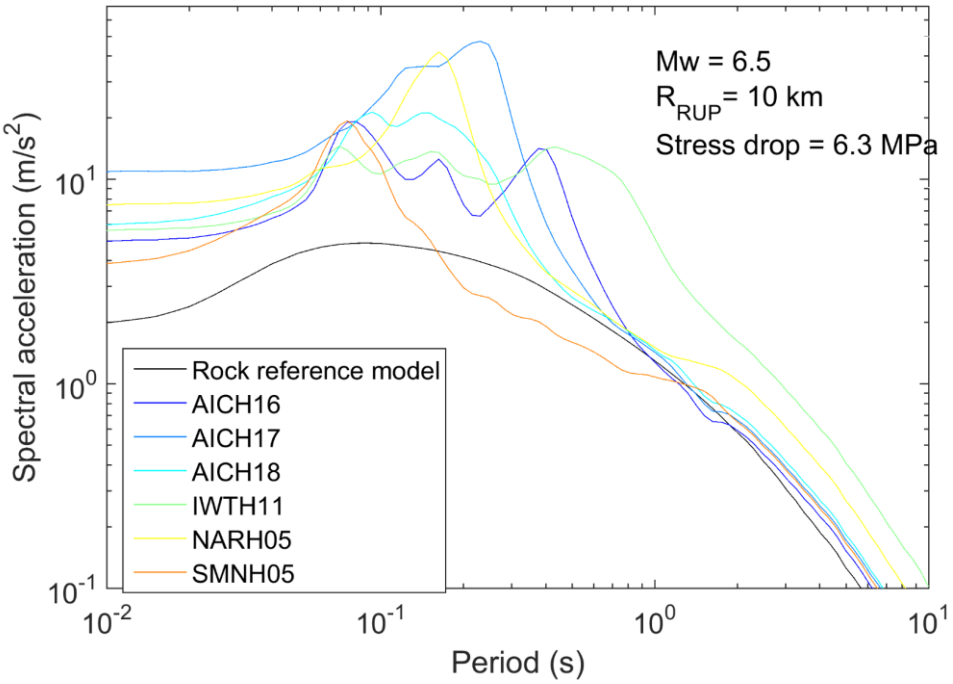

Figure 15 – Acceleration response spectra for the Swiss rock reference model (black line) and for six sample KiK-net sites (colored lines; the same of Figures 12 and 14). AICH16 and IWTH11 belong to class C; AICH17, AICH18 and NARH05 belong to class E; SMNH05 belongs to class B. The ratios between colored response spectra (including site amplification with respect to Swiss rock) and the rock-reference response spectra represent the response spectral amplification functions.

In the following set of figures (Figures 16 - 21) we display the response spectral amplification functions evaluated for the population of KiK-net sites; we distinguish between response spectral amplification functions obtained using either SB ratios (Figures 19-21) or empirical amplification functions (Figures 16 – 18) as input site-specific Fourier amplification.

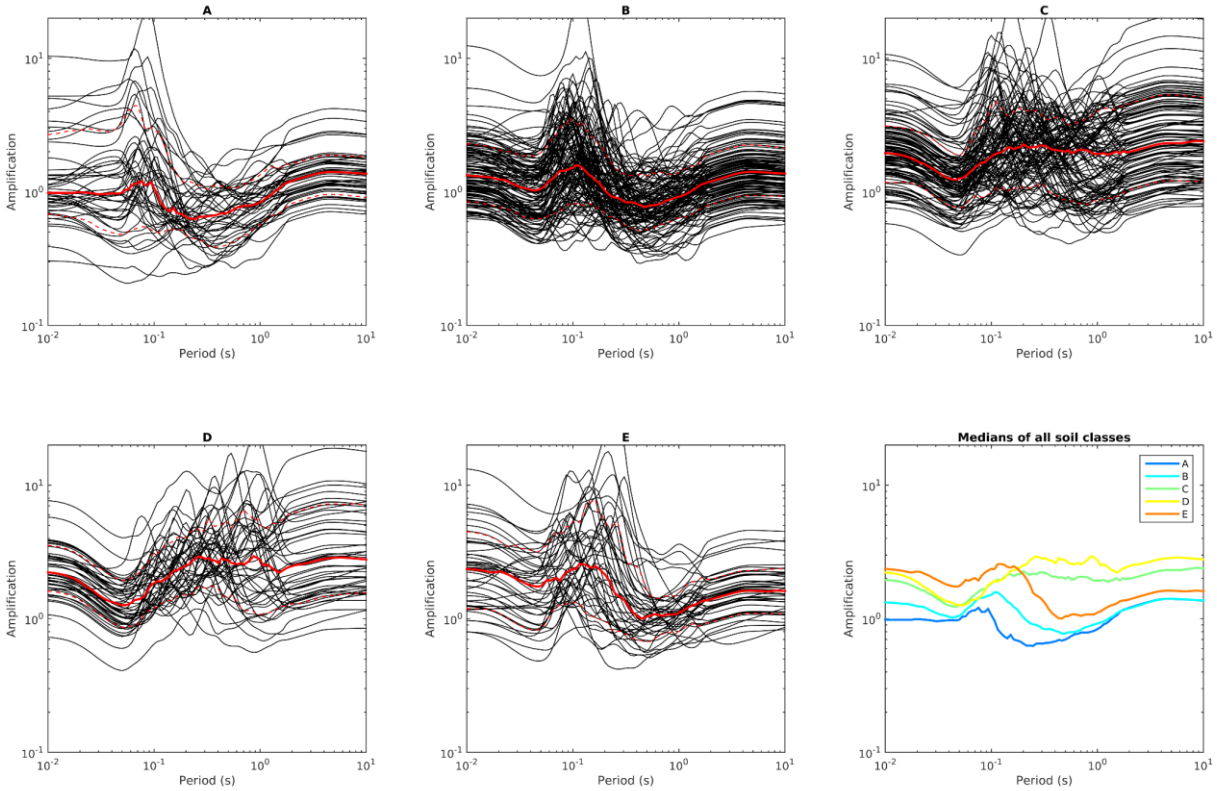

Figure 16 – Response spectral amplification curves (black lines) estimated adopting the empirical amplification functions from spectral modeling as input Fourier amplification functions. All KiK-net sites for which a reliable empirical amplification function is available (see section 5) were considered. The median, 15th and 85th percentiles are represented with continuous and dashed red lines, respectively. The median curves are displayed altogether in the lower right panel.

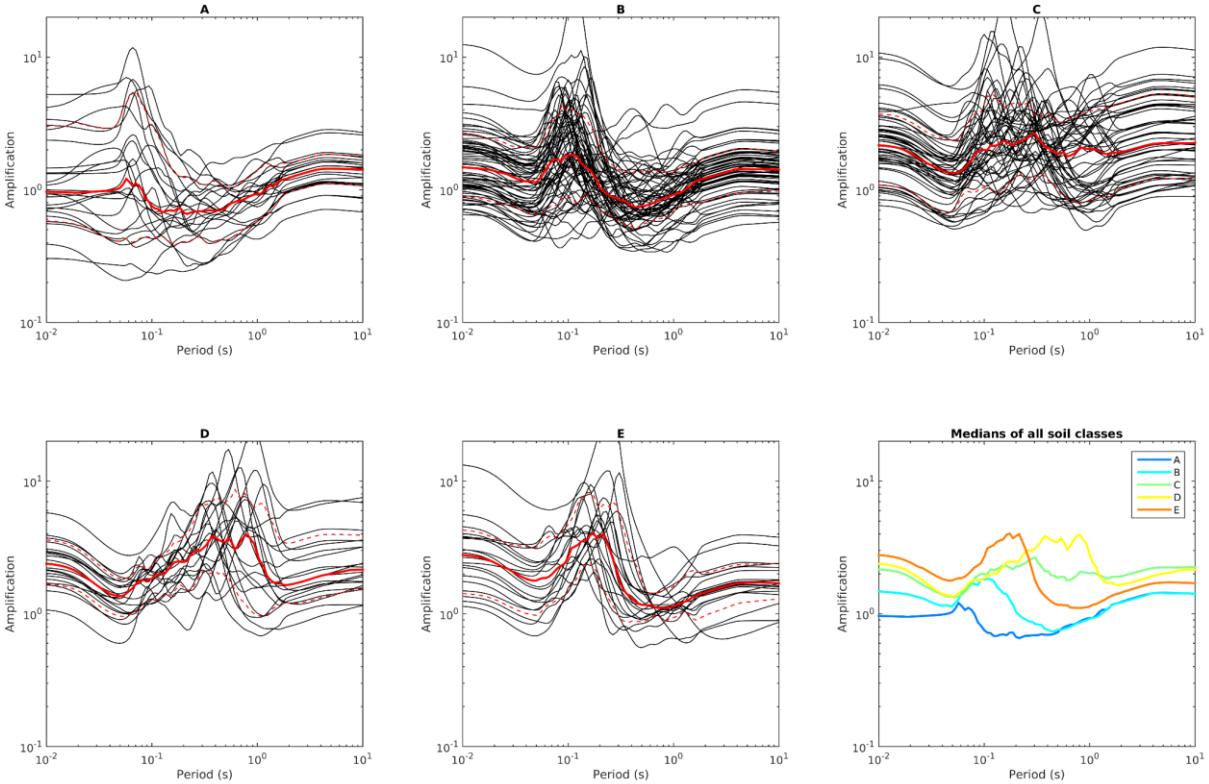

Figure 17 – Response spectral amplification curves (black lines) estimated adopting the empirical amplification functions from spectral modeling as input Fourier amplification functions. KiK-net sites from selection A for which a reliable empirical amplification function is available (see section 5) were considered. The median, 15th and 85th percentiles are represented with continuous and dashed red lines, respectively. The median curves are displayed altogether in the lower right panel.

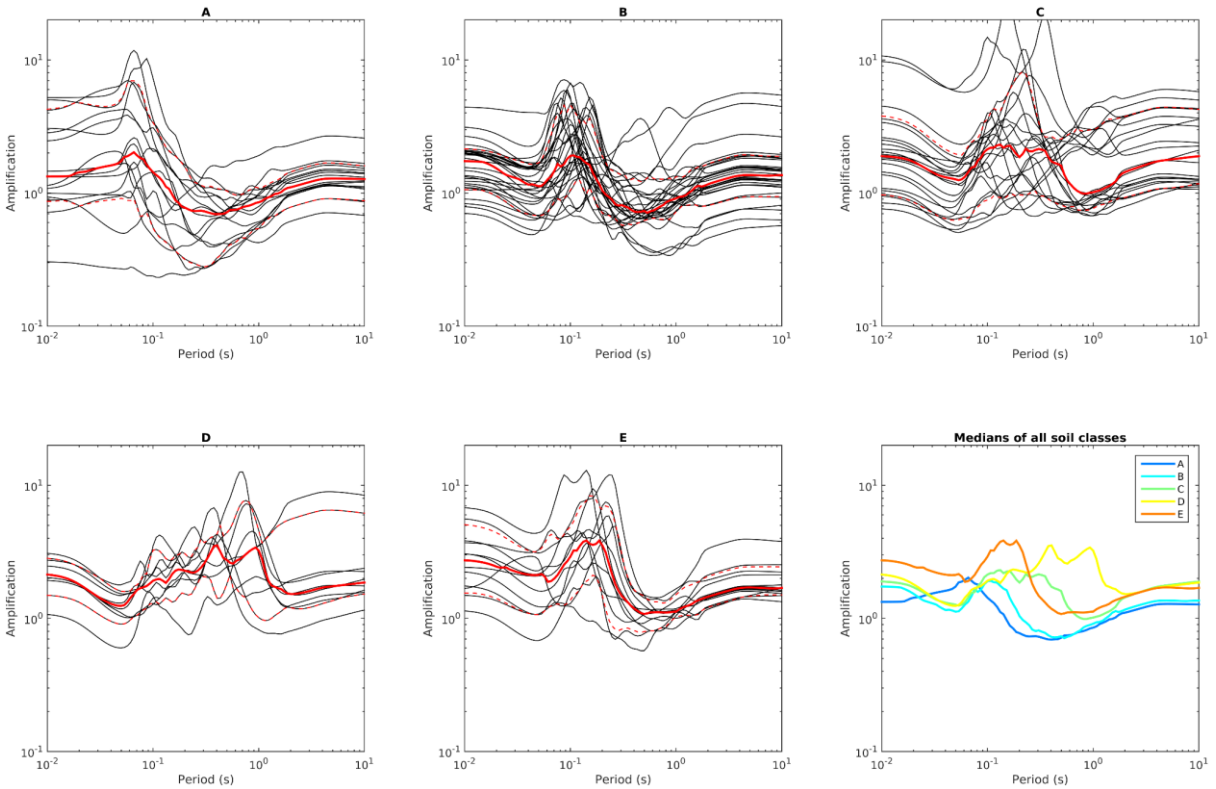

Figure 18 – Response spectral amplification curves (black lines) estimated adopting the empirical amplification functions from spectral modeling as input Fourier amplification functions. KiK-net sites from selection B for which a reliable empirical amplification function is available (see section 5) were considered. The median, 15th and 85th percentiles are represented with continuous and dashed red lines, respectively. The median curves are displayed altogether in the lower right panel.

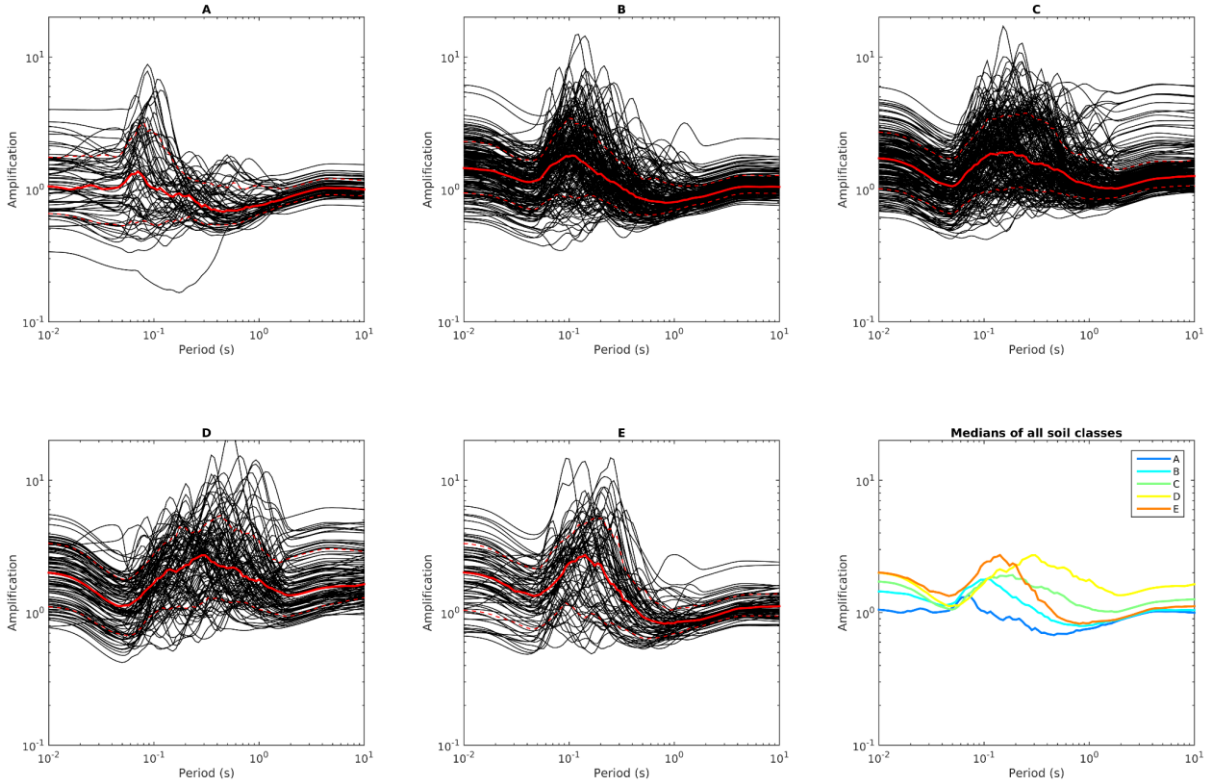

Figure 19 – Response spectral amplification curves (black lines) estimated adopting SB ratios as input Fourier amplification functions. All KiK-net sites were considered. The median, 15th and 85th percentiles are represented with continuous and dashed red lines, respectively. The median curves are displayed altogether in the lower right panel.

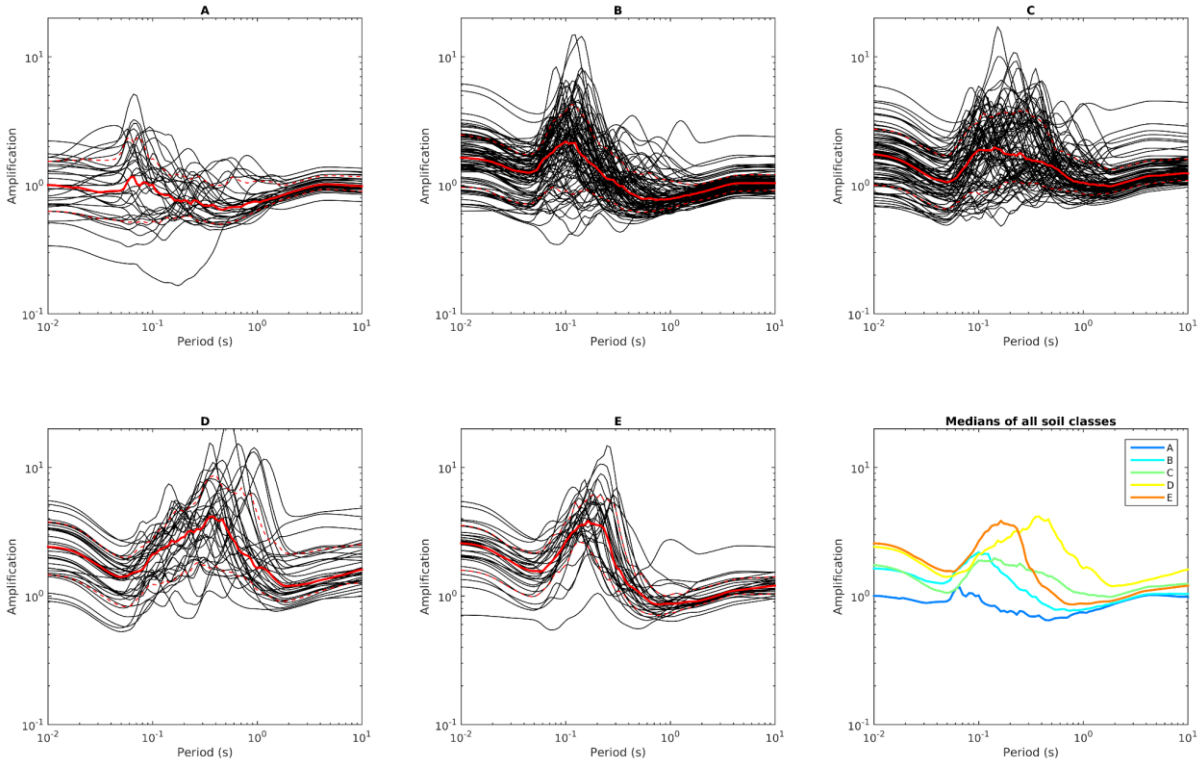

Figure 20 – Response spectral amplification curves (black lines) estimated adopting SB ratios as input Fourier amplification functions. KiK-net sites from selection A were considered. The median, 15th and 85th percentiles are represented with continuous and dashed red lines, respectively. The median curves are displayed altogether in the lower right panel.

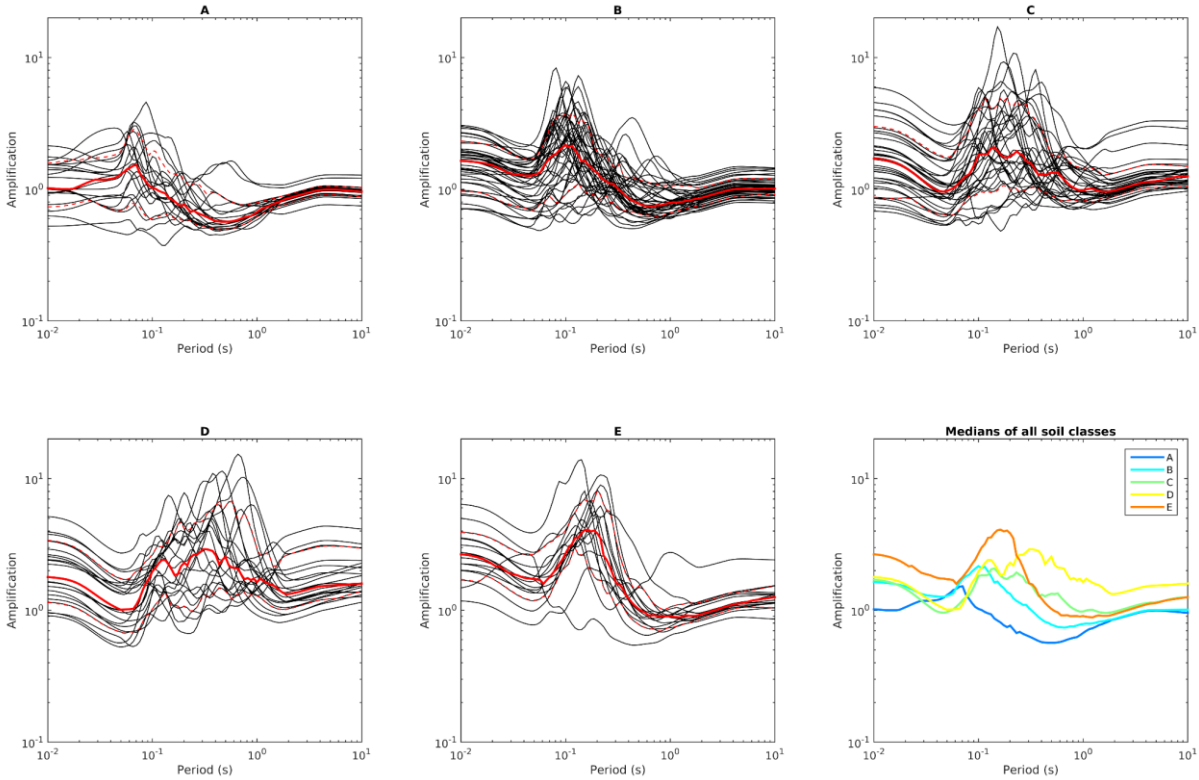

Figure 21 – Response spectral amplification curves (black lines) estimated adopting SB ratios as input Fourier amplification functions. KiK-net sites from selection B were considered. The median, 15th and 85th percentiles are represented with continuous and dashed red lines, respectively. The median curves are displayed altogether in the lower right panel.

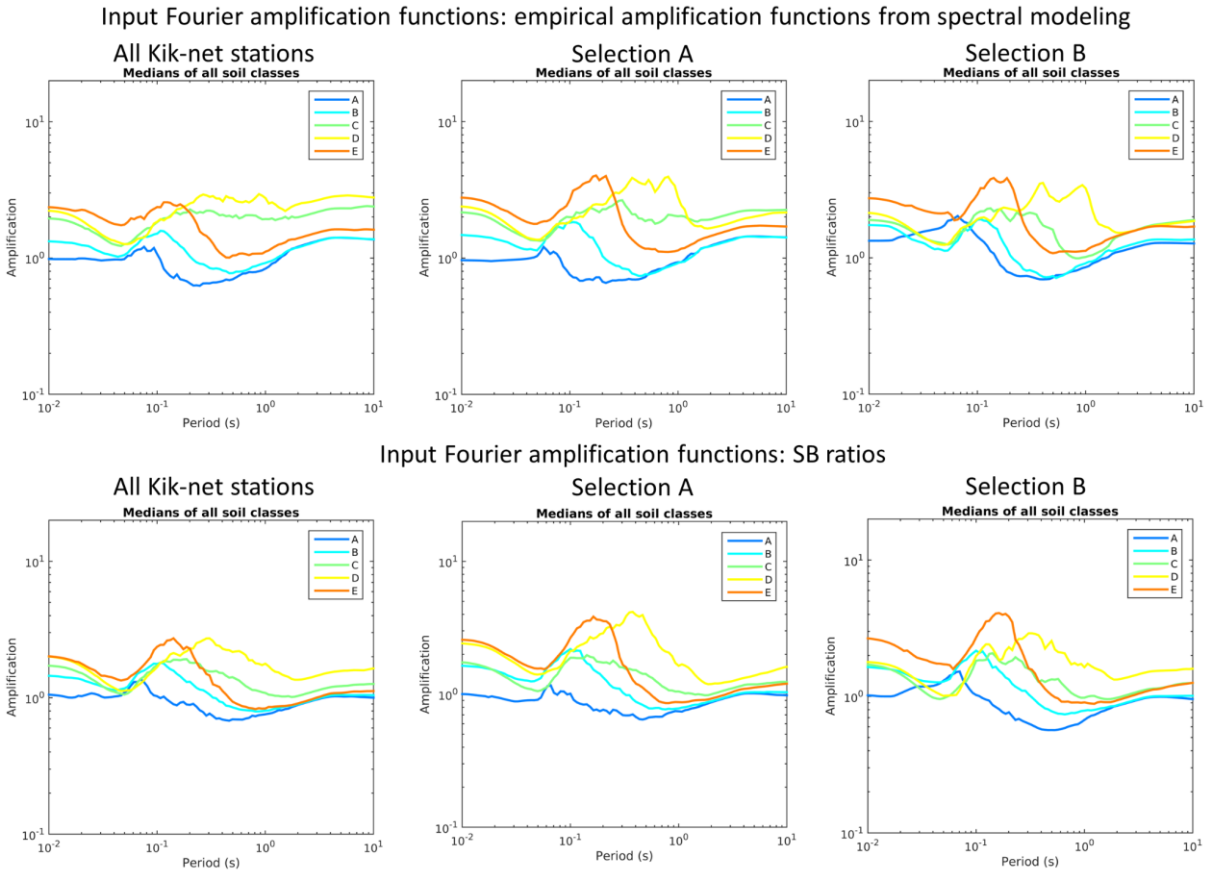

Figure 22 – Comparison among the medians of the various subsets of response spectral amplification functions, obtained adopting the empirical amplification functions (top panels) or SB ratios (bottom panel) as input Fourier amplification. Different KiK-net sites ensembles are considered: all stations (left panels), selection A stations (center panels), selection B stations (right panels).

Figure 22 offers an overview of the obtained response spectral amplification functions, comparing the median curves from different sets of KiK-net stations (from left to right: all available stations, selection A and B), and from different input site amplification functions (top: empirical amplification functions; bottom: SB ratios).

The variety of input Fourier amplification functions, sets of KiK-net stations and soil types allows to compare and comment on each element of differentiation.

Comparison among different soil classes
In all the subpanels of Figure 22, the following features can be observed:

- Moving from class A to D, the average level of amplification is increasing. This is consistent with the soil classification (rock in class A, stiffer soil in class B, becoming softer and softer towards D class);
- From class A to D, the fundamental period of resonance moves progressively toward higher values (~0.07 s in class A, ~0.4 s in class D);
- A particular case is represented by class E; the shallow impedance contrast between rock and sediments determines a relatively low value for the fundamental periods (around 0.16 s); on the other hand, the soft surficial layers produce high amplification (at approximately the same level of class D);
- The median curves referring to class A bear values lower than 1 (i.e. deamplification) for wide period intervals: in fact, a significant portion of the sites falling in class A are actually stiffer than the Swiss reference rock (see the individual black curves in the relevant panels).

Comparison among different KiK-net sites assortments
Although a consistent behaviour for the different classes can be tracked disregarding the considered KiK-net dataset (see previous paragraph), some differences are also evident.

- The main dissimilarity can be observed when switching from the entire KiK-net database to selection A sites; in the latter case, median curves have a more marked, narrower resonance period peak, reaching higher amplification values at its top.
  Understandably, this is the because selection A sites have a proven Vs profile, therefore their class affiliation is reliable, and consequently the sites falling in the same class are characterized by a higher degree of consistency;
- In general, minor differences are spotted when moving from selection A to B. When these become significant (see for instance class A and C in the upper right panels, or to a lesser extent classes A and D in the lower right panels), this is possibly because within selection B, the median curve is evaluated over a small population of individual functions (therefore global statistical estimators, as median or mean, might lose their robustness).

Comparison between different input Fourier amplification functions
In general, the use of SB ratios or empirical amplification functions as input for the computation of response spectral amplification yield similar results. Nevertheless,

- Comparing Figure 16 with 19 (and 17 –20, 18 – 21), it is evident that the populations of individual response spectral amplification functions from empirical amplifications are more scattered, while a greater consistency characterizes those from SB ratios;
- Globally (Figure 22) the response spectral amplifications from SB ratios have lower values at large periods (> 1 s). This is consistent with the comparison of SB ratios *vs* empirical amplification functions (see Figure 11: below 1 Hz, empirical amplification functions assume on average higher values).

The results shown in Figures 16-22, and commented above, refer to a single, although significant, source scenario combination: magnitude 6.5, stress drop 6.3 MPa, distance 10 km. However, as earlier anticipated and illustrated by Poggi and Fäh (2015) and Poggi et al. (2017), when site-specific response spectra are normalized to the rock reference ground motion, the output response spectral amplification functions have little sensitivity with respect to source parameters such as magnitude and distance (Figure 23).

Therefore, the population of computed response spectral curves is considered reasonably valid for a set of magnitude-distance combinations consistent with the selected illustrative seismic hazard scenario of Sion (itself considered in this study as representative of the hazard scenario in Switzerland in zone 3b, i.e. the zone where the highest levels of ground motion are expected).

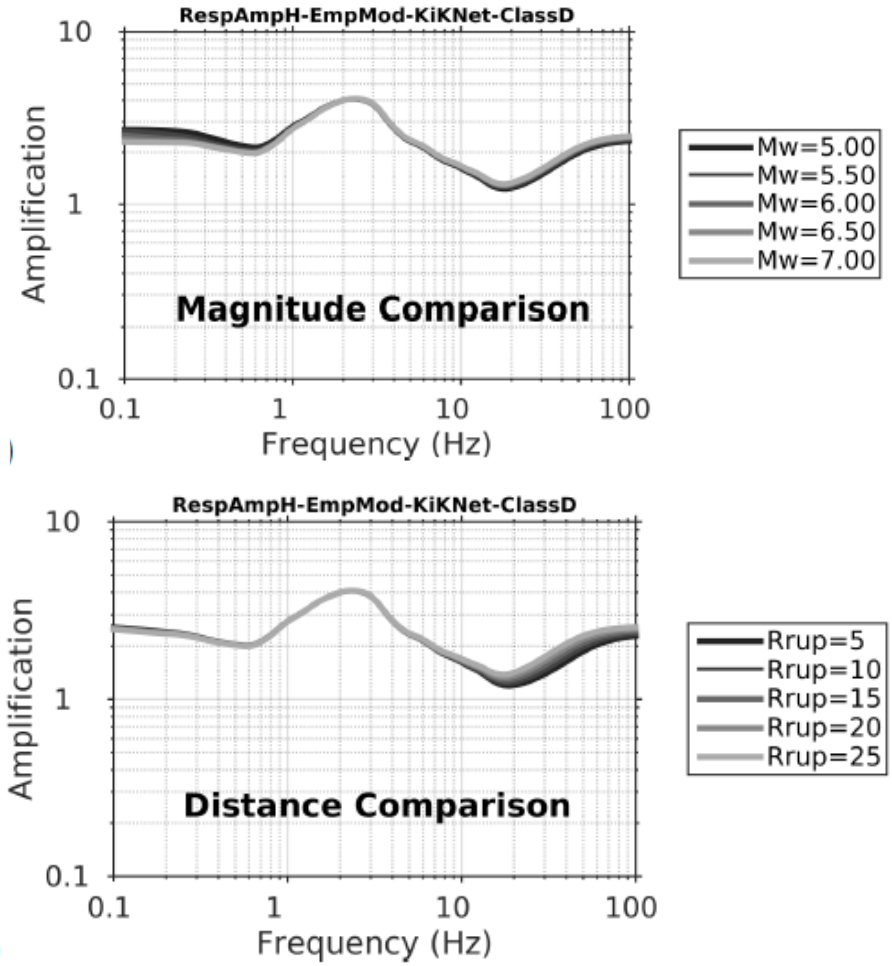

Figure 23: Example of sensitivity of response spectral amplification functions (selection A, SIA class D) with respect to magnitude (top) and distance (bottom). Figures drawn from Poggi and Fäh (2015).

8.0 High levels of ground motion

So far, we have reconstructed site amplification functions assuming the independence of the physical properties related to soil amplification on the level of applied ground motion. However, it is known (e.g. Darendeli, 2001) that the shear response of soils is strain-dependent; starting from the early works of Seed and Idriss (1969) and Hardin and Drnevich (1972) it is understood that soft soils can exhibit a nonlinear behavior during strong earthquakes, with decreasing shear modulus and increasing shear damping ratio with the strain level, after a threshold of significant ground motion is exceeded.
This section is dedicated to the assessment of the relevance of soil nonlinearity in ground motions determined by shallow events, in consistency with the Swiss scenario.

In search for empirical evidence of non-linear soil behavior, the whole available time span (1997-2016) of KiK-net recordings was scanned, and orientation-independent (Boore et al., 2006) PGAs for the horizontal component were jointly computed for the surface and borehole receivers' recordings, produced by the same events. Similarly to the procedure for the estimation of SB ratios and empirical amplification functions (paragraphs 4, 5), shallow events (hypocentral depth < 20 km) were considered; besides, orientation-independent PGAs were computed for recordings likely to bear significant levels of ground acceleration (events with $M_w \geq 3$, hypocentral distance < 200 km). In total, 80189 couples of surface and borehole PGAs were computed, covering the whole set of 689 KiK-net stations; the distribution of values of peak ground accelerations is illustrated in Figure 24.

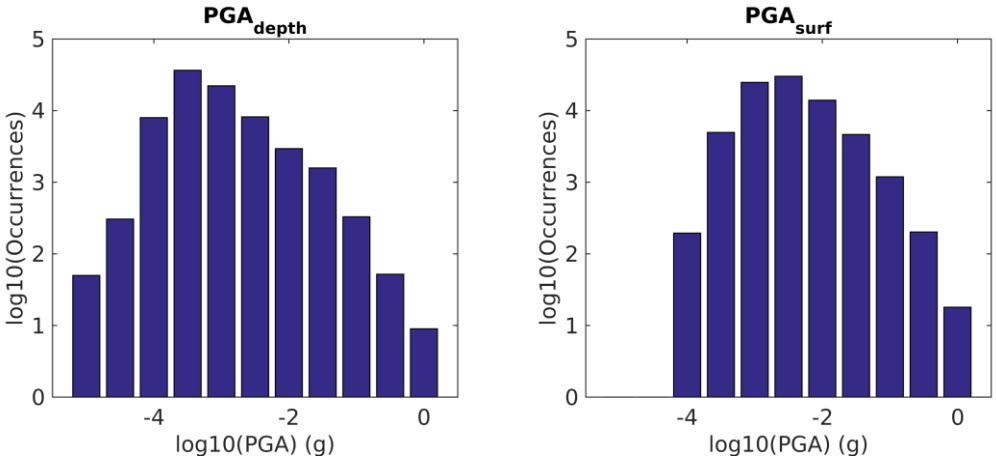

Figure 24 – histogram of the distribution of computed PGAs, recorded at the borehole (left panel) and at the surface (right) receivers.

This dataset of PGAs was sorted by attributing the acceleration values to the corresponding recording station. As frequently assumed in literature (e.g. Régnier et al., 2013), PGA is here considered as a measure of the level of ground-motion, and an approximate measure of the level of produced strain. The intention is to observe the distribution of surface PGAs (as a proxy of the strain response of softer shallow subsurface material, for which a possible nonlinear behavior might be expected (e.g. Darendeli, 2001) as a function of corresponding peak accelerations at the borehole receiver (measuring the response of the harder rock material at the base of the borehole, for which negligible nonlinearity is expected).
Plots representing PGAs measured at surface *vs* PGA at borehole for some sample KiK-net stations are represented in Figure 25. Collected data pairs appear to align along a line approximately parallel to 1:1, and placed above the latter. As expected, the peak acceleration at the surface is greater than that measured at depth; this is the effect of the soil amplification determined by the lower shear stiffness of the soil material closer to the surface. The linear pattern reflects the linearity of the soil response, i.e. a linear dependence between the applied stress (indirectly measured by PGA_{depth}) and produced strain (PGA at surface) which indicates a constant (strain-independent) shear modulus.

The examples reported in Figure 25 include values of $PGA_{depth} < 0.01$ g, i.e. they represent the soil behavior at low level of ground motion, where nonlinearity is not expected (Régnier et al., 2013). To assess the reliability of this linear approximation over the whole KiK-net dataset, and to mathematically model the linear soil response at low level of ground motion, we fitted for each station the couples of PGA_{surf}-$PGA_{depth,}$ with $PGA_{depth} < 0.01$, with the following form:

$$\log_{10}(PGA_{surf})=\log_{10}(PGA_{depth})+A \qquad (3)$$

Where *A* is the logarithm of the ratio between peak accelerations measured at the soil surface and at the borehole bottom, and it is therefore an approximate measure of soil amplification (Figure 26).

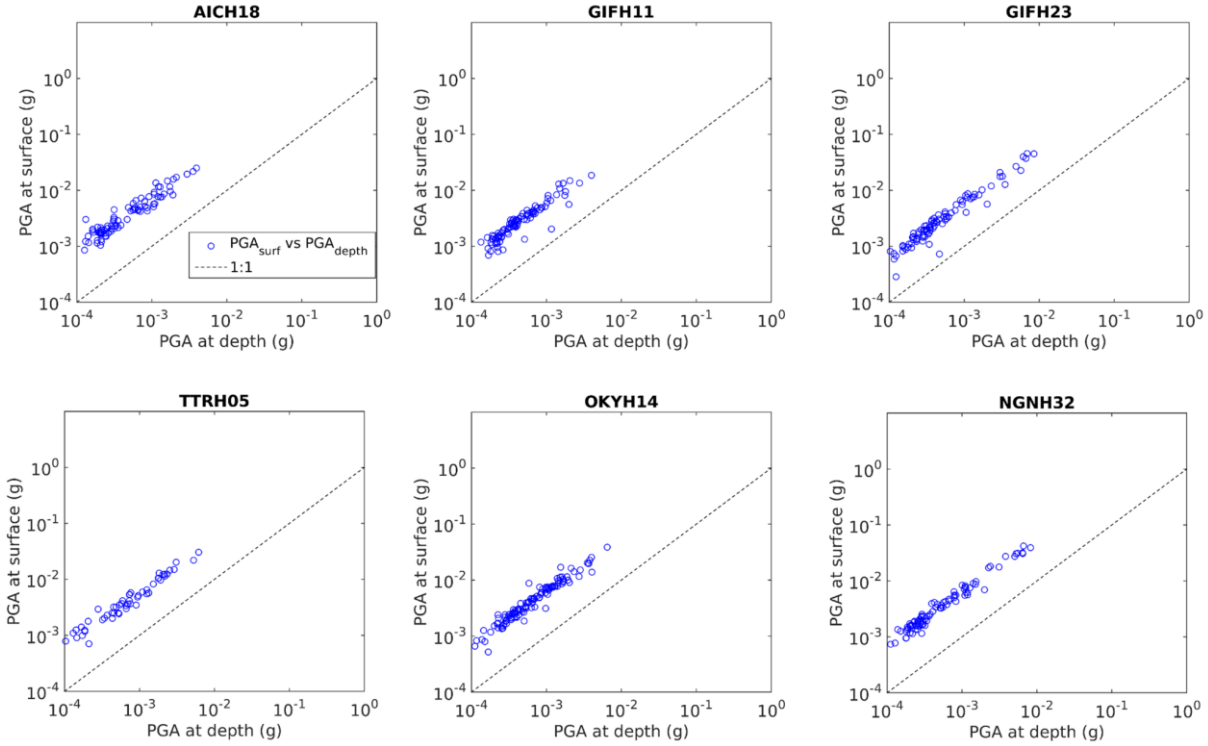

Figure 25 – couples of measured PGA at surface vs PGA at borehole (from recordings referring to the same event) for some sample KiK-net stations. The black dashed line represents the line where $PGA_{surf} = PGA_{depth}$.

As shown in Figure 26, the functional form introduced by equation 3 (red dashed line) is able to reproduce quite well the trend of the experimental data (the goodness of the fit is here estimated with the coefficient of determination R^2). Figure 27 represents the distribution of R^2 for all KiK-net stations: the vast majority of the coefficients of determinations has values close to 1, proving the applicability of equation 3 to the whole dataset.

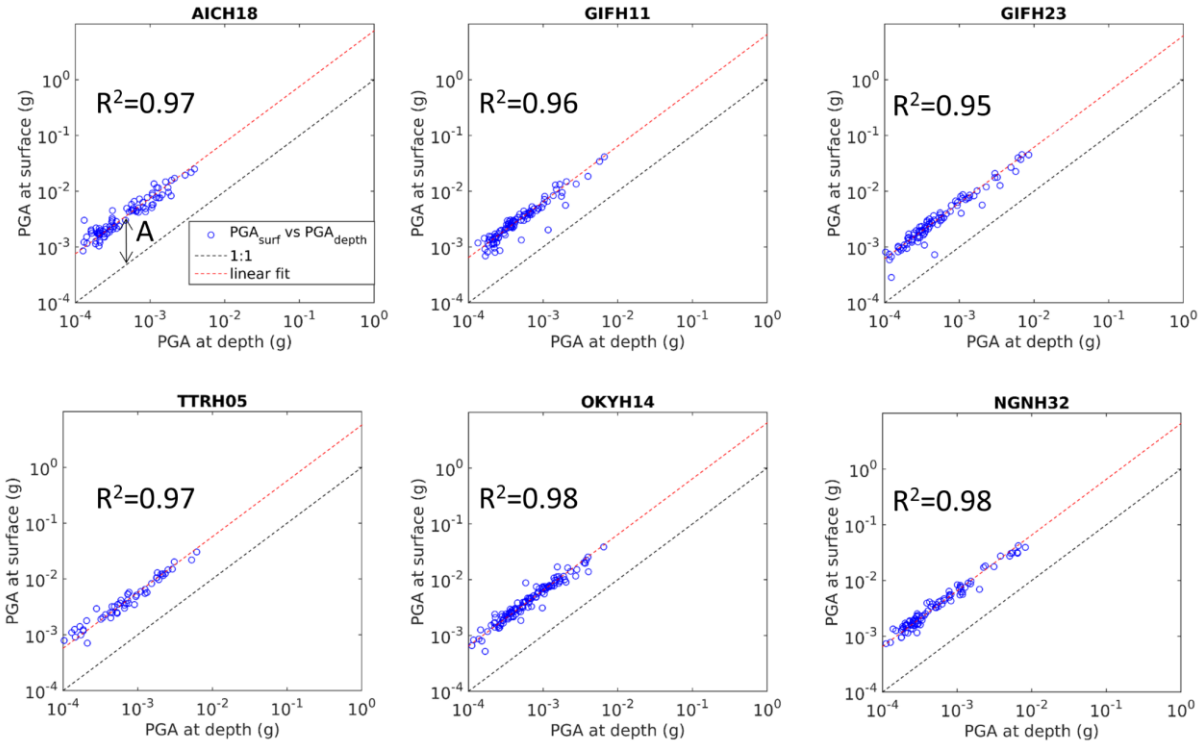

Figure 26 – Comparison between the sets of experimental pairs PGA_{surf}-PGA_{depth} (same of Figure 25) and their fit with equation 3 (red dashed line). The goodness of fit is expressed with the coefficient of determination R^2.

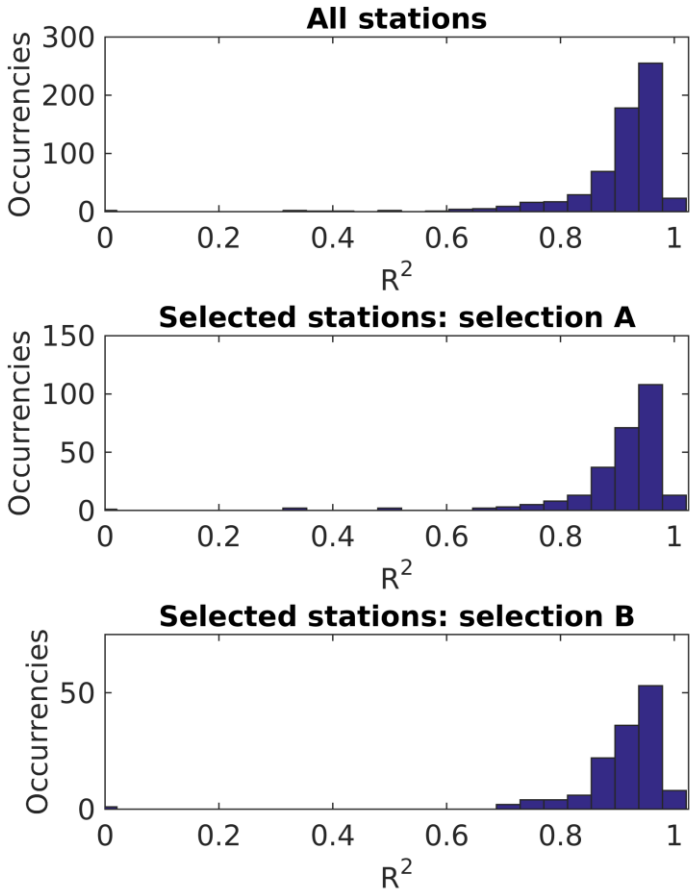

Figure 27 – goodness of fit between the pairs of experimental data PGA_{surf}-PGA_{depth} and equation 3. From top to bottom: histogram of the distribution of coefficients of determination (R^2) for the whole set of KiK-net stations (689 stations) and for the selected stations belonging to subset A (289 stations) and subset B (144 stations).

The obtained values for parameter *A* in equation 3 range between 0.2675 (2.5th percentile) and 1.0761 (97.5th percentile), corresponding to a ratio PGA_{surf}/PGA_{depth} of 1.89 and 11.91, respectively. As earlier anticpated, *A* is related to soil amplification: not surprisingly, its distribution shows some correlation with the soil class (Figure 28a) and with the ratio between Vs at the bottom of the borehole (Vs_{bh}) and at the surface (expressed in term of average Vs in the first 10 m, Vs10; Figure 28b).

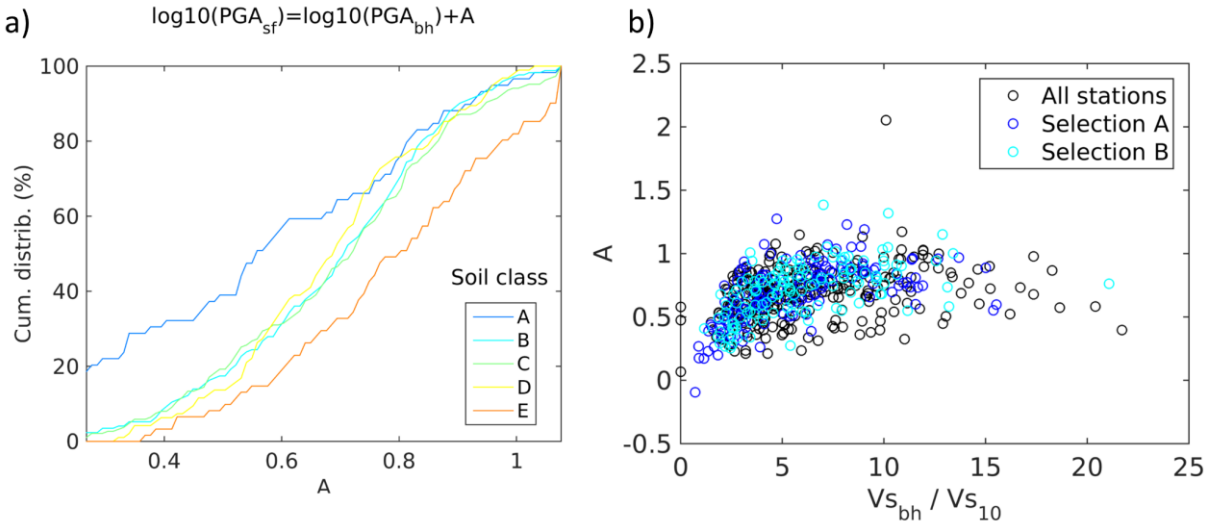

Figure 28 – Distribution of parameter A as a function of the soil class (a) and ratio between V_S at bedrock and V_S10 (b).

Once established the validity of modelling the linear relation PGA_{surf}-PGA_{depth} at PGA_{depth}<0.01 g with the simple form of equation 3, it is possible to extend the investigation to higher levels of strain: the intention is to assess whether strong ground motion actually determines a significant deviation from linearity.

Studies of Darragh and Shakal (1991), Chin and Aki (1991) and Beresenev et al. (1996) have indicated that nonlinear behavior of soil may become significant at surface accelerations exceeding 0.1 to 0.2 g. Therefore, to study the possible soil nonlinear response, we identified and selected the KiK-net stations with at least three exceedances of PGA_{surf} = 0.1 g. These amount to 47 for the entire ensemble of stations, 28 and 11 for subsets A and B, respectively, meaning that only a small fraction of stations (7-10%) have actually experienced large levels of ground motion from events with shallow hypocenter.

For the sake of brevity of presentation, we report here and discuss the data from the stations with significantly high values of PGA_{surf} belonging to selection B (11 sites in total), although similar results were obtained for the other KiK-net sites. As shown in Figure 29-31, the linear trend of equation 1 defined by data points at low level of ground motion (PGA_{depth}<0.01 g, red dashed line), is generally followed also beyond such threshold. Indeed, for some stations (see FKSH12, NGNH06, SMNH01, class C sites, Figure 30), for PGA_{surf} > 0.1 g it is possible to observe some deviation from the linear behavior, with (the few available) PGA_{surf} values below the red dashed lines. In fact, this deviation can be ascribed to a decrement of shear stiffness with increasing levels of strain (i.e. nonlinear soil behavior). Nevertheless, this does not hold true for other stations (in particular NIGH10, NIGH15, class B, Figure 29, NIGH11, NIGH18 class C, Figure 30, IBRH12, class E, Figure 31) where data points with PGA_{surf} > 0.1 g essentially keep aligning along the straight red line determined by the portion of dataset at low ground motion (PGA_{depth}<0.01).

In Figures 29-31 some PGA_{surf}-PGA_{depth} pairs clearly diverge from the global trend (linear or nonlinear) of the respective datasets, generally forming small vertical alignment of data points with approx. the same PGA_{depth} but varying PGA_{surf} values (see in particular FKSH09, FKSH13 in Figure 29, NIGH18 in Figure 30, IBRH11 and IBRH12 in Figure 31). These features are probably related to a malfunction of the borehole receiver, leading to anomalous PGA_{depth} values. To automatically identify these outliers, a swift algorithm based on the analysis of residuals towards the global trend of the dataset was developed (see black crossed data points in Figures 29-31).

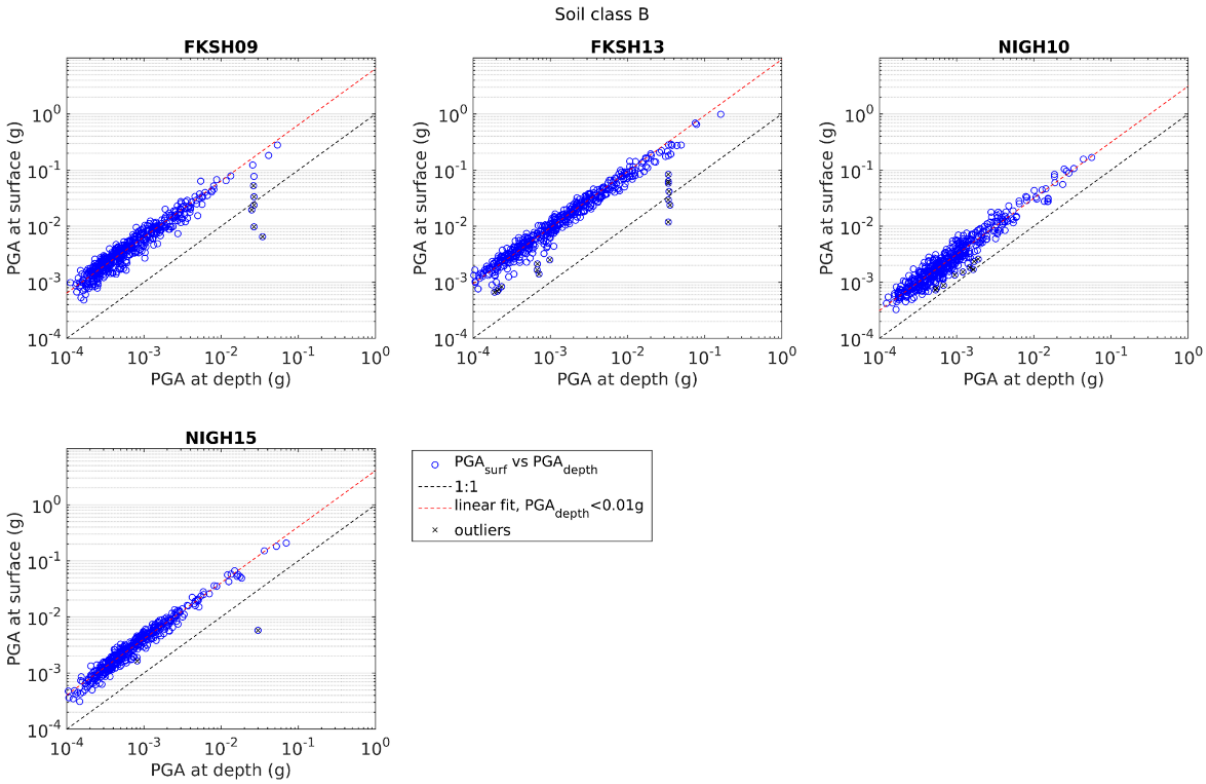

Figure 29 – KiK-net stations from selection B, soil class B, with at least three data points with PGA_{surf}>0.1 g. In blue the PGA_{surf}-PGA_{depth} pairs; those identified as outliers are marked with a black cross; the black dashed line indicates the 1:1 line; the red dashed line the fit of equation 3 with the data having PGA_{depth}<0.01 g.

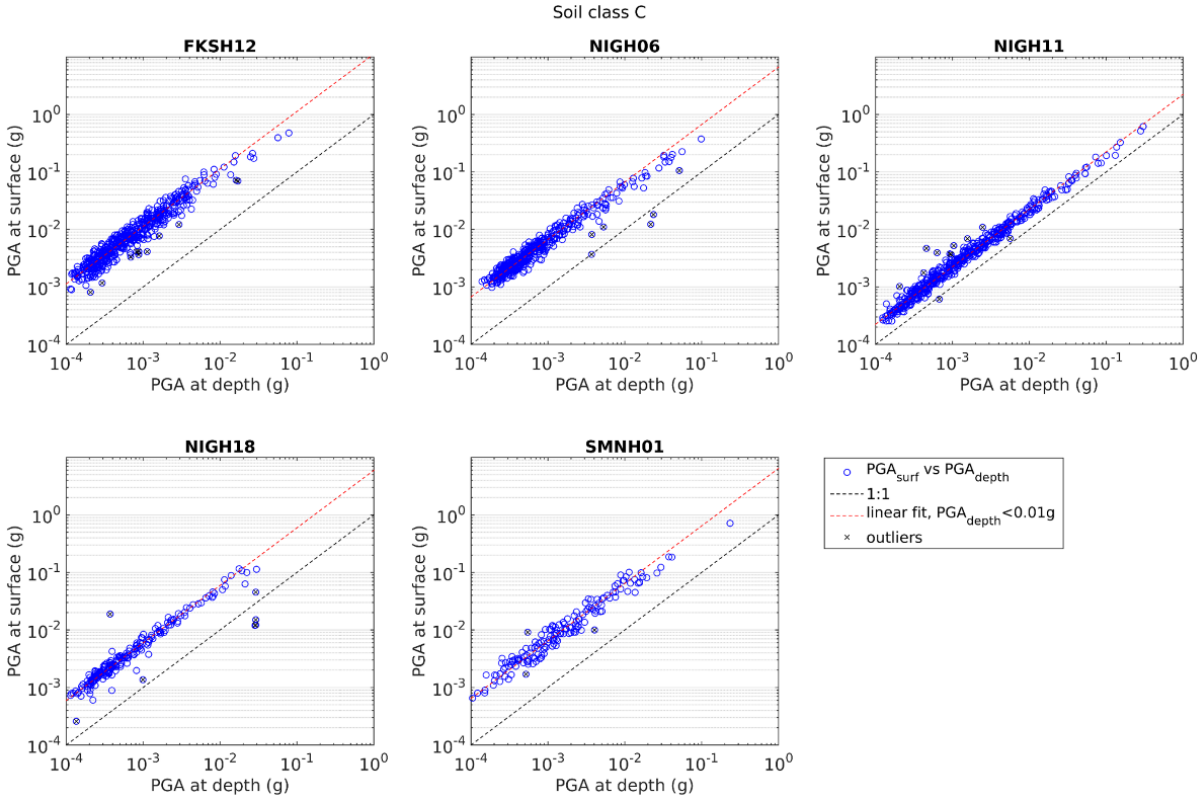

Figure 30 – KiK-net stations from selection B, soil class C, with at least three data points with PGA_{surf}>0.1 g.

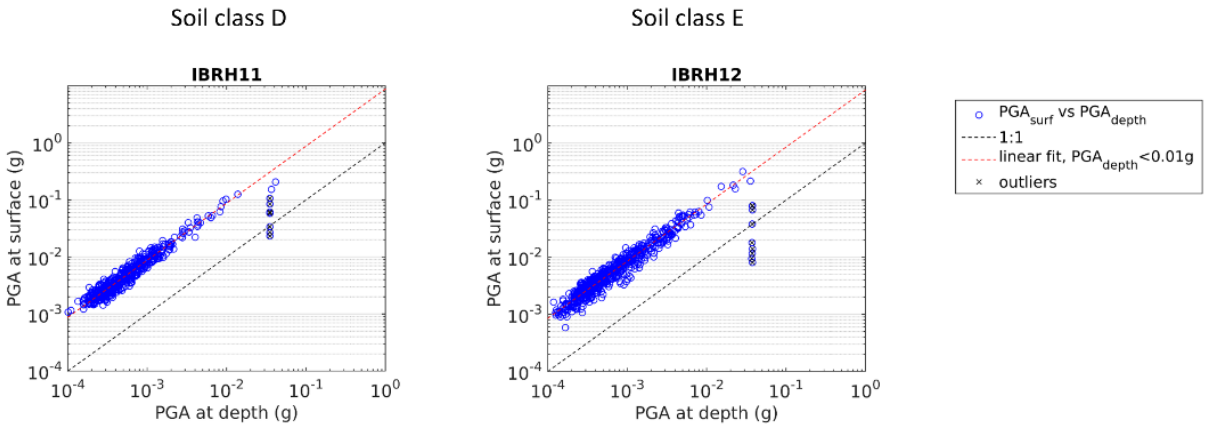

Figure 31 – KiK-net stations from selection B, soil class D and E, with at least three data points with PGA_{surf}>0.1 g.

For a closer focus on the agreement or divergence from linear soil behavior, we also computed the deviation of each PGA_{surf}-PGA_{depth} pair in Figures 29-31 from the linear trend defined by equation 3 and fitted on the dataset portion with $PGA_{depth} < 0.01$. The deviation is represented in terms of ratio between measured PGA_{surf} and the corresponding value at the red dashed line in Figures 29-31, defined as linear PGA_{surf} (Figures 32-34). With the representation in Figures 32-34, it is possible to confirm and quantify the observations earlier anticipated:

- For most of the stations, no significant deviation from a linear pattern (i.e. ratio = 1) is evident, even for $PGA_{surf} > 0.1$ g (see FKSH09, NIGH10, NIGH15, NIGH11, NIGH18, IBRH12);
- At the other sites (FKSH13, FKSH12, NIGH06, SMNH01, IBRH11) it is possible to argue a trend towards decreasing ratio values at high PGA_{surf}; however, the decrement is not dramatic (lowest values are around ratio = 0.5), particularly when compared with the deviations anyhow present at low PGA_{surf} (where nonlinear soil behavior is not to be expected), that are basically of the same order of magnitude.

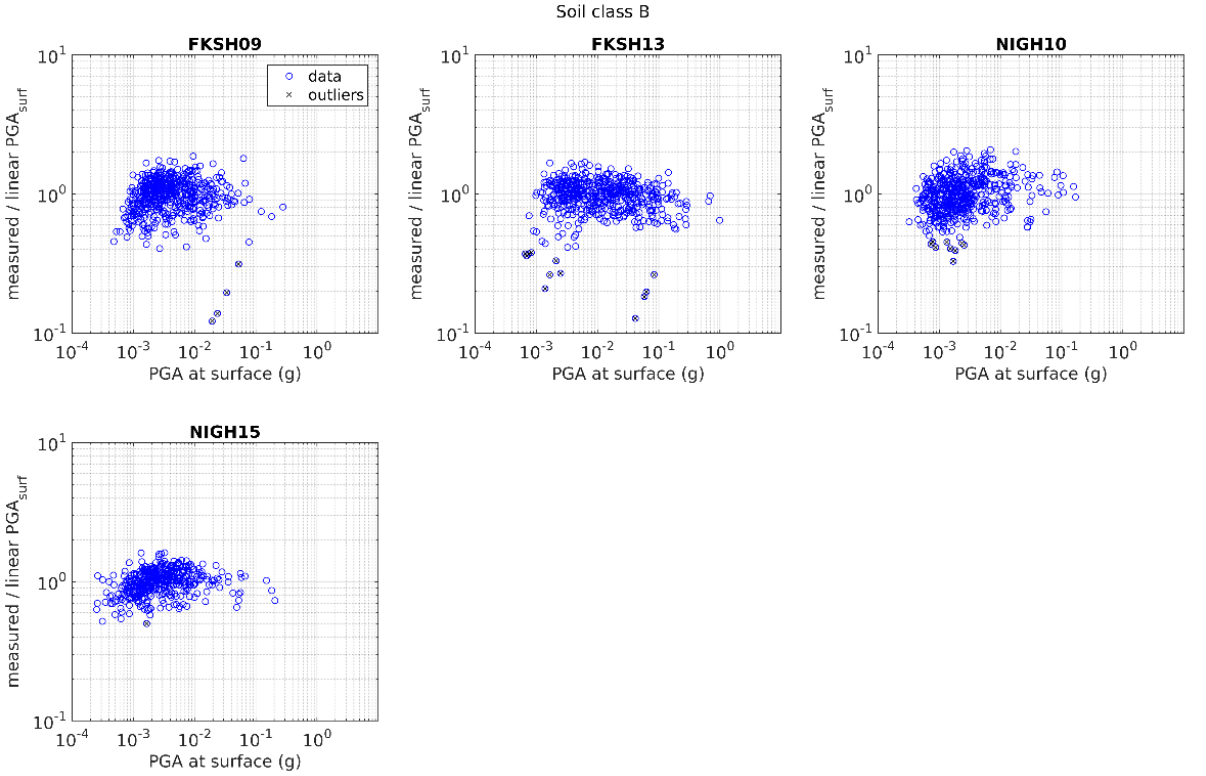

Figure 32 – KiK-net stations from selection B, soil class B, with at least three data points with PGA_{surf}>0.1 g. Ratio between measured and expected PGA_{surf} assuming a linear behavior (see Figure 29), as a function of measured PGA_{surf}

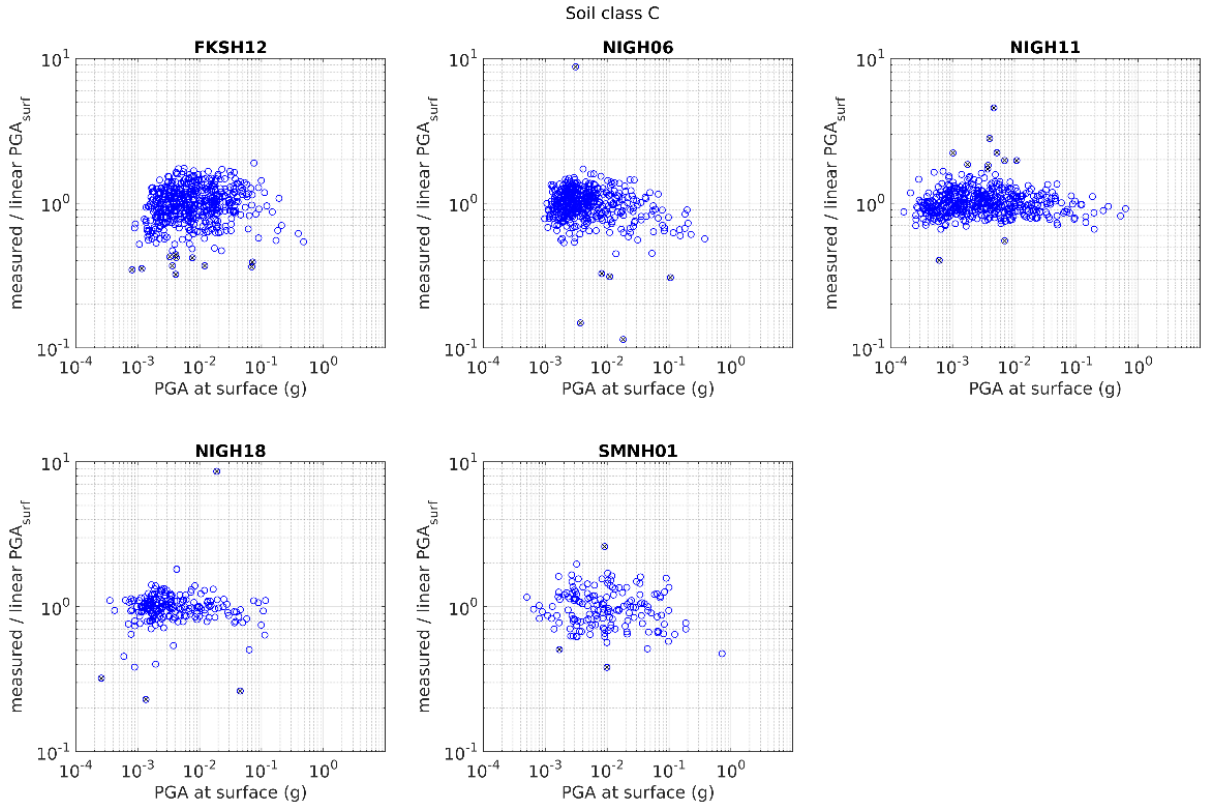

Figure 33 – KiK-net stations from selection B, soil class C, with at least three data points with PGA_{surf}>0.1 g. Ratio between measured and expected PGA_{surf} assuming a linear behavior (see Figure 30), as a function of measured PGA_{surf}

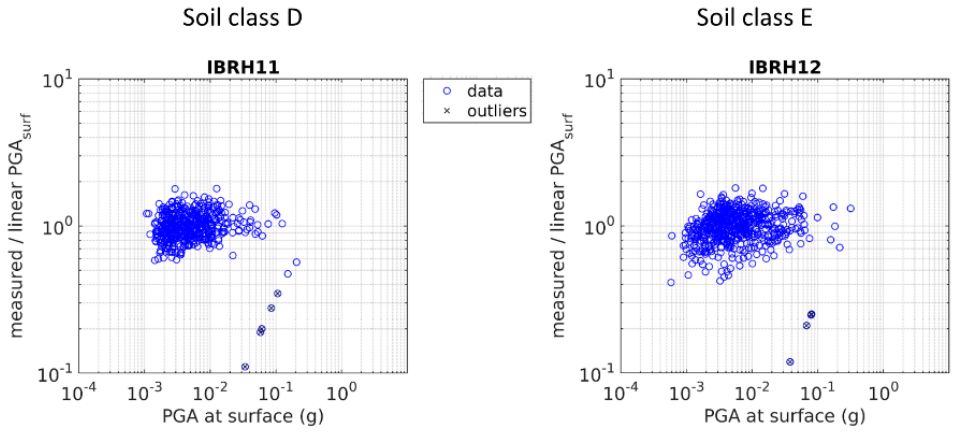

Figure 34 – KiK-net stations from selection B, soil class D and E, with at least three data points with PGA_{surf}>0.1 g. Ratio between measured and expected PGA_{surf} assuming a linear behavior (see Figure 31), as a function of measured PGA_{surf}

To conclude, it is possible to affirm from the analysis of the PGAs of the considered dataset, that

- Shallow events (with hypocentral depth < 20 km, compatible with the Swiss scenario) are able to produce levels of ground motion high enough (PGA_{surf} > 0.1 g) to potentially induce nonlinear soil behavior;
- Nevertheless, evidences of nonlinearity are observed only in a portion of sites where large strain levels are recorded; when this occurs, the deviations from a purely linear behavior are not particularly significant, especially when PGA is limited to values below 1 g.

- The modest relevance of nonlinearity is evident, when the expected levels of ground motion for Switzerland with 475 years return period are considered (Figure 35); in fact, these are generally below, or quite close to, the threshold of potential onset of soil nonlinear behavior.

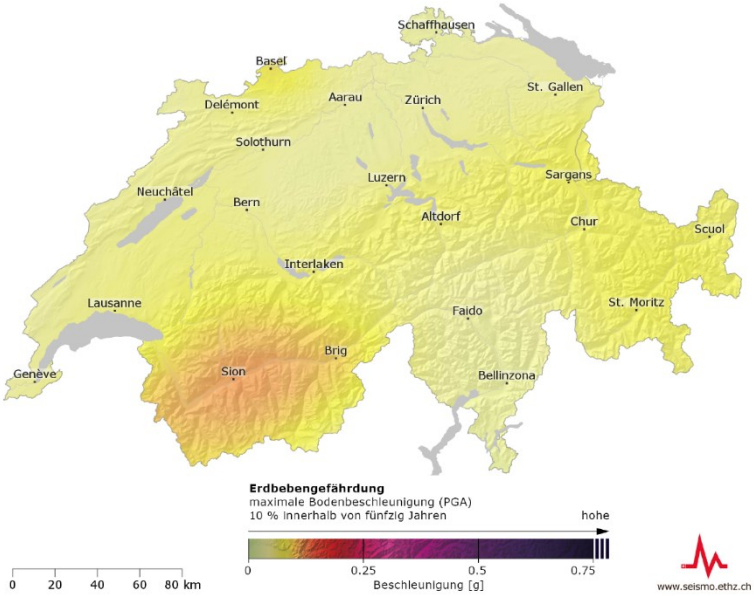

Figure 35 – Seismic hazard map for Switzerland: values of peak ground acceleration (PGA) with an exceedance probability of 10 % within fifty years (475 years return period; SED, 2015)

9.0 Seismic hazard input and normalized comparison with present elastic design spectra

The Swiss Seismological Service recently issued the latest seismic hazard model for Switzerland, contained in the SUIhaz 2015 report (SED, 2016). The report provides information about the potential size of earthquakes and where they may occur in the future; it describes how and under which assumptions the seismic hazard model was calculated, summarizes the main findings, and compares these to other models. Various products are based on the results of SUIhaz2015: among these, the uniform hazard spectra (UHS) determined for the whole territory of Switzerland, available on the data portal of the European Facility for Earthquake Hazard & Risk EFEHR (http://www.efehr.org).

The UHS for a given geographical location collects the value of expected ground acceleration for a range of periods from 0.01 to 4 s; UHS are available for six different return periods (from 73 to 9975 years), corresponding to a probability of exceeding the provided ground acceleration values of 50% to 0.5%, respectively, in a 50-year observation time.

Uniform hazard spectra contain the expected (in a statistical sense) level of ground acceleration at the reference rock, without including soil amplification. Therefore, the information from UHS (expected spectral acceleration at reference rock) can be reasonably combined with soil amplification data (the spectral response amplification curves, introduced in section 7), to produce site-specific uniform hazard spectra inclusive of site amplification for a wide variety of subsurface conditions. These will be finally collated with the elastic design spectra from present SIA 261 code.

As earlier anticipated, in this study the city of Sion has been selected as emblematic example, as it belongs to zone 3b, i.e. the zone in Switzerland where the highest levels of ground motion are expected. Consequently, the horizontal UHS for Sion was considered as seismic hazard input, in particular the

spectrum corresponding to a return period of 475 years, for consistency with SIA 261 normative (Figure 36).

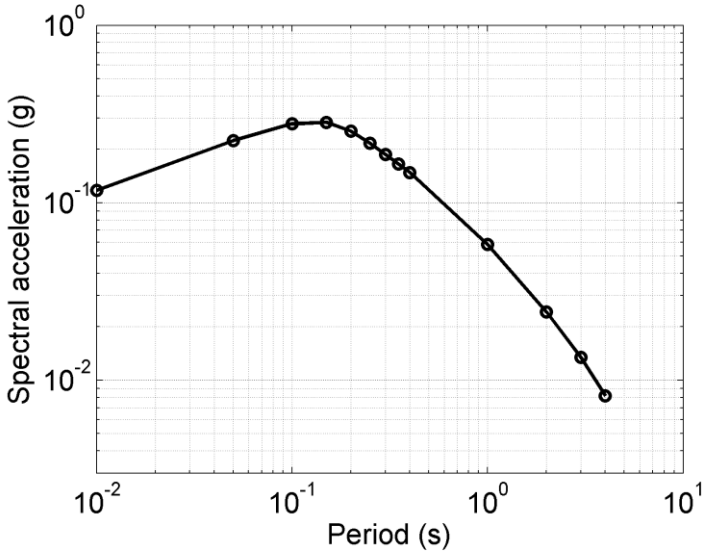

Figure 36 – Uniform hazard spectrum (UHS) for the city of Sion, return period 475 years (10% probability of exceedance in 50 years (SED, 2016).

As declared, the final objective of this study is a comparison between present elastic design spectra and a dataset of site-specific uniform hazard spectra. To obtain the latter, the horizontal UHS for Sion at the reference rock (Figure 36) is first normalized to its PGA value (the spectral acceleration at a period of 0.01 s), for consistency with the form of elastic design spectra of SIA 261, expressed in terms of SA/a_{gd} (where SA = spectral acceleration and a_{gd} = maximum horizontal ground acceleration, on soil A and with a return period of 475 years). In a second step, the soil amplification component is added to the normalized UHS by superimposing each of the site-specific response spectral amplification functions to the latter.

These final processing products are presented in Figures 37-42, once again subdivided by soil class, origin of input amplification (SB ratio or empirical amplification functions), and considered KiK-net sites assortments (all available stations, selection A and B). In each subpanel, the elastic design spectra from SIA 261 normative and Poggi and Fäh (2015) proposal (both with damping = 0.05) are included for comparison.

For clarity of presentation, we remind that Poggi and Fäh's (2015) proposal for elastic design spectra follows the SIA 261 normative functional form (equations 4), although with modified values for the parameters S, T_B and T_C (see table 2).

$$\frac{SA}{a_{gd}} = S\left(1 + \frac{(2.5\eta - 1)T}{T_B}\right) \quad for\ T < T_B \qquad (4)$$

$$\frac{SA}{a_{gd}} = 2.5S\eta \quad for\ T_B < T < T_c$$

$$\frac{SA}{a_{gd}} = 2.5S\eta\frac{T_C}{T} \quad for\ T_C < T < T_D$$

$$\frac{SA}{a_{gd}} = 2.5S\eta\frac{T_C T_D}{T^2} \quad for\ T > T_D$$

where $\eta = \sqrt{\frac{1}{(0.5+10\xi)}}$ with ξ = damping

Table 2 – value of S, T_B, T_C, T_D in the current SIA normative and in Poggi and Fäh's (2015) proposal

Soil class	Poggi and Fäh 2015				SIA 261 2014			
	S	T_B (s)	T_C (s)	T_D (s)	S	T_B (s)	T_C (s)	T_D (s)
A	1	0.06	0.25	2	1	0.15	0.4	2
B	1.8	0.08	0.2	2	1.2	0.15	0.5	2
C	2	0.1	0.25	2	1.15	0.2	0.6	2
D	3	0.15	0.35	2	1.35	0.2	0.8	2
E	2.6	0.12	0.2	2	1.40	0.15	0.5	2

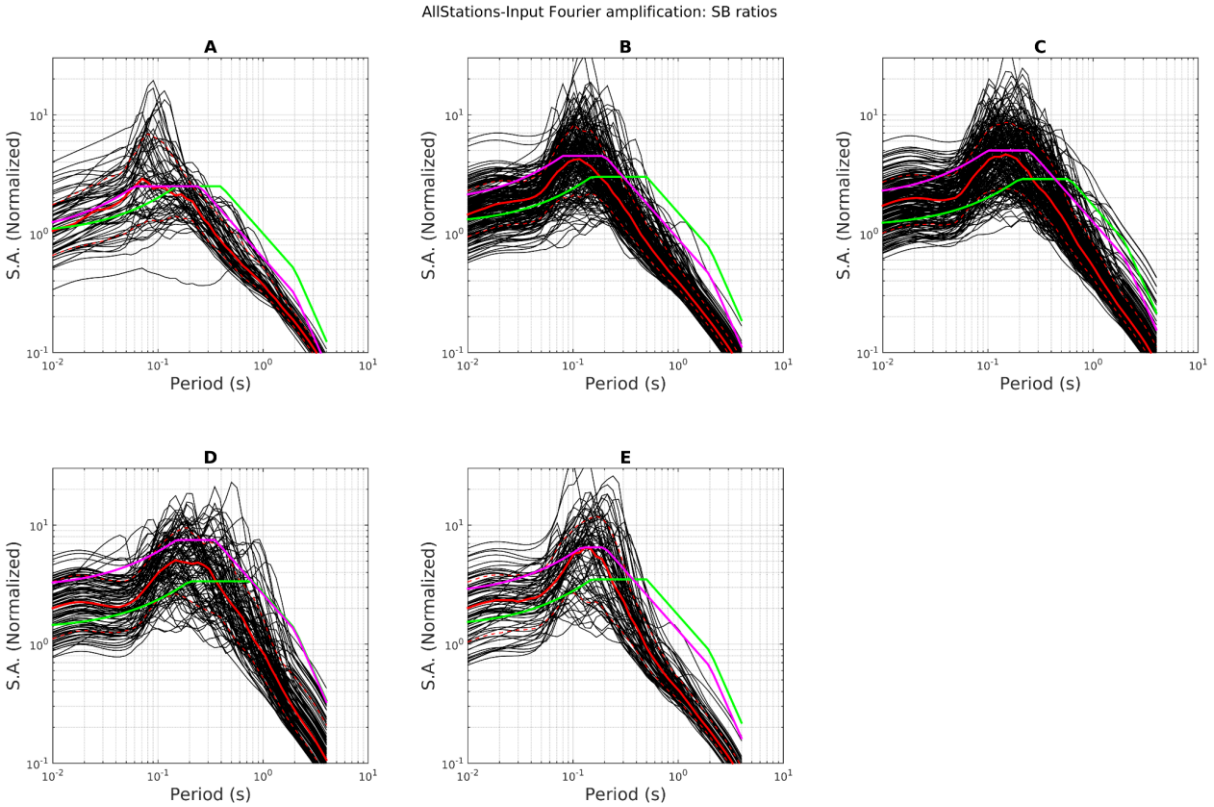

Figure 37 – Site-specific UHS, based on the normalized UHS for Sion with the addition of response spectral amplifications for KiK-net stations (black lines). The considered response spectral amplification derive the input Fourier amplification information from SB ratios. The median of the distribution of black curves for each soil class is indicated with a continuous red line; the 15th and 85th percentile with a dashed red line. The SIA 261 elastic design spectra are in green; those from the proposal of Poggi and Fäh (2015) in magenta.

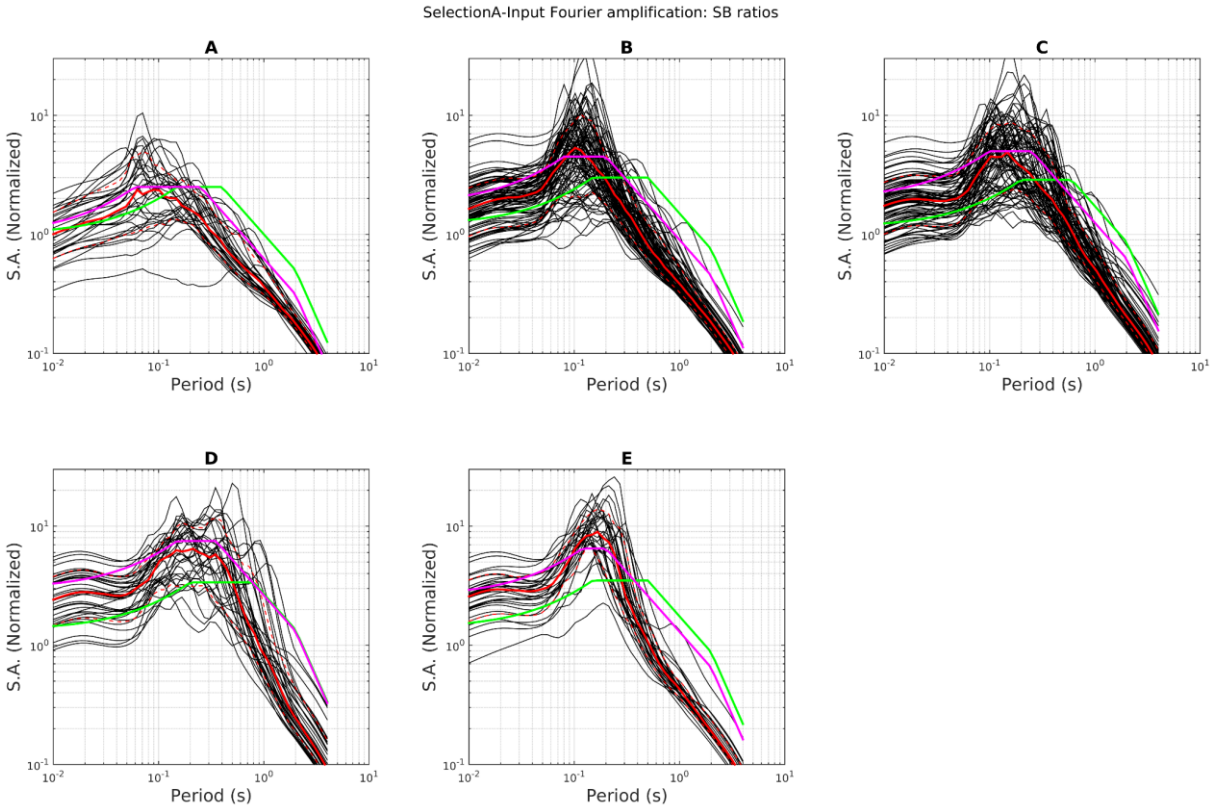

Figure 38 – Site-specific UHS, based on the normalized UHS for Sion with the addition of response spectral amplifications for selection A KiK-net stations (black lines). The considered response spectral amplification derive the input Fourier amplification information from SB ratios. The median of the distribution of black curves for each soil class is indicated with a continuous red line; the 15th and 85th percentile with a dashed red line. The SIA 261 elastic design spectra are in green; those from the proposal of Poggi and Fäh (2015) in magenta.

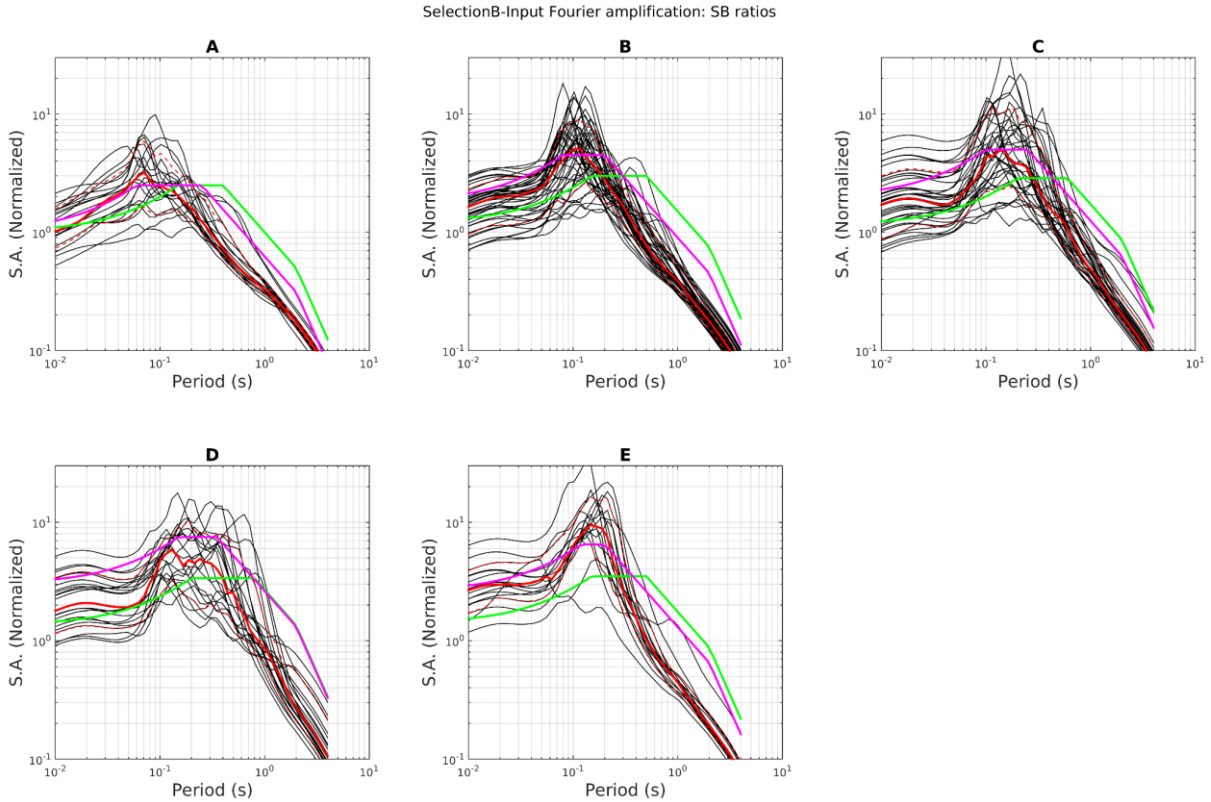

Figure 39 – Site-specific UHS, based on the normalized UHS for Sion with the addition of response spectral amplifications for selection B KiK-net stations (black lines). The considered response spectral amplifications derive the input Fourier amplification information from SB ratios. The median of the distribution of black curves for each soil class is indicated with a continuous red line; the 15th and 85th percentile with a dashed red line. The SIA 261 elastic design spectra are in green; those from the proposal of Poggi and Fäh (2015) in magenta.

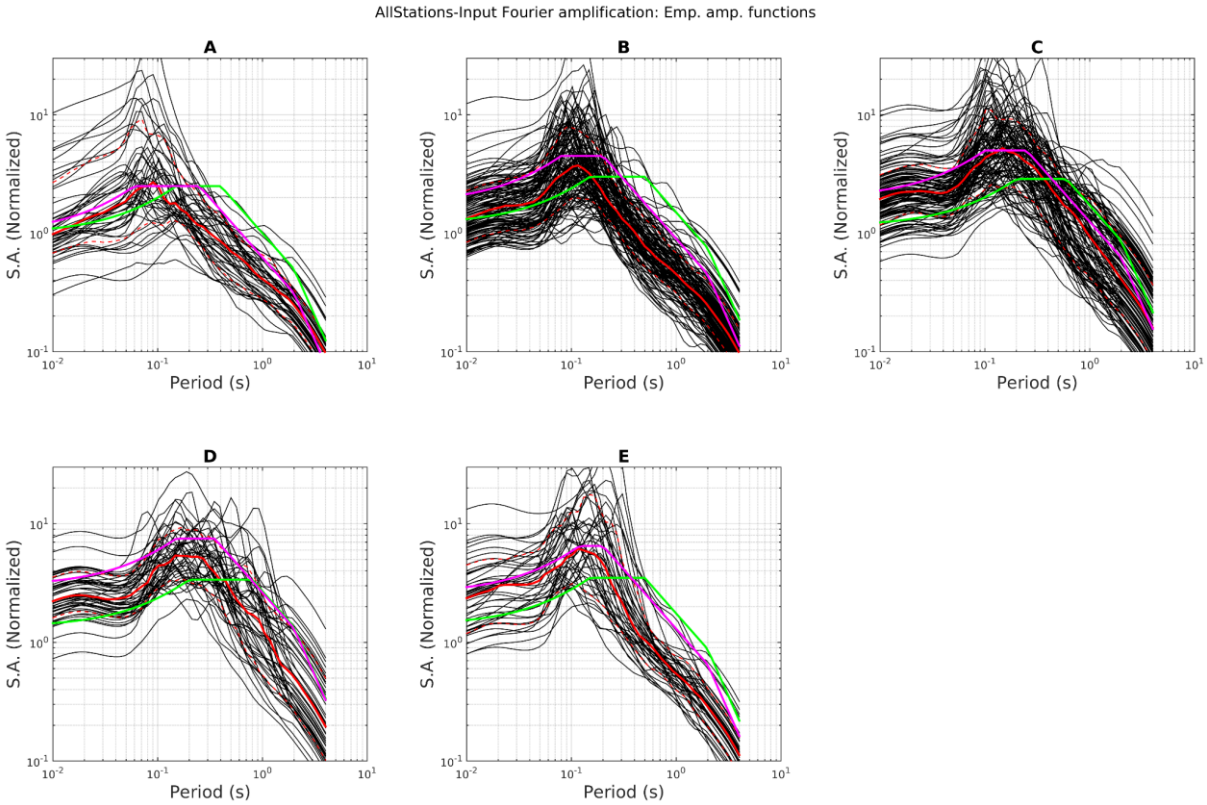

Figure 40 – Site-specific UHS, based on the normalized UHS for Sion with the addition of response spectral amplifications for all KiK-net stations with a reliable empirical amplification function (black lines). The considered response spectral amplification derives the input Fourier amplification information from empirical amplification functions from spectral modelling. The median of the distribution of black curves for each soil class is indicated with a continuous red line; the 15th and 85th percentile with a dashed red line. The SIA 261 elastic design spectra are in green; those from the proposal of Poggi and Fäh (2015) in magenta.

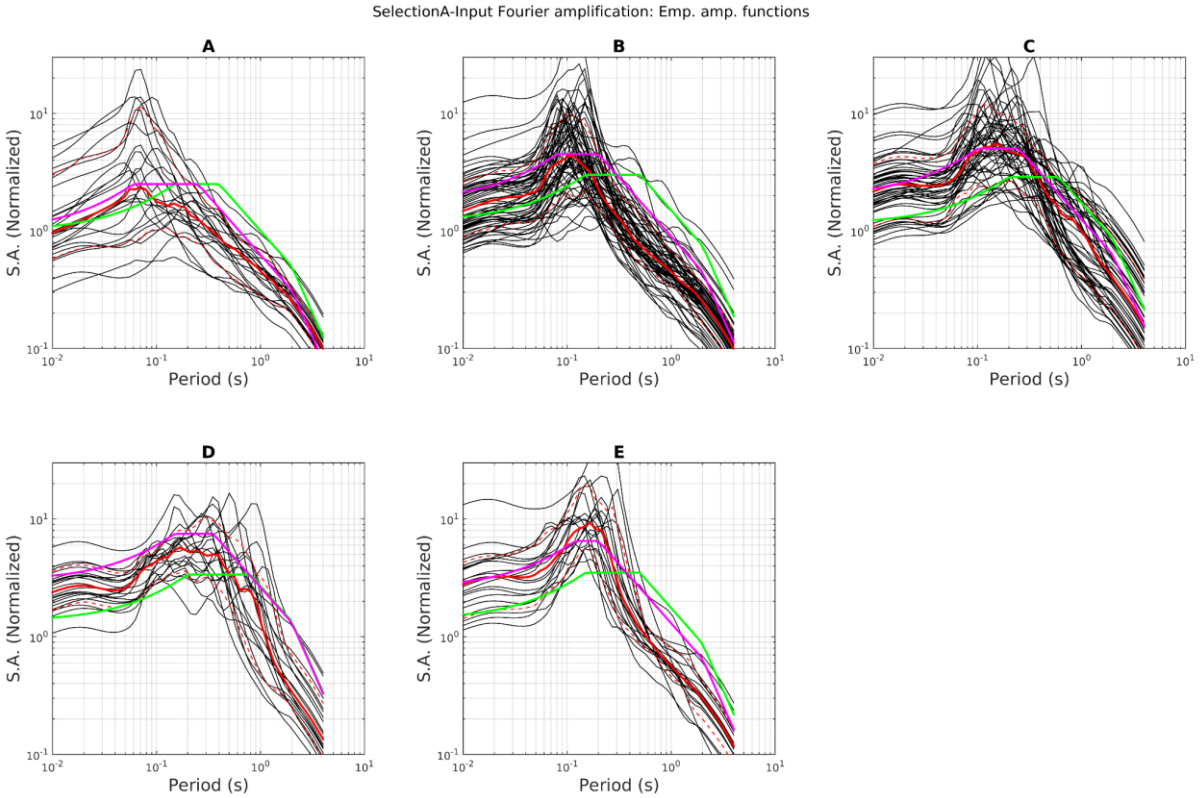

Figure 41 – Site-specific UHS, based on the normalized UHS for Sion with the addition of response spectral amplifications for selection A stations with a reliable empirical amplification function (black lines). The considered response spectral amplification derives the input Fourier amplification information from empirical amplification functions from spectral modelling. The median of the distribution of black curves for each soil class is indicated with a continuous red line; the 15th and 85th percentile with a dashed red line. The SIA 261 elastic design spectra are in green; those from the proposal of Poggi and Fäh (2015) in magenta.

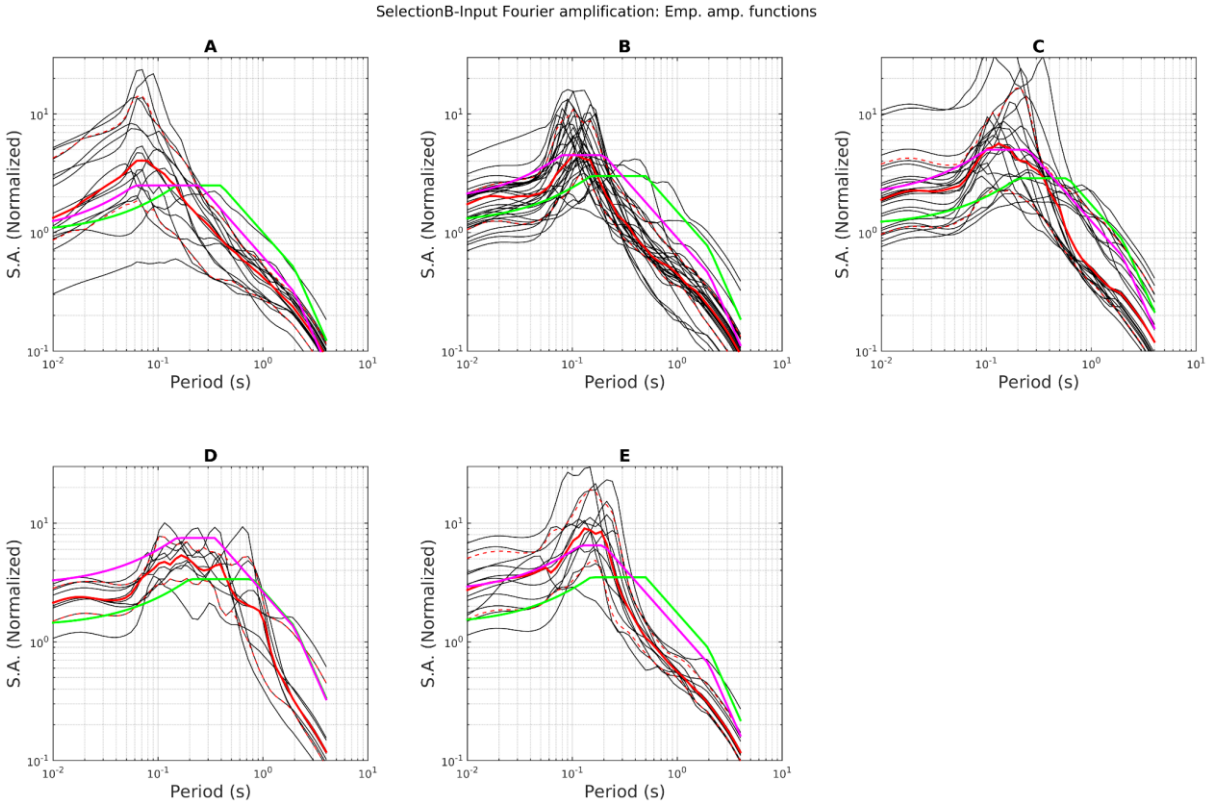

Figure 42 – Site-specific UHS, based on the normalized UHS for Sion with the addition of response spectral amplifications for selection B stations with a reliable empirical amplification function (black lines). The considered response spectral amplification derive the input Fourier amplification information from empirical amplification functions from spectral modelling. The median of the distribution of black curves for each soil class is indicated with a continuous red line; the 15th and 85th percentile with a dashed red line. The SIA 261 elastic design spectra are in green; those from the proposal of Poggi and Fäh (2015) in magenta.

A visual comparison among corresponding representations (e.g. Figure 37 and 40, 38 and 41, 39 and 42) allows noticing the greater scatter of site-specific UHS curves from empirical amplification functions, as already observed in section 5. For a more in-depth analysis of the results, we collected the median curves from every KiK-net sites subsets in Figures 43-44. Their agreement with elastic design spectra is discussed in the following section.

10.0 Discussion on the normalized comparison with elastic design spectra

A common feature among all subpanels produced in the previous section (Figures 43-44) is the mismatch between SIA 261 elastic design spectra (green lines) and the empirical median curves (black, blue, cyan lines); the design spectra's T_B-T_C plateau appears to be moved towards higher periods and to bear lower amplitudes when compared to the empirically-derived envelopes. This disagreement had already been evidenced in the work of Poggi and Fäh (2015), who proposed an updated version of design spectra preserving the original functional form of SIA 261 but modifying the values of S, T_B and T_C parameters to move the plateau towards higher amplification values (for all soil classes but A) and lower periods (magenta lines in Figures 43-44). This proposal agrees quite well with the empirical results presented in this study, with two exceptions:

- Class A, site-specific UHS from empirical amplification functions, selection B sites (Figure 43, left subpanel); the dashed cyan median curve exceeds the magenta below 0.1 s. Quite likely, this mismatch is to be ascribed to the low number of sites used for the calculation of the median (as already observed in section 7). In all the other cases (site-specific UHS from SB ratios, site-

specific UHS from empirical functions, all sites and selection A) this mismatch is not observed. Therefore, this exceedance is not considered as significant.

- Class E, site specific UHS from both empirical amplification functions and SB ratios, selection A and B (Figure 44). Differently from the previous case, this mismatch has to be considered as empirical evidence (selection A and B actually collect sites with proven shallow soft sediments-bedrock interface, therefore producing a high amplitude plateau).

Therefore, if the present form of SIA normative design spectra is to be preserved (equation 4), a different value for parameter S, soil class E, should be proposed. We identified this value as being S = 3.8, while keeping all other parameters (T_B, T_C, T_D) consistent with Poggi and Fäh's (2015) work. The obtained design spectrum is shown in Figure 45 (red line). It now overtops all the median curves from empirical data (black, blue and cyan lines, continuous or dashed), although with a considerable level of conservativism outside the T_B-T_C plateau (obviously due to the high value of S).
In summary, there is a the poor consistency between the empirical results we obtained in terms of site-specific UHS and the elastic design spectra following the SIA 261 functional form, even when its parameters S,T_B and T_C are modified (e.g. Poggi and Fäh, 2015, or the proposed correction for class E in Figure 45). In other words, it is difficult to fit the mathematical forms of equation 4 with the trend observed in the median curves from experimental data. This observation is valid for all soil classes (see all subpanels of Figures 43 and 44).

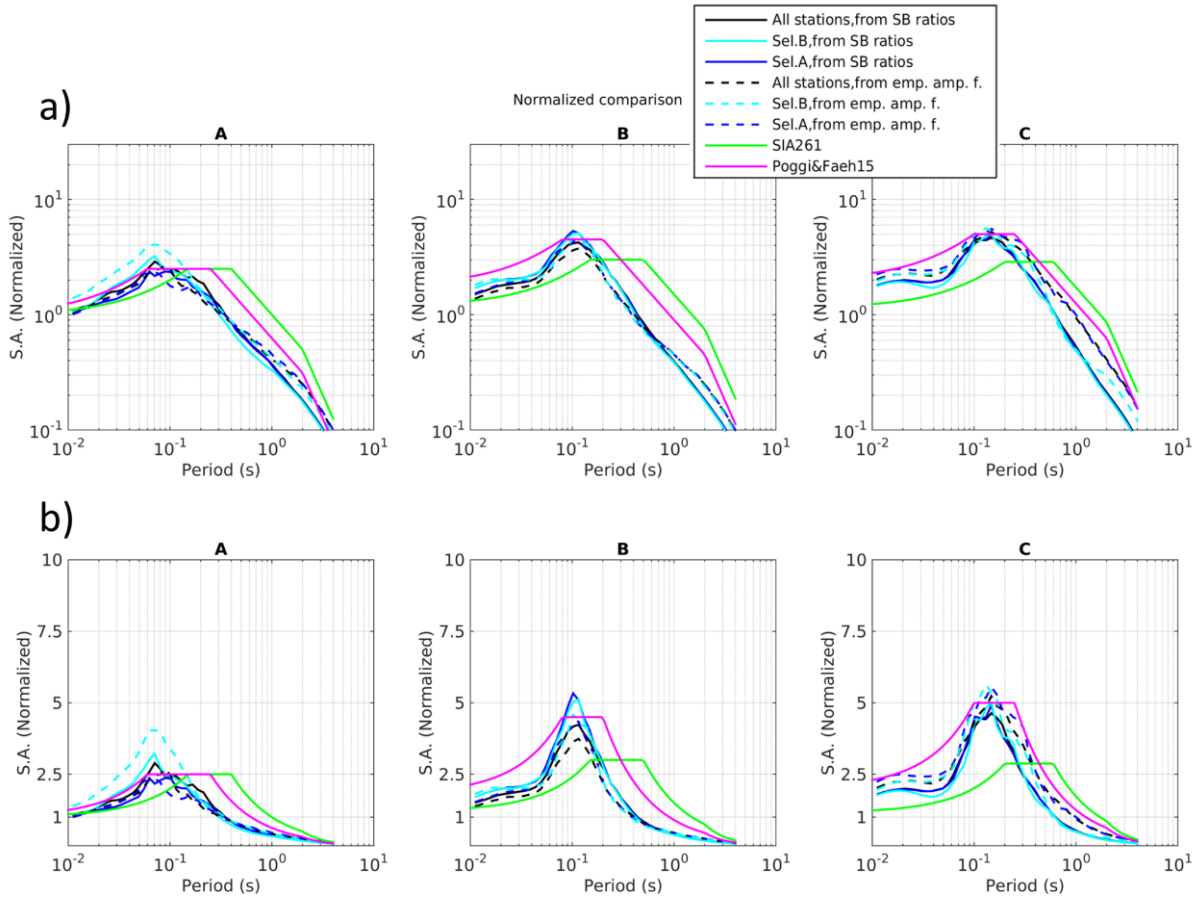

Figure 43 – a) comparison among median curves of normalized site-specific UHSs, subdivided by soil classes (from left to right, classes A, B, and C). Black, blue, cyan continuous lines: site-specific UHSs with input amplification from SB ratios; black, blue, cyan dashed lines: site-specific UHSs with input amplification from empirical amplification functions from spectral modelling. b) same as (a), with ordinate axis (normalized spectral acceleration) in linear scale

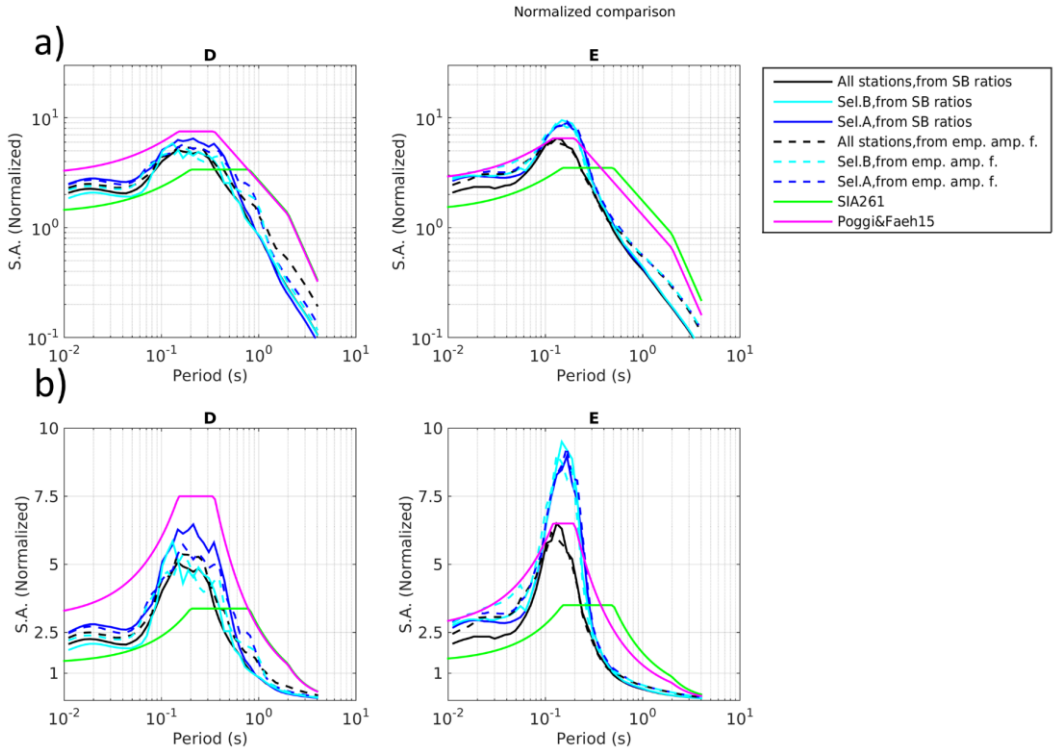

Figure 44 – a) comparison among median curves of site-specific UHS, subdivided by soil classes (left: class D; right, class E). Black, blue, cyan continuous lines: site-specific UHS with input amplification from SB ratios; black, blue, cyan dashed lines: site-specific UHS with input amplification from empirical amplification functions from spectral modelling. b) same as (a), with ordinate axis (normalized spectral acceleration) in linear scale

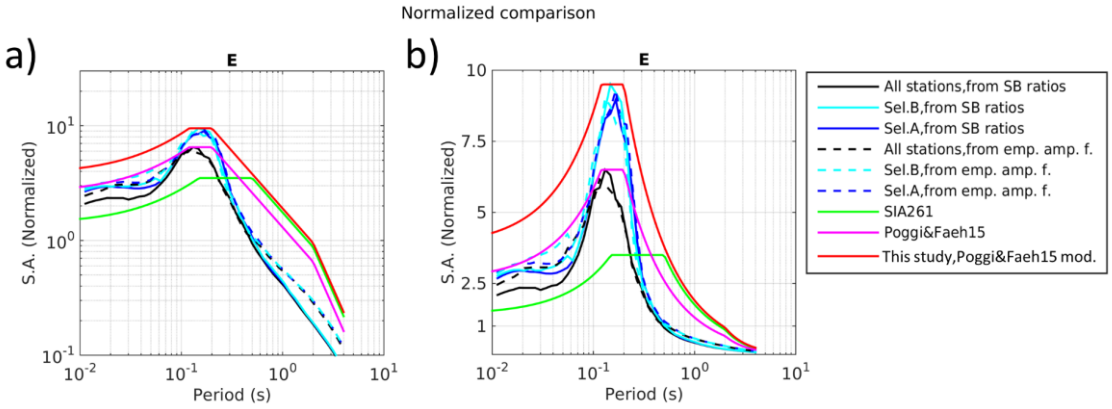

Figure 45 – a) elastic design spectra for class E (red line) modified to overtop the peak of the median curves of the empirical spectra (black, blue or cyan line according to the KiKnet station subset; continuous or dashed line according to the origin of the amplification function. The elastic design spectra for class E from SIA 261 normative and Poggi and Fäh's (2015) proposal are also included as green and magenta lines, respectively. b) same as (a), with ordinate axis (normalized spectral acceleration) in linear scale

In particular, two important points need to be considered:

- The functional form of SIA 2014 design spectra is not able to properly model the presence of resonance phenomena that affect sediment sites (both stiff and soft). Such phenomena produce a marked peak in the empirical normalized SA curves. It is indeed possible (as done in Figure 45) to increase the value of parameter S up to the peak due to resonance. However, this causes much too high values of spectral accelerations at both sides of the plateau (see again Figure 45);
- A consistent mismatch between design and empirical spectra is observed for all soil classes at long periods ($T>T_C$; see all subpanels in Figures 43-44). The design spectra appear to be considerably above the experimental median curves between about 0.6 to 3s periods. This

difference is smaller around the upper limit of the period range (around 3 s). In fact, empirical spectra generally decay "faster" (i.e. with a sharper slope) than the shape of the design spectra with a decrease as 1/T between T_C and T_D. This conservativism at high periods is somehow desirable in the perspective of a building code; nevertheless, the prescribed values of SA might be excessive when the expected hazard spectrum for the considered site is well constrained by reliable information about the site subsoil structure and amplification phenomena.

These observations might suggest the necessity to define a modified form for the elastic design spectra, possibly more complex than the present one (SIA 261, 2014), but able to fit with more accuracy the empirical median spectra. In this perspective, we have elaborated a revised version of the functional form of elastic design spectra; it is to be interpreted as a potential proposal, not as a conclusive solution, in particular for site-specific seismic hazard assessment (microzonation).
The main element of discontinuity with the current SIA 261 form is that our model includes up to two flat period intervals, or plateaus, to accommodate the marked peak related to resonance (with the highest amplitude plateau), without forcing the whole spectrum towards highly cautionary values of spectral acceleration (as it is observed with the present SIA 261 shape). For the same reason, the plateau intervals are generally bounded by shoulders with steeper slope.
The proposed scheme is based on the following equations:

$$\frac{SA}{a_{gd}} = S\left(1 + (2.5\eta - 1)\left(\frac{T}{T_B}\right)^2\right) \quad for\ T < T_B \qquad (5a)$$

$$\frac{SA}{a_{gd}} = S2.5\eta \qquad for\ T_B < T < T_C \qquad (5b)$$

$$\frac{SA}{a_{gd}} = S2.5\eta\left(\frac{T_C}{T}\right)^{3/2} \qquad for\ T_C < T < T_{B'} \qquad (5c)$$

$$\frac{SA}{a_{gd}} = S'2.5\eta \qquad for\ T_{B'} < T < T_{C'} \qquad (5d)$$

$$\frac{SA}{a_{gd}} = S'2.5\eta\left(\frac{T_{C'}}{T}\right) \qquad for\ T_{C'} < T < T_D \qquad (5e)$$

$$\frac{SA}{a_{gd}} = S'2.5\eta\left(\frac{T_D\, T_{C'}}{T^2}\right) \qquad for\ T > T_D \qquad (5f)$$

where $\eta = \sqrt{\frac{1}{(0.5+10\xi)}}$ with ξ = damping.

Equations 5b, 5d correspond to the two plateaus (T_B-T_C and $T_{B'}$-$T_{C'}$); 5a, 5b are the left and right ramps of the T_B-T_D plateau; 5e, 5f are the two intervals of decay at larger periods.
The greater complexity (and at the same time, flexibility) of the functional form we propose allowed to match with greater accuracy the median empirical spectra introduced in section 9. In Figures 46 and 47 we represent the proposed elastic design spectra for each soil class (A-E), while in table 3 we display the values of parameter S, and the anchor periods T_B,T_C, $T_{B'}$, $T_{C'}$,T_D; S' is not independent but it is forced to be $S' = S\left(\frac{T_C}{T_{B'}}\right)^{3/2}$ to ensure continuity of the design spectra.

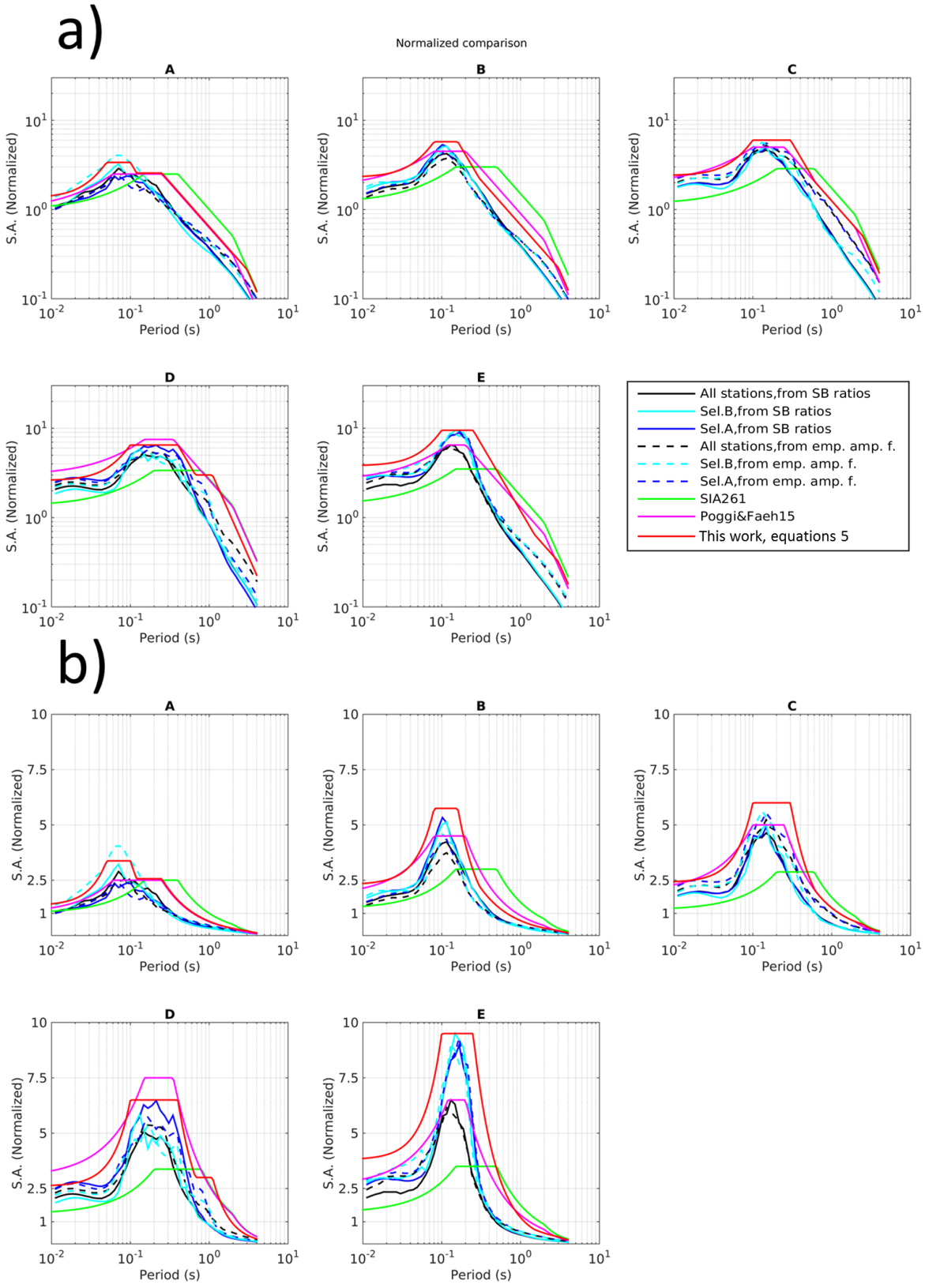

Figure 46 – a) elastic design spectra from equations 5, proposed for soil classes A-E (red lines), compared with the median curves of the empirical spectra (black, blue or cyan line according to the KiKnet station subset; continuous or dashed line according to the origin of the amplification function. The elastic design spectra from SIA 261 normative and Poggi and Fäh's (2015) proposal are also included as green and magenta lines, respectively. b) same as (a), with ordinate axis (normalized spectral acceleration) in linear scale.

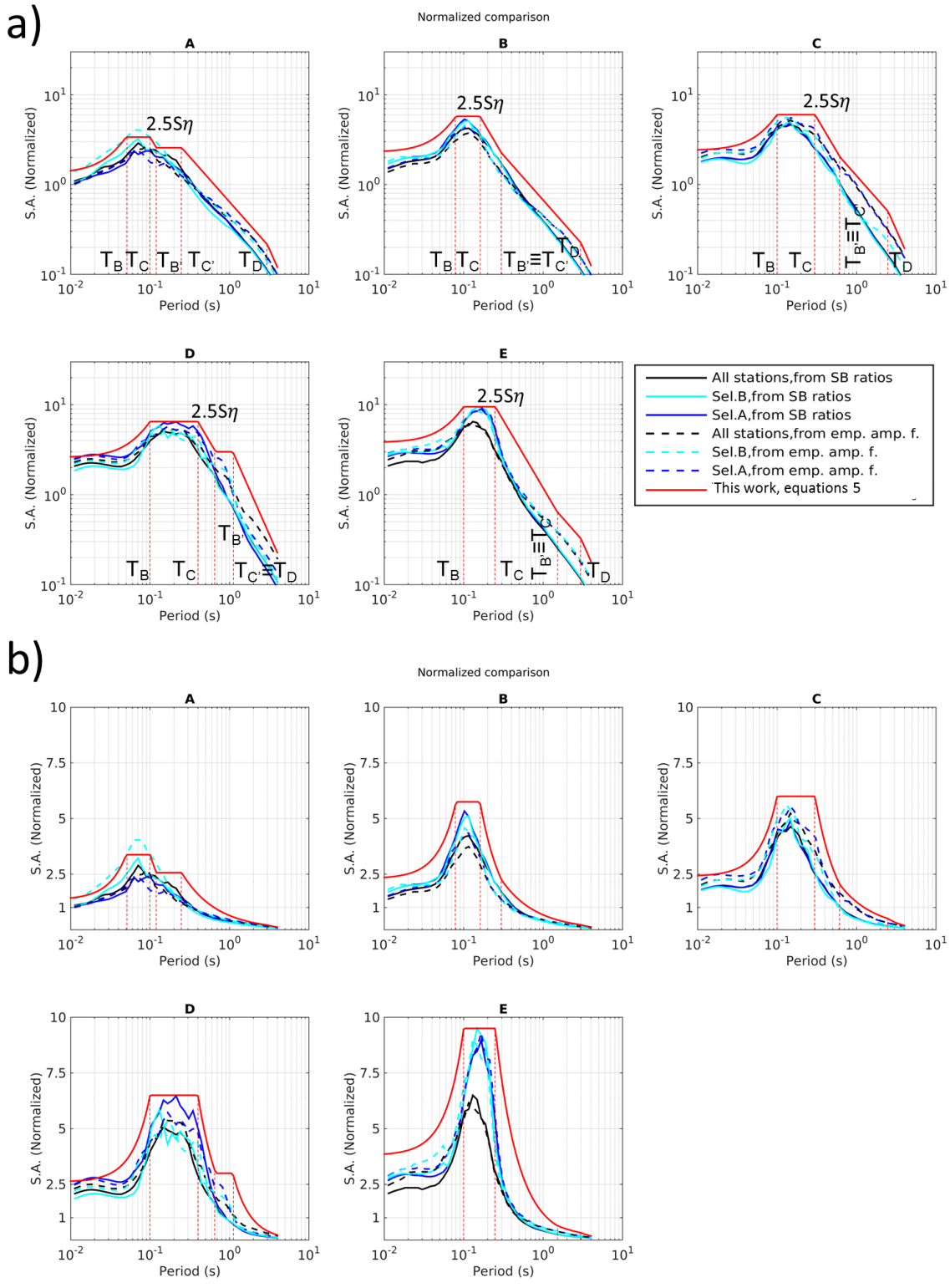

Figure 47 – a) elastic design spectra from equations 5, proposed for soil classes A-E (red lines), compared with the median curves of the empirical spectra (black, blue or cyan line according to the KiKnet station subset; continuous or dashed line according to the origin of the amplification function. The anchor periods (T_B, T_C, $T_{B'}$, $T_{C'}$, T_D) and the amplitude values of the first plateau (2.5Sη) are indicated in each subpanels; b) same as (a), with ordinate axis (normalized spectral acceleration) in linear scale.

Table 3 – Values of parameters T_B, T_C, $T_{B'}$, $T_{C'}$, T_D and S in equations 5.

Soil class	S	T_B (s)	T_C (s)	$T_{B'}$ (s)	$T_{C'}$ (s)	T_D (s)
A	1.35	0.05	0.10	0.12	0.25	3.0
B	2.30	0.08	0.16	0.30	0.30	3.0
C	2.40	0.10	0.30	0.62	0.62	2.5
D	2.60	0.10	0.40	0.67	1.10	1.1
E	3.80	0.10	0.25	1.50	1.50	3.0

Not all segments defined by equations 5a-f appear in all the class-specific design curves; some segments may be collapsed to null period intervals (so that some anchor periods coincide; Figure 47). All six different segments are included in the design spectra for class A; as for soil types B, C and E, a single-plateau spectrum is suitable, so that the S' plateau has null extension. Class D includes two plateaus but the amplitude decrease at high periods follows a single decay trend ($\sim T^{-2}$, equation 5f; therefore $T_{C'} \equiv T_D$). Alternatively, in order to obtain more conservatism at longer period, the shape of the SIA261 spectra could be selected in the proposed approach.

11.0 Absolute comparison with present elastic design spectra for specific sites

The assumption implied in the previous sections (9-10), allowing a direct comparison between *normalized* design spectra and *normalized* site-specific UHSs, is the equivalence between a_{gd} (described in SIA-261 as maximum horizontal-component ground acceleration expected on soil A with a return period of 475 years, varying across zones 1 to 3b) and the site-specific PGA from the horizontal UHS (return period 475 years as well) on rock (intended as Swiss reference rock, see section 9 and Poggi et al., 2012). This assumption of equivalence between a_{gd} and PGA is justified by the compatibility between their definitions; in fact, the Swiss reference rock (which PGA is referred to) has a Vs30 of 1100 m/s, therefore it is fully compatible with the soil A definition from SIA 261 normative (indicating Vs30 > 800 m/s). Furthermore, in the considered KiK-net database, the average Vs30 for A class sites is 1036 m/s, which becomes 1094 m/s for selection A sites (1003 m/s for selection B).

In the application of the building code, it is more important to compare absolute values for specific sites, in order to assess the level of conservatism. In this section, we therefore provide the comparison between *absolute* site-specific UHSs and *absolute* elastic design spectra for ten Swiss cities, belonging to different seismic zones according to SIA 261 norm (Sion in zone 3b; Basel in zone 3a; Chur in zone 2; Zurich, Bern, Geneva, Lausanne, Lugano, Luzern and St. Gallen in zone 1).
It is worth highlighting that for the computation of the spectral response amplification functions, two alternative propagation models - differing in the modelling of the distance-dependent geometrical decay – had to be adopted for the RVT (random vibration theory) simulations, depending on the geographical location of the considered city (Edwards and Fäh, 2013; Cauzzi et al., 2014). In fact, some selected cities (Chur, Lugano, Sion) belong to the alpine region, while the others are located in the Swiss foreland region. Although the resulting differences are significant in terms of absolute response spectra, when the latter are normalized with respect to the response spectrum at the reference rock (see section 7), the obtained amplification functions are essentially identical. We remind here that the response spectra amplification functions displayed in section 7 were derived adopting the propagation model for the Swiss alpine region, consistently with the subsequent choice of Sion (in the Swiss alpine region) as benchmark for the comparison between normalized site-specific UHSs and normalized design spectra (section 9).
Similarly to section 9, we draw then the appropriate horizontal-component UHSs on rock (475 year return period) for the ten selected cities from SUIhaz2015 (SED 2016); these UHSs are then multiplied for the amplification factors provided by the appropriate (either alpine or foreland region) spectral

response amplification functions, so to obtain site-specific UHSs referred to the site-specific seismic hazard. We highlight here the consistency between the considered UHS on rock (from SUIhaz2015) and the spectral response amplification functions, both referred to the Swiss reference rock. The obtained site-specific UHSs are finally subdivided by soil classes (SIA 261) and compared with the elastic design spectra.
For the scaling (i.e. anchoring value at small periods) of the normative spectra, it is possible to select, on one hand, a_{gd}, described in SIA-261 as a conservative choice for scaling; note that using a_{gd} presupposes also the affiliation of the considered site to a particular seismic zone, and the definition of these zones. Alternatively, with the intention of defining site-specific design spectra, it is possible to anchor them to the local PGA, deferring to a subsequent stage the choice of the desired level of conservatism. Note that the use of seismic hazard analysis products (such as PGA, or spectral acceleration at reference periods) for the definition of site-specific normative spectra is an approach which is being adopted in the revision of Eurocode 8 (Paolucci, 2017).
In this section, we successively implement both options (a_{gd} and PGA) for the scaling of the normative spectra proposed by Poggi and Fäh (2015) and in this work (see previous section). As anticipated, referring to a_{gd} implies that the normative spectra are expected to be conservative and include all median curves for the 10 cities; referring to PGA implies that the normative spectra are expected to follow the shape of the median curves of site-specific UHSs (similarly as observed in section 10, Figure 46).

In Figures 48-53 we then show the full comparison between design spectra (scaled with a_{gd}) and site-specific UHSs for the city of Sion, considering different sources for the Fourier amplification functions and different station subsets (all stations – selection A – selection B; for collation with Figures 37-42). Please note that the observed variability within each class is very high so that the distributions of different soil classes significantly overlap. The Poggi and Fäh (2015) spectrum scaled with a_{gd} is closer to the 85th percentile curve than to the median, with a partial exception for class E.

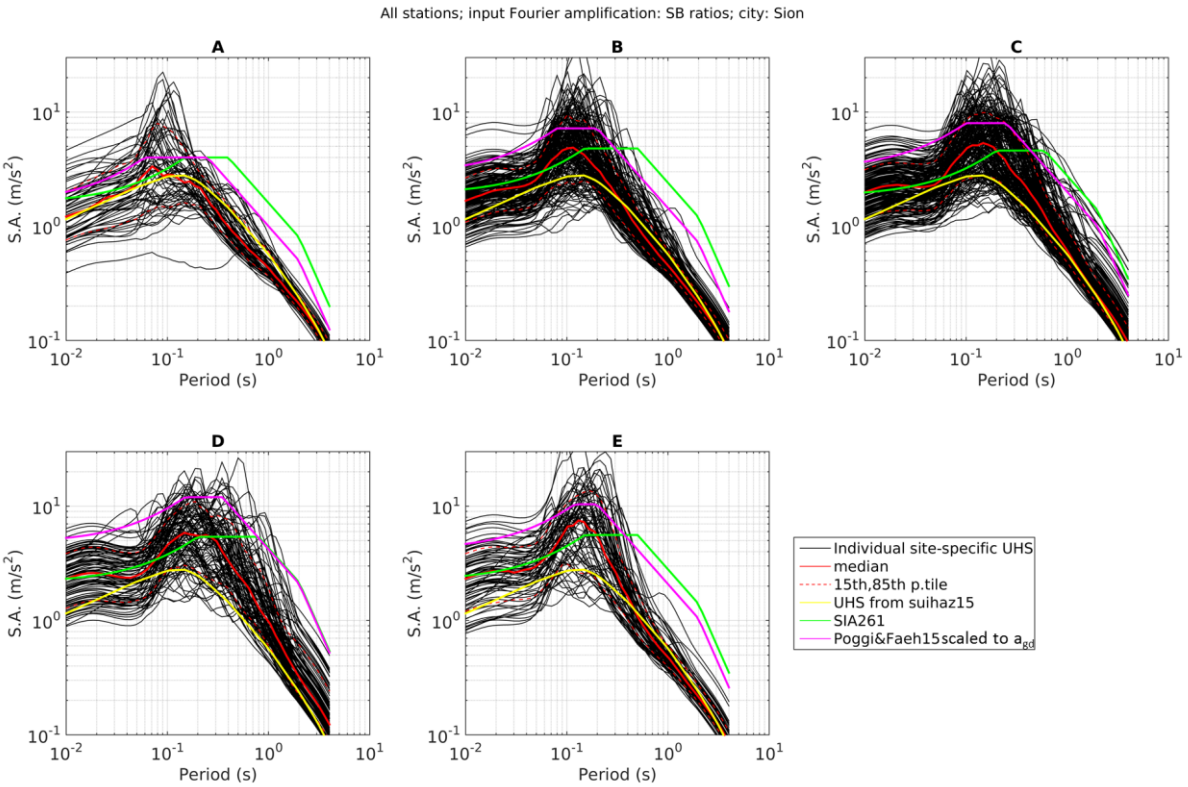

Figure 48 – Site-specific UHS, based on the UHS on rock for Sion (yellow line) with the addition of response spectral amplifications for all KiK-net stations (black lines). The considered response spectral amplifications are derived from the input Fourier amplification information from surface-to-borehole ratios. The median of the distribution of black curves for each soil class is indicated with a continuous red line; the 15th and 85th percentile with a dashed red line. The SIA 261 elastic design spectra are in green; those from the proposal of Poggi and Fäh (2015) in magenta.

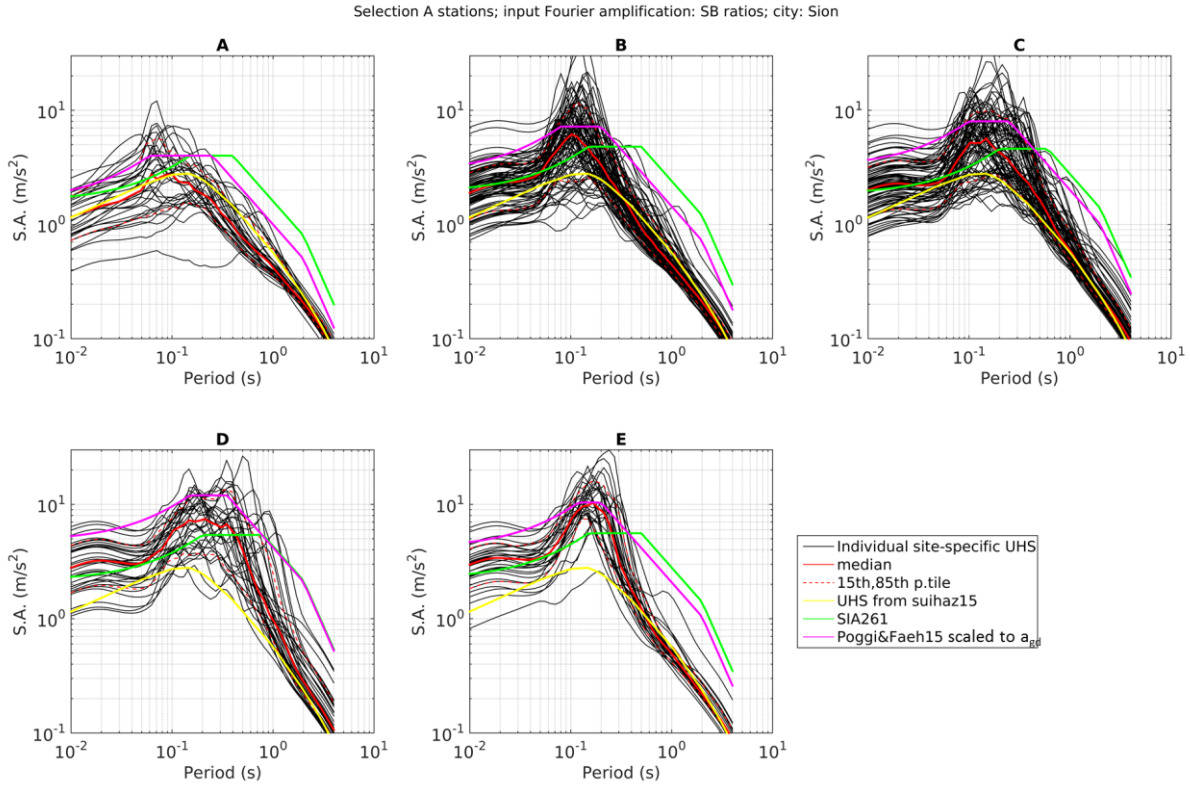

Figure 49 – Site-specific UHS, based on the UHS on rock for Sion (yellow line) with the addition of response spectral amplifications for selection A KiK-net stations (black lines). The considered response spectral amplifications are derived from the input Fourier amplification information from surface-to-borehole ratios. The median of the distribution of black curves for each soil class is indicated with a continuous red line; the 15th and 85th percentile with a dashed red line. The SIA 261 elastic design spectra are in green; those from the proposal of Poggi and Fäh (2015) in magenta.

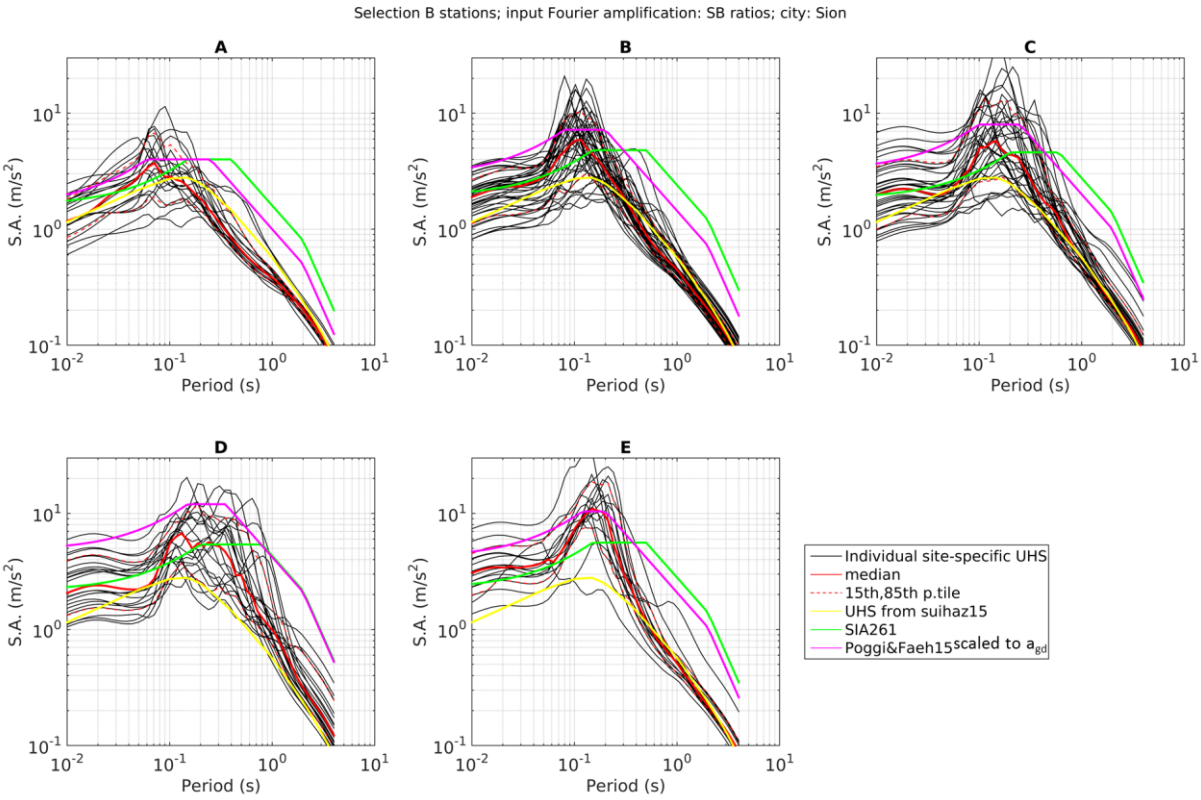

Figure 50 – Site-specific UHS, based on the UHS on rock for Sion (yellow line) with the addition of response spectral amplifications for selection B KiK-net stations (black lines). The considered response spectral amplifications are derived from the input Fourier amplification information from surface-to-borehole ratios. The median of the distribution of black curves for each soil class is indicated with a continuous red line; the 15th and 85th percentile with a dashed red line. The SIA 261 elastic design spectra are in green; those from the proposal of Poggi and Fäh (2015) in magenta.

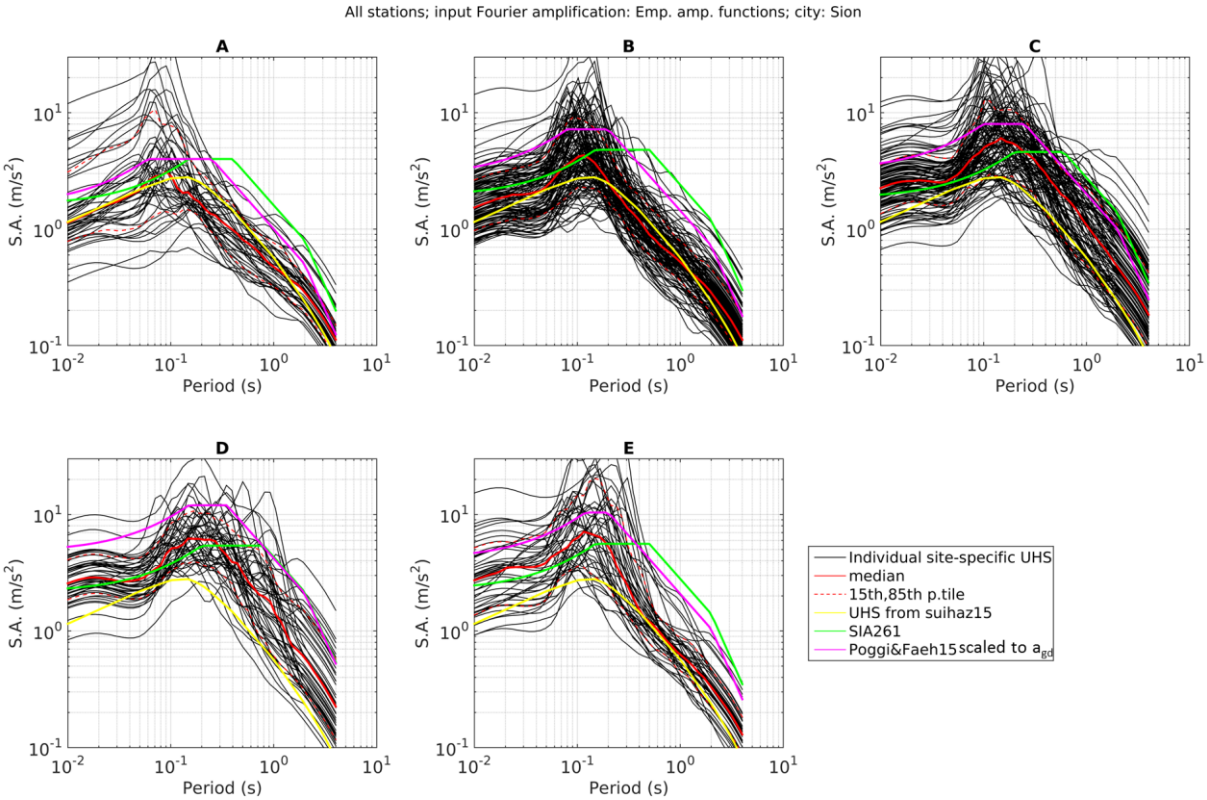

Figure 51 – Site-specific UHS, based on the UHS on rock for Sion (yellow line) with the addition of response spectral amplifications for all KiK-net stations with a reliable empirical amplification function (black lines). The considered response spectral amplifications are derived from the input Fourier amplification information from empirical amplification functions from spectral modelling. The median of the distribution of black curves for each soil class is indicated with a continuous red line; the 15th and 85th percentile with a dashed red line. The SIA 261 elastic design spectra are in green; those from the proposal of Poggi and Fäh (2015) in magenta.

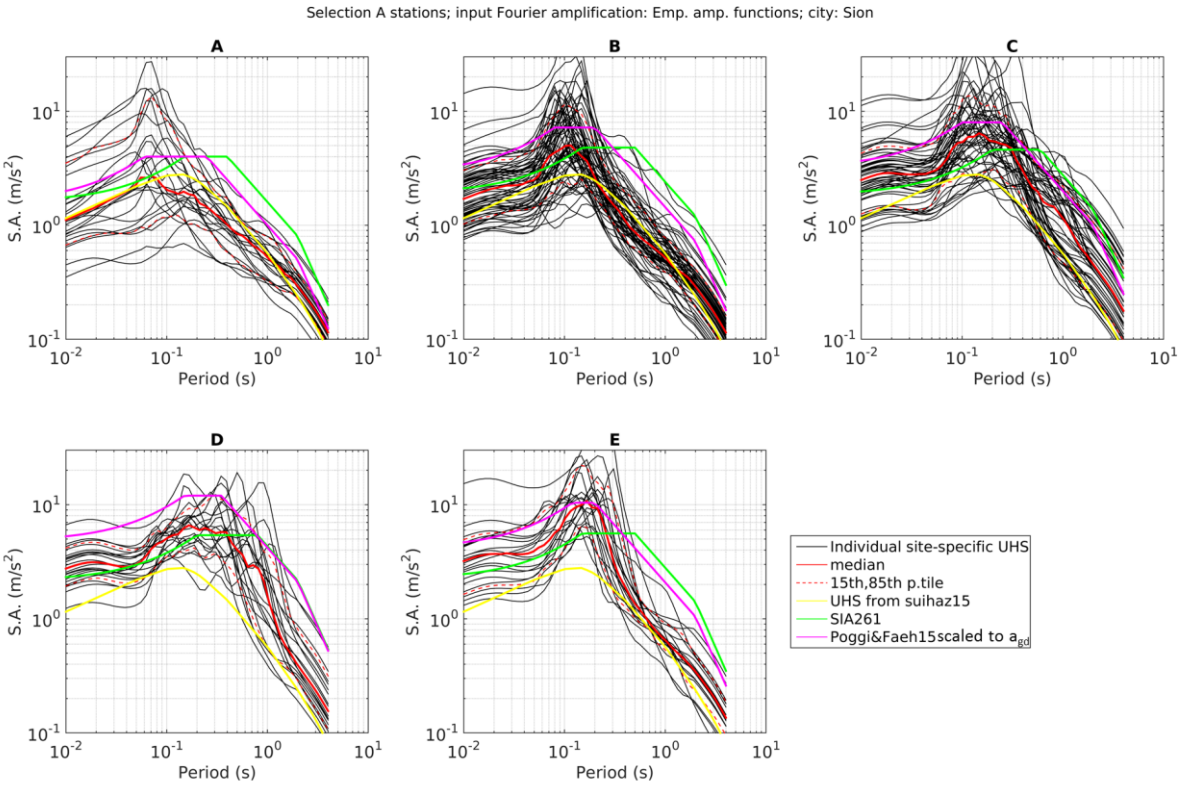

Figure 52 – Site-specific UHS, based on the UHS on rock for Sion (yellow line) with the addition of response spectral amplifications for selection A KiK-net stations with a reliable empirical amplification function (black lines). The considered response spectral amplifications are derived from the input Fourier amplification information from empirical amplification functions from spectral modelling. The median of the distribution of black curves for each soil class is indicated with a continuous red line; the 15th and 85th percentile with a dashed red line. The SIA 261 elastic design spectra are in green; those from the proposal of Poggi and Fäh (2015) in magenta.

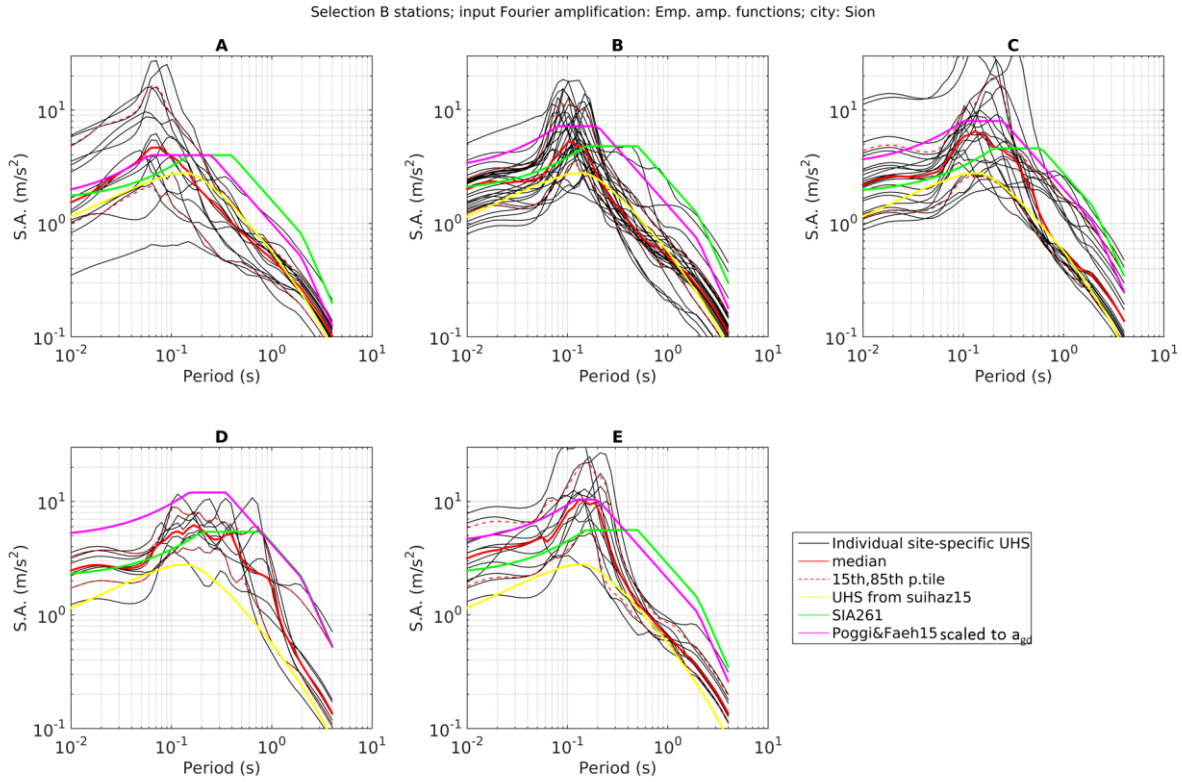

Figure 53 – Site-specific UHS, based on the UHS on rock for Sion (yellow line) with the addition of response spectral amplifications for selection B KiK-net stations with a reliable empirical amplification function (black lines). The considered response spectral amplifications are derived from the input Fourier amplification information from empirical amplification functions from spectral modelling. The median of the distribution of black curves for each soil class is indicated with a continuous red line; the 15th and 85th percentile with a dashed red line. The SIA 261 elastic design spectra are in green; those from the proposal of Poggi and Fäh (2015) in magenta.

Figures 54-63 present a summary of the results for all the considered cities, collecting the median curves from all examined subsets (red lines in Figures 48-53) in a single representation; in these plots we also include, besides the SIA 261 (2014) and Poggi and Fäh's (2015) normative spectra, the design spectral functions proposed in this work (section 10, equations 5, table 3); all design spectra are scaled with a_{gd}.

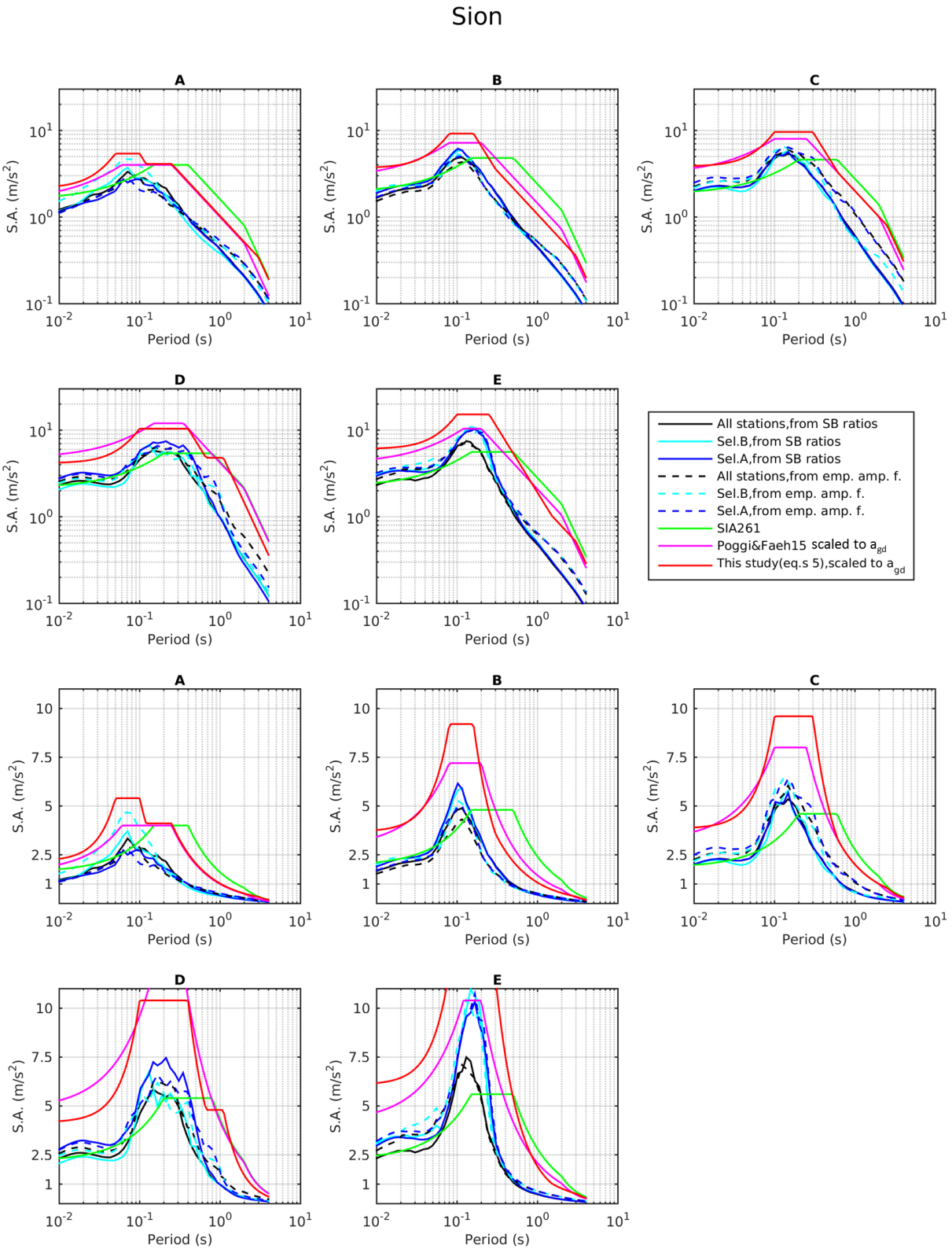

Figure 54 – Median curves of the empirical spectra for the city of Sion (black, blue or cyan line according to the KiKnet station subset; continuous or dashed line according to the origin of the amplification function). The elastic design spectra from SIA 261 normative (green line), Poggi and Fäh's (2015) modification (magenta) and this work's proposal (equations 5, red line) are also included. Top rows: ordinate axis (spectral acceleration) in logarithmic scale. Bottom rows: ordinate axis (spectral acceleration) in linear scale.

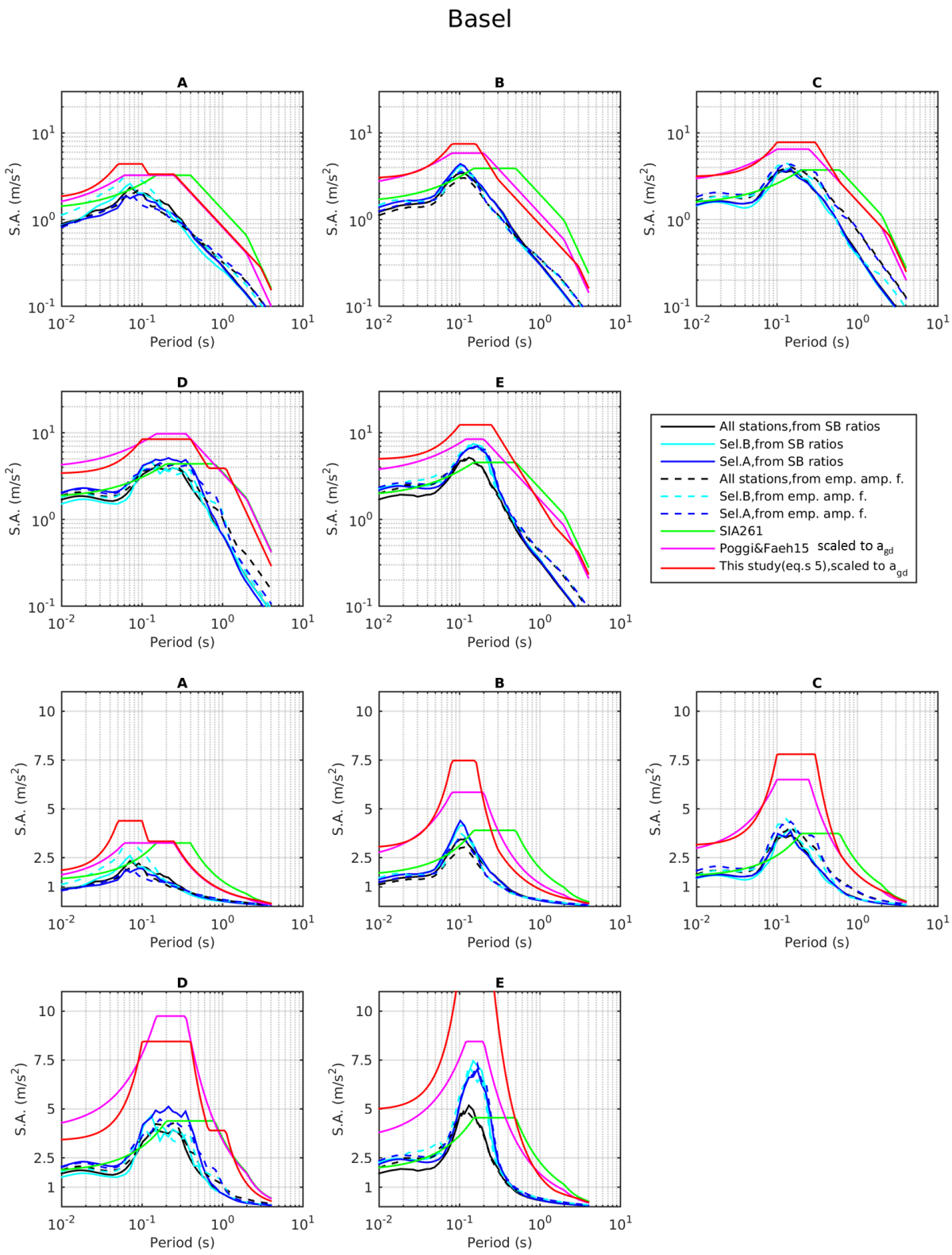

Figure 55 – Median curves of the empirical spectra for the city of Basel (black, blue or cyan line according to the KiKnet station subset; continuous or dashed line according to the origin of the amplification function). The elastic design spectra from SIA 261 normative (green line), Poggi and Fäh's (2015) modification (magenta) and this work's proposal (equations 5, red line) are also included. Top rows: ordinate axis (spectral acceleration) in logarithmic scale. Bottom rows: ordinate axis (spectral acceleration) in linear scale.

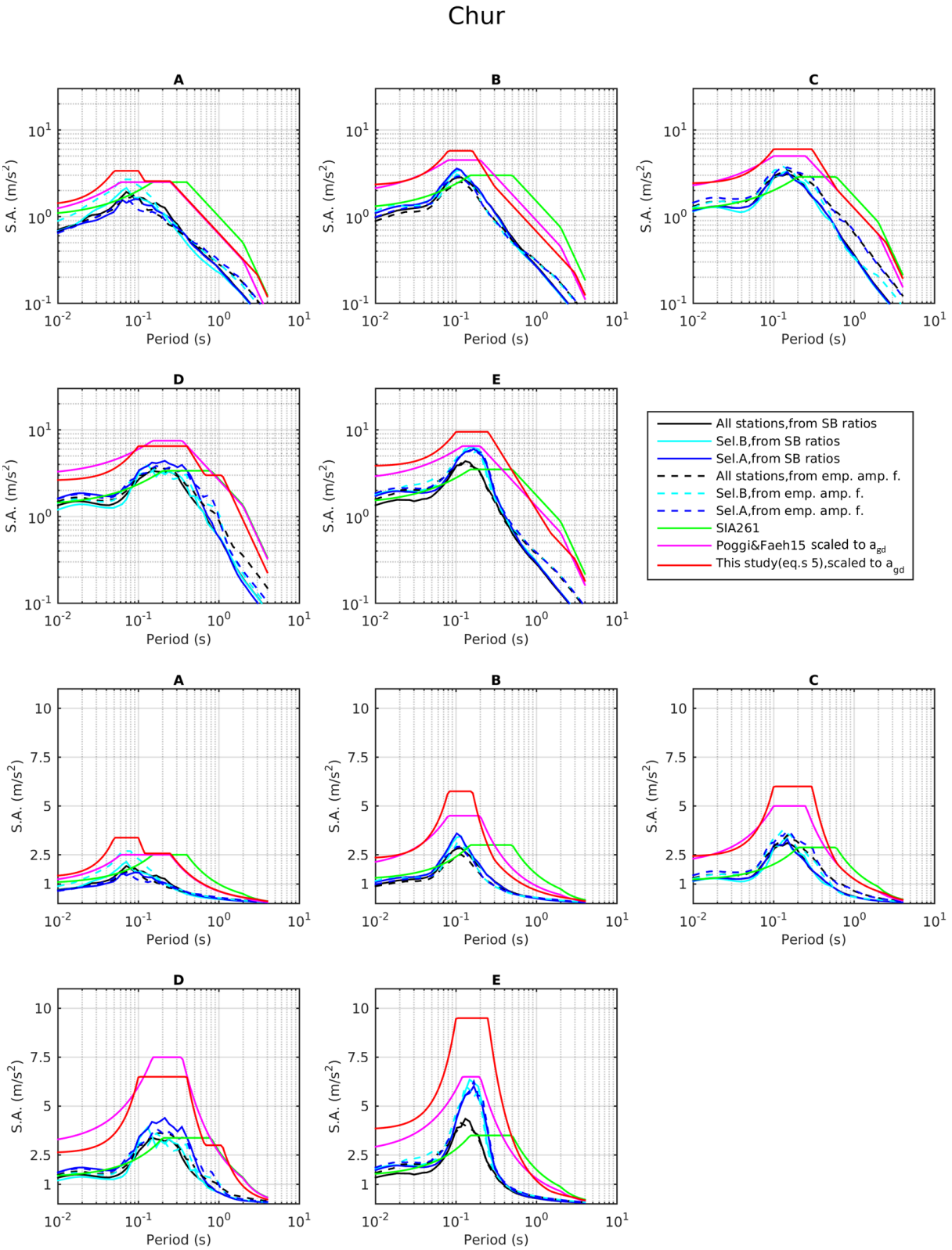

Figure 56 – Median curves of the empirical spectra for the city of Chur (black, blue or cyan line according to the KiKnet station subset; continuous or dashed line according to the origin of the amplification function). The elastic design spectra from SIA 261 normative (green line), Poggi and Fäh's (2015) modification (magenta) and this work's proposal (equations 5, red line) are also included. Top rows: ordinate axis (spectral acceleration) in logarithmic scale. Bottom rows: ordinate axis (spectral acceleration) in linear scale.

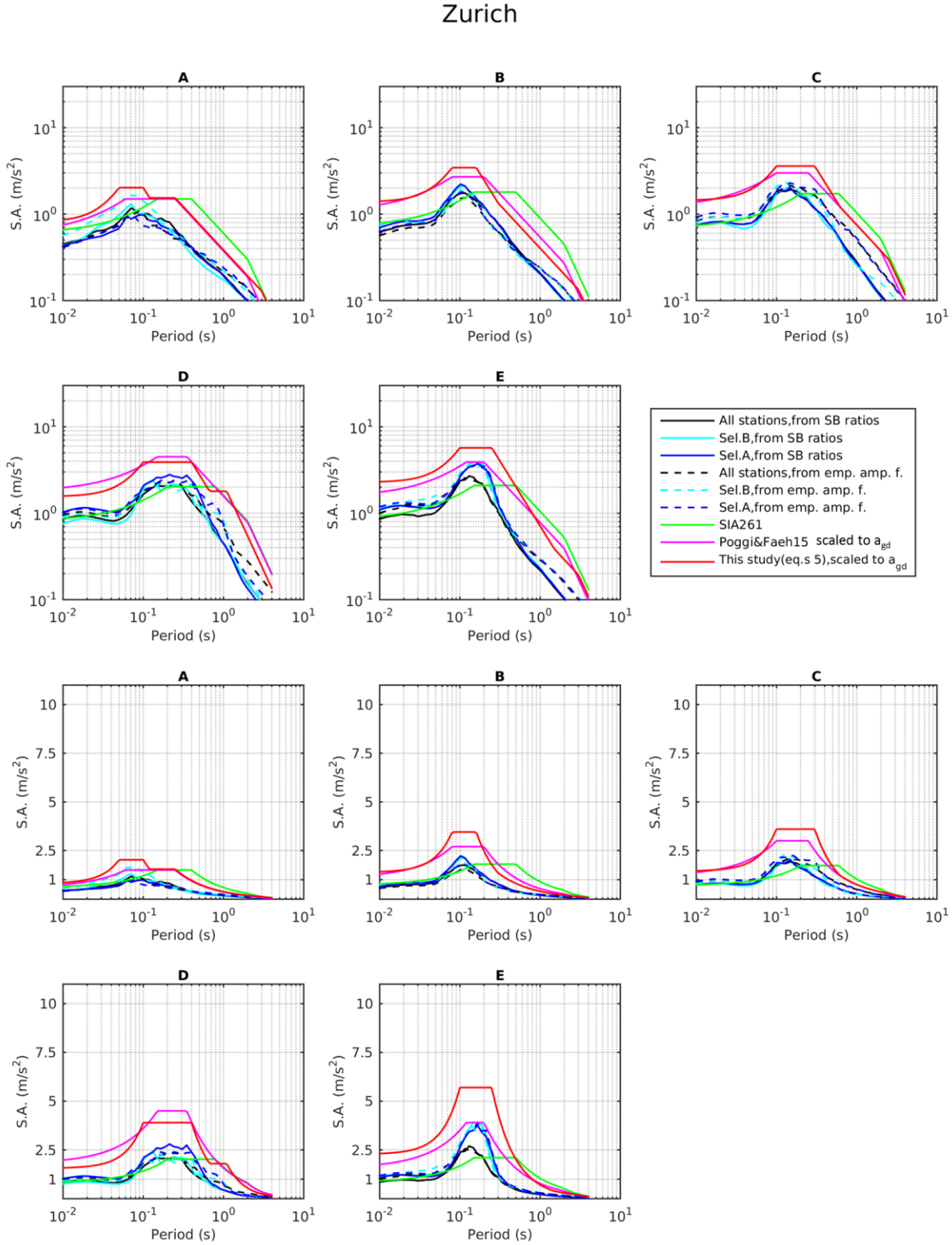

Figure 57 – Median curves of the empirical spectra for the city of Zurich (black, blue or cyan line according to the KiKnet station subset; continuous or dashed line according to the origin of the amplification function). The elastic design spectra from SIA 261 normative (green line), Poggi and Fäh's (2015) modification (magenta) and this work's proposal (equations 5, red line) are also included. Top rows: ordinate axis (spectral acceleration) in logarithmic scale. Bottom rows: ordinate axis (spectral acceleration) in linear scale.

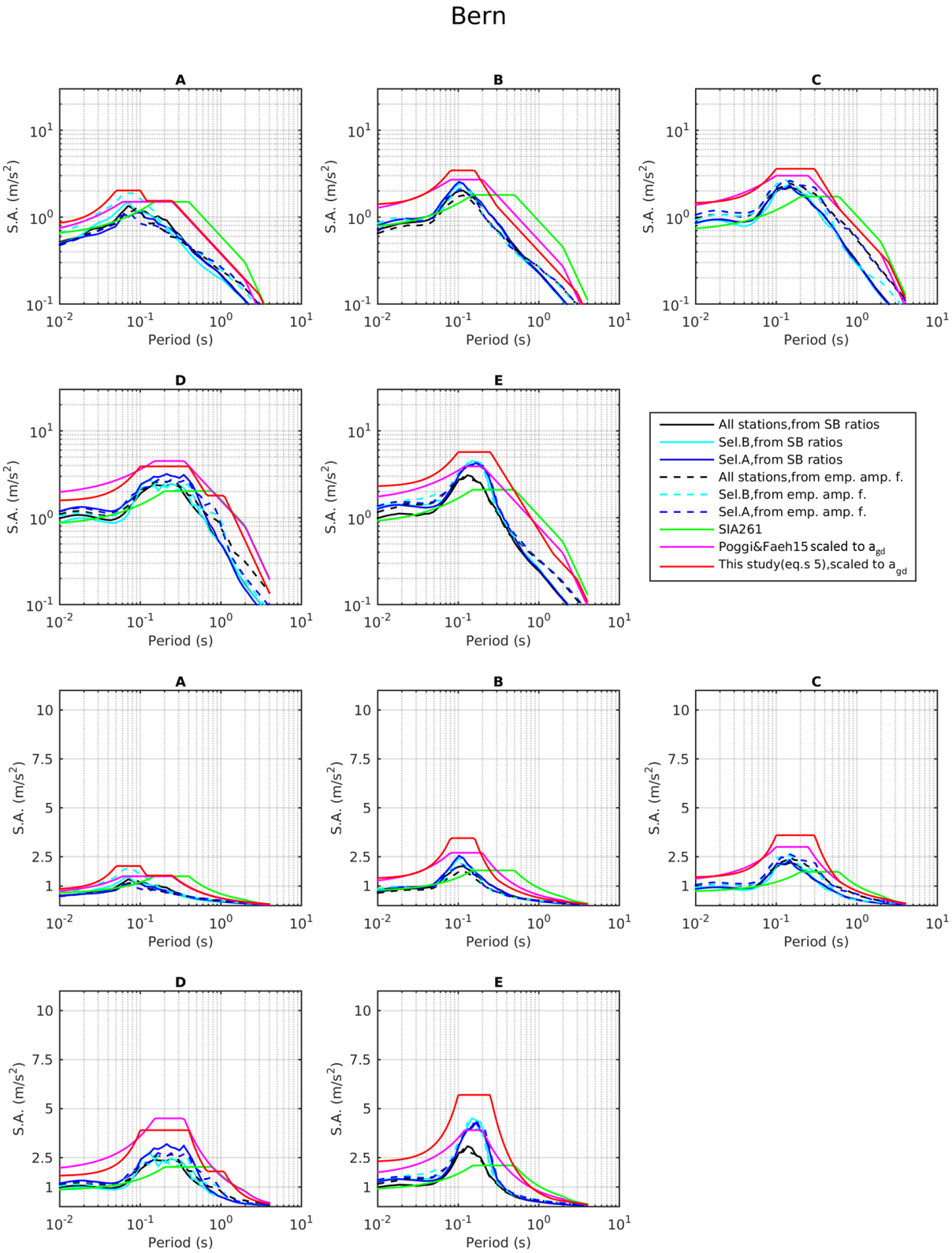

Figure 58 – Median curves of the empirical spectra for the city of Bern (black, blue or cyan line according to the KiKnet station subset; continuous or dashed line according to the origin of the amplification function). The elastic design spectra from SIA 261 normative (green line), Poggi and Fäh's (2015) modification (magenta) and this work's proposal (equations 5, red line) are also included. Top rows: ordinate axis (spectral acceleration) in logarithmic scale. Bottom rows: ordinate axis (spectral acceleration) in linear scale.

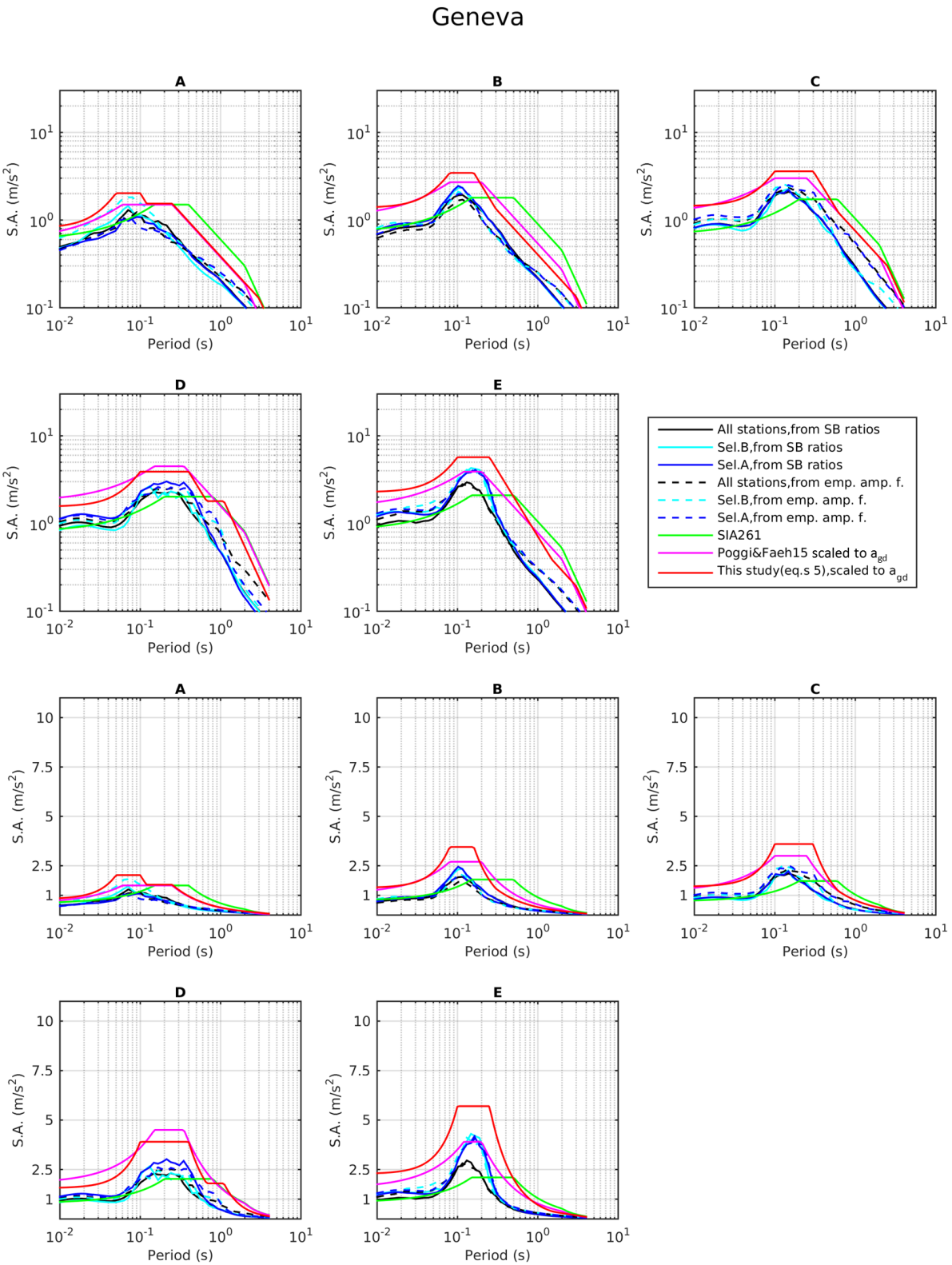

Figure 59 – Median curves of the empirical spectra for the city of Geneva (black, blue or cyan line according to the KiKnet station subset; continuous or dashed line according to the origin of the amplification function). The elastic design spectra from SIA 261 normative (green line), Poggi and Fäh's (2015) modification (magenta) and this work's proposal (equations 5, red line) are also included. Top rows: ordinate axis (spectral acceleration) in logarithmic scale. Bottom rows: ordinate axis (spectral acceleration) in linear scale.

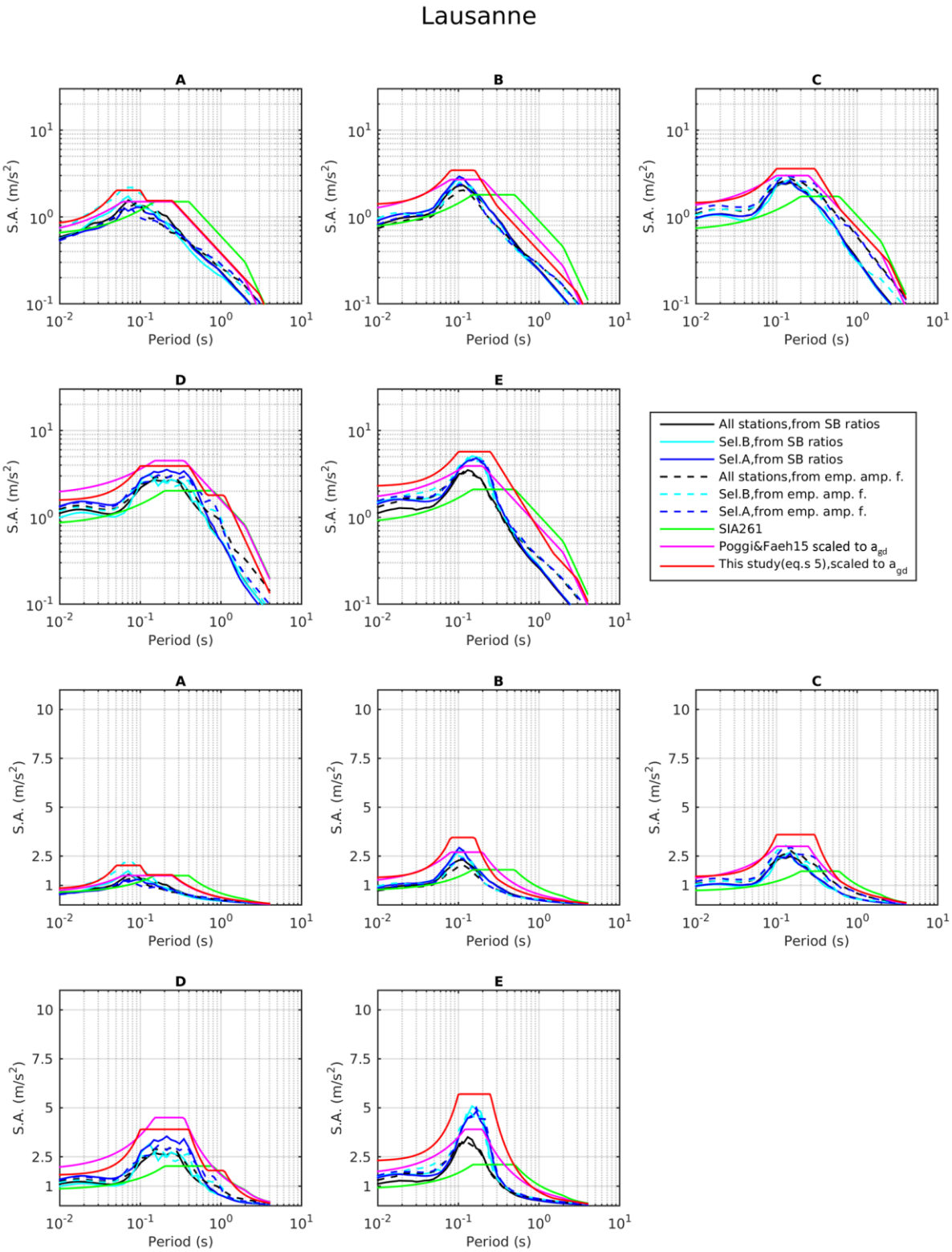

Figure 60– Median curves of the empirical spectra for the city of Lausanne (black, blue or cyan line according to the KiKnet station subset; continuous or dashed line according to the origin of the amplification function). The elastic design spectra from SIA 261 normative (green line), Poggi and Fäh's (2015) modification (magenta) and this work's proposal (equations 5, red line) are also included. Top rows: ordinate axis (spectral acceleration) in logarithmic scale. Bottom rows: ordinate axis (spectral acceleration) in linear scale.

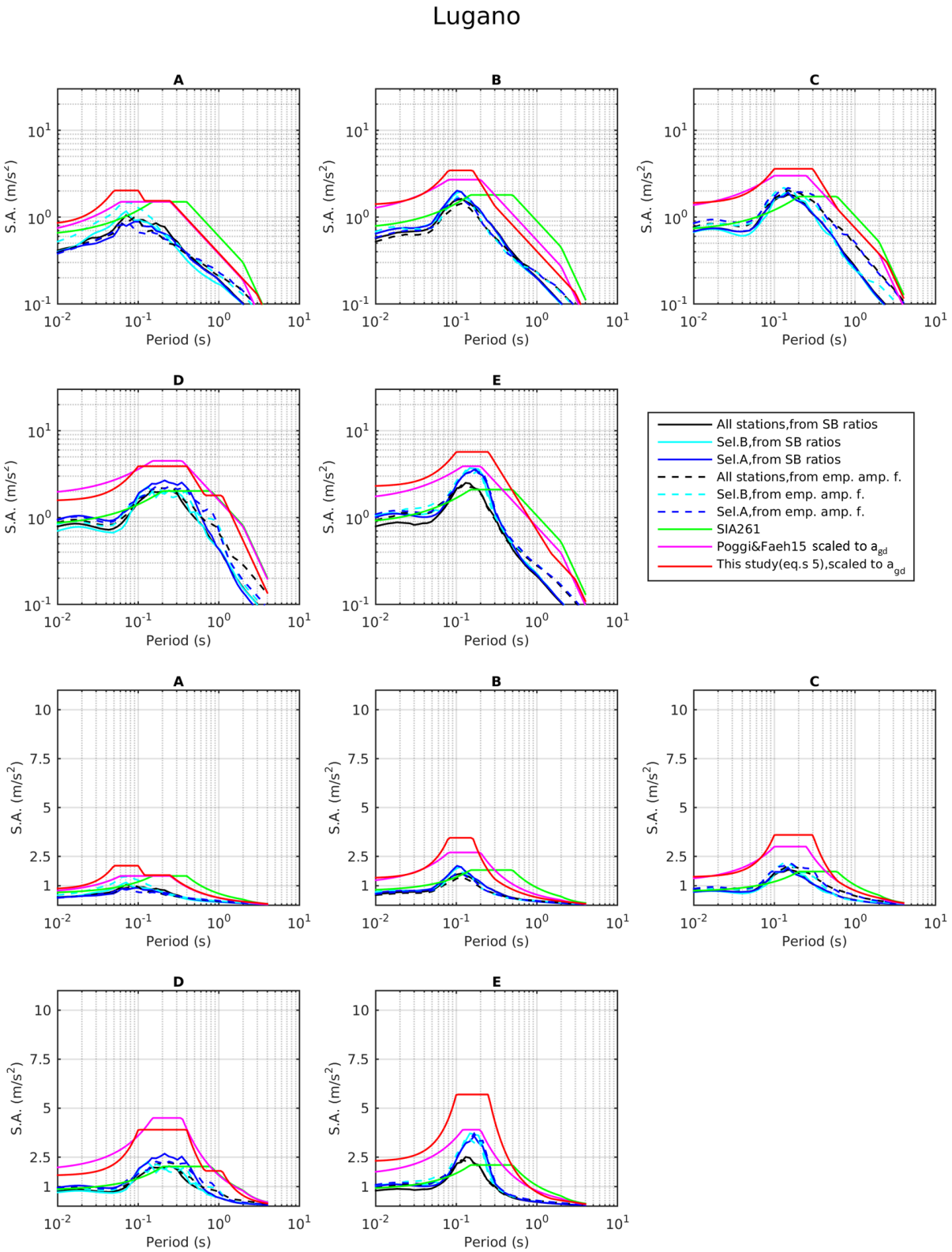

Figure 61– Median curves of the empirical spectra for the city of Lugano (black, blue or cyan line according to the KiKnet station subset; continuous or dashed line according to the origin of the amplification function). The elastic design spectra from SIA 261 normative (green line), Poggi and Fäh's (2015) modification (magenta) and this work's proposal (equations 5, red line) are also included. Top rows: ordinate axis (spectral acceleration) in logarithmic scale. Bottom rows: ordinate axis (spectral acceleration) in linear scale.

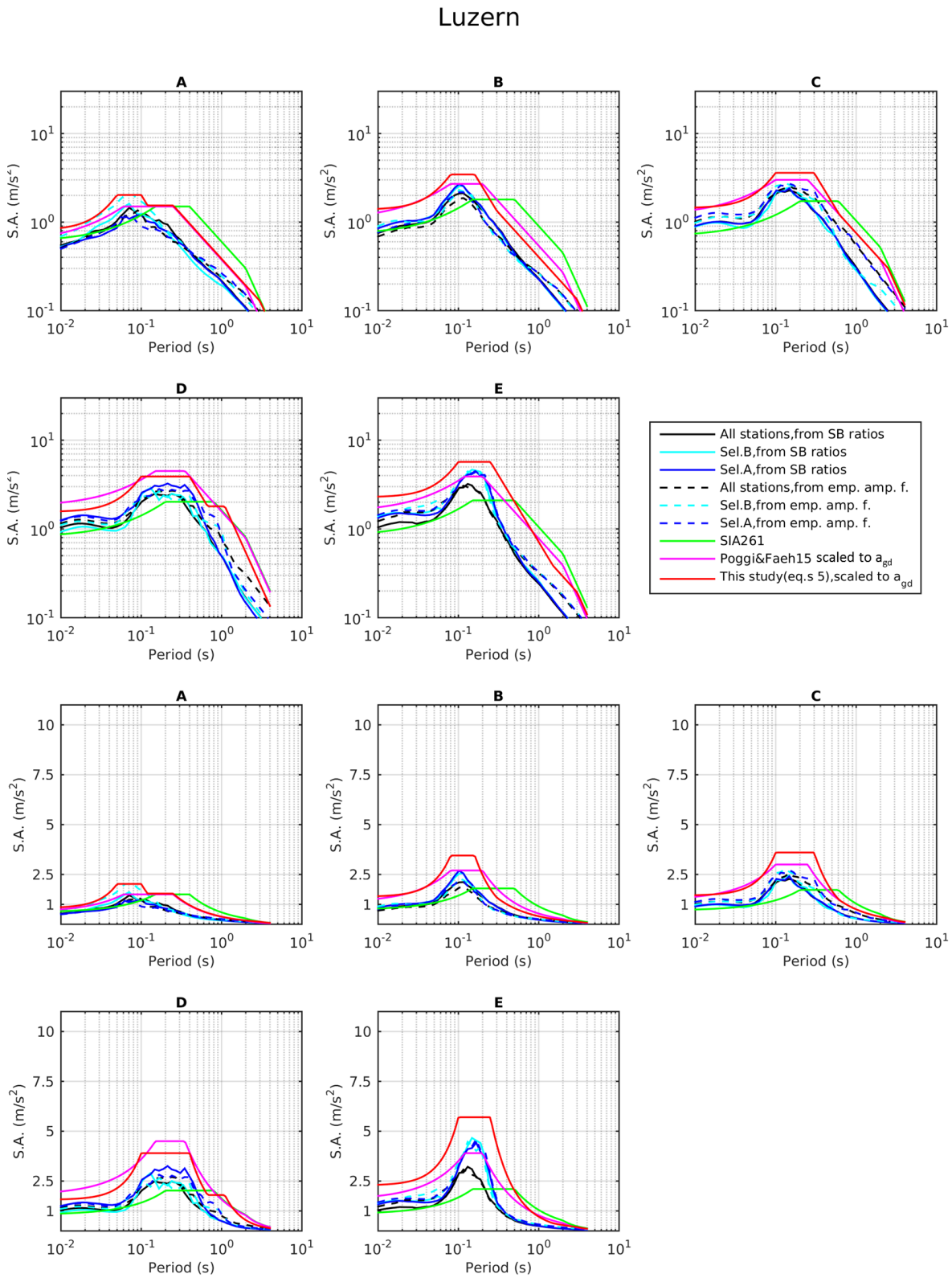

Figure 62– Median curves of the empirical spectra for the city of Luzern (black, blue or cyan line according to the KiKnet station subset; continuous or dashed line according to the origin of the amplification function). The elastic design spectra from SIA 261 normative (green line), Poggi and Fäh's (2015) modification (magenta) and this work's proposal (equations 5, red line) are also included. Top rows: ordinate axis (spectral acceleration) in logarithmic scale. Bottom rows: ordinate axis (spectral acceleration) in linear scale.

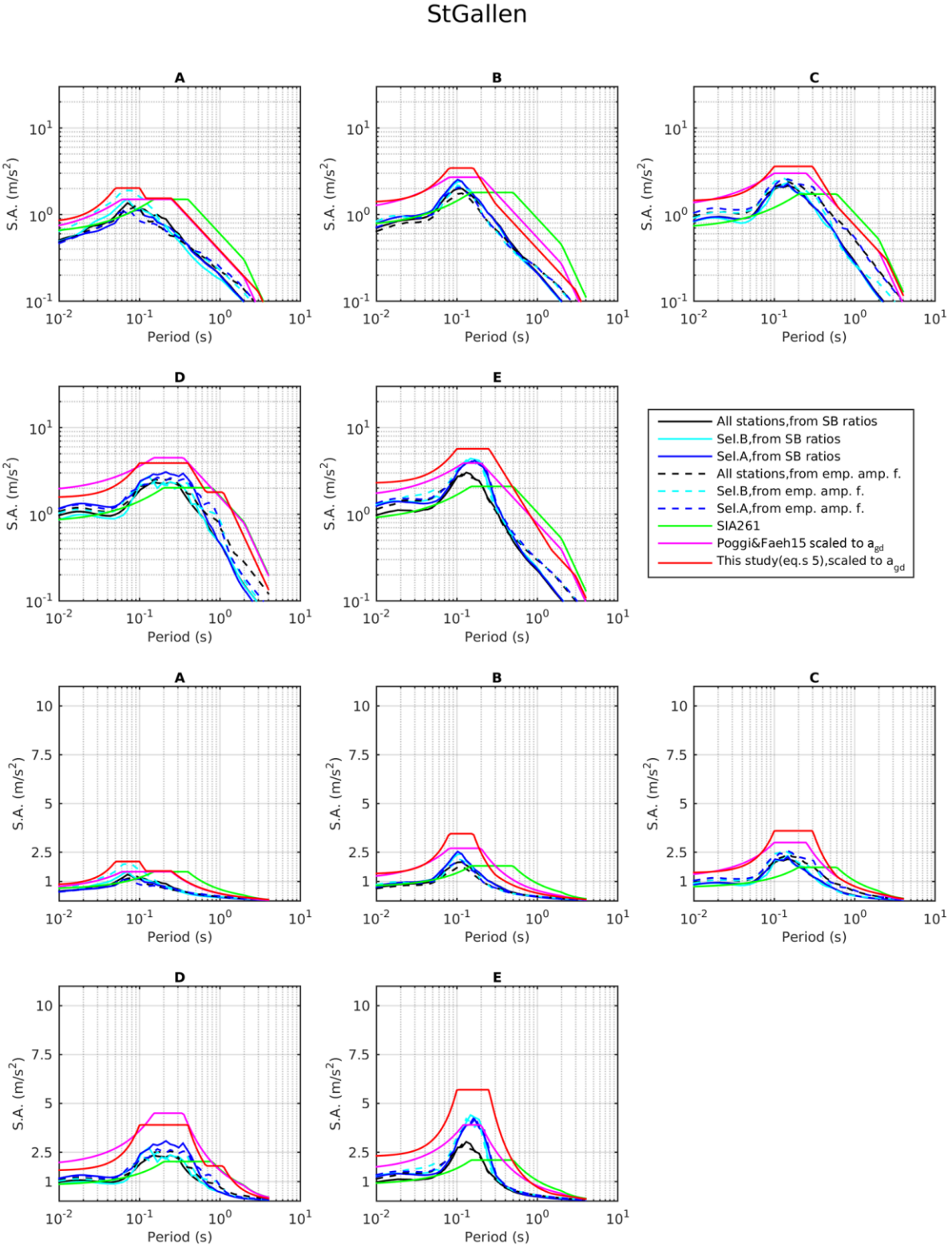

Figure 63 – Median curves of the empirical spectra for the city of St Gallen (black, blue or cyan line according to the KiKnet station subset; continuous or dashed line according to the origin of the amplification function). The elastic design spectra from SIA 261 normative (green line), Poggi and Fäh's (2015) modification (magenta) and this work's proposal (equations 5, red line) are also included. Top rows: ordinate axis (spectral acceleration) in logarithmic scale. Bottom rows: ordinate axis (spectral acceleration) in linear scale.

In Figures 58-63, due to the conservative scaling of the design spectra with a_{gd}, the medians over site-specific UHS generally show much lower values than the design spectra, in comparison with Figure 46 (normalized values). In fact, the difference between a_{gd} and PGA is, as expected, consistently positive (a_{gd} > PGA) for all ten cities. This difference cannot be attributed to a different rock reference for the two values; in fact, when changing the PGA reference from Vs30 = 1100 to 800 m/s (lower limit for soil A type), the increase is anyhow small (+5.25%, e.g. Danciu and Fäh, 2017, while the relative shift a_{gd} – PGA is +10-50%; see table 4).

Table 4 – values of horizontal a_{gd} and PGA for the cities of Basel, Chur, Sion, Zurich, with a return period of 475 years. The PGA is provided as referred to the Swiss reference rock (Vs30=1100 m/s, 3rd column) and also to a Vs30 of 800 m/s (last column). The correction factors for the change of reference are based on Danciu and Fäh (2017).

City (Zone)	a_{gd} (m/s^2) from SIA 261	PGA (m/s^2) referred to Vs30 = 1100 m/s	PGA (m/s^2) referred to Vs30 = 800 m/s
Basel (zone 3a)	1.3	0.85	0.89
Bern (zone 1)	0.6	0.49	0.52
Chur (zone 2)	1.0	0.67	0.71
Geneva (zone 1)	0.6	0.47	0.49
Lausanne (zone 1)	0.6	0.56	0.59
Lugano (zone 1)	0.6	0.39	0.41
Luzern (zone 1)	0.6	0.52	0.55
Sion (zone 3b)	1.6	1.15	1.21
St. Gallen (zone 1)	0.6	0.48	0.51
Zurich (zone 1)	0.6	0.43	0.45

Despite these differences, consistently with the observations introduced in sections 9-10 (normalized values), the SIA 261 design spectra (green lines in Figures 54-63) result as conservative at long periods but fail to allocate the amplitude peak of the site-specific UHSs due to resonance. The plateau segment of SIA 261 spectra is in fact placed at longer periods (for all soil types) with respect to the resonance peak, and as a consequence the median curves of the site-specific UHSs exceed the design spectrum in its left shoulder (low-period segment; see Figures 54-63).

The design spectra adopting the modified coefficients proposed by Poggi and Fäh (2015; magenta lines), again anchored to a_{gd}, overtop in most cases, for soil classes A-D, the median curves of site-specific UHSs; their plateau segment is placed at the peak related to amplification resonance (Figures 54-63). A partial exception is the median curve of site-specific UHSs derived from empirical amplification functions belonging to selection B (cyan dashed line) for soil class A, which in most cases (Sion, Figure 54; Chur, Figure 56; Zurich, Figure 57; Bern, Figure 58; Geneva, Figure 59; Lausanne, Figure 60; Luzern, Figure 62; St. Gallen, Figure 63) exceeds the Poggi and Fäh's (2015) design spectra; nevertheless, this mismatch has not been considered as significant, but likely it is to be ascribed to the low number of selection A sites used for the calculation of the median (as already observed in sections 7 and 10). In fact, in all the other cases (site-specific UHSs from SB ratios, site-specific UHSs from empirical functions, all sites and selection A) this exceedance is not observed.
As for soil type E, the Poggi and Fäh's (2015) design spectrum places the constant acceleration segment at the same period range of the resonance peak of site-specific hazard spectra. However, the spectral acceleration plateau is, at a number of cities, equalled (Geneva Figure 59; Bern, Figure 58; Sion Figure 54, St. Gallen, Figure 63) or surpassed (Lausanne, Figure 60; Luzern, Figure 62) by most of the empirically-derived median curves (i.e. those corresponding to selections A and B). This observation generally applies to those cities where a_{gd} (anchor value for elastic design spectra) and PGA (anchor value for site-specific UHSs) become close enough. In particular, class E design spectra are overtopped when the ratio a_{gd}/PGA drops below 1.2 (Lausanne = 1.10, Luzern = 1.15); the same spectra are equalled for a_{gd}/PGA ratios around 1.25 (Bern = 1.22; Geneva = 1.27; St. Gallen = 1.25); for the other cities, a_{gd}/PGA = 1.39 (Sion) – 1.54 (Lugano). For the case of Sion, the cause determining site-specific UHSs

tangent to the design spectrum are the high (relatively to PGA) values of the UHS on rock at period 0.1-0.2 s (which is the period interval of the resonance peak of class E sites, see section 7).
This observation indicates that the choice of a_{gd} for the scaling of normative spectra does not apply the same level of conservatism to all cities; this outcome (the poor agreement between seismic hazard analysis and the seismic zone attribution for some Swiss cities, here in particular Lausanne and Luzern) is in agreement with results from subproject 2 (see corresponding report). Therefore, as last step in this section, we will derive site-specific design spectra, incorporating "local" quantities from seismic hazard analyses into their definition.

Coming back to Figures 54-63, when considering the normative spectrum functional form proposed in this work (equations 5, red lines), this produces spectra which consistently surmount the median curves of site-specific hazard spectra, for all soil classes and at all considered cities; significant conservatism is allowed for (because of the scaling with a_{gd}), both at short and long periods.

As last step, we derive and assess site-specific design spectra, incorporating "local" quantities from seismic hazard analyses into their definition. The design spectra from Poggi and Fäh's (2015) proposal and this work (equations 5) were hence scaled with site-specific PGA (i.e. a_{gd} was replaced by PGA in equations 4-5). It is worth remarking that the use of seismic hazard analysis products (such as PGA, or spectral acceleration at reference periods) for the definition of normative spectra is an approach that, at the time of writing of this report (November 2017), is intended to be adopted in the revision of Eurocode 8 (Paolucci, 2017).
The results obtained for all the considered cities are displayed in the following Figures 64-73. It should be noted that Figure 64 (Sion) is indeed similar to Figure 46, but this is not necessarily the case for Figures 65-73, based on the UHS on rock of other cities. As already observed in section 10, the resonance peak from site-specific UHSs consistently (i.e. for all cities) overtops the Poggi and Fäh (2015) spectrum for soil type E (this occurs also for some cities for types A, B, C). On the contrary, the design spectrum proposed by our work and scaled to PGA, generally (i.e. considering all cities and soil classes) closely follows the shape of the median envelopes of the hazard spectra inclusive of site amplification.

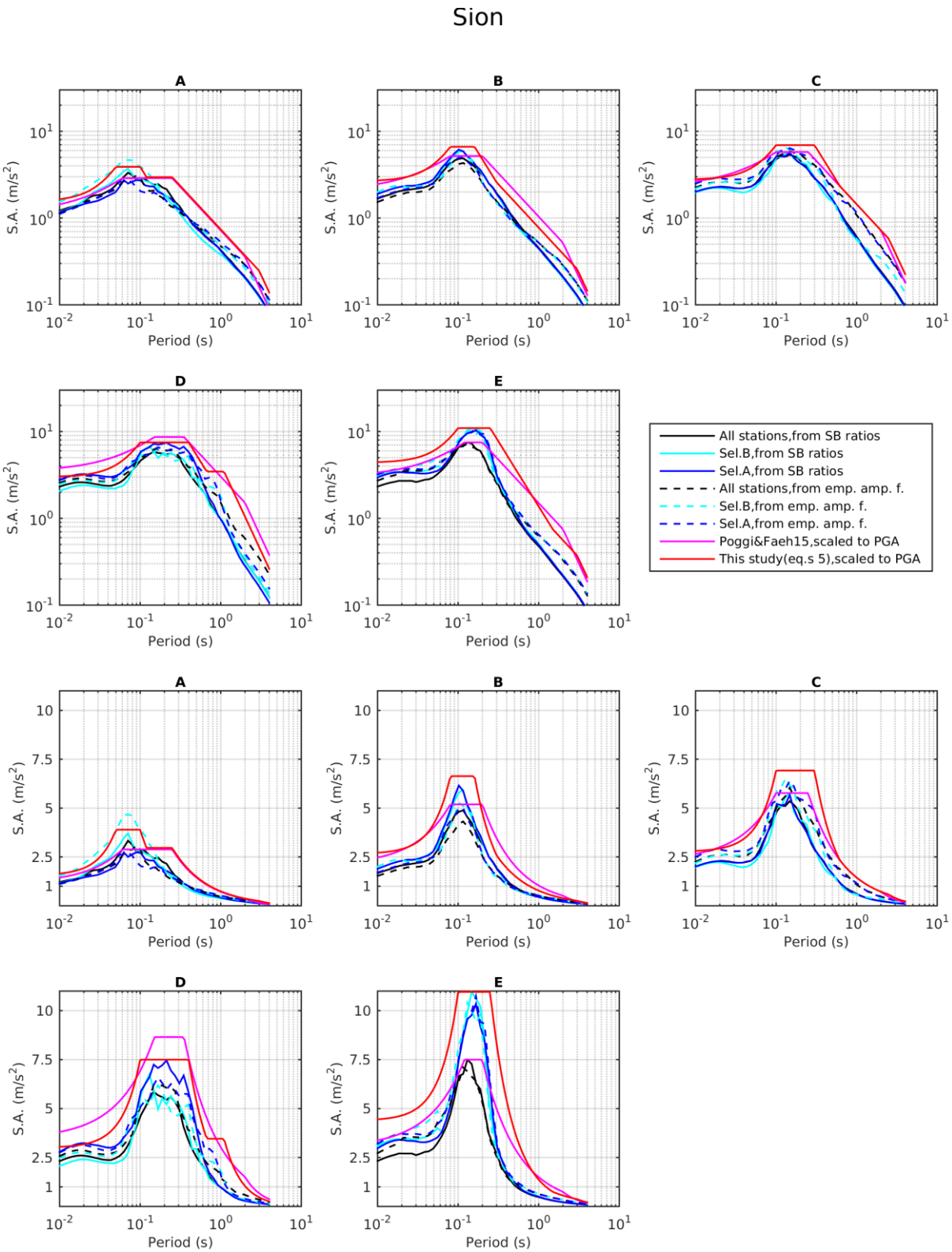

Figure 64 – Median curves of the empirical spectra for the city of Sion (black, blue or cyan line according to the KiKnet station subset; continuous or dashed line according to the origin of the amplification function). The elastic design spectra from Poggi and Fäh's (2015) proposal and this work's proposal (equations 5) are also included (both scaled to PGA) as magenta and red lines, respectively. Top rows: ordinate axis (spectral acceleration) in logarithmic scale. Bottom rows: ordinate axis (spectral acceleration) in linear scale.

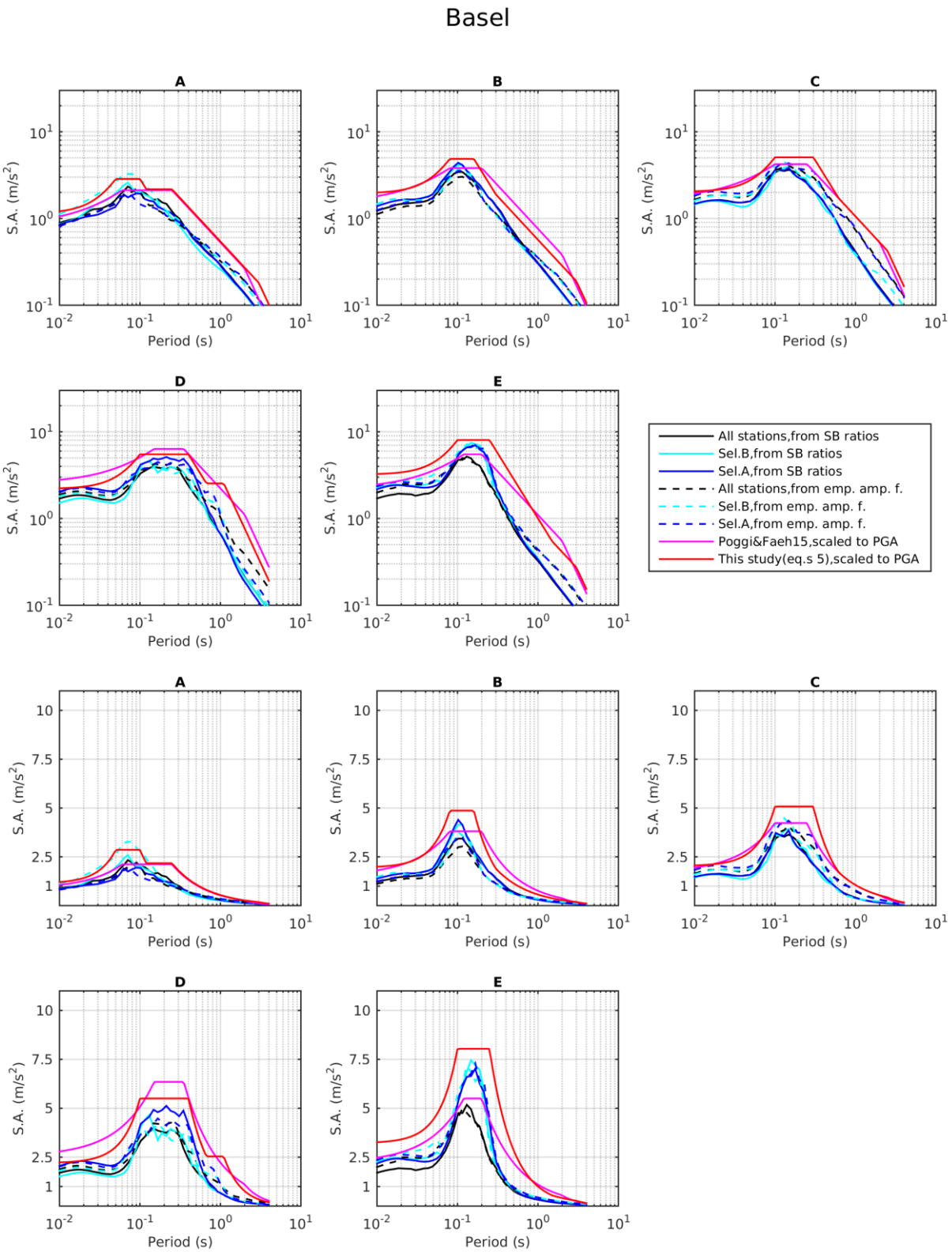

Figure 65 – Median curves of the empirical spectra for the city of Basel (black, blue or cyan line according to the KiKnet station subset; continuous or dashed line according to the origin of the amplification function). The elastic design spectra from Poggi and Fäh's (2015) proposal and this work's proposal (equations 5) are also included (both scaled to PGA) as magenta and red lines, respectively. Top rows: ordinate axis (spectral acceleration) in logarithmic scale. Bottom rows: ordinate axis (spectral acceleration) in linear scale.

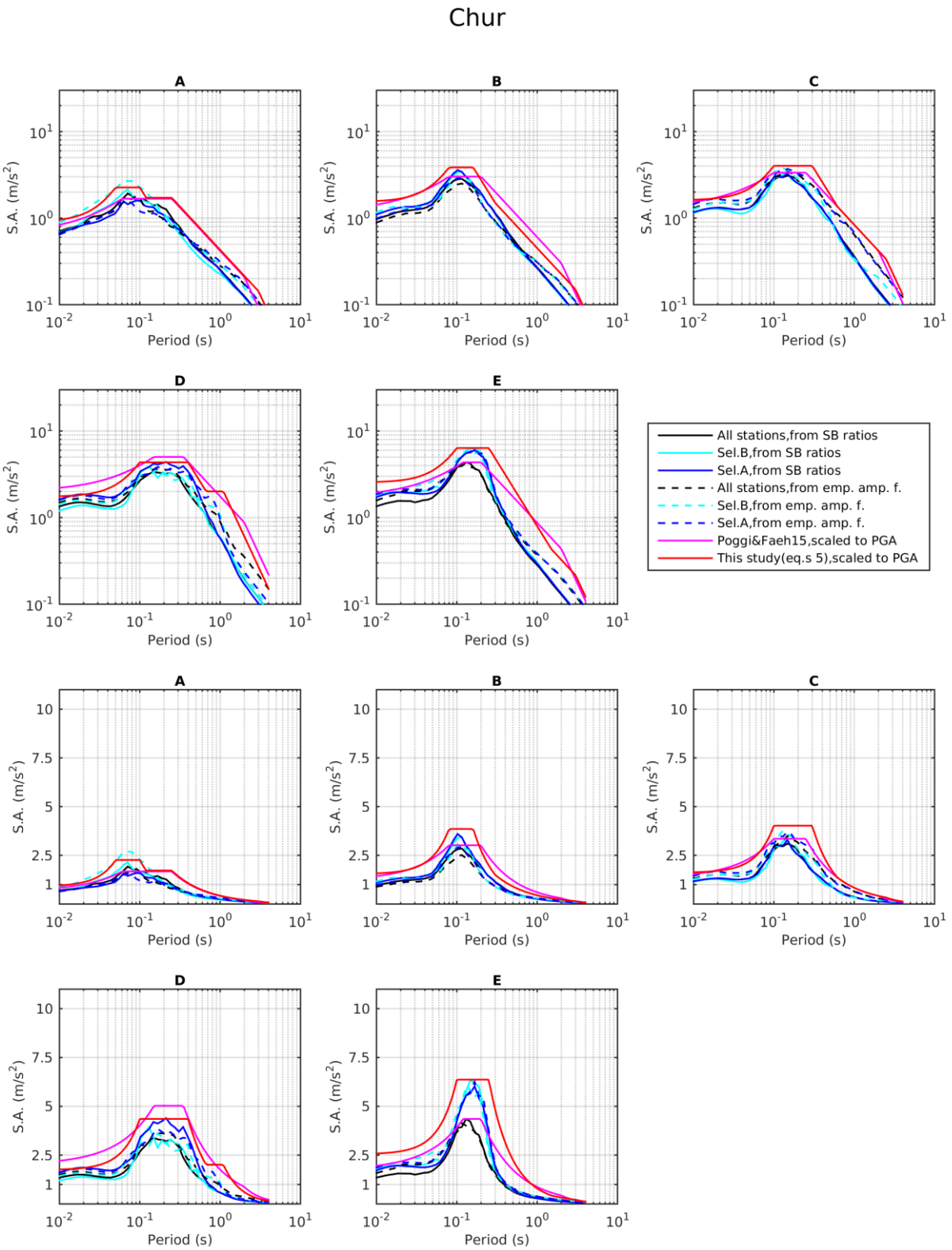

Figure 66 – Median curves of the empirical spectra for the city of Chur (black, blue or cyan line according to the KiKnet station subset; continuous or dashed line according to the origin of the amplification function). The elastic design spectra from Poggi and Fäh's (2015) proposal and this work's proposal (equations 5) are also included (both scaled to PGA) as magenta and red lines, respectively. Top rows: ordinate axis (spectral acceleration) in logarithmic scale. Bottom rows: ordinate axis (spectral acceleration) in linear scale.

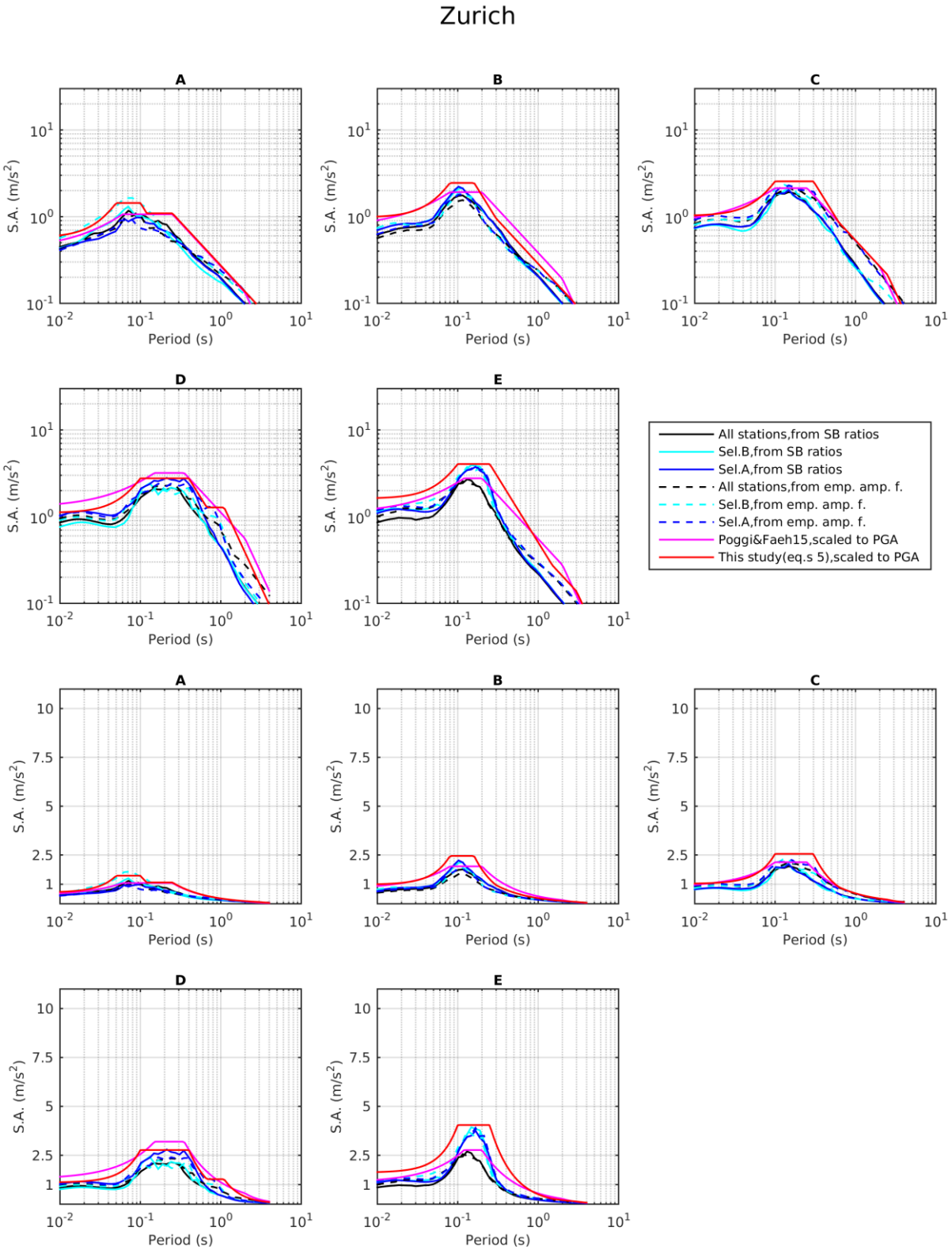

Figure 67 – Median curves of the empirical spectra for the city of Zurich (black, blue or cyan line according to the KiKnet station subset; continuous or dashed line according to the origin of the amplification function). The elastic design spectra from Poggi and Fäh's (2015) proposal and this work's proposal (equations 5) are also included (both scaled to PGA) as magenta and red lines, respectively. Top rows: ordinate axis (spectral acceleration) in logarithmic scale. Bottom rows: ordinate axis (spectral acceleration) in linear scale.

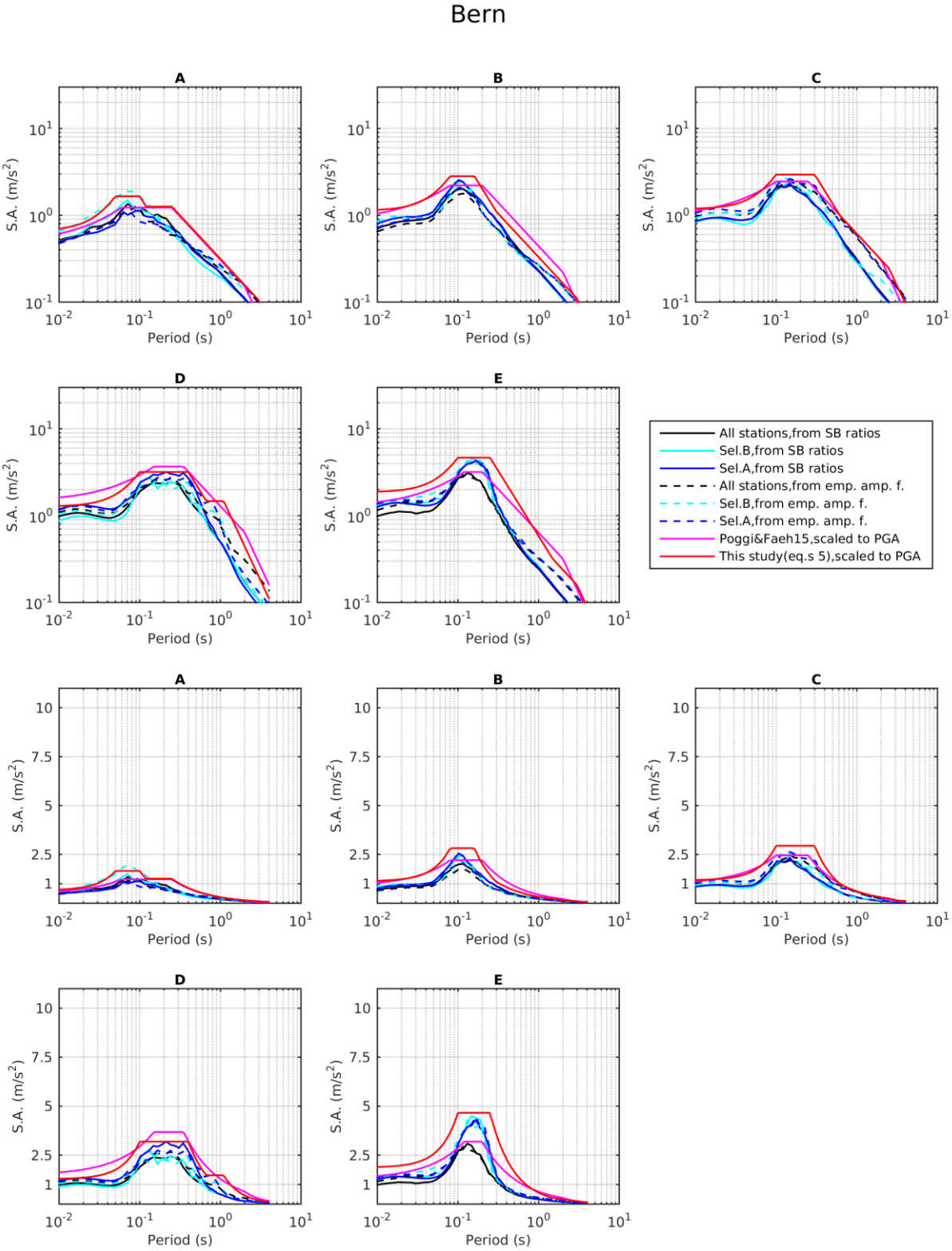

Figure 68 – Median curves of the empirical spectra for the city of Berm (black, blue or cyan line according to the KiKnet station subset; continuous or dashed line according to the origin of the amplification function). The elastic design spectra from Poggi and Fäh's (2015) proposal and this work's proposal (equations 5) are also included (both scaled to PGA) as magenta and red lines, respectively. Top rows: ordinate axis (spectral acceleration) in logarithmic scale. Bottom rows: ordinate axis (spectral acceleration) in linear scale.

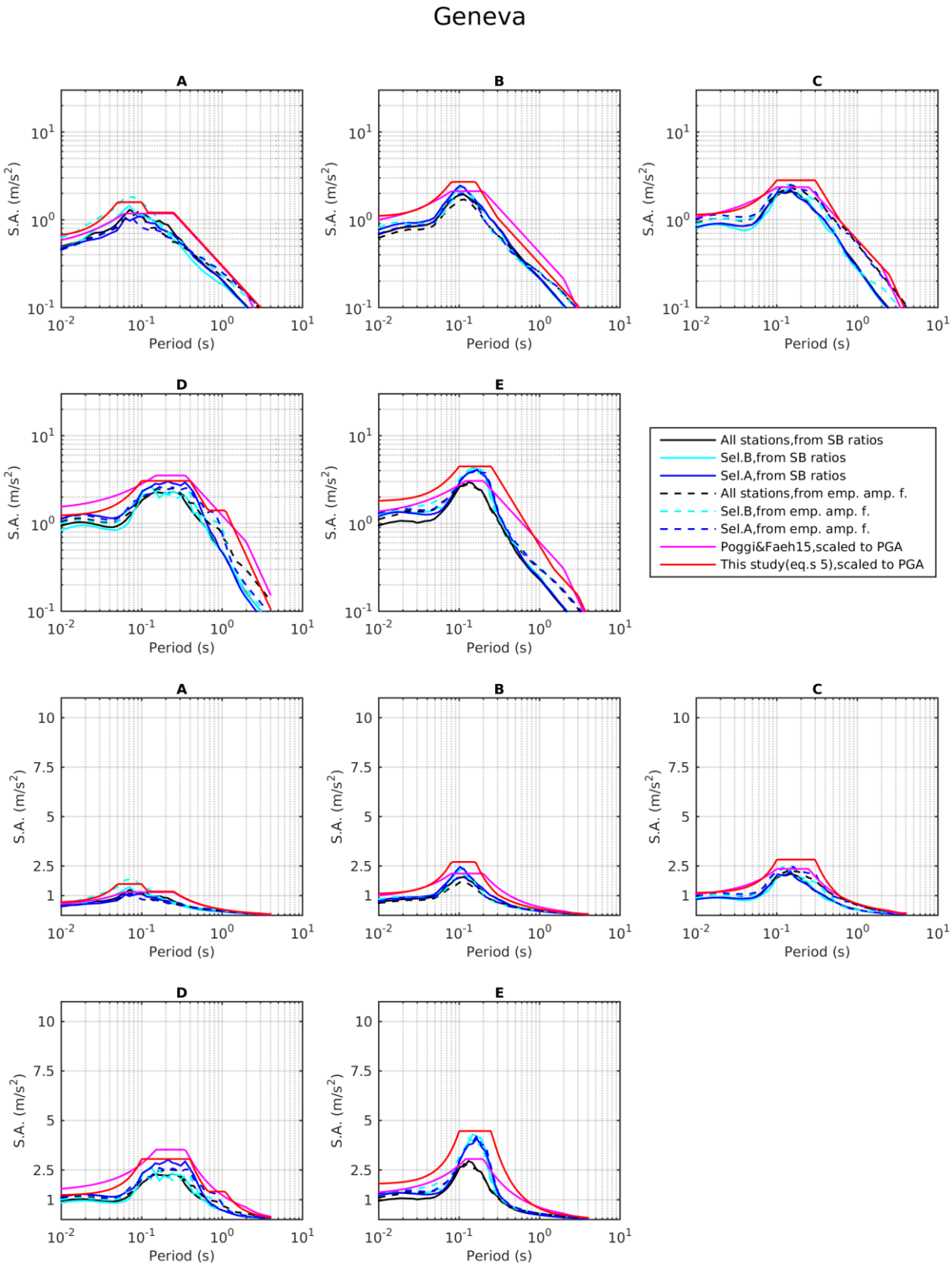

Figure 69 – Median curves of the empirical spectra for the city of Geneva (black, blue or cyan line according to the KiKnet station subset; continuous or dashed line according to the origin of the amplification function). The elastic design spectra from Poggi and Fäh's (2015) proposal and this work's proposal (equations 5) are also included (both scaled to PGA) as magenta and red lines, respectively. Top rows: ordinate axis (spectral acceleration) in logarithmic scale. Bottom rows: ordinate axis (spectral acceleration) in linear scale.

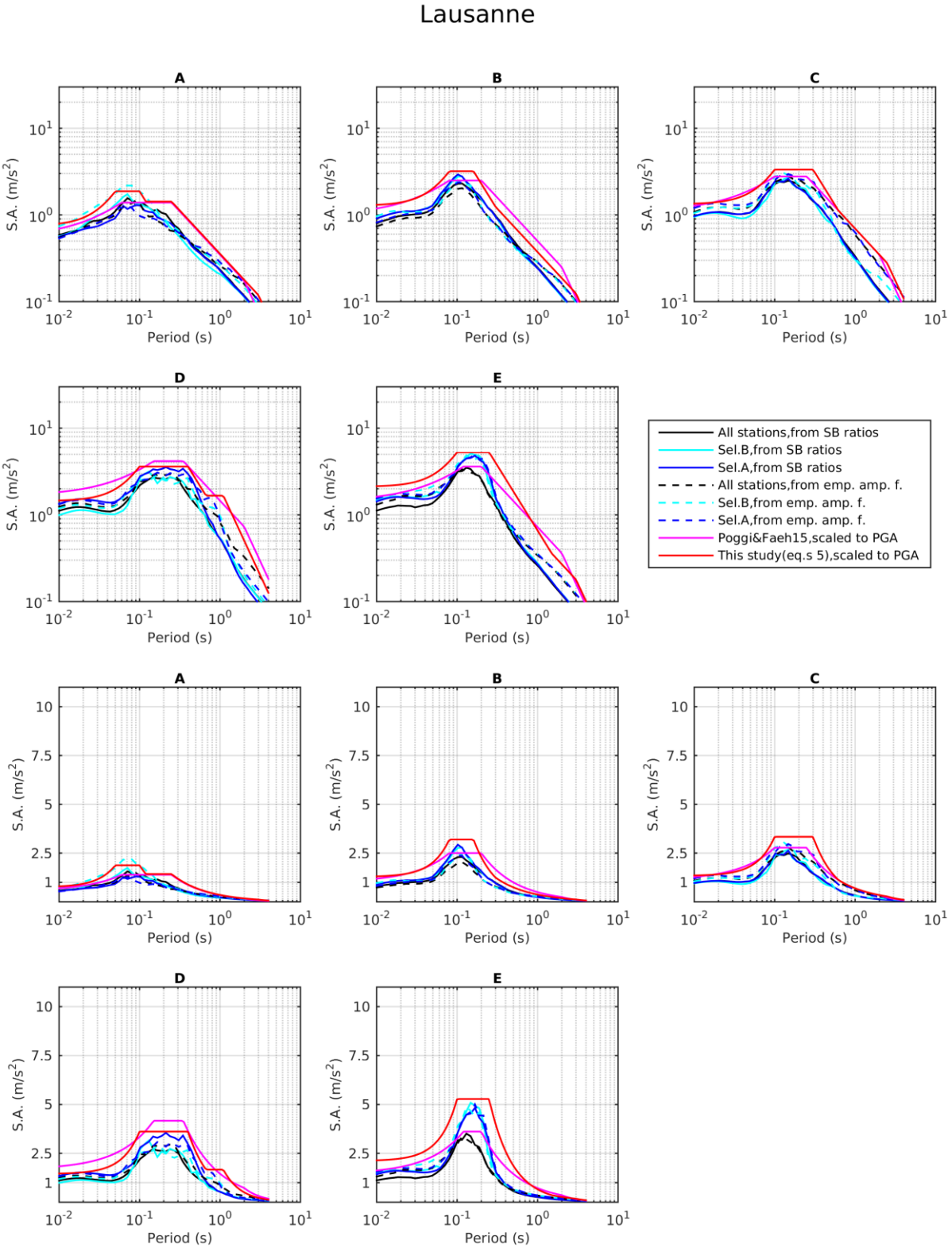

Figure 70 – Median curves of the empirical spectra for the city of Lausanne (black, blue or cyan line according to the KiKnet station subset; continuous or dashed line according to the origin of the amplification function). The elastic design spectra from Poggi and Fäh's (2015) proposal and this work's proposal (equations 5) are also included (both scaled to PGA) as magenta and red lines, respectively. Top rows: ordinate axis (spectral acceleration) in logarithmic scale. Bottom rows: ordinate axis (spectral acceleration) in linear scale.

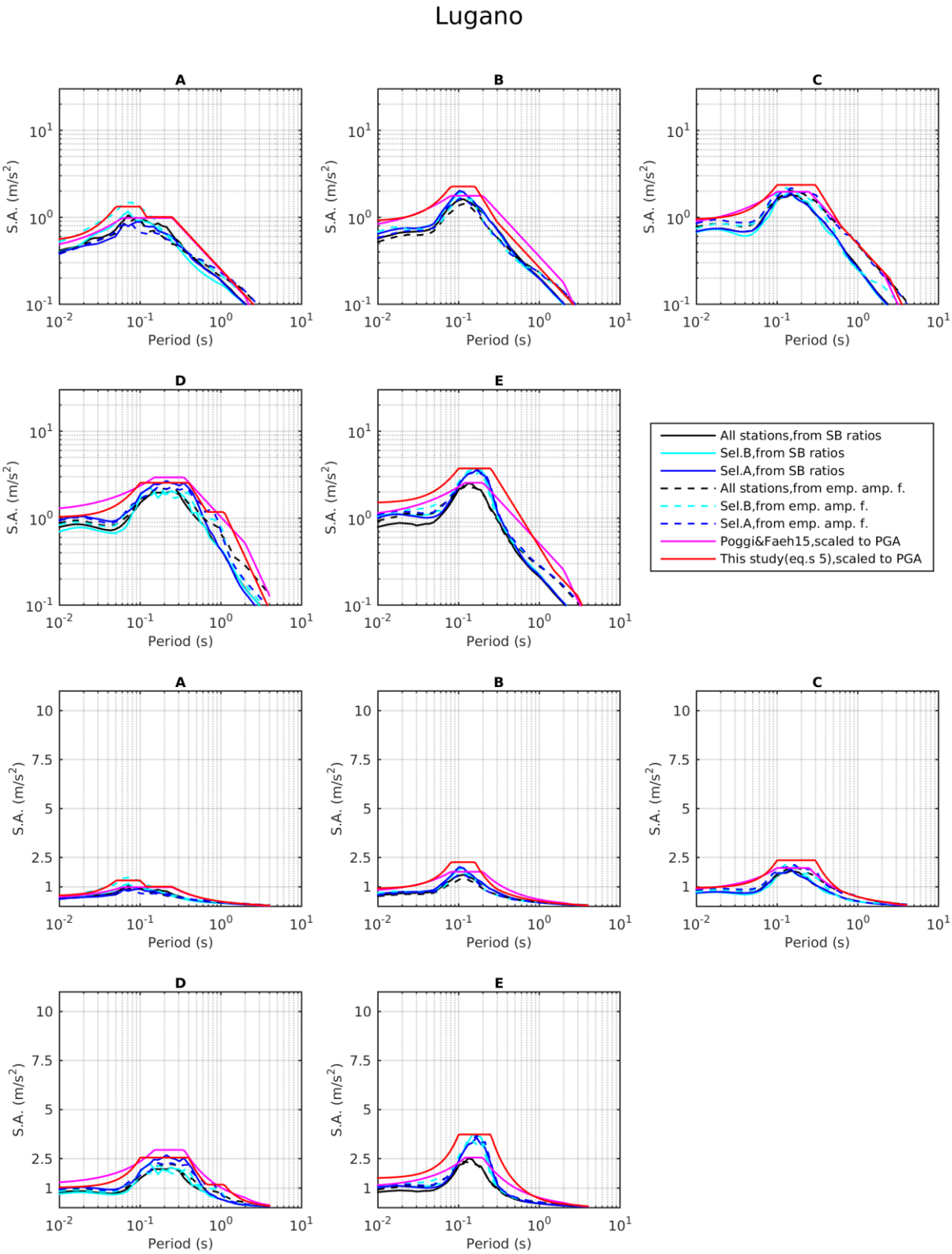

Figure 71 – Median curves of the empirical spectra for the city of Lugano (black, blue or cyan line according to the KiKnet station subset; continuous or dashed line according to the origin of the amplification function). The elastic design spectra from Poggi and Fäh's (2015) proposal and this work's proposal (equations 5) are also included (both scaled to PGA) as magenta and red lines, respectively. Top rows: ordinate axis (spectral acceleration) in logarithmic scale. Bottom rows: ordinate axis (spectral acceleration) in linear scale.

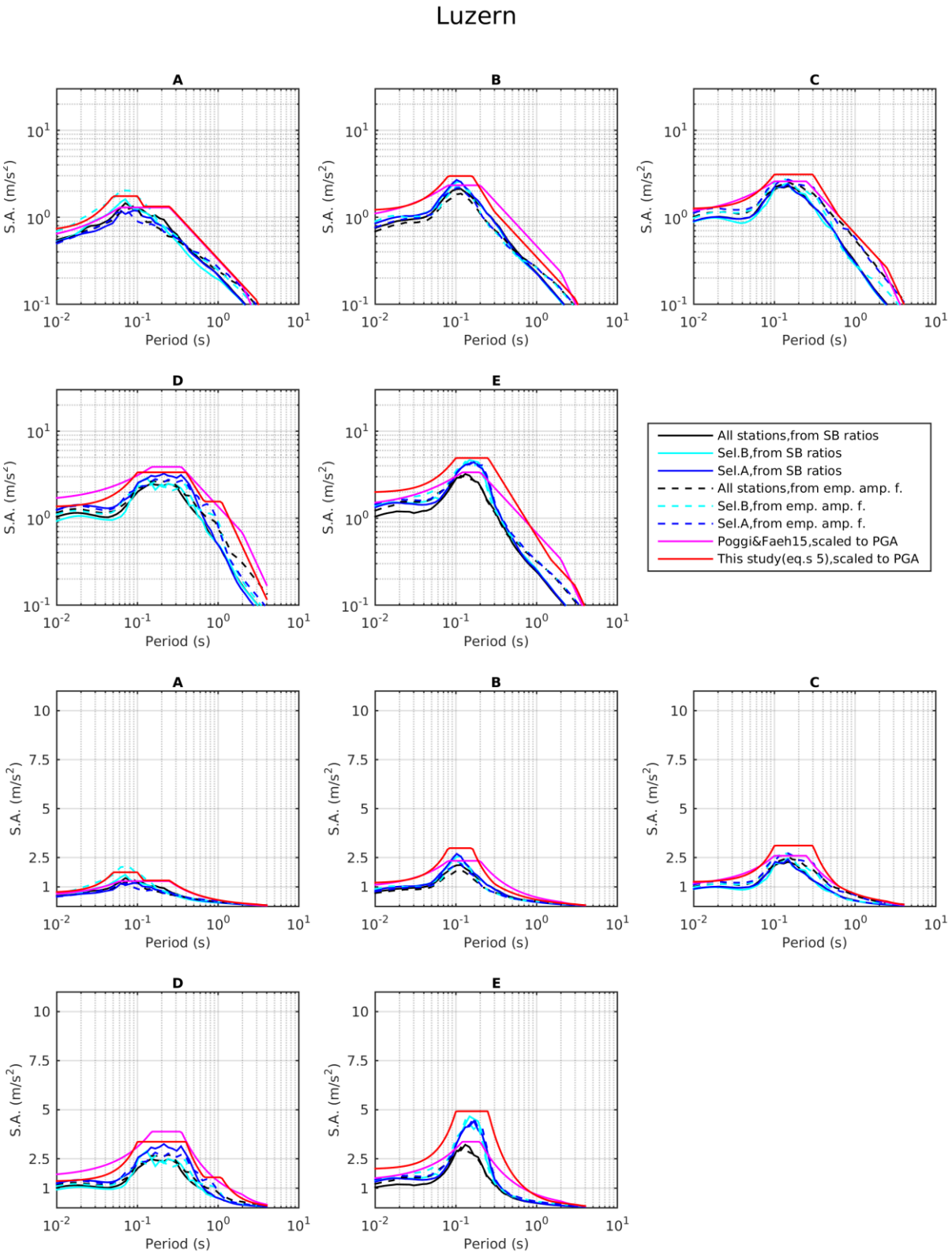

Figure 72 – Median curves of the empirical spectra for the city of Luzern (black, blue or cyan line according to the KiKnet station subset; continuous or dashed line according to the origin of the amplification function). The elastic design spectra from Poggi and Fäh's (2015) proposal and this work's proposal (equations 5) are also included (both scaled to PGA) as magenta and red lines, respectively. Top rows: ordinate axis (spectral acceleration) in logarithmic scale. Bottom rows: ordinate axis (spectral acceleration) in linear scale.

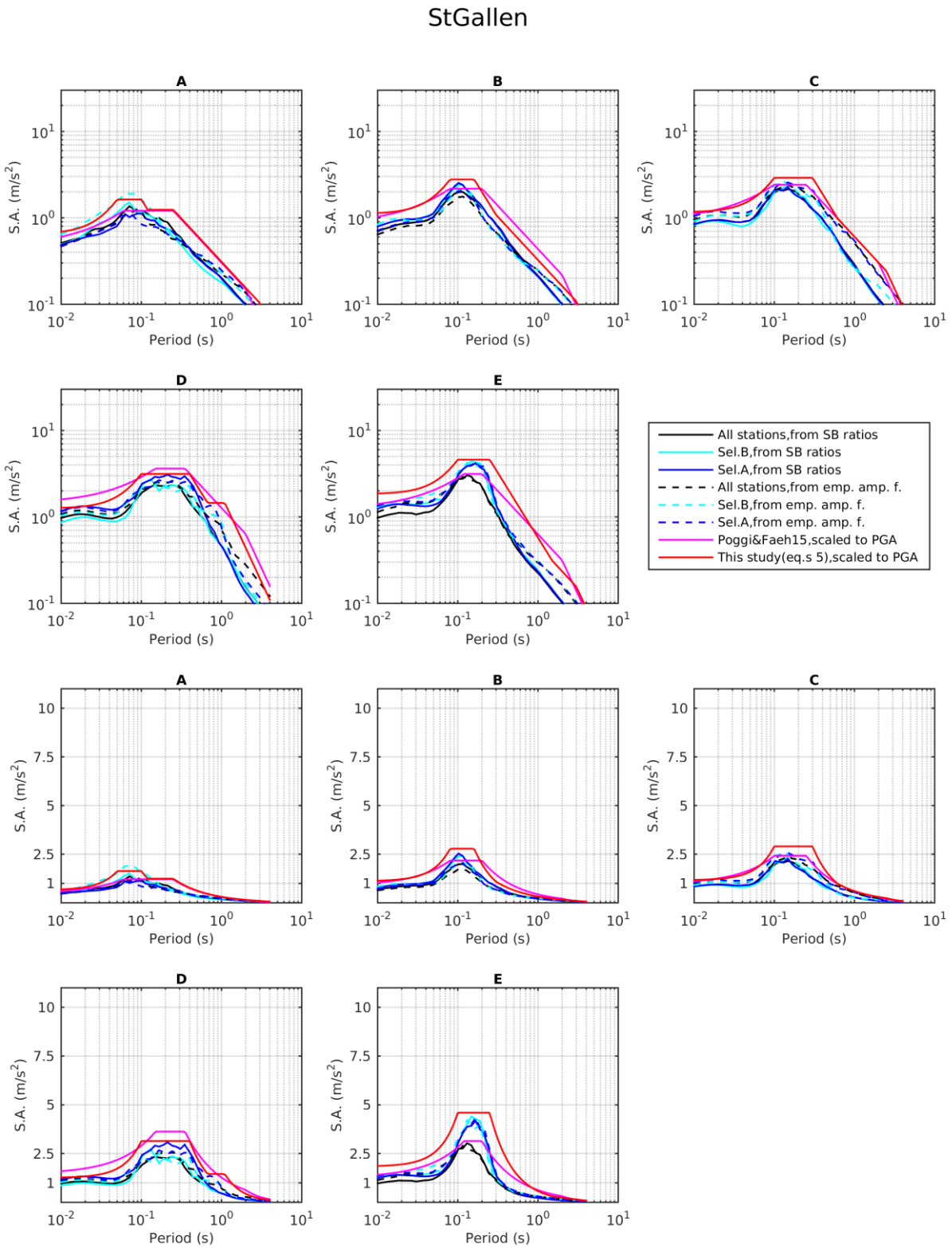

Figure 73 – Median curves of the empirical spectra for the city of St. Gallen (black, blue or cyan line according to the KiKnet station subset; continuous or dashed line according to the origin of the amplification function). The elastic design spectra from Poggi and Fäh's (2015) proposal and this work's proposal (equations 5) are also included (both scaled to PGA) as magenta and red lines, respectively. Top rows: ordinate axis (spectral acceleration) in logarithmic scale. Bottom rows: ordinate axis (spectral acceleration) in linear scale.

12.0 Alternative proposal from an ambiguity in E soil class definition in SIA261

As anticipated in section 3, the present version of SIA 261 normative contains a partly ambiguous definition for E soil class, when this is based on the sole proxy of Vs30. In fact, the description for this particular soil category is more a geological one, rather than a geophysical one. E class is in fact defined as sediments with Vs properties similar to classes C or D, with a limited extent in depth (5-20 m) and underlain by a shallow stiff formation (Vs>800 m/s). The ambiguity with respect to a purely Vs30-based classification lies in the interpretation whether

- Soil E sites should have the same Vs30 of classes C or D (e.g. Vs30<500 m/s), but differ from these depending on the depth of the seismic bedrock, or
- Only the upper sediments should have an average Vs compatible with the average Vs of classes C and D; therefore sites falling into E class should have a $V_{S,H800}$ < 500 m/s (where $V_{S,H800}$ is the average S-wave velocity down to a depth H_{800}, where a stiff formation with Vs>800 m/s is encountered, with 5< H_{800}<20 m). This definition is closer to the approach that appears to be currently followed for soil types designation in the revision of Eurocode 8 (Paolucci, 2017).

This ambiguity is relevant to our study as the classification of the set of KiK-net stations is based exclusively on the provided S-wave velocity profile; the geological information regarding the weathering formations is in fact unavailable in terms of univocal correlation with European soil types. For the core part of our study (sections 2 – 11) we have assumed as definition for class E the first one of the two presented above (Vs30<500 m/s and depth H_{800} between 5-20 m), consistently with the work of Poggi and Fäh (2015). For the sake of completeness, we have also carried out the main stages of sections 2-10 adopting the alternative criterion for E type soils (V_{SH800}<500 m/s and 5<H_{800}<20 m), focusing on the discrepancies in terms of grouping of amplification patterns brought by a different class E definition. The results are given in detail in Appendix A.

Here we directly discuss the final observations (i.e. the comparison with elastic design spectra) for this different grouping of sites. The medians of site-specific UHSs derived from response spectral amplification curves were recomputed, for those soil classes (A, B, E) affected by the change of definition for type E soil. These are then collated with normative spectra, or their proposed modifications, adopting a *normalized* (as in sections 9-10, and also Poggi and Fäh, 2015), or an *absolute* strategy of comparison (as in section 11).

Figure 74 presents the *normalized* comparison between the recomputed median envelopes of site-specific UHSs and the SIA 261 normative design spectra (and its Poggi and Fäh's amendment, 2015). Studying Figures 43 and 44 (on one hand) against Figure 74, the following observations can be formulated:

- As far as class A is concerned, the exceedance of Poggi and Fäh's (2015) proposed spectrum by selection B sites (as seen in Figure 43, lower left panel) is now almost negligible (Figure 74, lower left panel); in general, for all KiK-net sites assortments (all stations, selections A and B), the median envelope reaches lower values of normalized spectral acceleration;
- A decrease of normalized SA is also noticed for class B, so that the median curves from site-specific UHS have now at their peaks approximately the same values of the SIA 261 plateau of the design spectrum, although moved towards lower periods (Figure 74, central column panels);
- The median curves from class E do not exceed anymore the design spectrum proposed by Poggi and Fäh (2015) (compare Figure 44 with Figure 74, right hand side panels); however, the peaks of the median envelope are now at the lower limit of the plateau of the Poggi and Fäh's (2015) design spectrum (previously, they were centred with respect to the plateau; see Figure 44).

We can conclude that the adoption of an alternative definition for class E (based on the sole knowledge of the Vs profile, disregarding possible geological considerations) has led to different median envelopes for the population of site-specific UHS for the soil types A, B and E (Figure 74 versus Figures 43,44). It is worth remarking that the individual site-specific UHS curves are the same in both cases; the

discrepancies between the results appearing in Figure 74 and Figures 43-44 are due to a different grouping of the same population of spectra.

Indeed, the use of a less restrictive criterion for class E ($V_{S,H800}$ in place of Vs30 <500 m/s) has increased the absolute and relative number of E sites. Stations with higher $V_{S,H800}$ have been added to the original group (obviously preserving the $5<H_{800}<20$ m constraint) leading to a more smoothed average site response with lower median values of amplification, and moving the f_0 peak towards higher frequencies (or lower periods).

Sites now defined as E class, originally (i.e., with the classification adopted in the previous chapters) belonged to A or B types. These classes now "lose" their portion of stations with softer surficial cover; therefore, the global (median) responses are characterized by lower values of amplification.
Consequently, for all involved classes (A, B, E) the medians of the populations of site specific UHS are "flattened" down towards lower spectral accelerations, and their comparison with design spectra leads to different conclusions with respect to those presented in sections 10-11.

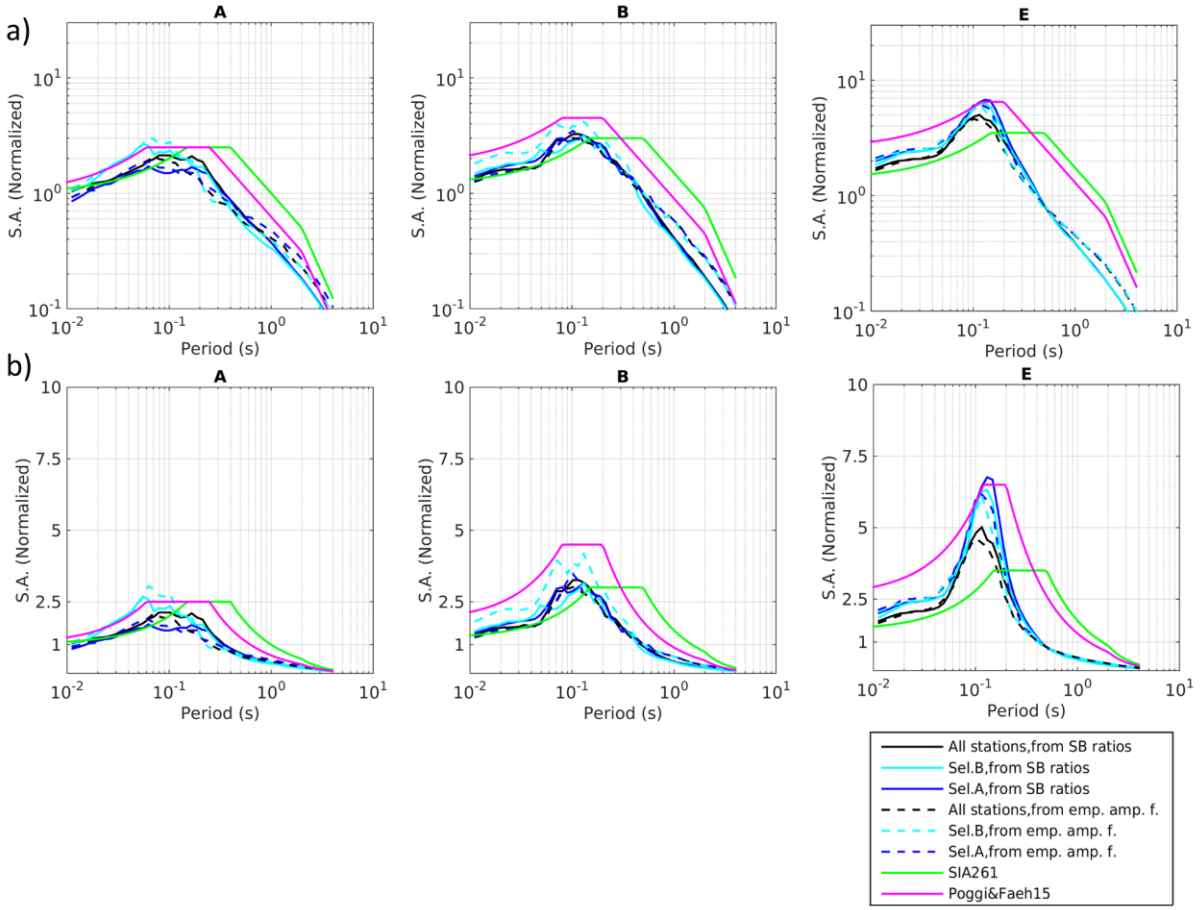

Figure 74 – a) median of site-specific UHS, classified by soil class, adopting the alternative definition for class E (involving $V_{S,H800}$ < 500 m/s and $5<H_{800}<20$ m). b) same as (a), with ordinate axis (normalized spectral acceleration) in linear scale

The alteration in the shape of the median site-specific UHS for soil types A, B and E requires an alternative formulation for the corresponding design spectra, different from the one appearing in section 10. Maintaining the same functional form of equations 5, we modified some of the values of parameter S and anchor periods T_B, T_C, $T_{B'}$, $T_{C'}$ and T_D to fit the bundle of experimental curves (Figure 75 and Table 5).
The design spectra bear now lower (normalized) SA amplitudes at the plateau segment T_B-T_C (also $T_{B'}$-$T_{C'}$ for class A); see the lower values for S parameter at classes A, B, E and the modified anchor period values (in italics in Table 5). Furthermore, as the experimental envelope for soil type E is now "flattened"

down but has also a wider lateral extent (see observations above), we had to significantly adapt the high-period flank of the design spectrum, moving T_C and $T_{B'} \equiv T_{C'}$ towards higher periods.

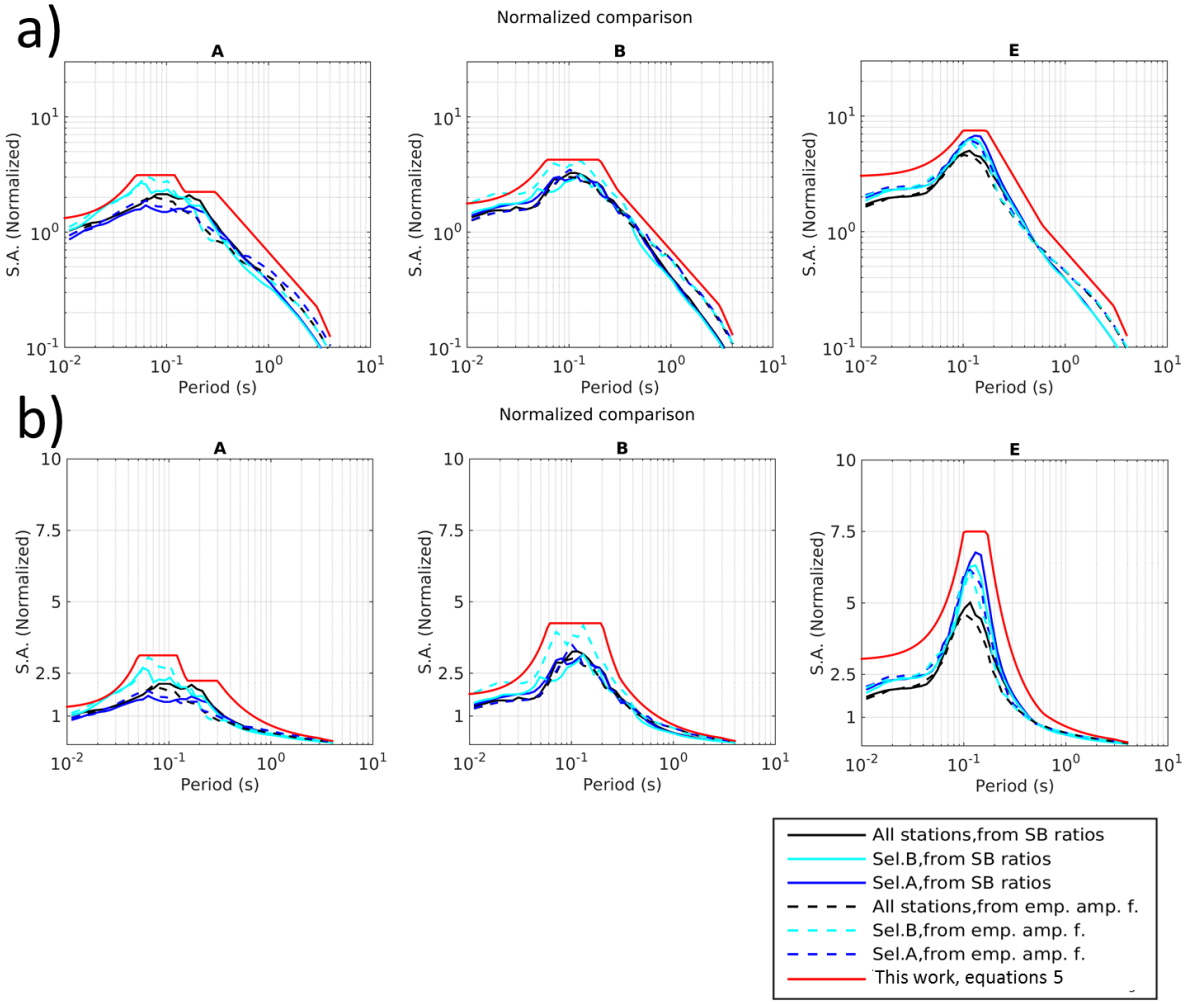

Figure 75 – a) elastic design spectra from equations 5, proposed for soil classes A,B,E (red lines), compared with the median curves of the empirical spectra (black, blue or cyan line according to the KiKnet station subset; continuous or dashed line according to the origin of the amplification function. The median curves were computed on soil type groups resulting from the alternative criterion for E class ($V_{S,H800}$ < 500 m/s and 5<H_{800}<20 m). b) same as (a), with ordinate axis (normalized spectral acceleration) in linear scale

Table 5 – Values of parameters T_B, T_C, $T_{B'}$, $T_{C'}$, T_D, and S in equations 5 for the design spectra appearing in Figure 49 (red lines). Values modified from table 3 are in italics.

Soil class	S	T_B (s)	T_C (s)	$T_{B'}$ (s)	$T_{C'}$ (s)	T_D (s)
A	*1.25*	0.05	0.12	*0.15*	*0.30*	3.0
B	*1.70*	*0.06*	*0.20*	0.30	0.30	3.0
E	*3.00*	0.10	*0.17*	*0.60*	*0.60*	3.0

The following figures (76-85) refer to the comparison between the *absolute* values of spectral acceleration expected at ten Swiss cities for different soil conditions (site-specific UHSs), and the *absolute* spectral accelerations of elastic design spectra. The figures include the proposed spectra according to Poggi and Fäh (2015), and the functional form presented in this report (using the parameters' values for S, T_A-T_D introduced in this section), both scaled with the site-specific PGA. The figures with scaling to a_{gd} of the design spectra are included in Appendix A.
We remind that the reorganization into soil classes followed in this section and Appendix A affects soil types A, B and E, but not C and D (whose median curves are the same as of Figures 54-63, section 11).

In fact, as seen in Figure 74, the different criterion for class E produces median curves of empirical spectra for classes A and B, which bear acceleration values lower than those obtained following the soil type E definition adopted until section 11. This applies also to class E median functions, whose resonance peak shifts also leftward towards lower period values.

The conservatism shown in the set of representations in Appendix A (Figures 20A-29A, design spectra scaled to a_{gd}) is absent, and normative functions closely follow (but they are not exceeded by) the median envelopes of the sets of site-specific UHSs. This is in contrast with section 11, where the Poggi and Fäh's (2015) normative spectra scaled to PGA were frequently surpassed (see classes A, B and E in Figures 64-73). The functional form from equations 5 proves here again flexible enough to reproduce the features observed in the hazard spectra including site amplification. See in particular class E, where the Poggi and Fäh's (2015) spectra are tangent, in their plateau, to the resonance peak of the median curves; on the contrary, this peak is adequately fitted by the form proposed in this work.

The different outcomes obtained in this section, when compared to sections 10-11, in terms of collation design spectra – median curves of site-specific UHSs, highlight the importance of robust (and univocal) soil type definition criteria in grouping sites with consistent amplification behaviour.

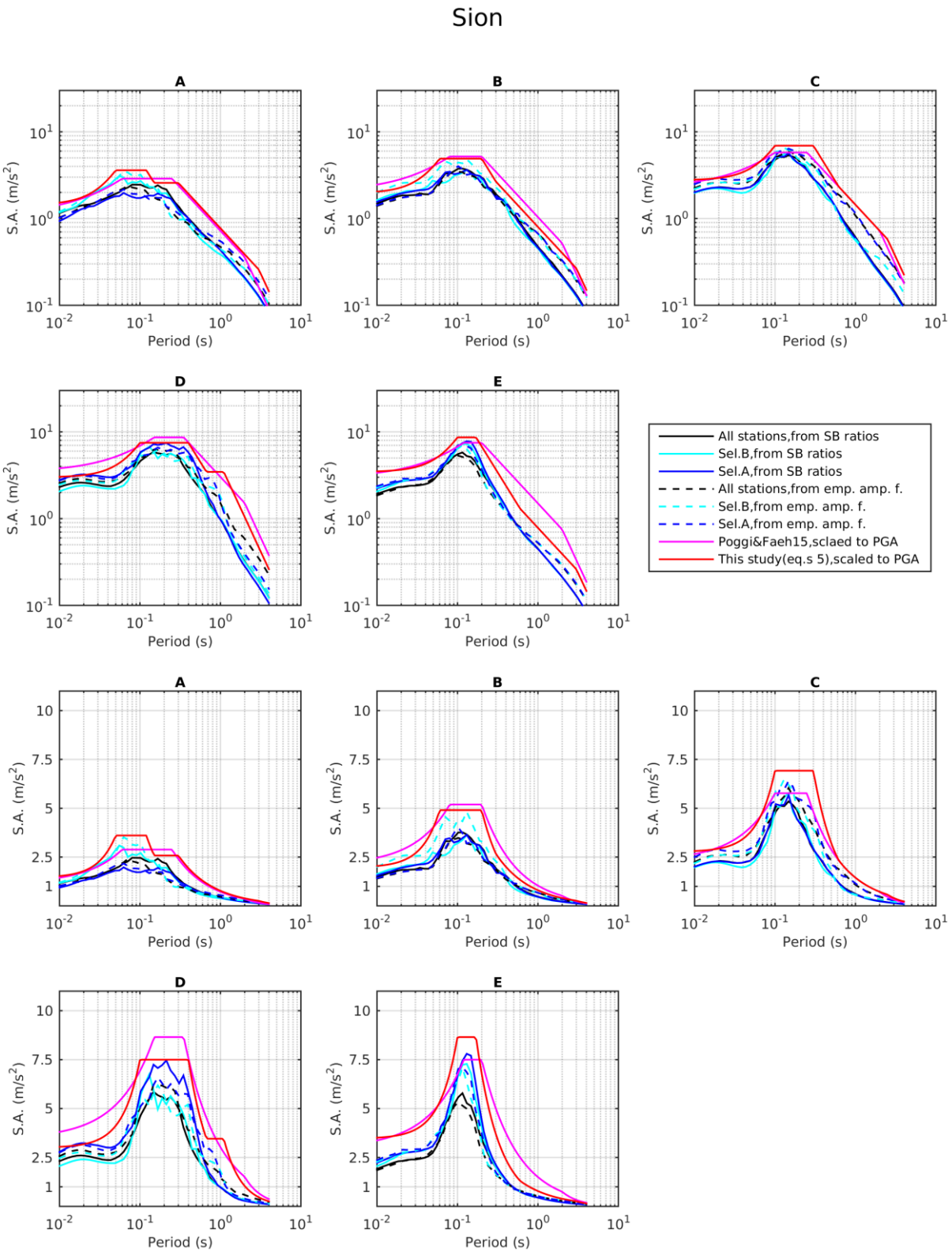

Figure 76 – Median curves of the empirical spectra for the city of Sion (black, blue or cyan line according to the KiKnet station subset; continuous or dashed line according to the origin of the amplification function). The elastic design spectra from Poggi and Fäh's (2015) proposal and this work's proposal (equations 5) are also included (both scaled to PGA) as magenta and red lines, respectively. Top rows: ordinate axis (spectral acceleration) in logarithmic scale. Bottom rows: ordinate axis (spectral acceleration) in linear scale.

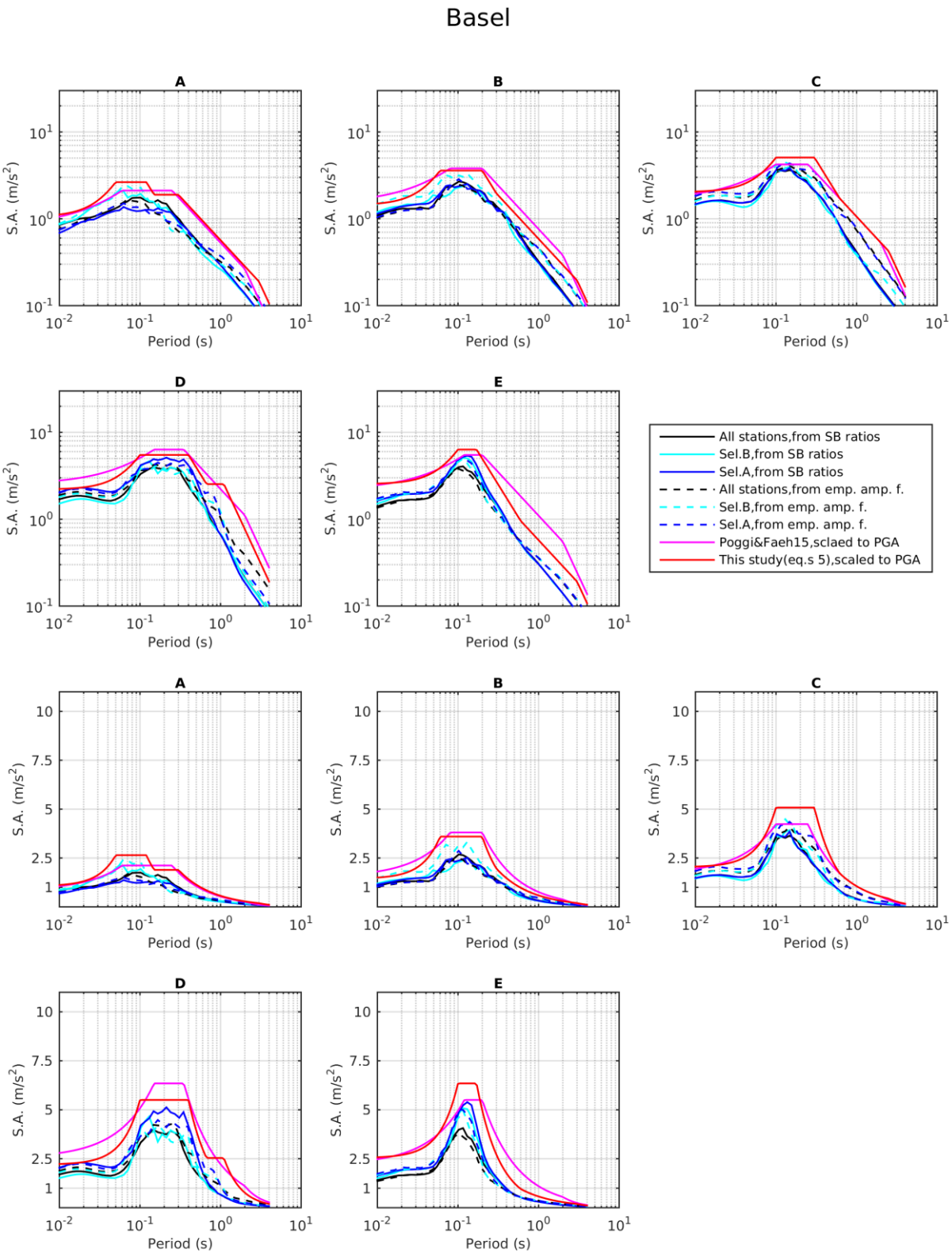

Figure 77 – Median curves of the empirical spectra for the city of Basel (black, blue or cyan line according to the KiKnet station subset; continuous or dashed line according to the origin of the amplification function). The elastic design spectra from Poggi and Fäh's (2015) proposal and this work's proposal (equations 5) are also included (both scaled to PGA) as magenta and red lines, respectively. Top rows: ordinate axis (spectral acceleration) in logarithmic scale. Bottom rows: ordinate axis (spectral acceleration) in linear scale.

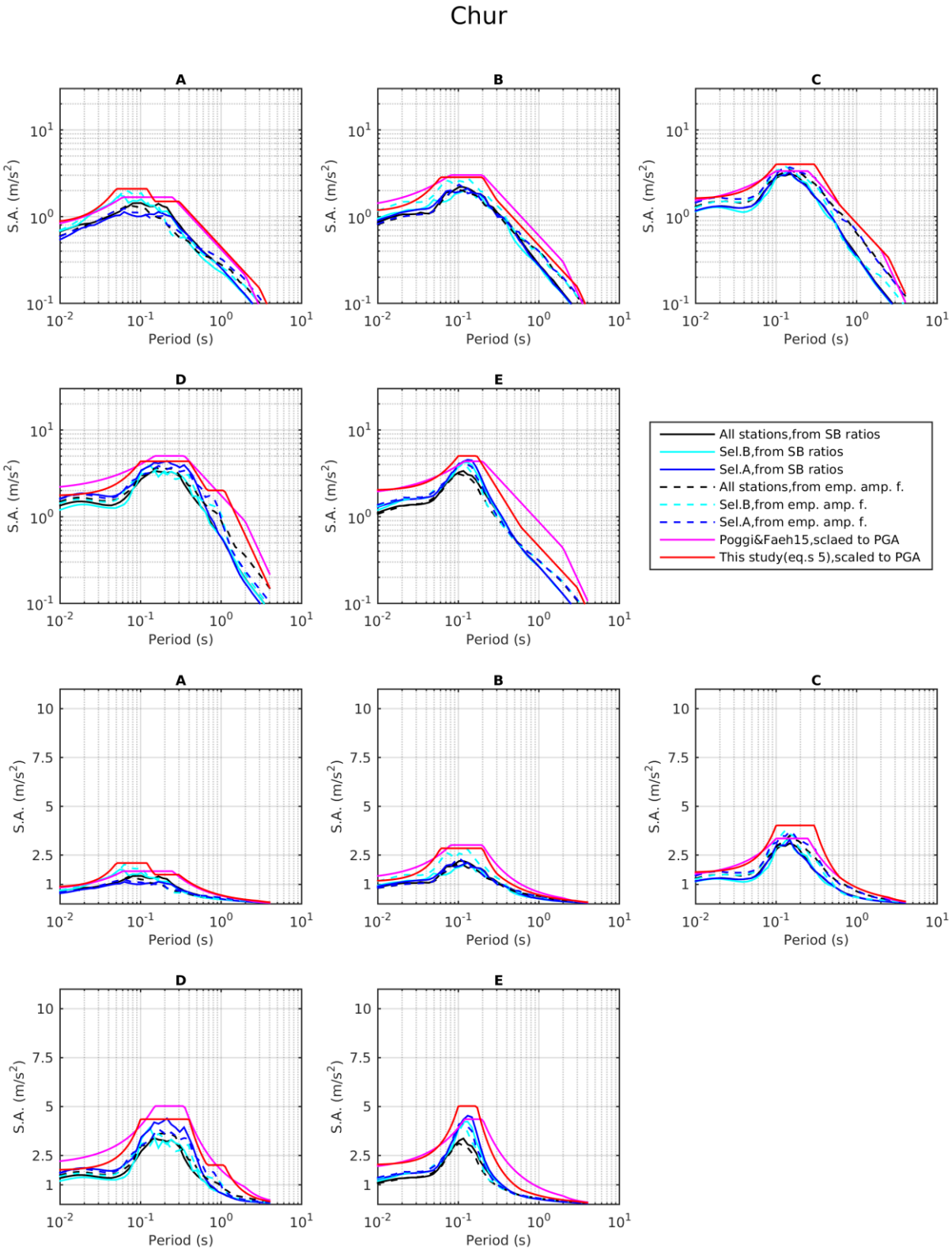

Figure 78 – Median curves of the empirical spectra for the city of Basel (black, blue or cyan line according to the KiKnet station subset; continuous or dashed line according to the origin of the amplification function). The elastic design spectra from Poggi and Fäh's (2015) proposal and this work's proposal (equations 5) are also included (both scaled to PGA) as magenta and red lines, respectively. Top rows: ordinate axis (spectral acceleration) in logarithmic scale. Bottom rows: ordinate axis (spectral acceleration) in linear scale.

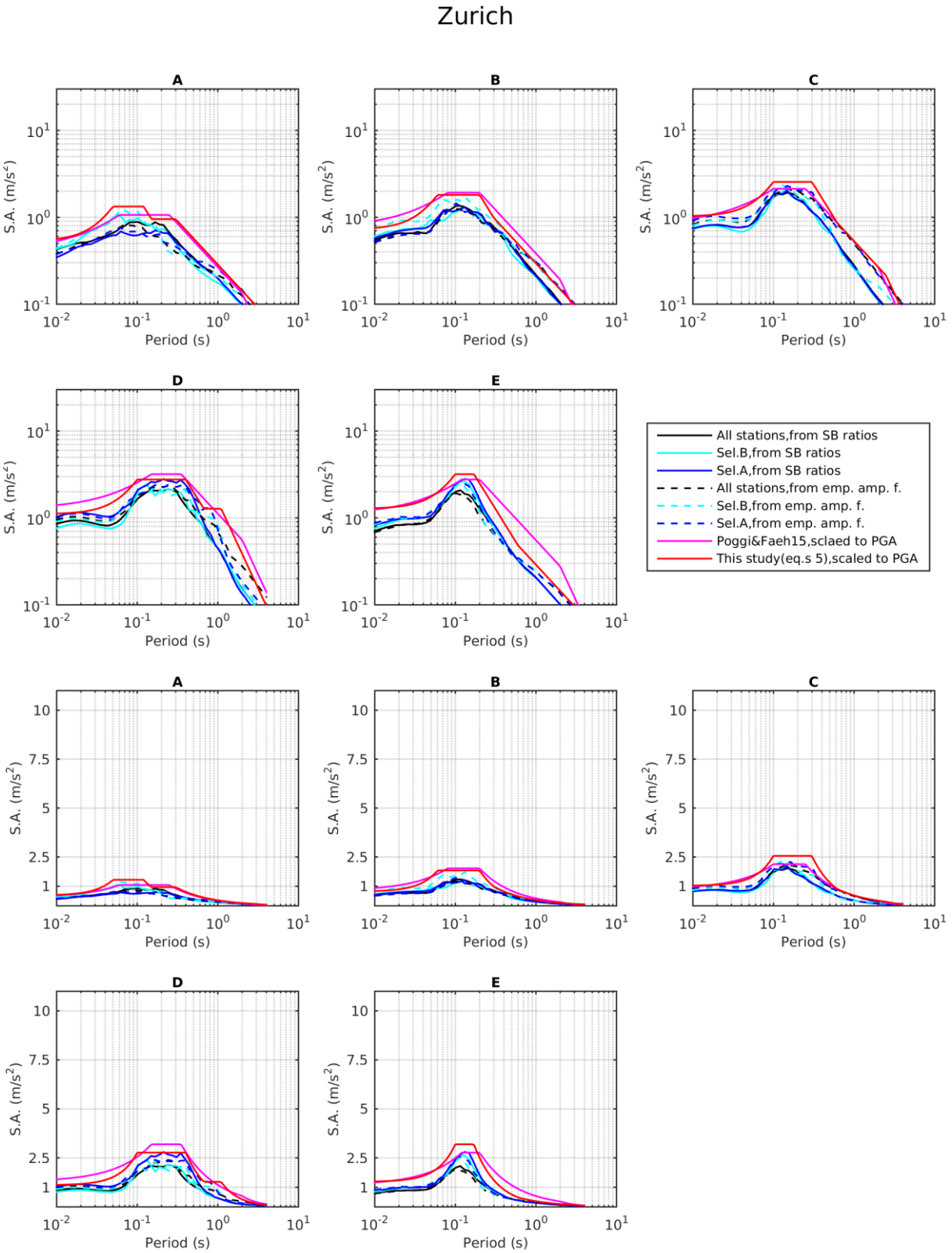

Figure 79 – Median curves of the empirical spectra for the city of Zurich (black, blue or cyan line according to the KiKnet station subset; continuous or dashed line according to the origin of the amplification function). The elastic design spectra from Poggi and Fäh's (2015) proposal and this work's proposal (equations 5) are also included (both scaled to PGA) as magenta and red lines, respectively. Top rows: ordinate axis (spectral acceleration) in logarithmic scale. Bottom rows: ordinate axis (spectral acceleration) in linear scale.

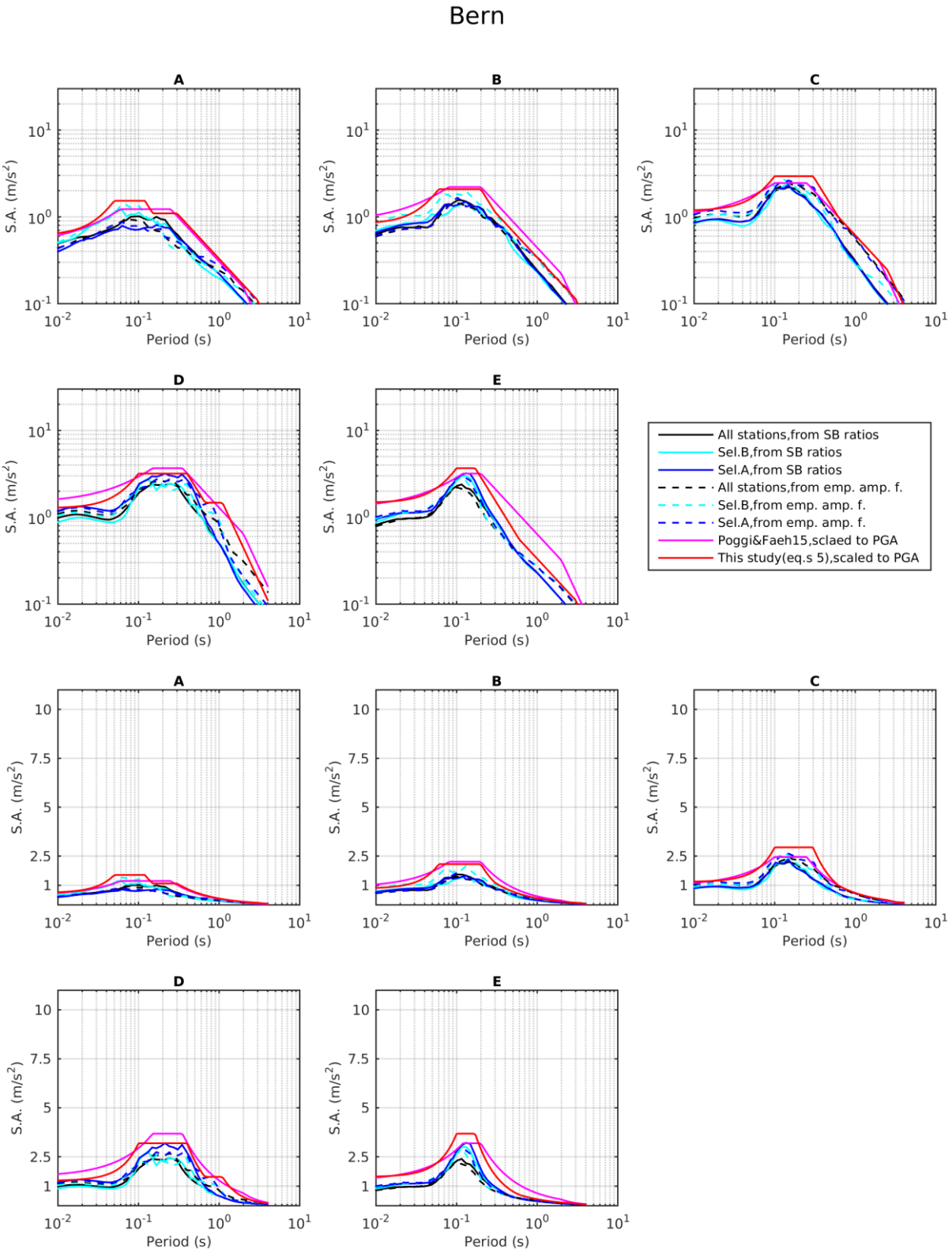

Figure 80 – Median curves of the empirical spectra for the city of Bern (black, blue or cyan line according to the KiKnet station subset; continuous or dashed line according to the origin of the amplification function). The elastic design spectra from Poggi and Fäh's (2015) proposal and this work's proposal (equations 5) are also included (both scaled to PGA) as magenta and red lines, respectively. Top rows: ordinate axis (spectral acceleration) in logarithmic scale. Bottom rows: ordinate axis (spectral acceleration) in linear scale.

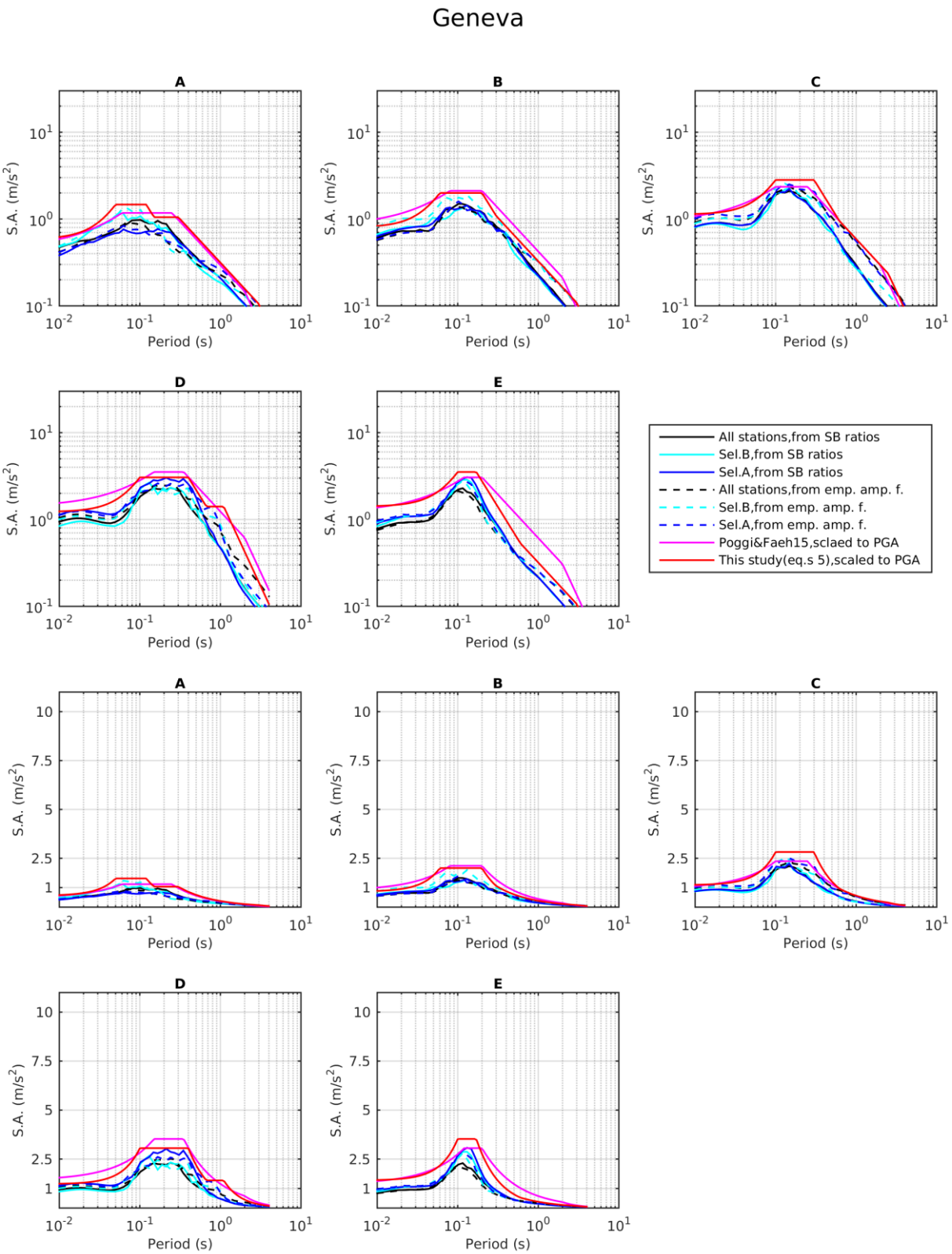

Figure 81 – Median curves of the empirical spectra for the city of Geneva (black, blue or cyan line according to the KiKnet station subset; continuous or dashed line according to the origin of the amplification function). The elastic design spectra from Poggi and Fäh's (2015) proposal and this work's proposal (equations 5) are also included (both scaled to PGA) as magenta and red lines, respectively. Top rows: ordinate axis (spectral acceleration) in logarithmic scale. Bottom rows: ordinate axis (spectral acceleration) in linear scale.

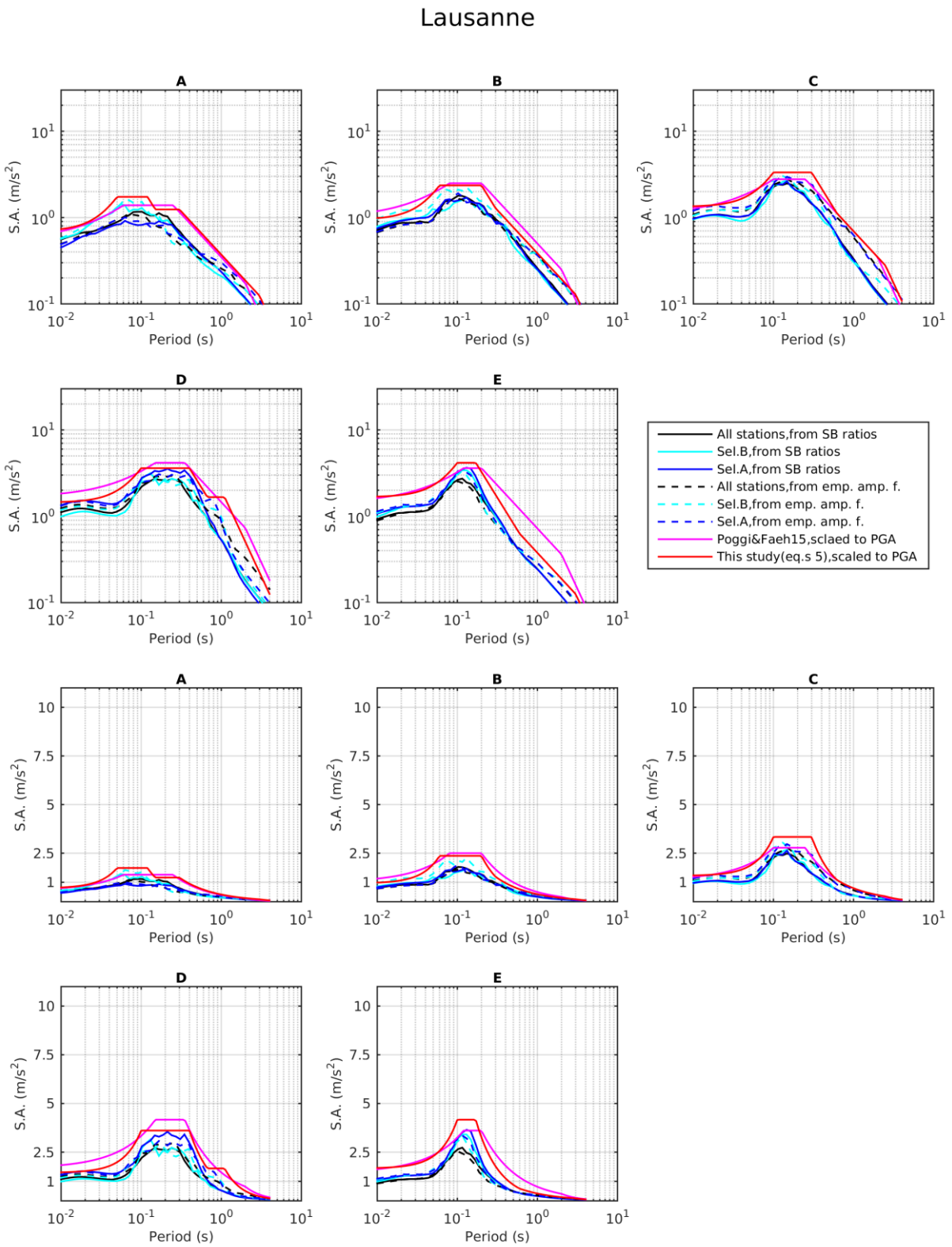

Figure 82 – Median curves of the empirical spectra for the city of Lausanne (black, blue or cyan line according to the KiKnet station subset; continuous or dashed line according to the origin of the amplification function). The elastic design spectra from Poggi and Fäh's (2015) proposal and this work's proposal (equations 5) are also included (both scaled to PGA) as magenta and red lines, respectively. Top rows: ordinate axis (spectral acceleration) in logarithmic scale. Bottom rows: ordinate axis (spectral acceleration) in linear scale.

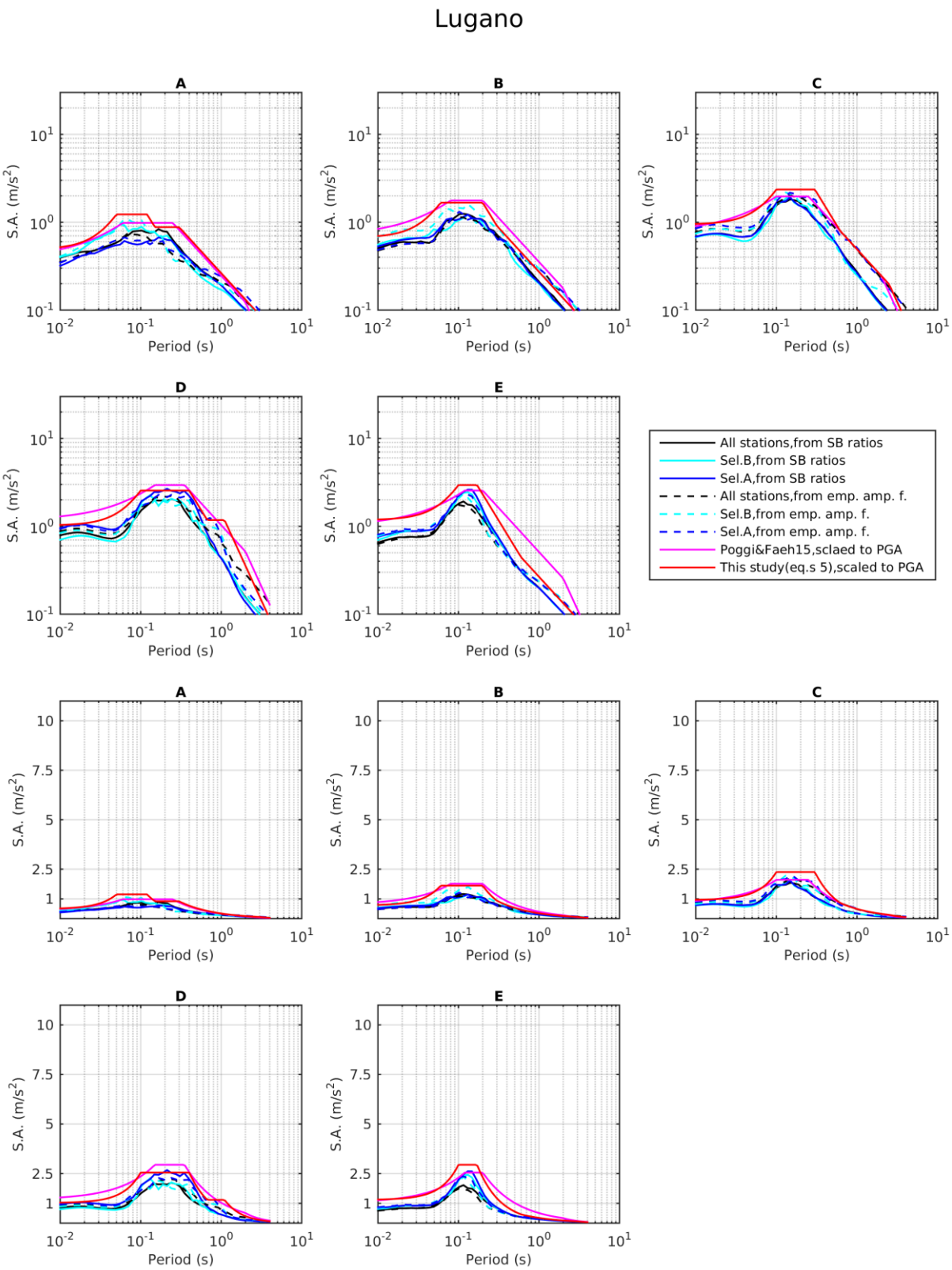

Figure 83 – Median curves of the empirical spectra for the city of Lugano (black, blue or cyan line according to the KiKnet station subset; continuous or dashed line according to the origin of the amplification function). The elastic design spectra from Poggi and Fäh's (2015) proposal and this work's proposal (equations 5) are also included (both scaled to PGA) as magenta and red lines, respectively. Top rows: ordinate axis (spectral acceleration) in logarithmic scale. Bottom rows: ordinate axis (spectral acceleration) in linear scale.

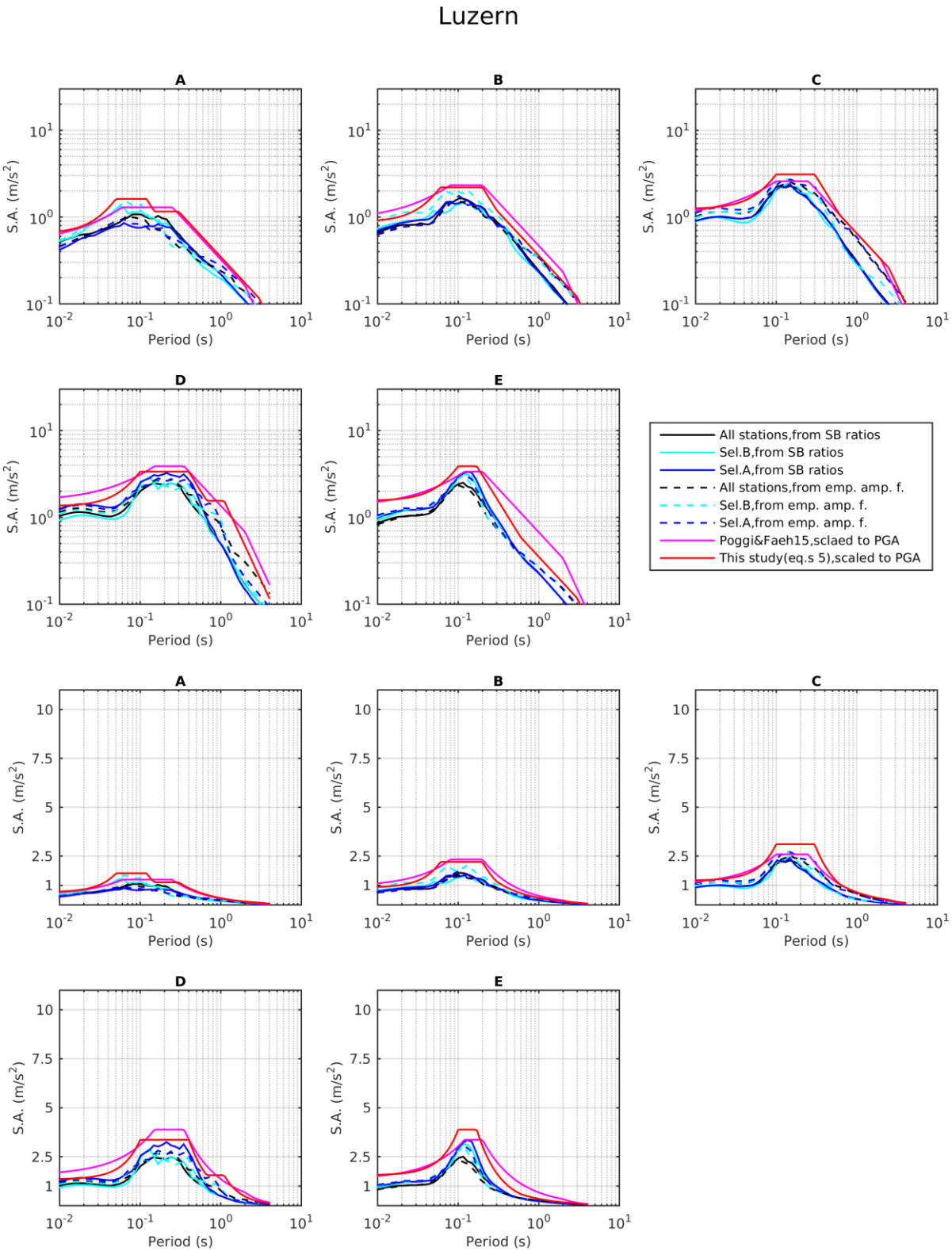

Figure 84 – Median curves of the empirical spectra for the city of Luzern (black, blue or cyan line according to the KiKnet station subset; continuous or dashed line according to the origin of the amplification function). The elastic design spectra from Poggi and Fäh's (2015) proposal and this work's proposal (equations 5) are also included (both scaled to PGA) as magenta and red lines, respectively. Top rows: ordinate axis (spectral acceleration) in logarithmic scale. Bottom rows: ordinate axis (spectral acceleration) in linear scale.

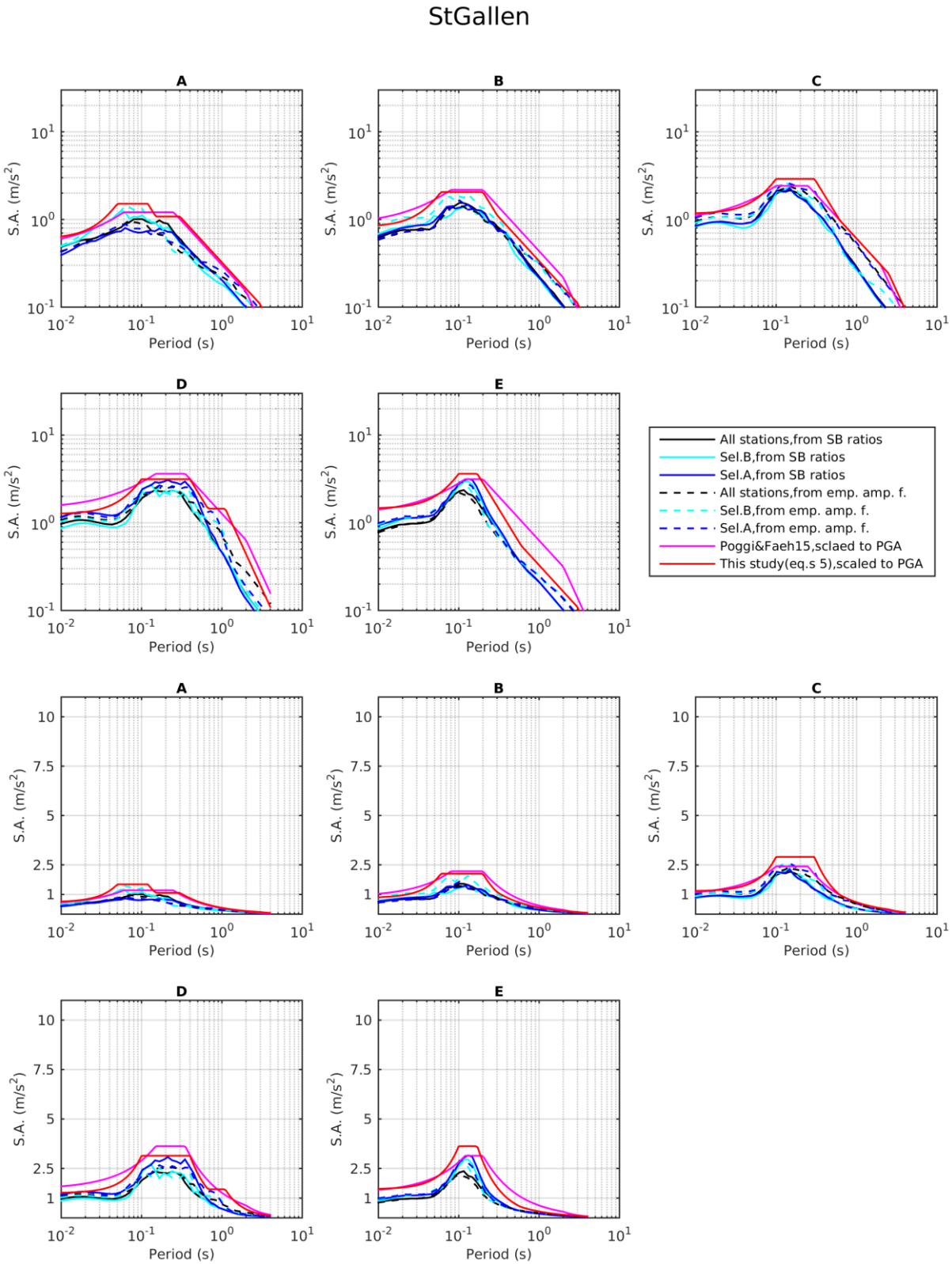

Figure 85 – Median curves of the empirical spectra for the city of Luzern (black, blue or cyan line according to the KiKnet station subset; continuous or dashed line according to the origin of the amplification function). The elastic design spectra from Poggi and Fäh's (2015) proposal and this work's proposal (equations 5) are also included (both scaled to PGA) as magenta and red lines, respectively. Top rows: ordinate axis (spectral acceleration) in logarithmic scale. Bottom rows: ordinate axis (spectral acceleration) in linear scale.

13.0 Conclusions

This report summarizes the data collection, processing and elaborations carried out in the framework of strategy 1 ("An updated classification of empirical amplification functions") of the project "Development of site-specific elastic design spectra for future building codes".
Sections 2 and 3 present the database used for the present study. We use waveforms from the Japanese network of borehole stations KiK-net, and describe the quality-control operations we performed for this data. Sections 4 and 5 illustrate the strategy we followed to obtain, from triggered waveforms, two types of estimates of the Fourier amplification functions for each site of the KiK-net network. The first estimate is based on the collation of data acquired by surface and borehole receivers (surface-to-borehole (SB) ratios), the second one applies a complex procedure of spectral modelling to obtain empirical amplification functions from the records of the surface stations alone. In chapter 6, these two sets of Fourier amplification functions are brought to a common reference, which is the Swiss reference rock. Section 7 details how the obtained Fourier amplification functions were translated to the domain of response spectra, to yield response spectral amplification curves. Chapters 8 discusses the relevance of nonlinear soil behaviour. In section 9, the dataset of the response spectral amplification functions is combined with a seismic hazard input, considered representative of the hazard scenario in Switzerland (the uniform hazard spectra for the city of Sion). Site-specific UHSs are hence obtained, sorted by soil type and then compared with the elastic design spectra of the current SIA 261 2014 normative (chapter 10); both sets of spectra are normalized to a common reference. A proposal for the amendment of this norm is also formulated. In chapter 11, the normalization criterion adopted in section 9 and 10 is put aside and the absolute values from site-specific and design spectra are compared for 10 Swiss cities, belonging to different seismic zones in the present Swiss normative. Finally, in section 12 we discuss the consequences of a different grouping of site-specific UHSs by soil type arising from a potential ambiguity in the definition of class E based on the sole Vs30 proxy; in particular, we focus on the changes affecting the comparison with normative design spectra. The repetition of all the processing steps of sections 3-11, although assuming this alternative soil-type classification scheme, is presented in detail in Appendix A.
Throughout this process, several elements of discussion and observations have arisen: we collect them here, subdivided into main topics, to provide a conclusive message for this work.

Information about sites' subsurface condition
In this work, it has proven to be fundamental that we control the reliability of the V_S profiles provided by KiK-net for each of its instrumented sites. This has allowed, at each step of our process, to sort the datasets of processing outputs (e.g. Fourier amplification functions, site-specific UHS) into verified soil class subsets. In this case, applying a median or mean operator over each soil-class subset actually allows capturing the average trend for the given soil class.
At the same time, at each processing step, we compared the soil type subgroups with verified V_S profiles with the corresponding subset including all available KiK-net sites (no control over the accuracy of the velocity model). The latter consistently produce less homogeneous subgroups, since a portion of sites is attributed to a wrong soil class. In this case, applying a median or mean operator over processing outputs (apparently) belonging to the same soil type yields a smoothed average trend, where the features proper of that particular soil class are smeared.
This demonstrates the key role played by the data about sites' subsurface condition, which is to be considered also in the architecture of seismic building codes. When this piece of information is not based on in-situ measurements but it is somehow inferred (e.g. soil class derived from surficial geological observations or indirect site proxies) a sufficiently conservative approach (in terms of design spectra) should be prescribed. Vice versa, when a more constrained and complete knowledge of the subsoil structure is available through site-specific investigations, this should be exploited in defining realistic SA design values consistent with the actual subsoil configuration. Understandably, this topic is strictly intertwined with the issue of the criteria for the definition of soil classes (see later in this section). Approximate and indirect information about the subsurface should inevitably lead to few, rather generic site classes. As additional pieces of information become available (Vs30, f0, H_{800}, or the complete Vs

profile), it would be possible to differentiate more soil types than described in the building codes, and then attribute the investigated site to a site-specific design spectrum.
This aspect (availability and reliability of soil subsurface condition) is to be considered when comparing the procedure and the results obtained by strategy 1 and 2 ("Seismic Hazard Compatible Ground Motion Selection") of this project. In our case (strategy 1) the input database is constituted by relatively few sites (~700 KiK-net sites) with velocity profiles provided by invasive surveys (downhole test); even so, this information was held as trustworthy only for a subset of stations. In the case of strategy 2, the starting base of data comprises a much larger number of records and sites, however with less reliable information about subsurface condition (not documented, and/or obtained from non-invasive techniques, or simply inferred, for its vast majority).

Soil type classification
Another critical aspect related to the reconstruction of the average behaviour for a set of sites belonging to the same soil type, is the criterion for the definition of the soil class. In our work, considering the present SIA 261 classification criterion, and since we had velocity profiles for the various KiK-net stations but no structured geological description, we based our categorization on the Vs30 proxy and on H_{800} (depth at which Vs>800 m/s, although for class E only). The potential ambiguities in the use of Vs30 alone are illustrated in chapter 12 and Appendix A. Furthermore, a Vs30-only criterion groups in the same class sites with some variability in the resonance frequency values, whose peak is the main feature of Fourier and response spectral amplification functions. Consequently, global statistics (i.e. mean or median) conducted over the population of a given soil type produce a smoothed and not precautionary average image. The variability observed within each soil class is very large, and the soil classes are overlapping with their distributions of observed amplifications or derived UHSs.
Hence, we highlight the need for a better-constrained definition of the soil types. As anticipated in the previous paragraph, an architecture involving different levels of knowledge could be proposed. Few generic soil classes should be envisaged when little is known (or is simply inferred) about the subsurface structure, subdividing into more specific subclasses as more detailed information about the site condition becomes available (e.g. site proxies such as Vs30, f0, H_{800}, or the complete Vs profile from non-invasive or invasive surveys). This however requires a strategy to make design spectra for the generic soil classes sufficiently conservative, so that more information obtained from measurements at a particular site allows for a reduction in the design values (and not an a-priori increase).

Obtaining reliable amplification functions at instrumented sites
Throughout the process illustrated in this report, two different estimates of amplification functions for instrumented sites were considered and compared: surface to borehole ratios and empirical amplification functions obtained from spectral modelling. Indeed, SB ratios, based on the direct comparison between records at the surface and at the bedrock, are to be held as more reliable. At the same time, these are based on a peculiar and expensive installation configuration (two coupled stations, one at the bottom and one at the surface of a borehole), that is available only at few stations in Switzerland. In this perspective, the reconstruction of amplification functions from surface records only is advantageous and promising.
Our study has observed a satisfactory match between SB ratios and empirical amplification functions, with deviations concentrated at low (<1 Hz) and high frequencies (15-20 Hz). The first ones are probably to be ascribed to limitations related to the wavelength scale of low frequencies when SB ratios are computed; the second ones to how the anelastic attenuation is modelled in the empirical amplification function estimation (i.e. through the attenuation parameter *kappa*).
Further studies should then aim i) at improving the robustness of the estimation of empirical amplification functions through spectral modelling; ii) at improving the reconstruction and modelling of the anelastic component of site amplification, also through direct measurement.

Relevance of nonlinear soil behaviour
This study has discussed the potential relevance of nonlinear soil behaviour at high levels of ground motion. The empirical results show that this phenomenon is not necessarily observed at all sites, and

that it arises at PGA values just around those used for the design of normal buildings in Switzerland (i.e. higher levels of ground motion would be required to determine significant nonlinear phenomena).

Comparison between empirical site-specific uniform hazard spectra and elastic design spectra
Combining the site-specific response spectral amplification functions with a seismic uniform hazard spectrum (the UHS for Sion) allowed obtaining uniform hazard spectra including the site amplification term. These were collated with the elastic design spectra from the current SIA 261 2014 normative, all normalized to the same reference quantity (peak acceleration on rock). The collation site-specific UHSs *vs* design spectra was also repeated in terms of absolute comparison (i.e. discarding any common normalization) for ten Swiss cities, located in different seismic zones (1,2,3a,3b) according to SIA normative. Two critical points of mismatch were identified:

- for all soil classes, the elastic design spectra (from SIA 261) place the plateau period interval at higher periods (and lower spectral acceleration values) with respect to the peak of the median class-specific empirical UHSs. Consequently, the empirical curves of spectral acceleration exceed the design spectra at short periods (approximately below 0.2 s).
- on the other hand, at long periods (above ~0.5 s) the design spectra overcome the average empirical spectra, producing conservativism that might be desirable in earthquake risk mitigation.

A better match was observed with the SIA 261 form adopting the reviewed values of control periods and plateau proposed by Poggi and Fäh (2015). In addition, in this case the design spectra show conservativism at high periods (for classes A-D). Nevertheless, limitedly to class E, the design spectrum fails to fit the marked peak of the empirical curves related to resonance phenomena.
In the absolute comparison site-specific UHSs vs design spectra, we have observed the key role played by parameter a_{gd} (peak horizontal acceleration at class A soils, depending on the seismic zone according to SIA normative) in determining the distance between design spectra and expected spectral acceleration at a given site (the latter obtained combing seismic hazard analysis and site amplification). a_{gd} controls the amplitude of the normative spectra; when this value does not appear to be consistent with the results of seismic hazard analysis (e.g. UHS) for the considered site, the design spectra is likely to be exceeded; this is the case of Lausanne in our study.
It is worth remarking that the use of seismic hazard analysis products (such as PGA, or spectral acceleration at reference periods) for the definition of normative spectra is an approach that, at the time of writing of this report (November 2017), is intended to be adopted in the revision of Eurocode 8. It will replace a_{gd} and allows for a site-specific definition of design spectra. Taking into consideration these issues, we have formulated a proposal of amendment of the elastic design spectra form by scaling the spectra to the site-specific PGA from the seismic hazard. Our scheme includes six different types of period intervals (not necessarily present in the design spectra of all soil classes), and it is therefore more complex and more flexible, showing a good fit with the soil-class UHS obtained for the 10 cities. Our design spectra comprise generally steeper sloping period intervals; plateau segments have higher amplitudes, to accommodate the pronounced peaks linked to resonance, and for two soil classes (A, D) two flat period ranges are incorporated.
Such type of spectra might be beneficial for site-specific seismic hazard studies (microzonation). Consistently with the observations already introduced in this "Conclusions" section, the intention is to provide a flexible form for the definition of elastic design spectra, able to match an expected hazard spectrum for the considered site when this curve is constrained by detailed knowledge of the site subsurface (e.g. through microzonation or site-specific studies). On the other hand, when this information is lacking or just partly reliable, a more conservative solution (particularly at long periods) should be preferred, adopting the more elementary (and precautionary) functional form already prescribed by SIA 261 norm (possibly modified as in Poggi and Fäh 2015). Such conservative choice should take into considerations the large variability observed in one soil class, and not simply the mean or median.

14.0 References

Aoi, S., T. Kunugi, H. Fujiwara (2004). Strong-motion seismograph network operated by NIED: K-NET and KiK-net. J. Jpn. Assoc. Earthquake Eng., 4, 65-74.

Bard, P.-Y., M. Campillo, F. J. Chavez-Garcia, and F. Sanchez-Sesma (1988). The Mexico earthquake of September 19, 1985—A theoretical investigation of large- and small-scale amplification effects in the Mexico City Valley, Earthq. Spectra 4, no. 3, 609–633.

Beresnev, I. A., K. L. Wen (1996). Nonlinear soil response - a reality? Bull. Seismol. Soc. Am., 86, 1964-1978.

Bonilla, L. F., J. H. Steidl, J. Gariel, and R. J. Archuleta (2002). Borehole response studies at the Garner Valley downhole array southern California, Bull. Seismol. Soc. Am. 92, 165–3279.

Boore, D. (2003). Simulation of ground motion using the stochastic method. Pure and Applied Geophysics, 160, 635-676.

Boore, D. M., J. J. Bommer (2005). Processing of strong-motion accelerograms: needs, options and consequences. Soil Dyn. Earthq. Eng., 25, 93-115.

Boore D.M., J. Watson-Lamprey, and N. A. Abrahmnson (2006). Orientation-Independent Measures of Ground Motion. BSSA, 96, no.4, 1502-1511.

Borcherdt, R. D. (1970). Effects of local geology on ground motion near San Francisco Bay, Bull. Seismol. Soc. Am. 60, 29–61.

Brune, J. N. (1970). Tectonic stress and the spectra of seismic shear waves from earthquakes. J. Geophys. Res., 75, 4997-5009.

Brune, J. N. (1971). Seismic sources, fault plane studies and tectonics. Eos Transactions American Geophysical Union, 52, 178-187.

Cadet H., P.Y., Bard, and A. Rodriguez-Marek (2010). Defining a Standard Rock Site: Propositions Based on the KiK-net Database. Bulletin of the Seismological Society of America, Vol. 100, No. 1, pp. 172–195.

Cartwright D.E., and M.S. Longuet-Higgins (1956). The statistical distribution of the maxima of a random function. Proc. Roy. Soc. Lond., 237:212-232.

Cauzzi, C., B. Edwards, D. Fäh, J. Clinton, S. Wiemer, P. Kästli, G. Cua and D. Giardini (2014). New predictive equations and site amplification estimates for the next-generation Swiss ShakeMaps. GJI, 200, 421-438.

Chin, B. H., K. Aki (1991). Simultaneous study of the source, path, and site effects on strong ground motion during the 1989 Loma Prieta earthquake: a preliminary result on pervasive nonlinear site effects. Bull. Seismol. Soc. Am., 81, 1859-1884.

Danciu L. and Fäh D. (2017). Adjustments Of The 2015 Updates Of The Swiss Hazard Model To Different Rock Conditions (Vs-Kappa Adjustment), Technical Report SED 2017/06, Swiss Seismological Service, ETH Zurich, Switzerland

Darendeli, M. B. (2001). Development of a new family of normalized modulus reduction and material damping curves. Ph.D. thesis, University of Texas at Austin.

Darragh, R. B., A. F. Shakal (1991). The site response of two rock and soil station pairs to strong and weak ground motion. Bull. Seismol. Soc. Am., 81, 1885-1899.

Edwards, B., and and D. Fäh (2013). A stochastic ground motion model for Switzerland. Bull. Seism. Soc. Am., 103, 78-98.

Edwards, B., C. Michel, V. Poggi, and D. Fäh (2013). Determination of Site Amplification from Regional Seismicity: Application to the Swiss National Seismic Networks. Seismological Research Letters Volume 84, Number 4

Edwards, B and D. Fäh (2017). Prediction of Earthquake Ground Motion at Rock Sites in Japan: Evaluation of Empirical and Stochastic Approaches for the PEGASOS Refinement Project. Geophysical Journal International - GJI-16-0959 in press.

Fujiwara, H., S. Aoi, T. Kunugi, S. Adachi (2004). Strong-motion observation networks of NIED: K-NET and KiK-net. Cosmos Report, http://www.cosmos-eq.org/Projects/Fujiwara_paper.pdf, last accessed September 2004.

Hardin, B. O., V. P. Drnevich (1972). Shear modulus and damping in soils: measurement and parameter effects. J. Soil Mech. Found., 98, 603-624.

Katsumata, A. (1996). Comparison of magnitudes estimated by the Japan Meteorological Agency with moment magnitudes for intermediate and deep earthquakes. Bull. Seismol. Soc. Am., 86, 832-842.

Kawase, H. (2006). Site effects derived from spectral inversion method for K-NET, KiK-net, and JMA strong motion network with special reference to soil nonlinearity in high PGA records, Bull. Earthq. Res. Inst., 81, 309-315.

Oth, A., D. Bindi, S. Parolai, D. Di Giacomo (2010). Earthquake scaling characteristics and the scale-(in) dependence of seismic energy-to-moment ratio: Insights from KiK-net data in Japan. Geophys. Res. Lett., 37, doi: 10.1029/2010GL044572.

Paolucci, R. (2017). Seismic Action and Site Effects: Work in Progress for the Revision of Eurocode 8. SED PSHA Workshop 2017, Lenzburg (Switzerland), 5-7 September 2017.

Poggi V., B. Edwards, and D. Fah (2011). Derivation of a Reference Shear-Wave Velocity Model from Empirical Site Amplification. Bulletin of the Seismological Society of America, Vol. 101, No. 1, pp. 258–274

Poggi V., B. Edwards, and D. Fah (2013). Reference S-Wave Velocity Profile and Attenuation Models for Ground-Motion Prediction Equations: Application to Japan. Bulletin of the Seismological Society of America, Vol. 103, No. 5, pp. 2645–2656

Poggi V., B. Edwards, and D. Fah (2017). Development of hazard- and amplification-consistent elastic design spectra. Soil Dynamics and Earthquake Engineering, submitted July 2017.

Poggi V., and D. Fäh (2015). A proposal for horizontal and vertical elastic design spectra, input for the new Swiss code for dams. Technical Report SED/BFE/R/01/30072015

Régnier J, H. Cadet, L F. Bonilla, E. Bertrand and J.F. Semblat (2013). Assessing nonlinear behavior of soils in seismic site response: statistical analysis on kik-net strong motion data. BSSA, 103, no.3, 1750-1770.

Seed, H. B., I. M. Idriss (1969). Influence of soil conditions on ground motions during earthquakes, University of California, Institute of Transportation and Traffic Engineering, Soil Mechanics Laboratory.

SED (2015). Seismic Hazard Maps. Available online, at http://www.seismo.ethz.ch/de/knowledge/seismic-hazard-switzerland/maps/hazard/, retrieved 27.6.2017.

SED (2016). Seismic Hazard Model 2015 for Switzerland (SUIhaz2015) Report. Available online, at http://www.seismo.ethz.ch/export/sites/sedsite/knowledge/.galleries/pdf_knowledge/SUIhaz2015_final-report_16072016_2.pdf, retrieved 27.6.2017.

SIA (2014). SIA 261 Einwirkungen auf Tragwerke. Schweizerischer Ingenieur- und Architekentverein, Zurich, Switzerland.

Wald, D. J., and R.W. Graves (1998). The seismic response of the Los Angeles basin, California, Bull. Seismol. Soc. Am. 88, no. 2, 337–356.

Yamanaka, H., K. Seo, and T. Samano (1989). Effects of sedimentary layers on surface-wave propagation, Bull. Seismol. Soc. Am. 79, no. 3, 631–644.

APPENDIX A - Possible ambiguity in E soil class definition

The present version of SIA 261 normative contains a partly ambiguous definition for E soil class, when this is based on the sole proxy of Vs30. In fact, the description for this particular soil category is more a geological one, rather than a geophysical one. E class is in fact defined as sediments with Vs properties similar to classes C or D, with a limited extent in depth (5-20 m) and underlain by a shallow stiff formation (Vs>800 m/s). The ambiguity with respect to a purely Vs30-based classification lies in the fact whether

- Soil E sites should have the same Vs30 of classes C or D (e.g. Vs30<500 m/s), but differ from these depending on the depth of the seismic bedrock (5-20 m), or
- only the upper sediments should have an average Vs compatible with the average Vs (intended as Vs30) of classes C and D; therefore, sites falling into E class should have a Vs_{z800} < 500 m/s (where Vs_{z800} is the average S-wave velocity down to a depth *z800* where a stiff formation with Vs>800 m/s is encountered, with 5<z800<20 m). This definition is closer to the approach that appears to be currently followed for soil types designation in the revision of Eurocode 8 (Paolucci R., 2017).

This ambiguity is relevant to our study as the classification of the set of KiK-net stations is based exclusively on the provided S-wave velocity profile; the geological information regarding the weathering formations is in fact unavailable in terms of univocal correlation with European soil types.
For the core part of our study (sections 3 – 11) we assumed as definition for class E the first one of the two presented above (Vs30<500 m/s and *z800* depth between 5-20 m), consistently with the work of Poggi and Fäh (2015). For the sake of completeness, in this appendix we follow the main stages of sections 3-11 adopting the alternative criterion for E type soils (Vs_{z800}<500 m/s and *z800* depth between 5-20 m), focusing on the discrepancies in terms of grouping of amplification patterns brought by a different class E definition. As a first step, we redistributed the KiK-net sites among the various SIA classes: the alternative classification is represented in Figure1A, which is the counterpart of Figure 4.

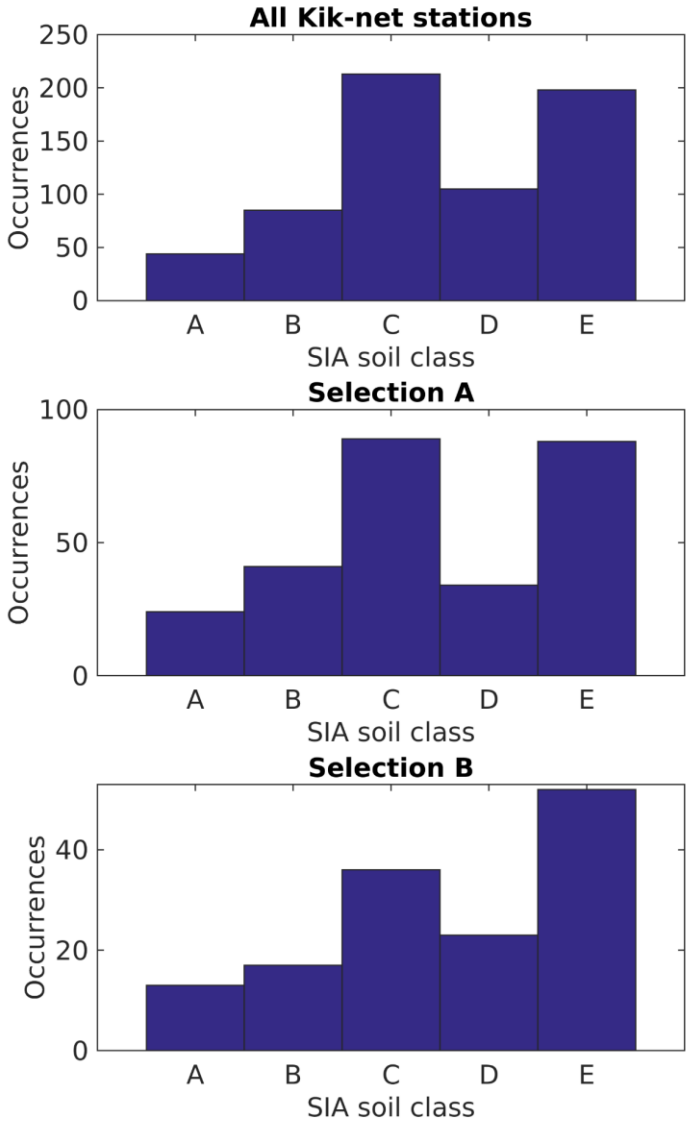

Figure 1A – Distribution of KiK-net stations among soil classes A-E of SIA 2014 normative, assuming an alternative criterion for class E. From top to bottom: the entire dataset (~700 stations), subsets of reliable stations A (289 sites) and B (144 sites).

The main difference with respect to Figure 4 is the fact that E sites are now the largest station group (together with C), while A and B class subsets are smaller. This is because the new E class criterion is less restrictive, and many formerly B (55%), and A sites (32%), are now to be considered type E stations. The definition of soil E adopted in the main part of this study restricts class E to few sites with very soft sediments overlying a shallow bedrock; as the overall Vs30 is < 500 m/s, the Vsz800 (average Vs of surficial sediments) is forced to be extremely low (140 – 380 m/s, average 252 m/s). This shallow and significant impedance contrast leads to high value of amplification and f_0 peak of approximately 8 Hz (Figures 5-7, 8-10).

On the other hand, assuming the Vs_{z800} < 500 m/s criterion produces for class E a more copious set of sites with a less abrupt contrast (mean value of Vs_{z800} = 318 m/s); as a consequence, the Fourier amplification functions (SB ratios, Figures 2A-4A; empirical amplification functions, Figures 5A-7A) bear a lower amplitude peak, moved towards higher frequencies. The median curves for classes A and

B show slight changes as well, with lower and wider f_0 peaks. Figures 8A, 9A are dedicated to the comparison for selection A stations.

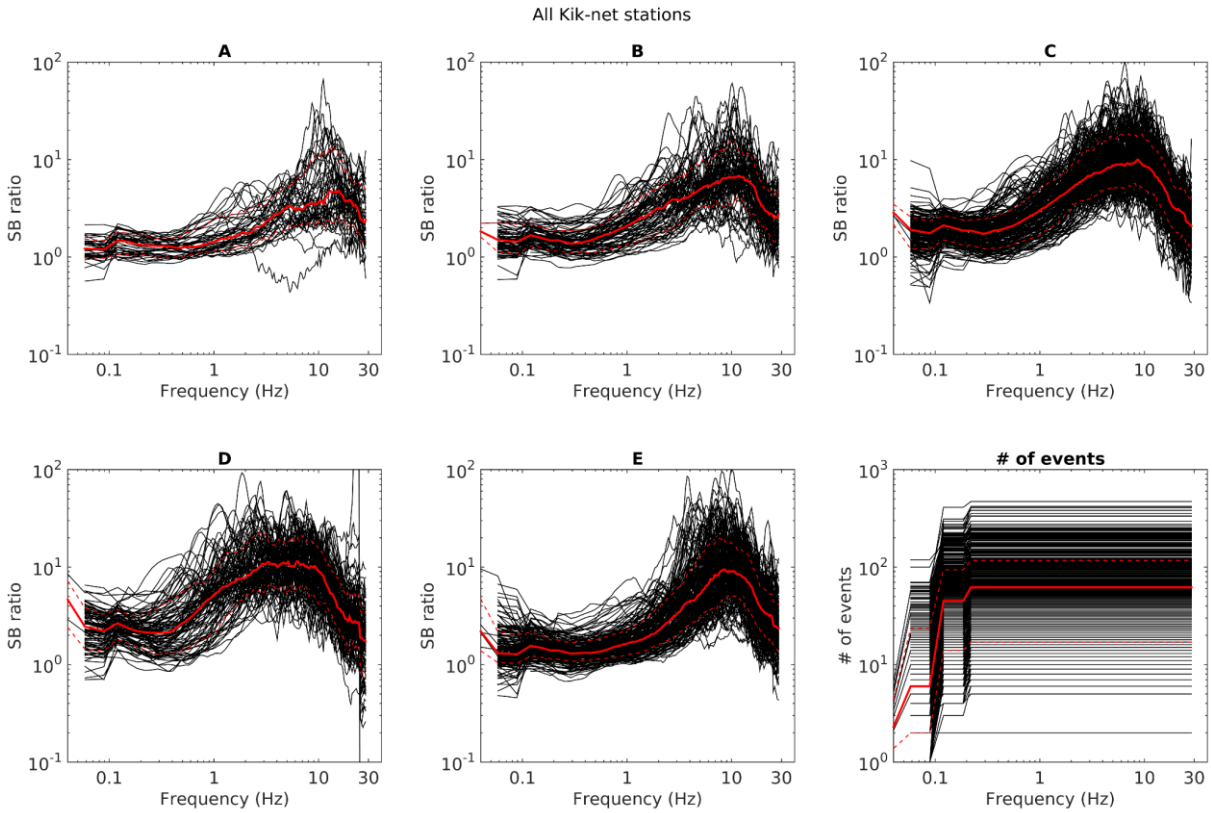

Figure 2A – surface to borehole ratios (black lines) for all the available KiK-net stations, referred to the Japanese reference Vs profile. Subpanels 1-5 collect the surface to borehole ratios for soil classes A-E according to SIA normative (Vs_{z800} < 500 m/s criterion has been adopted for the definition of class E). The median for each group is represented with a red line; the 15th and 85th percentile with red dashed lines. The panel in the lower right corner indicates the number of events employed for the estimation of the frequency components of each single surface to borehole ratio.

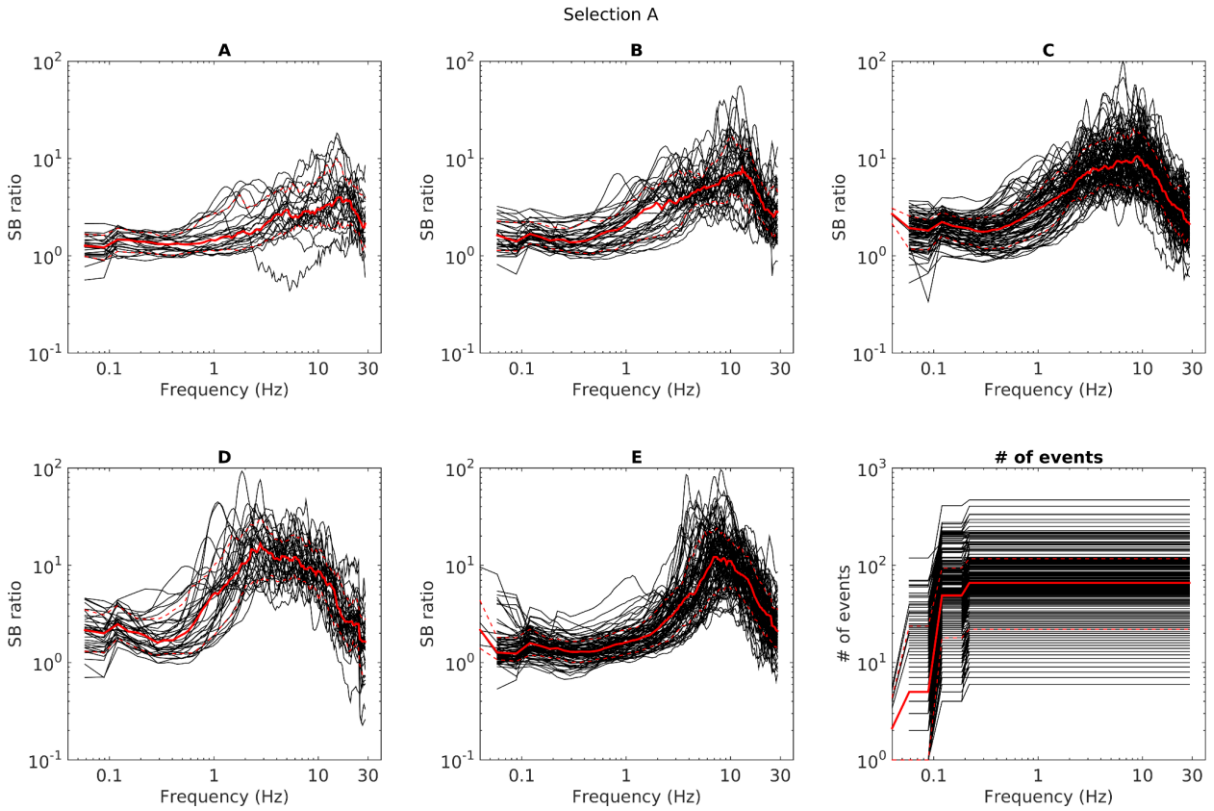

Figure 3A – surface to borehole ratios (black lines) for selection A KiK-net stations, referred to the Japanese reference Vs profile. Subpanels 1-5 collect the surface to borehole ratios for soil classes A-E according to SIA normative (Vs_{z800} < 500 m/s criterion has been adopted for the definition of class E). The median for each group is represented with a red line; the 15th and 85th percentile with red dashed lines. The panel in the lower right corner indicates the number of events employed for the estimation of the frequency components of each single surface to borehole ratio.

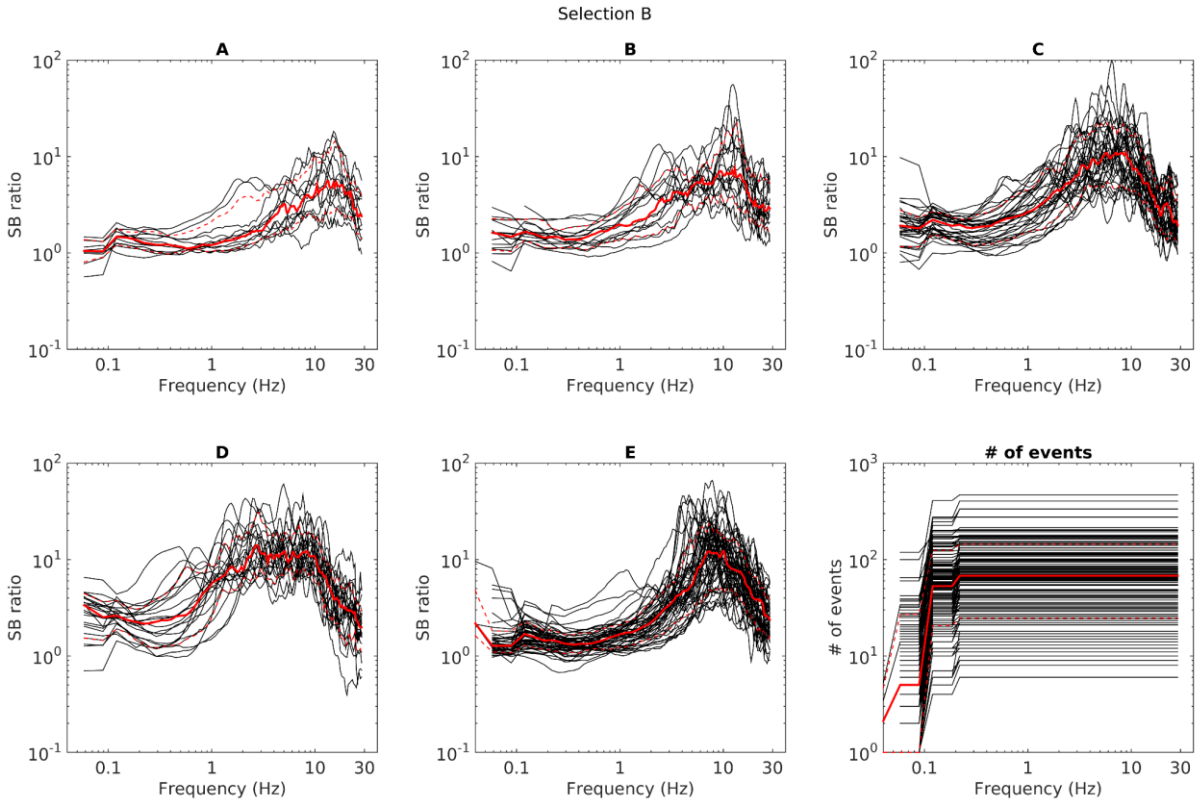

Figure 4A – surface to borehole ratios (black lines) for selection B KiK-net stations, referred to the Japanese reference Vs profile. Subpanels 1-5 collect the surface to borehole ratios for soil classes A-E according to SIA normative (Vs_{z800} < 500 m/s criterion has been adopted for the definition of class E). The median for each group is represented with a red line; the 15th and 85th percentile with red dashed lines. The panel in the lower right corner indicates the number of events employed for the estimation of the frequency components of each single surface to borehole ratio.

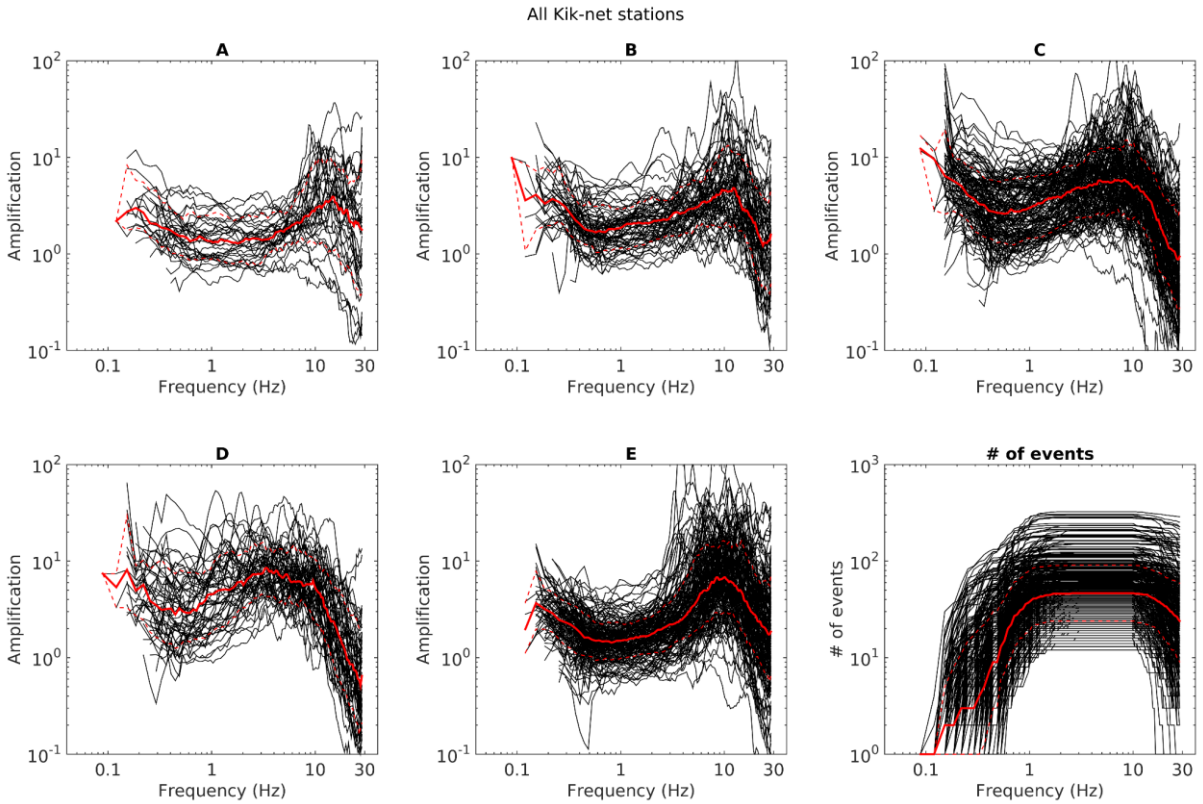

Figure 5A – Site amplification functions (black lines) for all the available KiK-net stations, referred to the Japanese reference Vs profile. Subpanels 1-5 collect the amplification functions for soil classes A-E according to SIA normative (Vs_{z800} < 500 m/s criterion has been adopted for the definition of class E). The median for each group is represented with a red line; the 15th and 85th percentile with red dashed lines. The panel in the lower right corner indicates the number of events concurring to the estimation of each single amplification function, with no distinction for soil class

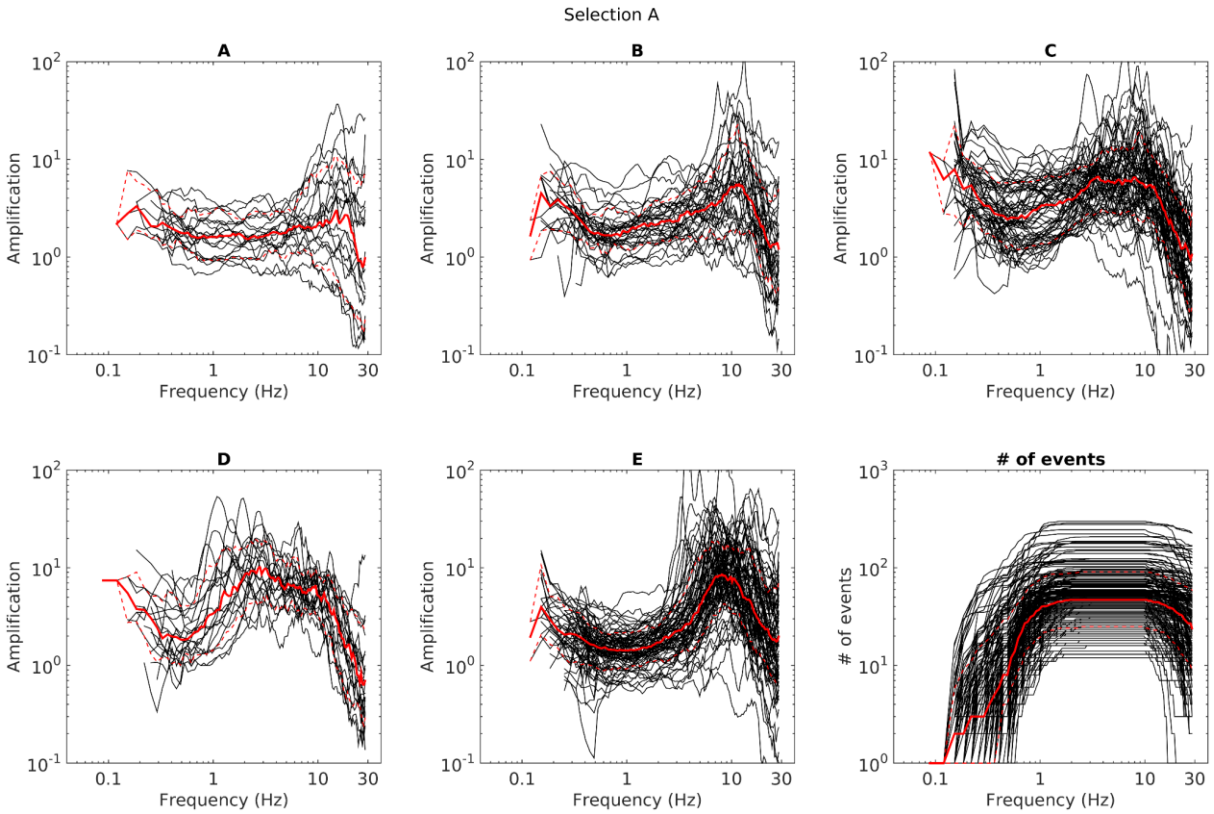

Figure 6A – Site amplification functions (black lines) for selection A KiK-net stations, referred to the Japanese reference Vs profile. Subpanels 1-5 collect the amplification functions for soil classes A-E according to SIA normative (Vs_{z800} < 500 m/s criterion has been adopted for the definition of class E). The median for each group is represented with a red line; the 15th and 85th percentile with red dashed lines. The panel in the lower right corner indicates the number of events concurring to the estimation of each single amplification function, with no distinction for soil class

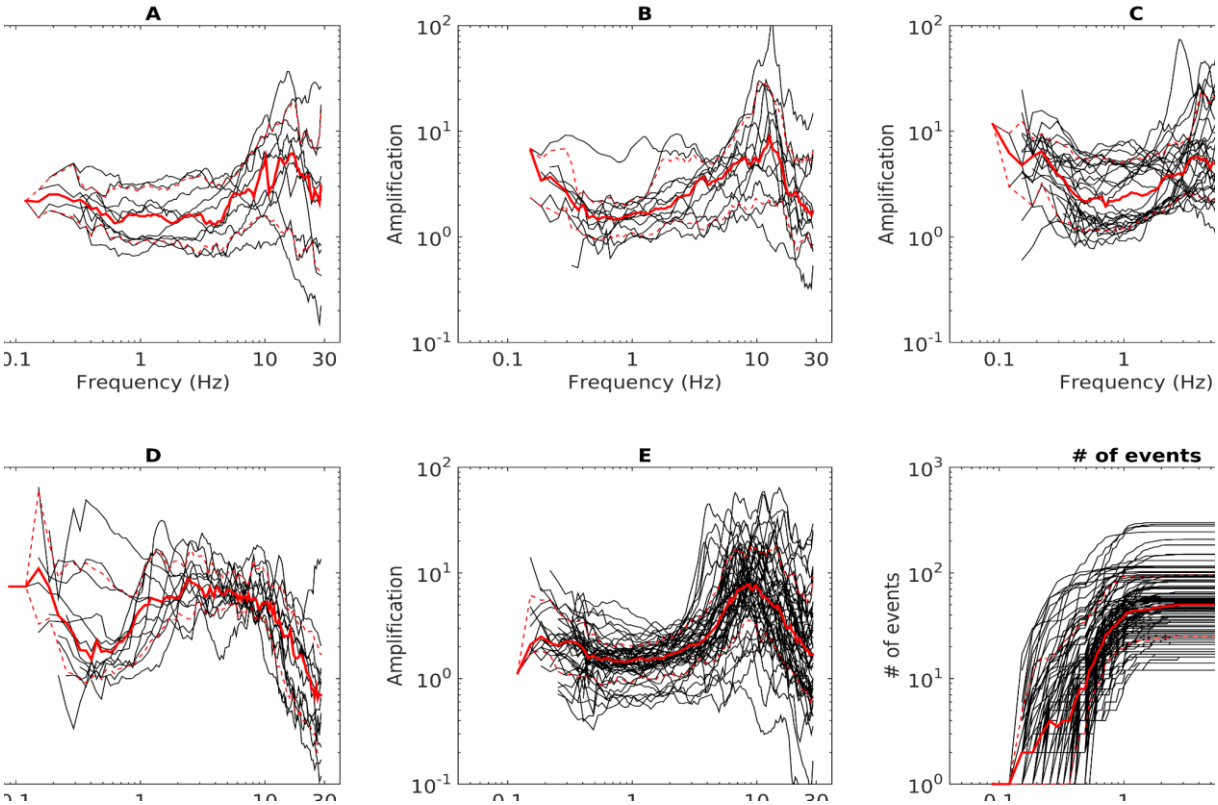

Figure 7A – Site amplification functions (black lines) for selection A KiK-net stations, referred to the Japanese reference Vs profile. Subpanels 1-5 collect the amplification functions for soil classes A-E according to SIA normative (Vs_{z800} < 500 m/s criterion has been adopted for the definition of class E). The median for each group is represented with a red line; the 15th and 85th percentile with red dashed lines. The panel in the lower right corner indicates the number of events concurring to the estimation of each single amplification function, with no distinction for soil class

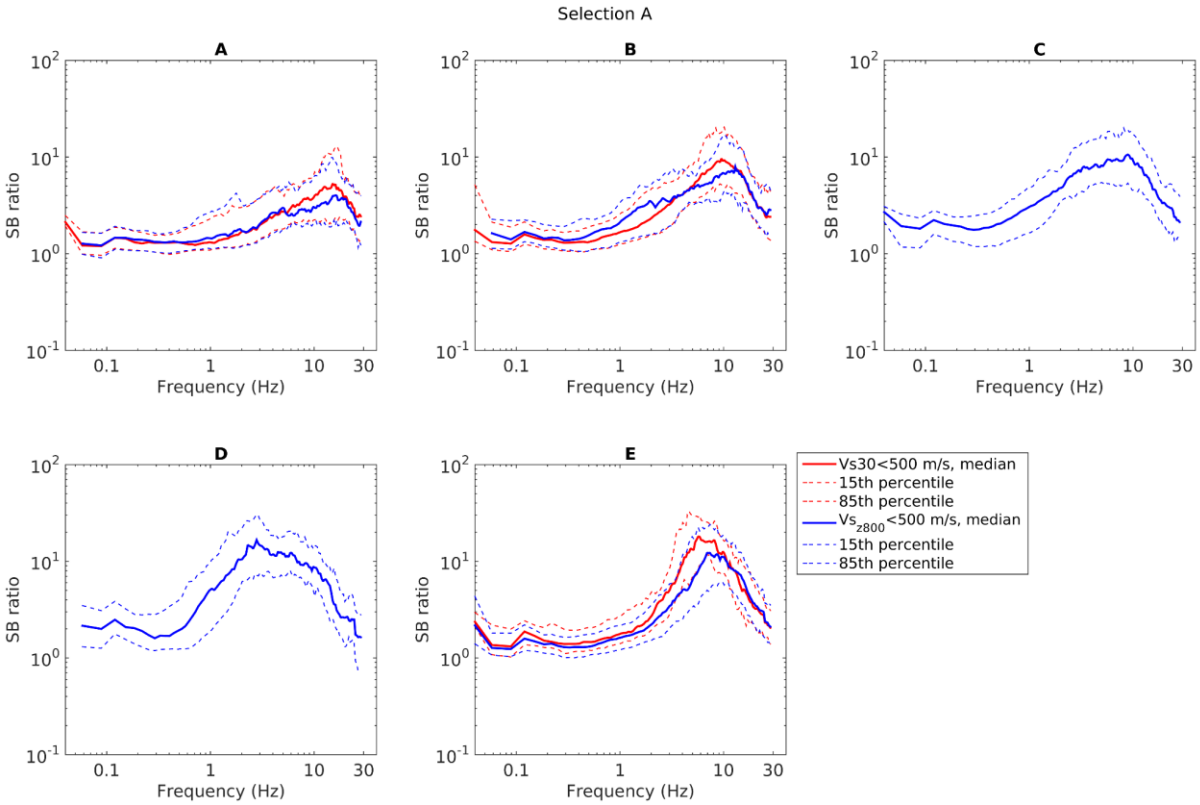

Figure 8A – comparison between medians of SB ratios for each soil class type, assuming either the Vs30 < 500 m/s (red lines) or Vs_{z800} < 500 m/s (blue lines) criterion for the definition of E class. Only selection A sites were used for this comparison. For classes C and D, red and blue lines are the same.

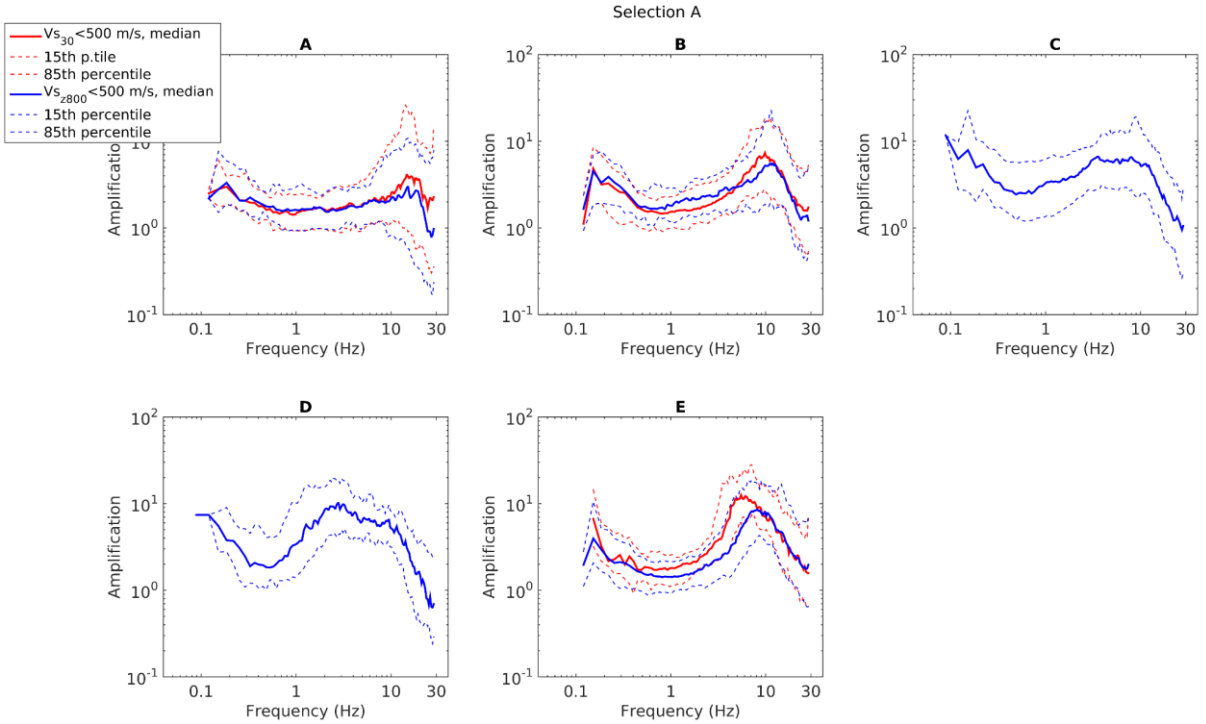

Figure 9A – comparison between medians of empirical amplification functions for each soil class type, assuming either the Vs30 < 500 m/s (red lines) or Vs_{z800} < 500 m/s (blue lines) criterion for the definition of E class. Only selection A sites were used for this comparison. For classes C and D, red and blue lines are the same.

Besides the consequences on the median of the Fourier amplifications, we also analysed whether the assumption of an alternative class distribution criterion affects the consistency of the amplification pattern within each soil class. For this purpose, in Figures 10A-11A we display the absolute distance from the median of the 15th and 85th percentiles, collating the two classification norms, arguing that wider 15-85th percentiles are evidence of a reducing consistency in terms of amplification. Although we expect a greater scatter of amplification response, particularly for class E, no significant difference in the pattern of the 15th-85th percentile boundaries is anyhow evident in Figures 10A-11A, suggesting that the level of global coherence wihin the individual soil classes is not changing dramatically.

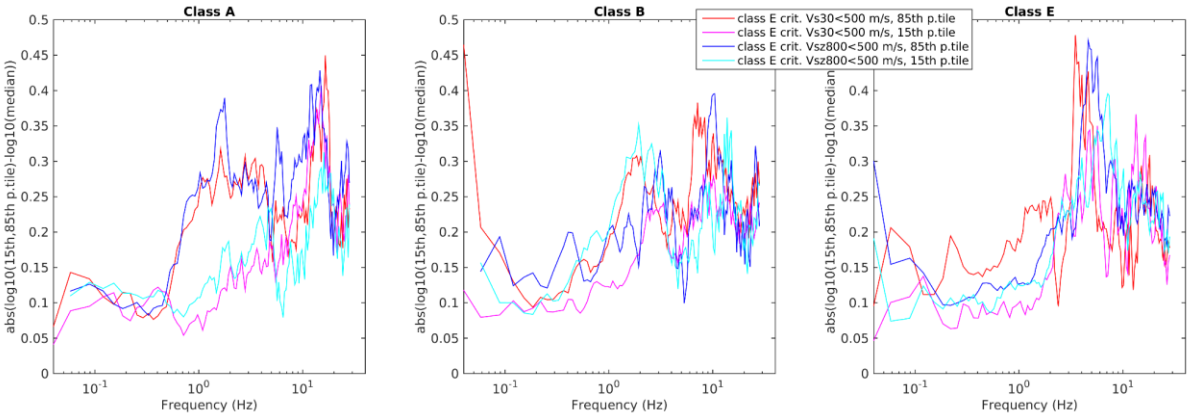

Figure 10A – absolute distance between 15th-85th percentiles and the corresponding median curves (SB ratios) for selection A sites, assuming the two different classification criteria (blue and cyan lines vs red and magenta lines, respectively).

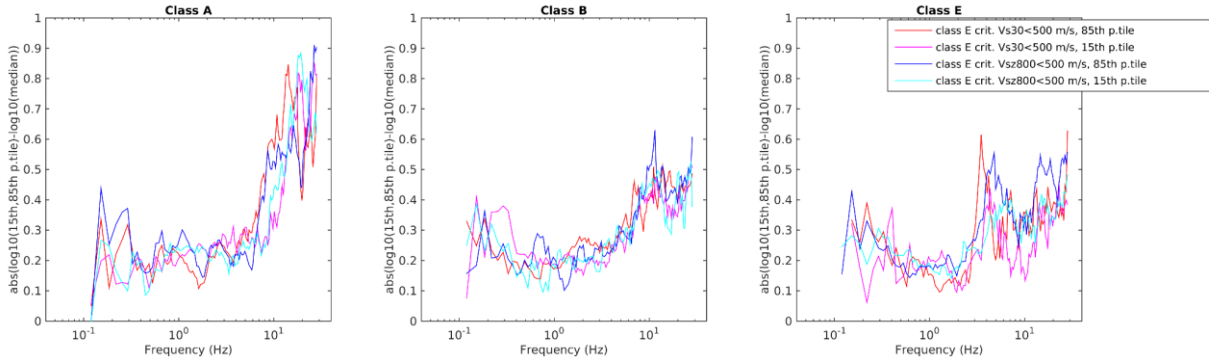

Figure 11A – absolute distance between 15th-85th percentiles and the corresponding median curves (emprical amplification functions) for selection A sites, assuming the two different classification criteria (blue and cyan lines vs red and magenta lines, respectively).

Following the processing workflow described in the core of this report, we move here as well from the Fourier to the response spectra domain, computing the response spectra amplification functions (section 7) and grouping them by soil types according to the alternative subdivision criterion attended in this appendix. Figures 12A-14A are dedicated to the response spectra amplification curves using SB ratios as input amplification functions (hence they correspond to Figures 19-21); Figures 15A-16A are dedicated to the response spectra amplification curves from empirical amplification functions (therefore they are the counterparts of Figures 16-18).

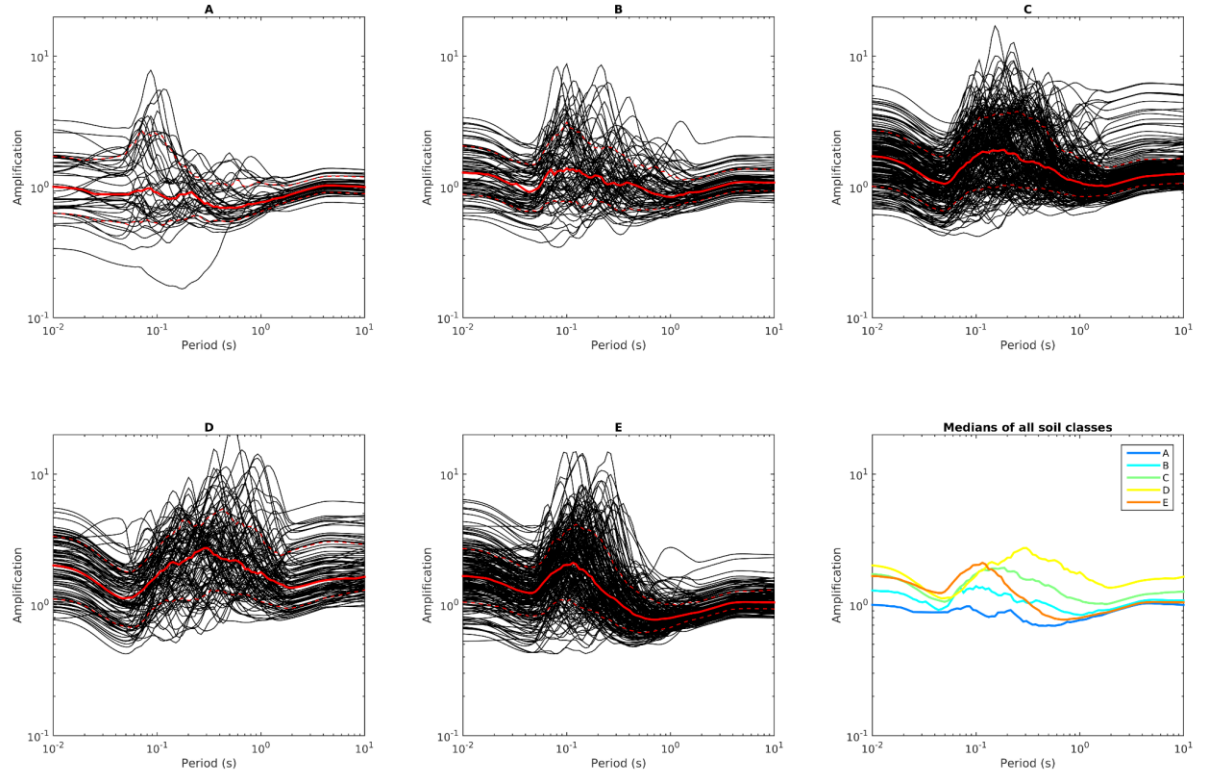

Figure 12A – Response spectral amplification curves (black lines) estimated adopting SB ratios as input Fourier amplification functions. All available KiK-net sites were considered. The median, 15th and 85th percentiles are represented with continuous and dashed red lines, respectively. The median curves are displayed altogether in the lower right panel.

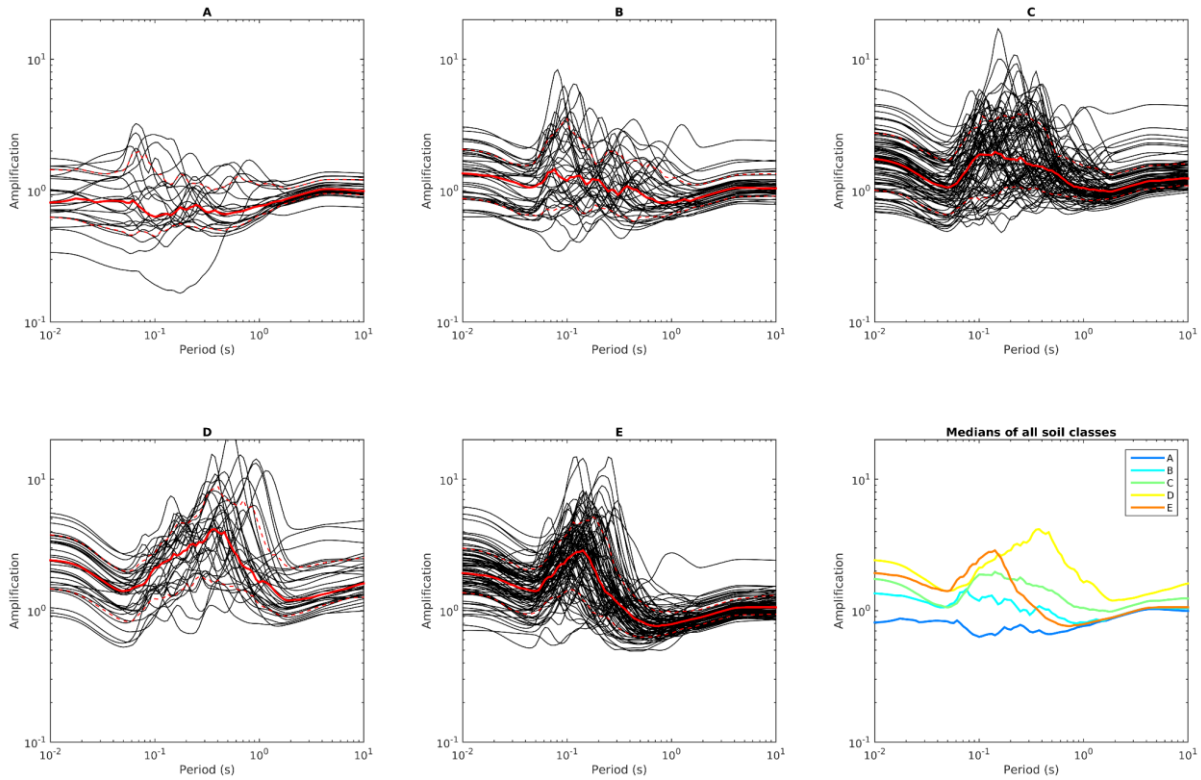

Figure 13A – Response spectral amplification curves (black lines) estimated adopting SB ratios as input Fourier amplification functions. Selection A KiK-net sites were considered. The median, 15th and 85th percentiles are represented with continuous and dashed red lines, respectively. The median curves are displayed altogether in the lower right panel.

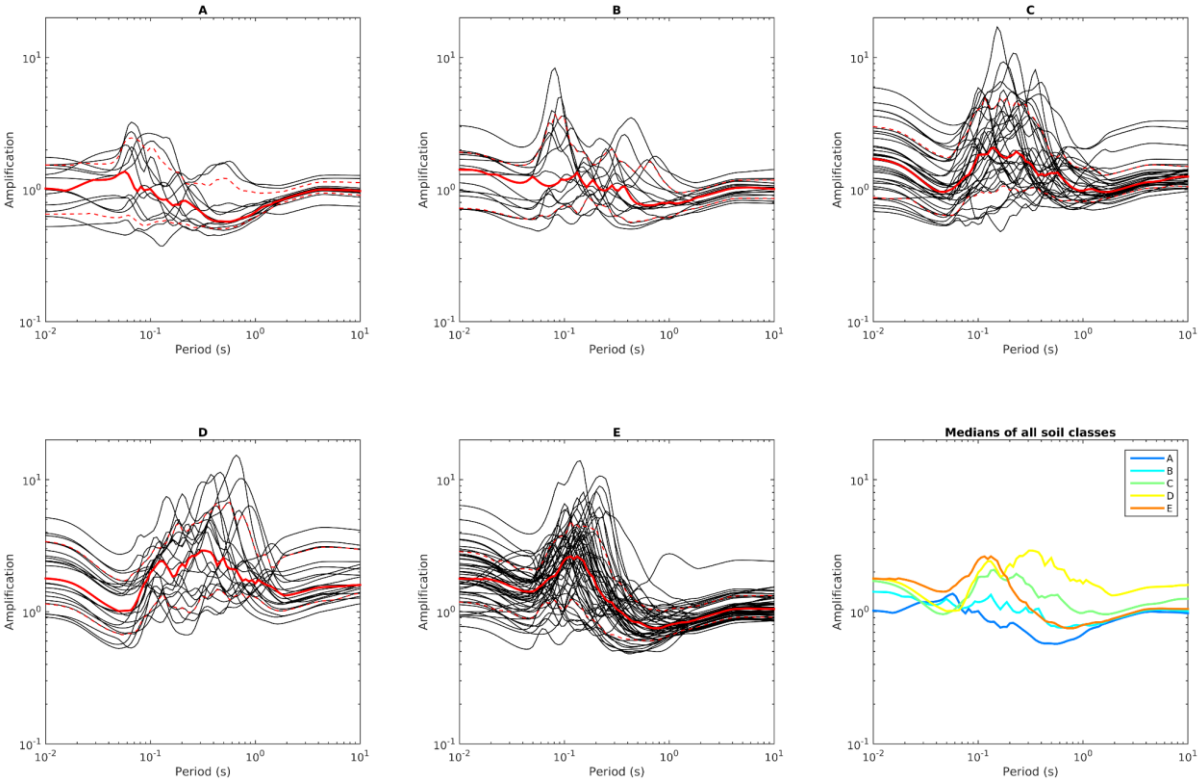

Figure 14A – Response spectral amplification curves (black lines) estimated adopting SB ratios as input Fourier amplification functions. Selection B KiK-net sites were considered. The median, 15th and 85th percentiles are represented with continuous and dashed red lines, respectively. The median curves are displayed altogether in the lower right panel.

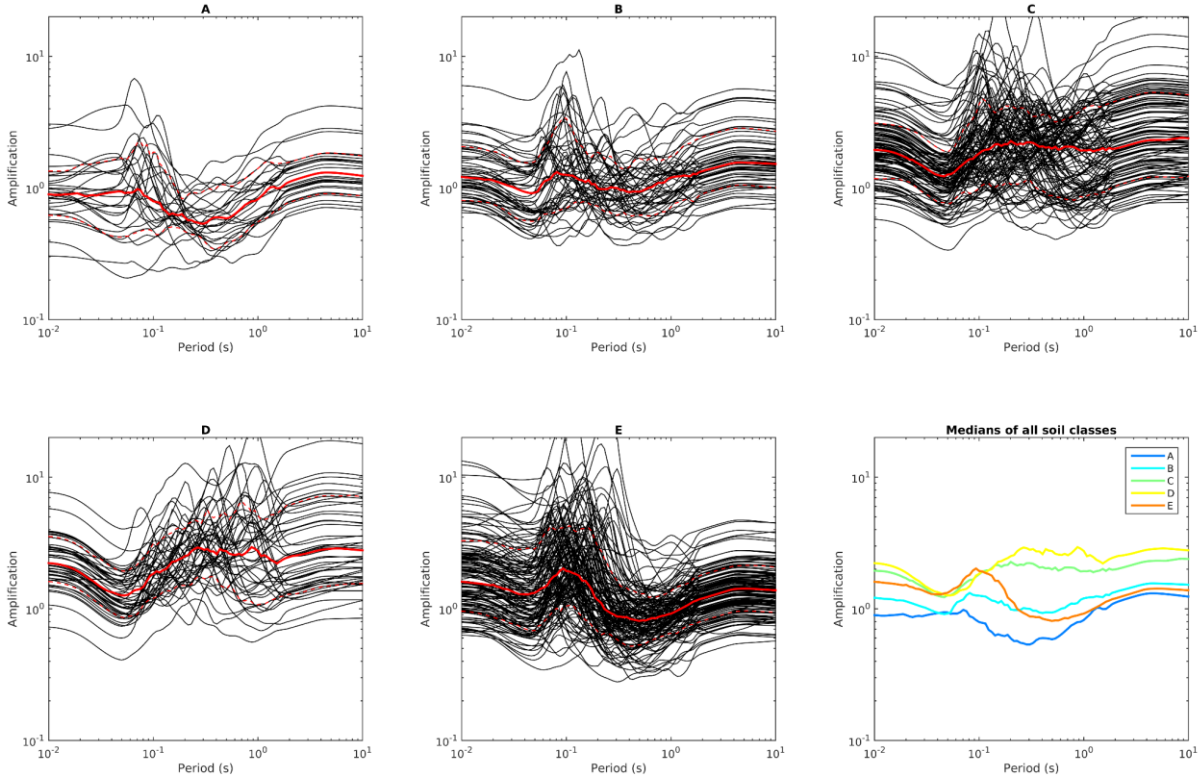

Figure 15A – Response spectral amplification curves (black lines) estimated adopting empirical amplification functions as input Fourier amplification functions. All available KiK-net sites with a reliable empirical amplification function were considered. The median, 15th and 85th percentiles are represented with continuous and dashed red lines, respectively. The median curves are displayed altogether in the lower right panel.

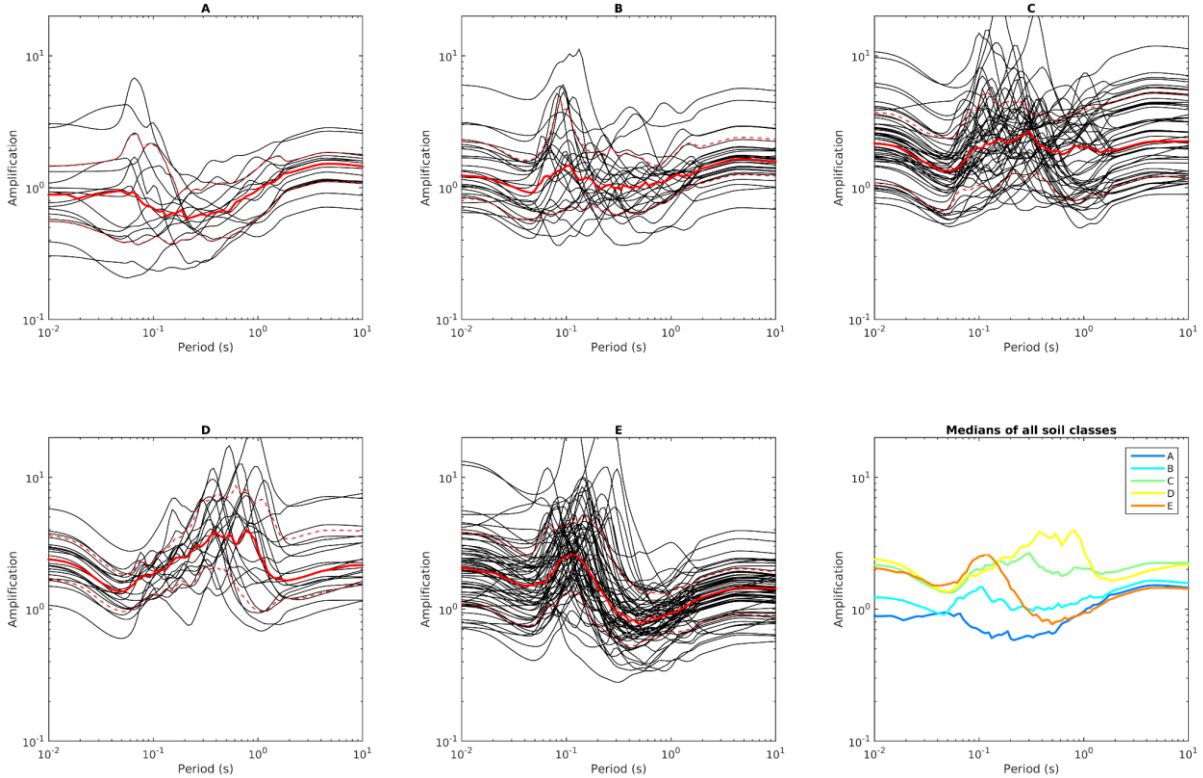

Figure 16A – Response spectral amplification curves (black lines) estimated adopting empirical amplification functions as input Fourier amplification functions. Selection A KiK-net sites with a reliable empirical amplification function were considered. The median, 15th and 85th percentiles are represented with continuous and dashed red lines, respectively. The median curves are displayed altogether in the lower right panel.

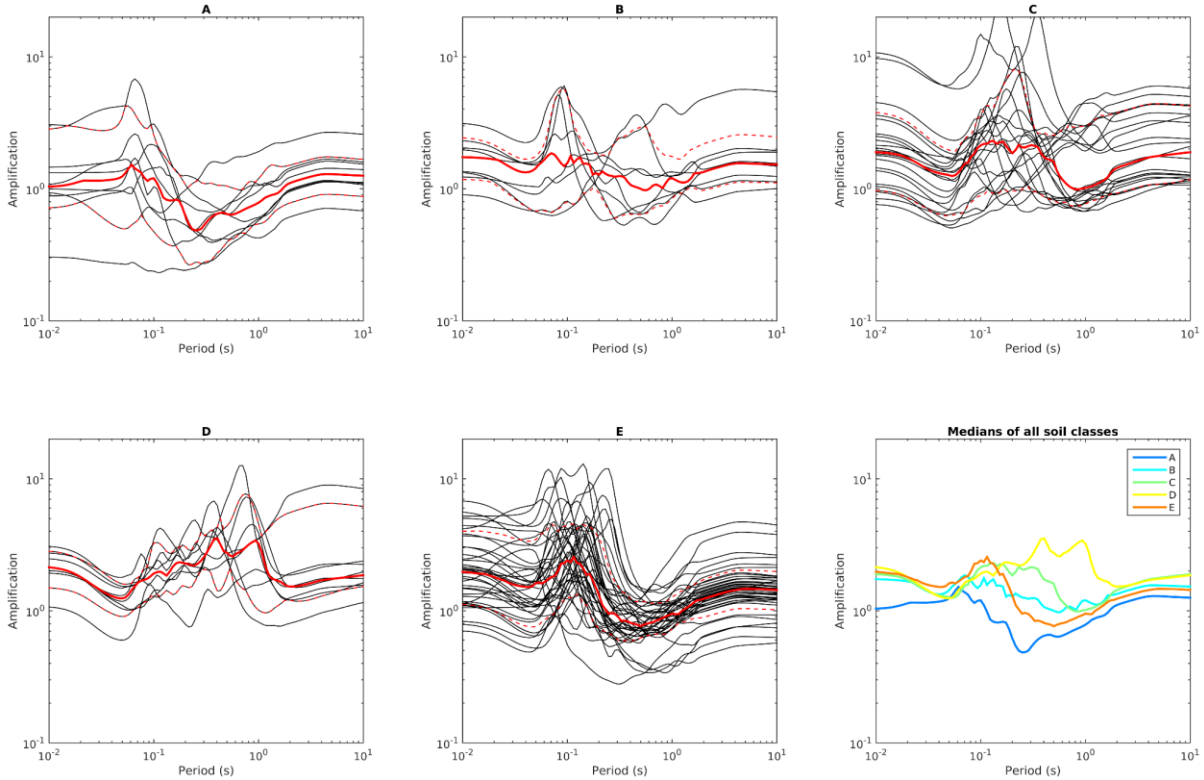

Figure 17A – Response spectral amplification curves (black lines) estimated adopting empirical amplification functions as input Fourier amplification functions. Selection B KiK-net sites with a reliable empirical amplification function were considered. The median, 15th and 85th percentiles are represented with continuous and dashed red lines, respectively. The median curves are displayed altogether in the lower right panel.

The discrepancies introduced by the adopted class E definition are analysed in detail for selection A sites, with the help of Figure 18A. Moving from left- to right-hand side panels in Figure 18A, the median curves for class E show less pronounced peaks, located at lower periods.

As for class A and B, their median response spectral amplifications appear now "flattened" towards lower values of amplification. These observations are fully compatible with and derive from the changes identified in the repartition of the Fourier amplification functions (see Figures 8A, 9A).

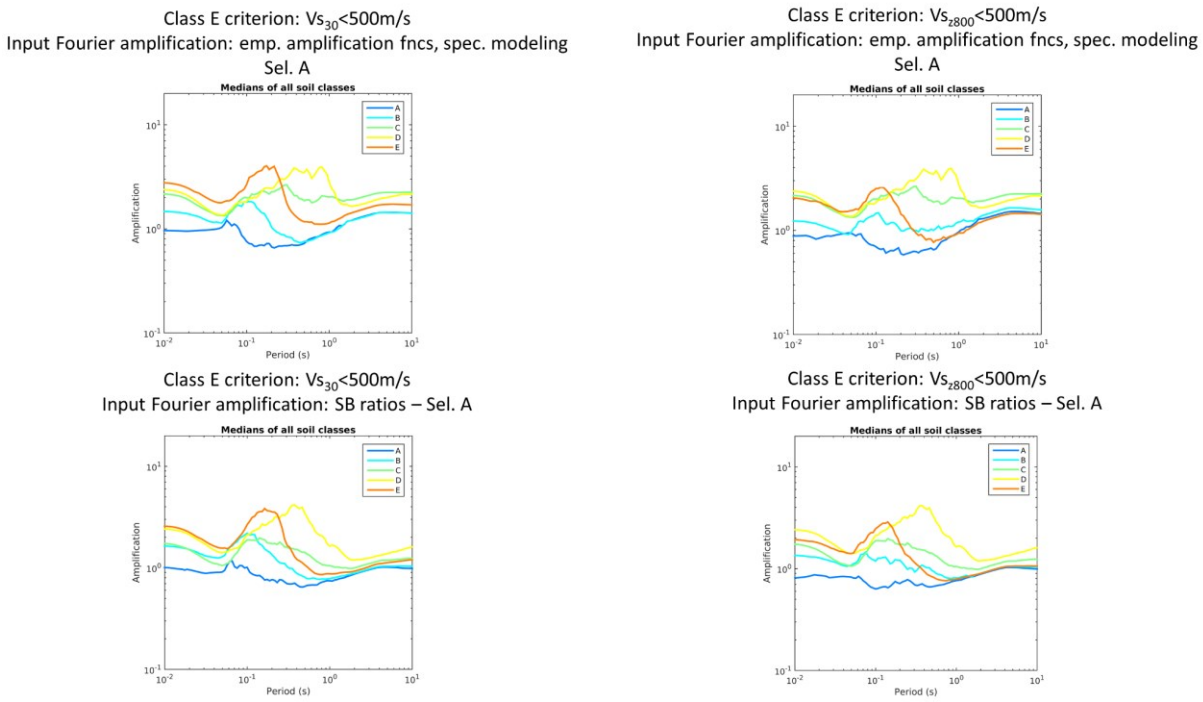

Figure 18A – Comparison between class-specific median curves of response spectral amplification functions, assuming two different definitions for class E. Left column: criterion involving Vs30 < 500 m/s; right column: criterion requiring Vs_{z800} < 500 m/s. Top row: input Fourier amplification drawn from empirical amplification functions. Bottom: input Fourier amplification drawn from SB ratios. Selection A stations only were considered for this representation.

This different redistribution of the same sites into soil types inevitably affects also the shape of the median curves (for each soil class) of site-specific UHSs, obtained from the combination of response spectra amplification functions and uniform hazard spectra on rock from seismic hazard analysis (section 9).
We repeat here the collation between these populations of site-specific UHSs and elastic design spectra, following the two approaches developed in the main body of this report (sections 9 - 11):

- a comparison between normalized (to PGA) site-specific UHSs and normalized (to a_{gd}) design spectra, based on Sion scenario (sections 9,10);
- a comparison between site-specific UHSs and design spectra, both in their absolute values, focusing on 10 cities of the Swiss territory (section 11).

Therefore, following the normalized comparison approach, the medians of site-specific UHS derived from response spectral amplification curves were recomputed, for those soil classes (A, B, E) affected by the change of definition for type E soil; these are shown in Figure 19A, again collated with the SIA 261 normative design spectra and Poggi and Fäh's proposal (2015). Comparing Figures 43, 44 with Figure 19A, the following observations can be formulated:

- As far as class A is concerned, the exceedance of Poggi and Fäh's (2015) proposed spectrum by selection B sites (as seen in Figure 43, left panels) is now almost negligible (Figure 19A, left panels); in general, for all KiK-net sites assortments (all stations, selections A and B), the median envelope reaches lower values of normalized spectral acceleration;
- A decrease of normalized S.A. is also noticed for class B, so that the median curves from site-specific UHS have now - at their peaks - approximately the same values of the SIA 2014 norm plateau, although moved towards lower periods (Figure 19A, central column panels);
- The median curves from class E do not exceed anymore the design spectrum proposed by Poggi and Fäh (2015; compare Figure 44 with Figure 19A, right hand side panels); however, the peaks of the median envelope are now at the lower limit of the plateau of the design spectrum (previously, they were centred with respect to the plateau; see Figure 44).

The adoption of an alternative definition for class E (based on the sole knowledge of the Vs profile, disregarding possible geological considerations) has led to different median envelopes for the population of site-specific UHS for the soil types A, B and E (Figure 19A versus Figures 43,44). It is worth remarking that the individual site-specific UHS curves are exactly the same in both cases; the discrepancies between the results appearing in Figure 19A and Figures 43-44 are to be ascribed to a different grouping of the same population of spectra.
Indeed, the use of a less restrictive criterion for class E (Vs_{z800} in place of Vs30 <500 m/s) has increased the absolute and relative number of E sites. Stations with higher Vs_{z800} have been added to the original group (obviously preserving the 5<z800<20 m constraint) leading to a more smoothed average site response with lower median values of amplification, and moving the f_0 peak towards higher frequencies (or lower periods).
Sites now defined as E class originally (i.e., with the classification adopted in the main body of this study) belonged to A or B types. These classes "lose" their portion of stations with softer surficial cover; therefore, the global (median) responses are characterized by lower values of amplification.

Consequently, for all involved classes (A, B, E) the medians of the populations of site specific UHS are "flattened" down towards lower spectral accelerations, and their comparison with design spectra leads to different conclusions with respect to those presented in section 10.

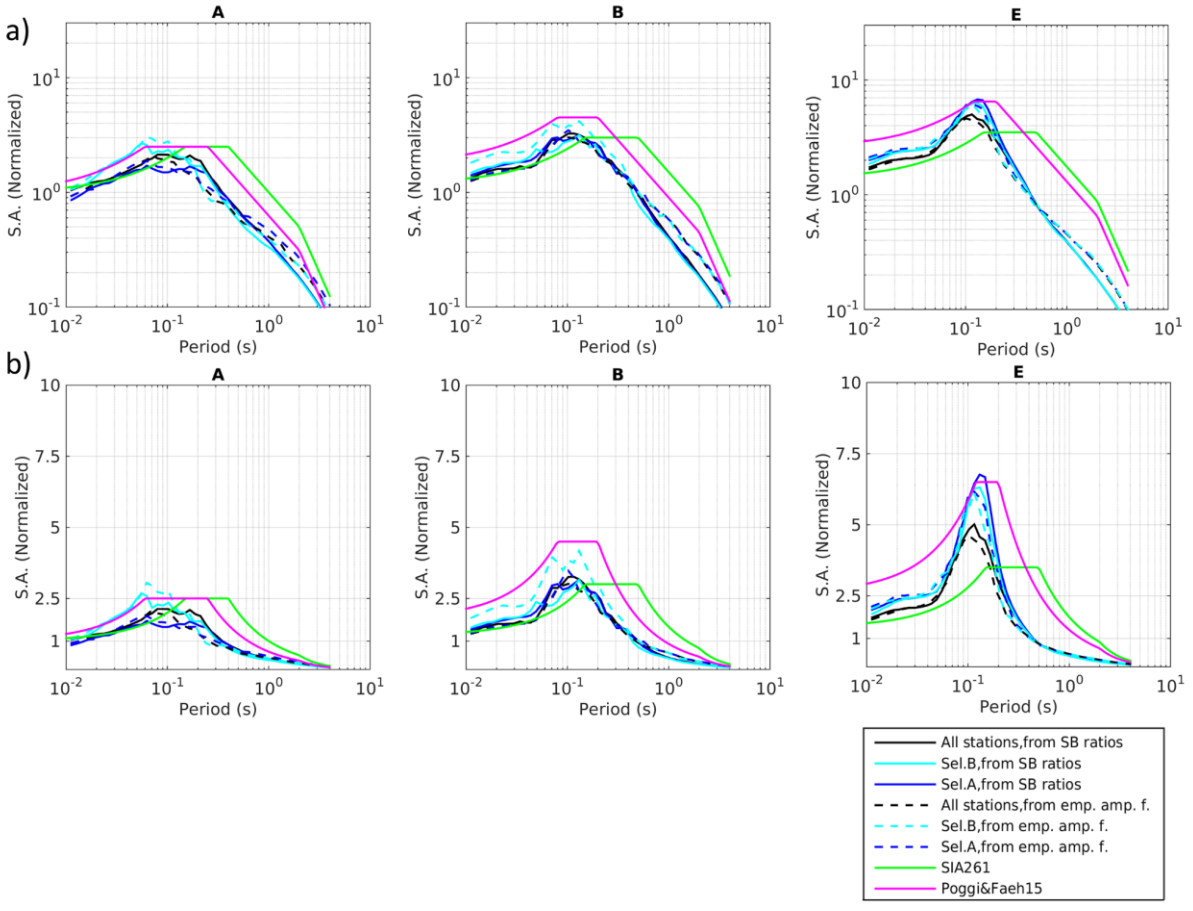

Figure 19A – a) median of site specific UHS, classified by soil class, adopting the alternative definition for class E (involving Vs_{z800} m/s < 500 m/s). b) same as (a), with ordinate axis (normalized spectral acceleration) in linear scale.

In the following figures (20A-29A, one for each considered city), we rather display the results obtained for the *absolute* comparison empirical spectra – elastic design spectra (similarly to section 11). These figures include the panels collating the median curves of site-specific UHSs (considering various sites' selections) with the corresponding design spectra from the SIA 261 (2014) form and its subsequent

modification by Poggi and Fäh (2015; i.e. corresponding to Figures 54-63 in section 11). We also include the proposal for normative spectra formulated in this work (equations 5, section 10), using the parameters' values (S, TA-T_D) shaped on the site-specific hazard spectra sorted by classes according to the soil type subdivision followed in this appendix (Table 5). All design spectra in this set of plots are scaled to a_{gd}, retaining the zone subdivision of SIA 261. For the further step of site-specific design spectra incorporating seismic hazard output (i.e. Poggi and Fäh's, 2015 and this work's normative spectra scaled to the PGA expected at each city), see Figures 76-85 in section 12.
We remind that the reorganization into soil classes followed in this appendix affects soil types A, B and E, but not C and D (whose median curves are the same as in Figures 54-63).

As already noticed for Figures 18A, 19A, the different criterion for class E produces median curves of empirical spectra for classes A and B which bear acceleration values lower than those obtained following the soil type E definition adopted in the main body of this report. This applies as well to class E median functions, whose resonance peak shifts also leftward towards lower period values. Despite these changes, similarly to Figures 54-63, the SIA 261 (2014) design spectra (green lines) are generally overcome by or tangent to the empirically-derived median curves at low periods (< 0.2 s), while they show considerable conservatism at longer periods. On the contrary, and differently from Figures 54-63, we do not observe any exceedance of the Poggi and Fah's (2015) and this report's design spectra (magenta and red lines, respectively) for any soil type and any considered city. Both functional forms largely overtop all median envelopes of site-specific UHSs, due to the conservative a_{gd} scaling. While for class E Poggi and Fah's (2015) version places the plateau segment at periods slightly higher than the actual resonance peak, the design spectra functions proposed in this work appear to reproduce more closely, although at higher spectral acceleration levels (because of a_{gd} scaling), the trend of the hazard spectra inclusive of site amplification.

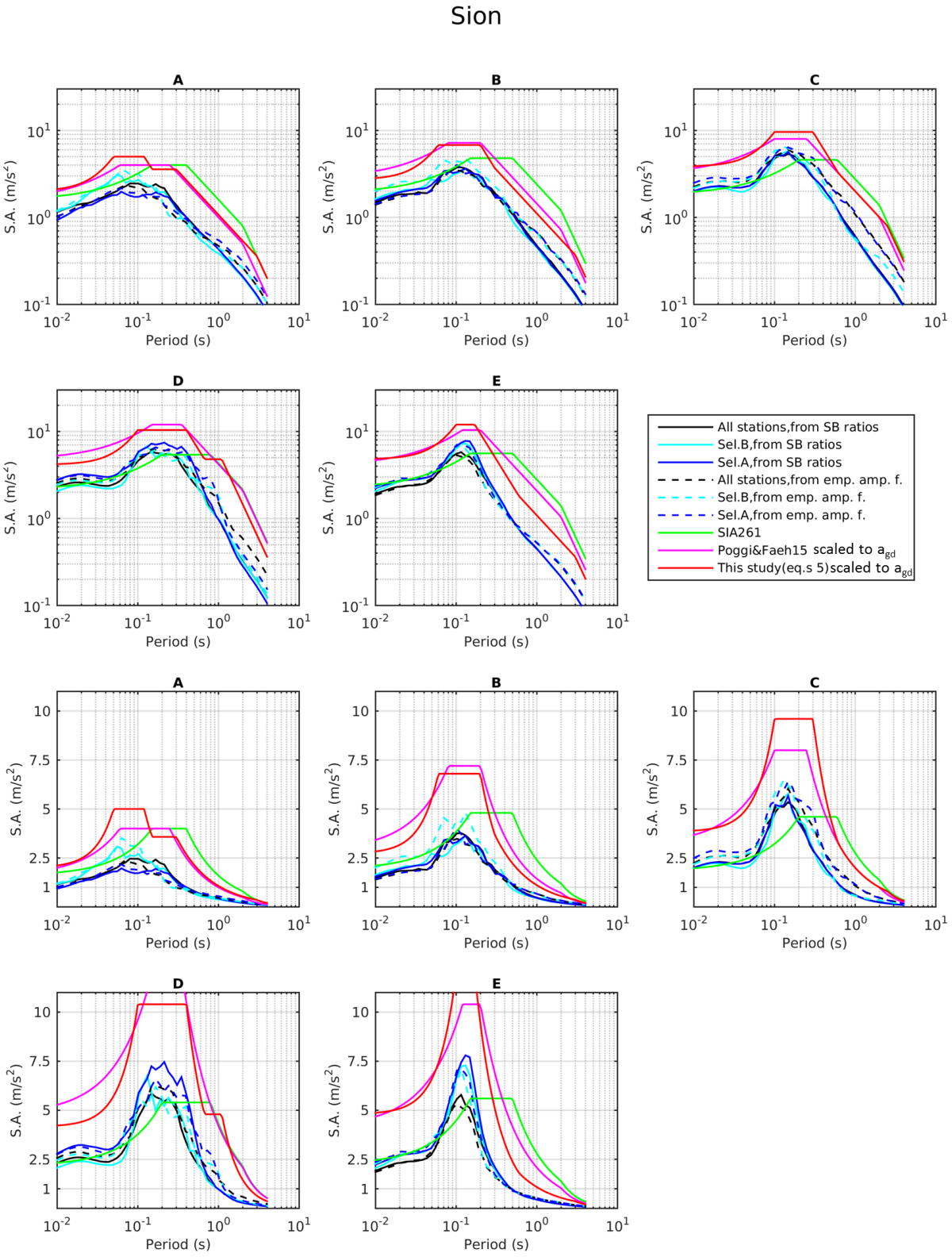

Figure 20A – Median curves of the empirical spectra for the city of Sion (black, blue or cyan line according to the KiKnet station subset; continuous or dashed line according to the origin of the amplification function). The elastic design spectra from SIA 261 normative (green line), Poggi and Fäh's (2015) modification (magenta) and this work's proposal (equations 5, red line) are also included. Top rows: ordinate axis (spectral acceleration) in logarithmic scale. Bottom rows: ordinate axis (spectral acceleration) in linear scale.

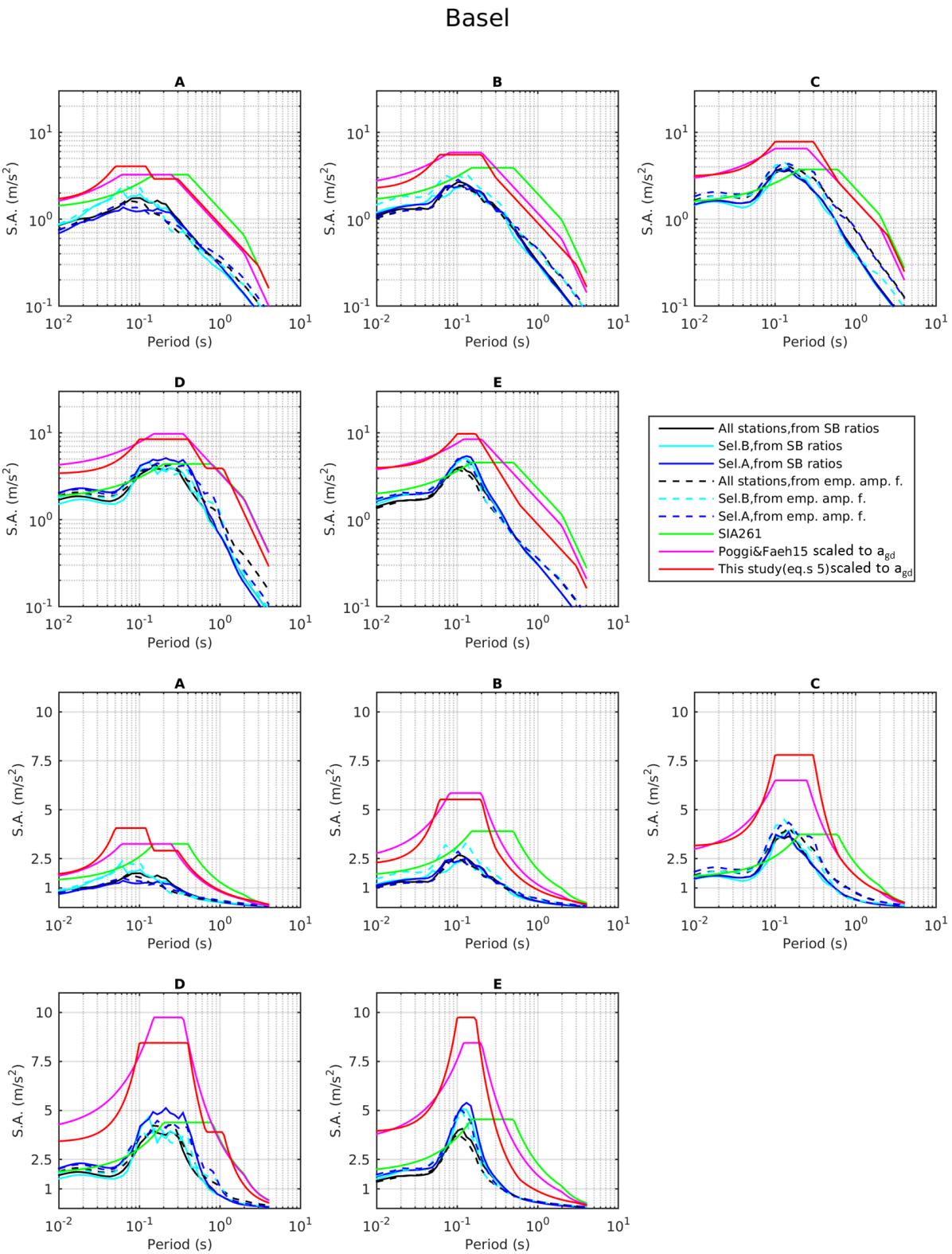

Figure 21A – Median curves of the empirical spectra for the city of Basel (black, blue or cyan line according to the KiKnet station subset; continuous or dashed line according to the origin of the amplification function). The elastic design spectra from SIA 261 normative (green line), Poggi and Fäh's (2015) modification (magenta) and this work's proposal (equations 5, red line) are also included. Top rows: ordinate axis (spectral acceleration) in logarithmic scale. Bottom rows: ordinate axis (spectral acceleration) in linear scale.

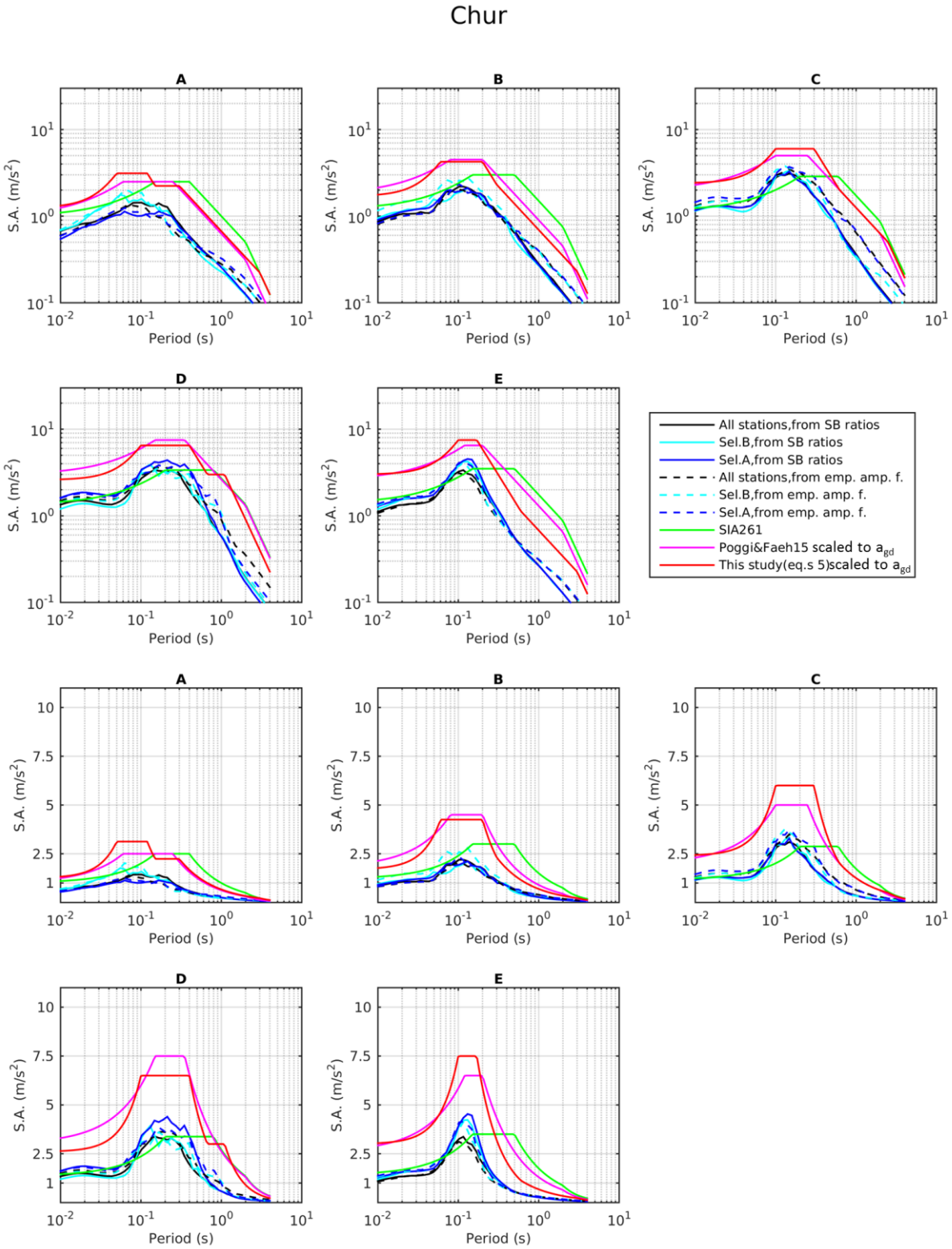

Figure 22A – Median curves of the empirical spectra for the city of Chur (black, blue or cyan line according to the KiKnet station subset; continuous or dashed line according to the origin of the amplification function). The elastic design spectra from SIA 261 normative (green line), Poggi and Fäh's (2015) modification (magenta) and this work's proposal (equations 5, red line) are also included. Top rows: ordinate axis (spectral acceleration) in logarithmic scale. Bottom rows: ordinate axis (spectral acceleration) in linear scale.

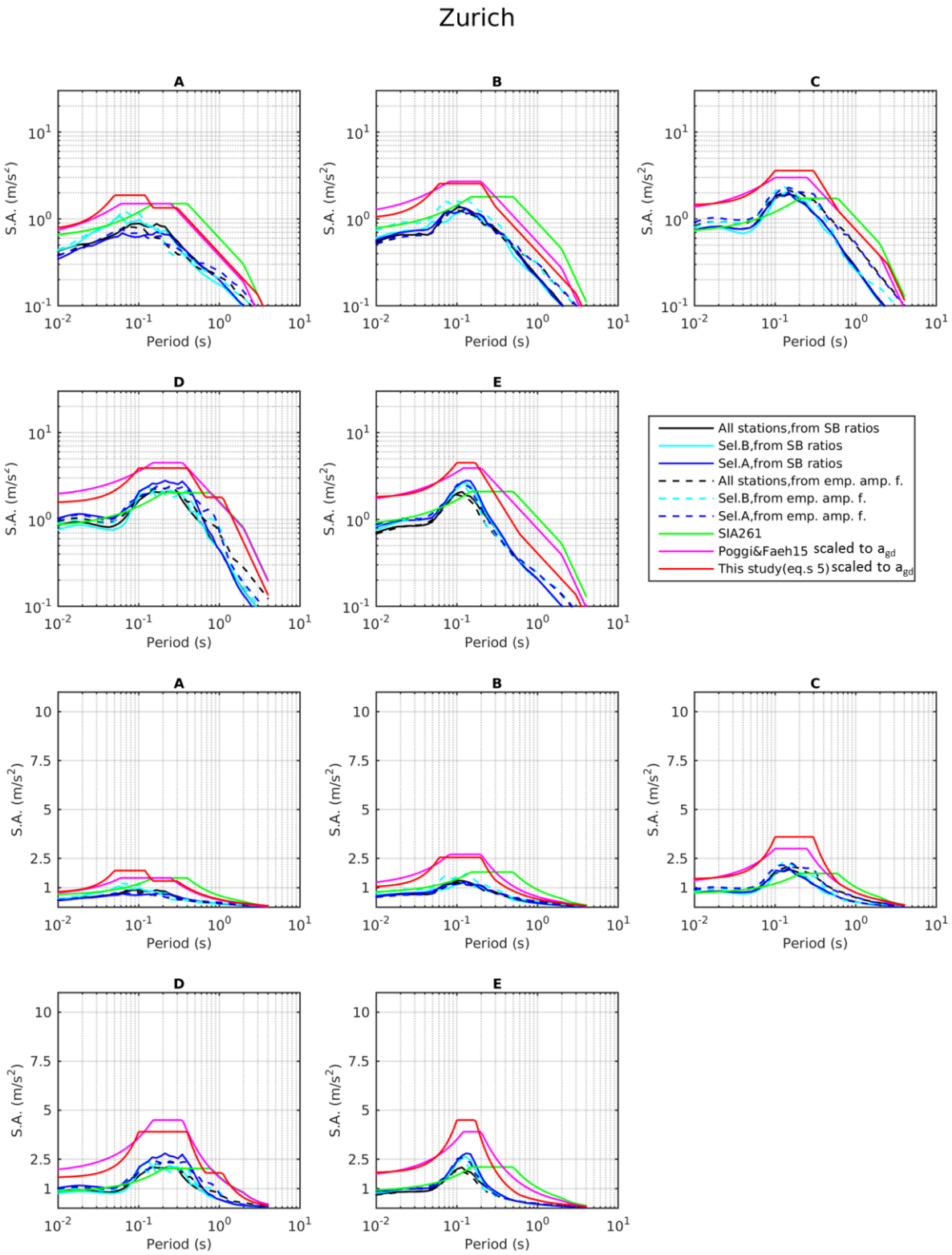

Figure 23A – Median curves of the empirical spectra for the city of Zurich (black, blue or cyan line according to the KiKnet station subset; continuous or dashed line according to the origin of the amplification function). The elastic design spectra from SIA 261 normative (green line), Poggi and Fäh's (2015) modification (magenta) and this work's proposal (equations 5, red line) are also included. Top rows: ordinate axis (spectral acceleration) in logarithmic scale. Bottom rows: ordinate axis (spectral acceleration) in linear scale.

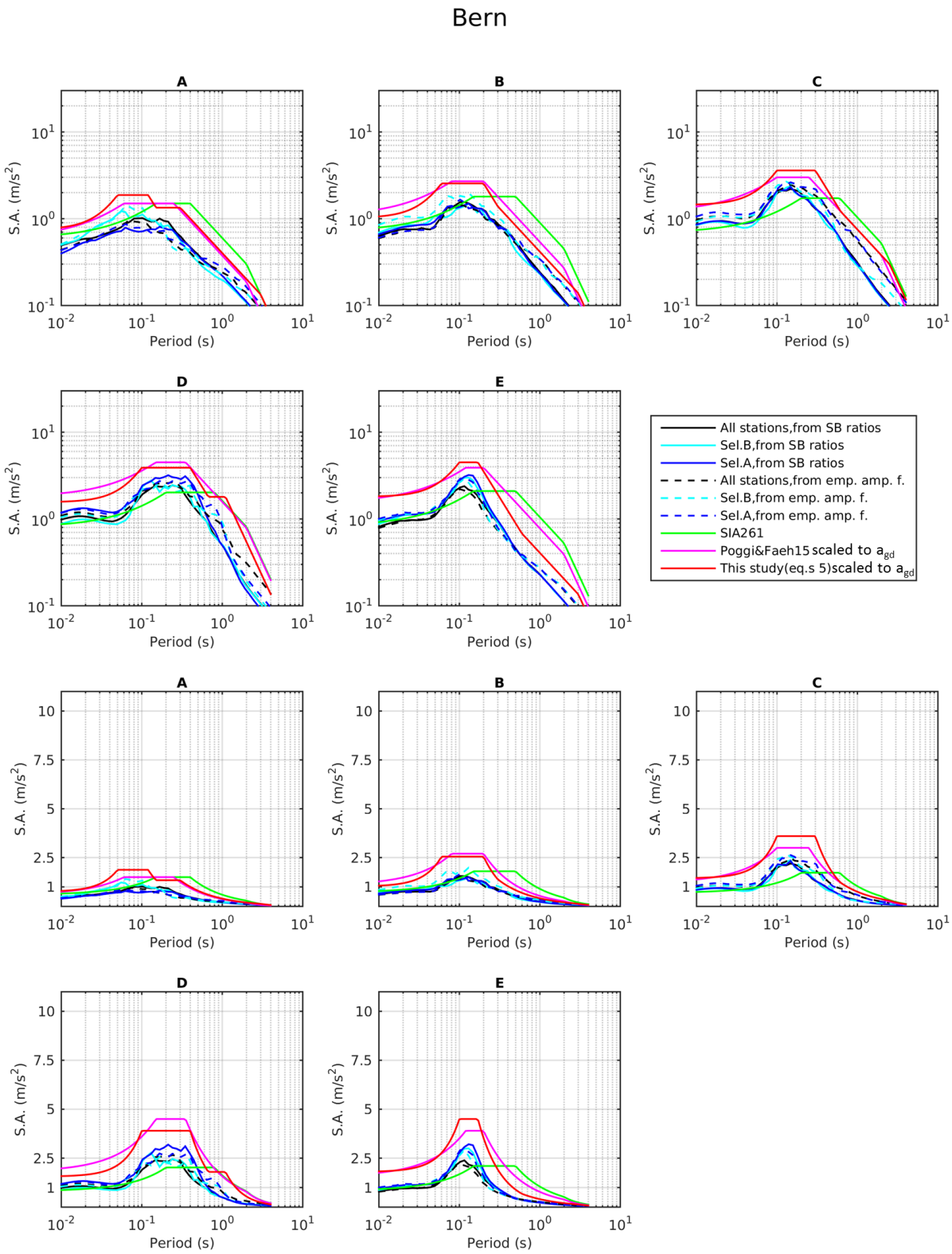

Figure 24A – Median curves of the empirical spectra for the city of Bern (black, blue or cyan line according to the KiKnet station subset; continuous or dashed line according to the origin of the amplification function). The elastic design spectra from SIA 261 normative (green line), Poggi and Fäh's (2015) modification (magenta) and this work's proposal (equations 5, red line) are also included. Top rows: ordinate axis (spectral acceleration) in logarithmic scale. Bottom rows: ordinate axis (spectral acceleration) in linear scale.

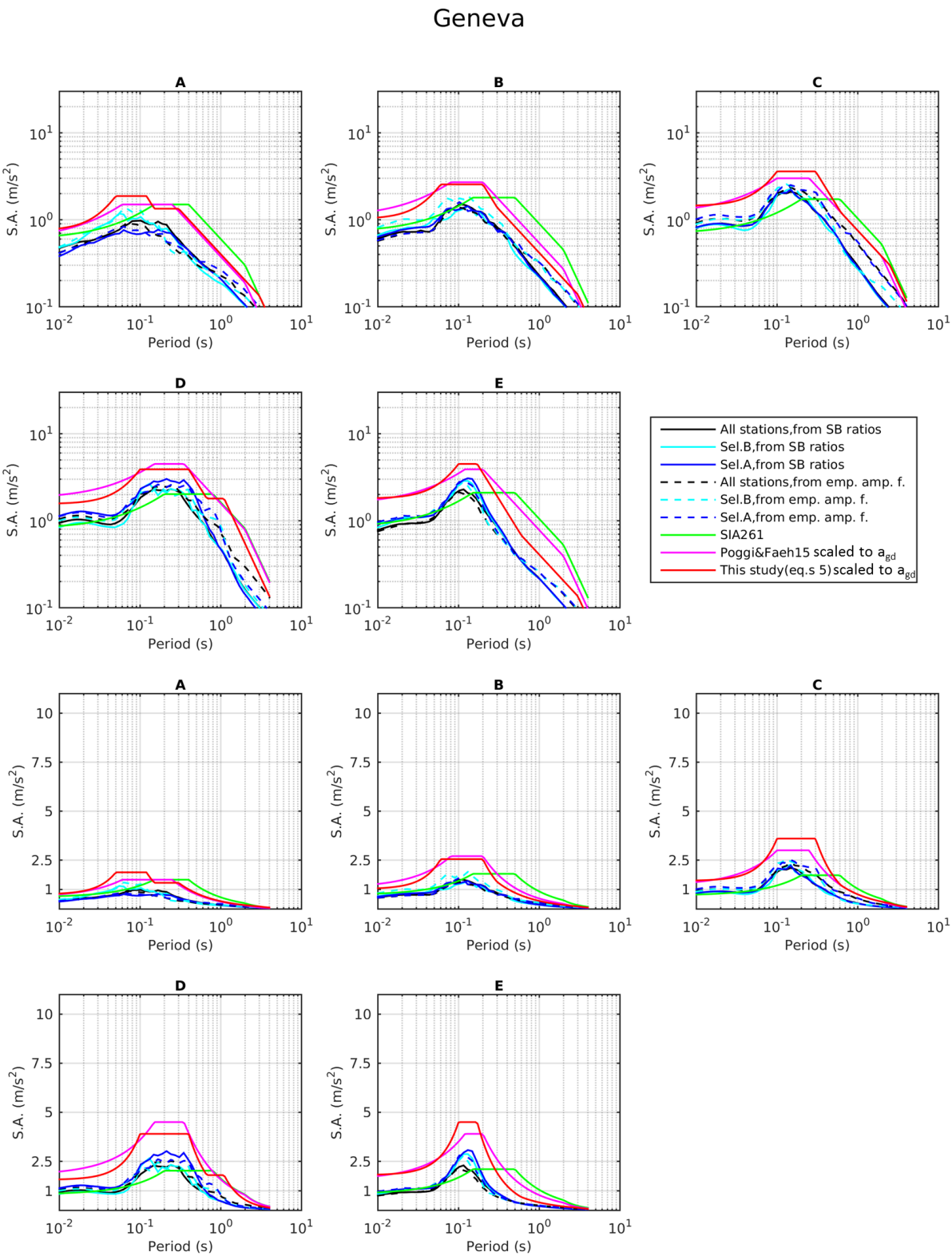

Figure 25A – Median curves of the empirical spectra for the city of Geneva (black, blue or cyan line according to the KiKnet station subset; continuous or dashed line according to the origin of the amplification function). The elastic design spectra from SIA 261 normative (green line), Poggi and Fäh's (2015) modification (magenta) and this work's proposal (equations 5, red line) are also included. Top rows: ordinate axis (spectral acceleration) in logarithmic scale. Bottom rows: ordinate axis (spectral acceleration) in linear scale.

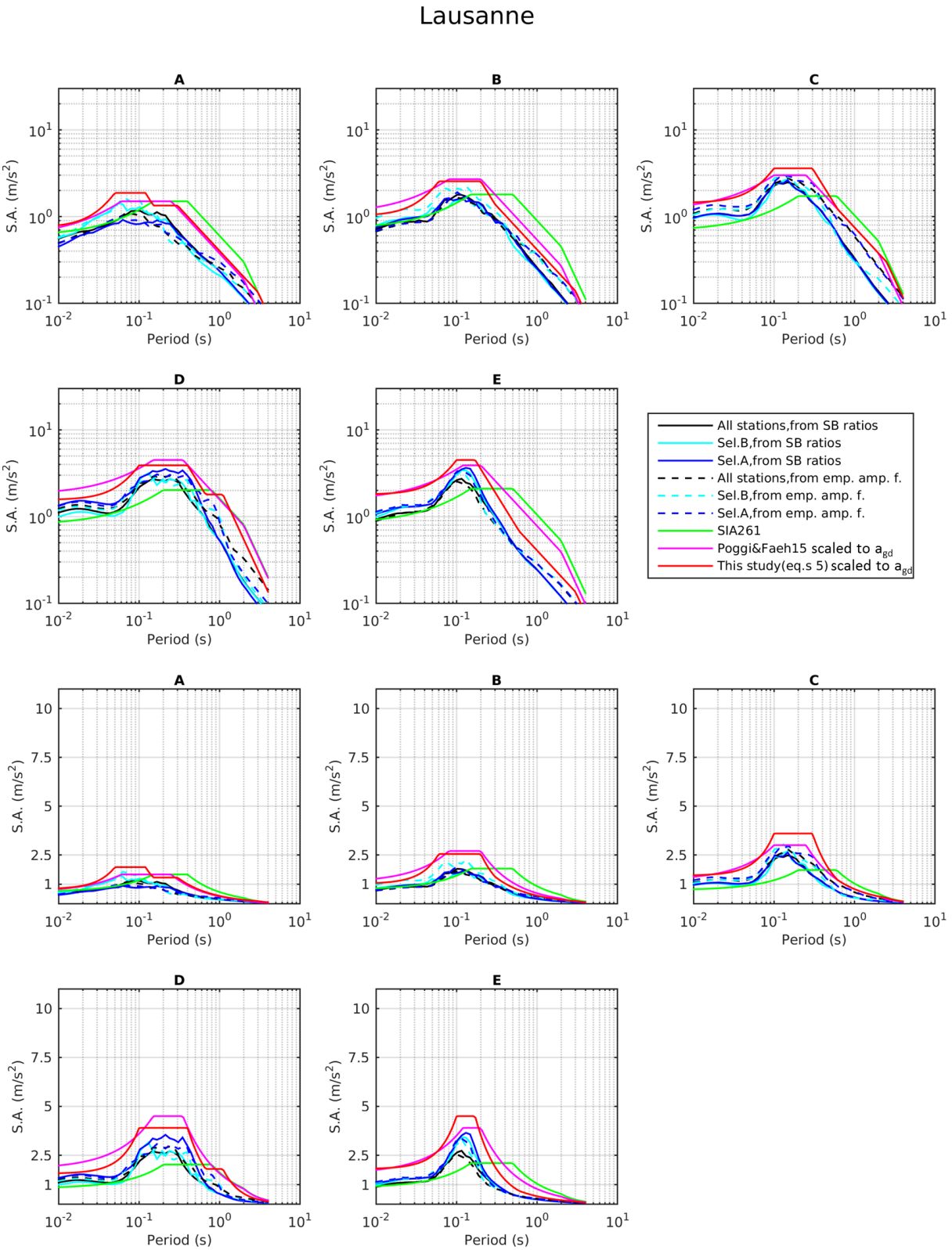

Figure 26A – Median curves of the empirical spectra for the city of Lausanne (black, blue or cyan line according to the KiKnet station subset; continuous or dashed line according to the origin of the amplification function). The elastic design spectra from SIA 261 normative and Poggi and Fäh's (2015) proposal are also included as green and magenta lines, respectively. Top rows: ordinate axis (spectral acceleration) in logarithmic scale. Bottom rows: ordinate axis (spectral acceleration) in linear scale.

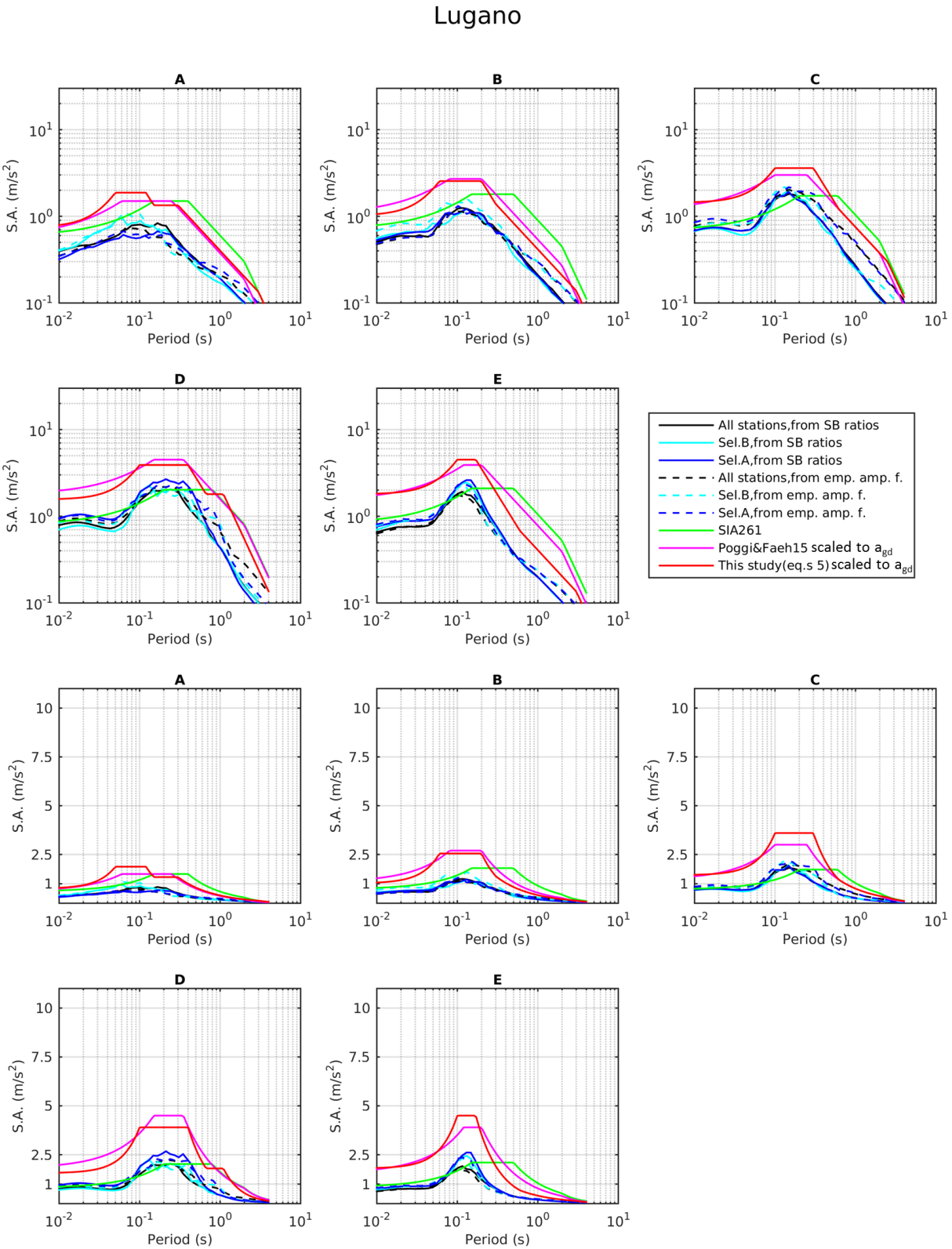

Figure 27A – Median curves of the empirical spectra for the city of Lugano (black, blue or cyan line according to the KiKnet station subset; continuous or dashed line according to the origin of the amplification function). The elastic design spectra from SIA 261 normative (green line), Poggi and Fäh's (2015) modification (magenta) and this work's proposal (equations 5, red line) are also included. Top rows: ordinate axis (spectral acceleration) in logarithmic scale. Bottom rows: ordinate axis (spectral acceleration) in linear scale.

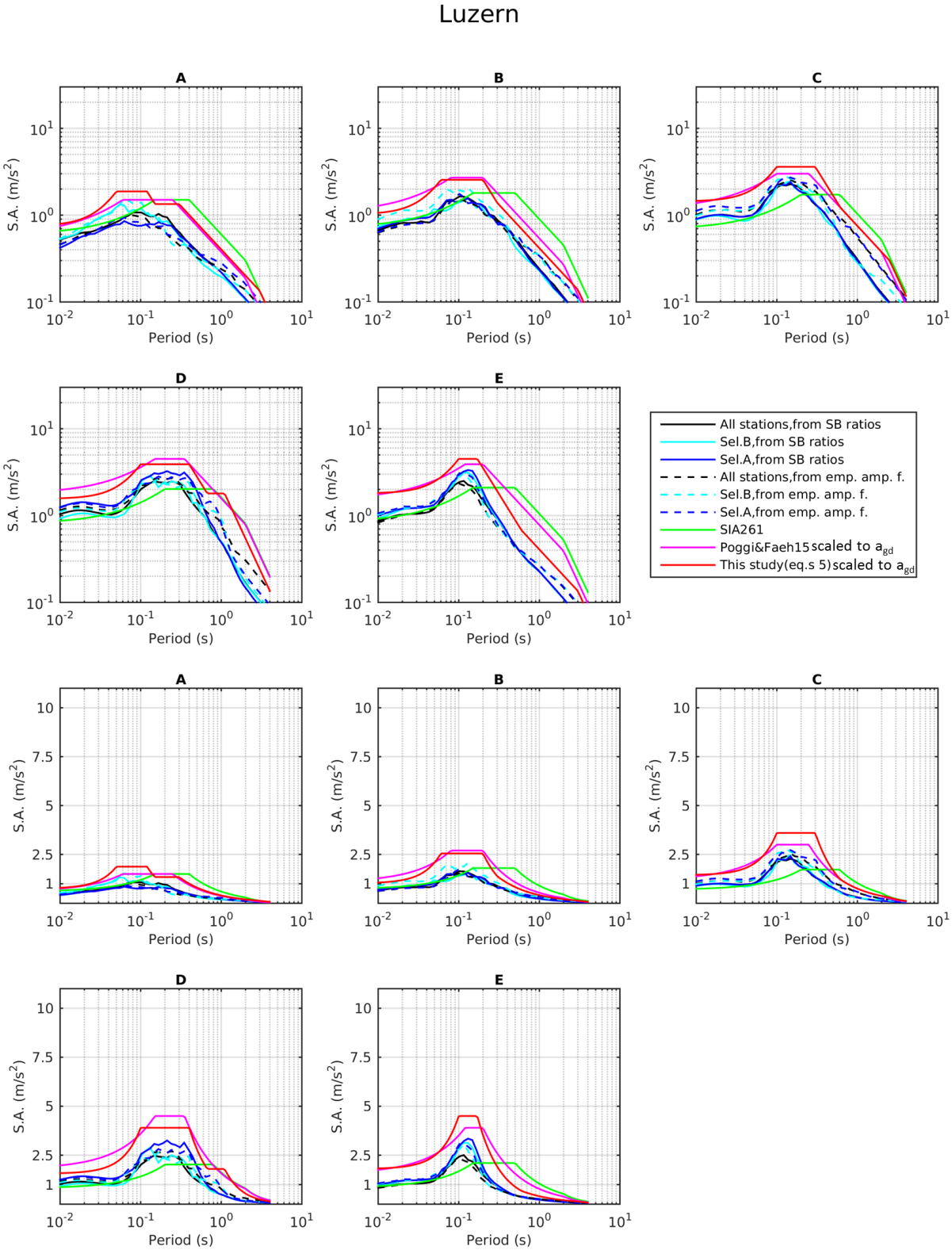

Figure 28A – Median curves of the empirical spectra for the city of Luzern (black, blue or cyan line according to the KiKnet station subset; continuous or dashed line according to the origin of the amplification function). The elastic design spectra from SIA 261 normative (green line), Poggi and Fäh's (2015) modification (magenta) and this work's proposal (equations 5, red line) are also included. Top rows: ordinate axis (spectral acceleration) in logarithmic scale. Bottom rows: ordinate axis (spectral acceleration) in linear scale.

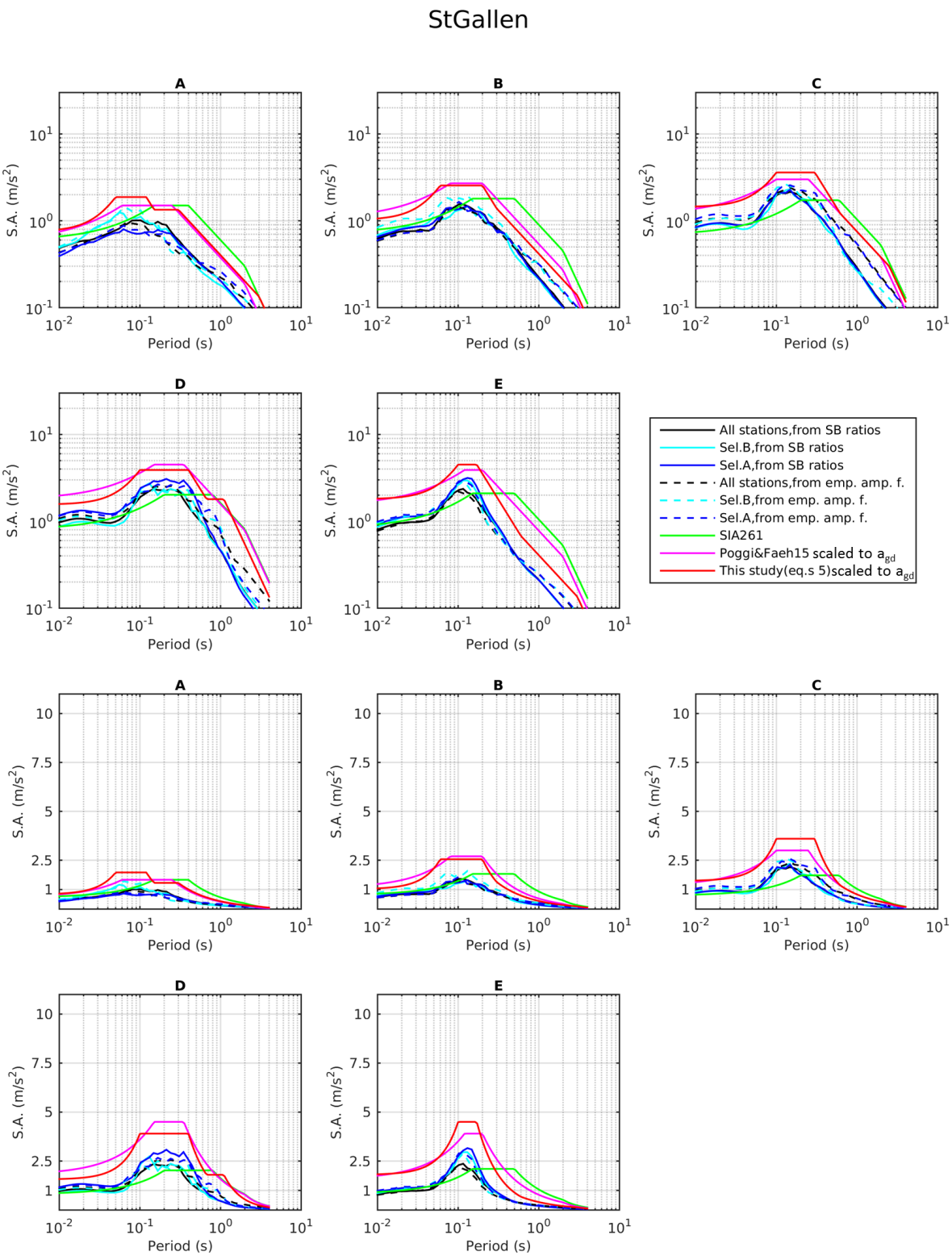

Figure 29A – Median curves of the empirical spectra for the city of Luzern (black, blue or cyan line according to the KiKnet station subset; continuous or dashed line according to the origin of the amplification function). The elastic design spectra from SIA 261 normative (green line), Poggi and Fäh's (2015) modification (magenta) and this work's proposal (equations 5, red line) are also included. Top rows: ordinate axis (spectral acceleration) in logarithmic scale. Bottom rows: ordinate axis (spectral acceleration) in linear scale.

As a final step, and once again following the workflow adopted in the main body of the report (section 11), the scaling with PGA (in place of a_{gd}) of both the Poggi and Fäh's (2015) and this work's proposition

for elastic design spectra, was applied (i.e. a_{gd} was replaced by PGA in equations 4-5). The relevant figures are shown in the main text (Figures 76-85, section 12). The conservatism shown in the previous set of figures (Figures 20A-29A, design spectra scaled to a_{gd}) is absent, and normative functions now closely follow (but they are not overcome) the median envelopes of the sets of site-specific UHSs. In particular, the functional form from equations 5 proves flexible enough to reproduce the features observed in the hazard spectra comprehensive of site amplification.

The analyses presented in this appendix reproduce the workflow adopted in this subproject, assuming a different V_{S30}-based interpretation of the class E definition from SIA 261 norm (2014). The population of response spectra amplification functions for a variety of near-surface configurations, combined with seismic hazard input (UHS), are the same as those presented in the main body of this report; however, these are differently sorted into the same soil types, determining different shapes for the median envelopes for classes A, B, and obviously E. These differences are not negligible, leading to lower values of median spectral acceleration for soils A, B, E; as for the latter, we observe also a shift of the resonance peak towards lower periods. Understandably, the (normalized and absolute) comparison with elastic design spectra do not bring to the same conclusions as in sections 10 and 11; indeed, the SIA 261 (2014) form is still consistently surpassed at low periods, but its Poggi and Fäh's (2015) modification now bounds the median curves of site-specific UHSs, even for soil type E.
As a conclusion, we believe that the results of this appendix highlight the importance of robust soil type definition criteria in grouping sites with consistent amplification behaviour.

APPENDIX B – Comparison with Poggi and Fäh's (2015) study for SFOE

This appendix includes:

B.1) A re-elaboration of final product (median curves of site-specific UHSs) of the Poggi and Fäh's (2015) work for SFOE (hereinafter referred to as PF2015), adopting the soil classes definition followed in Appendix A (not considered in that study);

B.2) A comparison between the final output (again intended as median curves of site-specific UHSs) of PF2015 and this work. This comparison is performed taking into account both the soil type definition attended in the main body of this work (same of PF2015), and the alternative one from Appendix A.

B.1 Re-elaboration of results of the Poggi and Fäh's (2015) work, using the soil type definition of Appendix A

PF2015 implements a workflow similar to that followed in this report, although using various sets of input Fourier amplification functions that only in one case (empirical amplification functions from spectral modelling from KiK-net recordings) are compatible with those employed for this report. The final product of PF2015 is a dataset of *normalized* (as in section 10 of this work) site-specific UHSs, obtained combining the UHS on reference rock of Sion (assumed as seismic hazard input representative for all Switzerland) with response spectra amplification functions for a wide variety of near-surface configurations.

We have recovered from the PF2015 database the set of normalized site-specific UHSs referring to the same earthquake scenario used in this work (M_w = 6.5, R_{rup} = 10 km, SD = 6.3 MPa, see section 7), and derived from empirical amplification functions from spectral modelling (using KiK-net recordings). We have sorted these individual functions adopting both the original soil classification criterion (Figure 1B) and the soil type definition from appendix A (not considered in PF2015, Figure 2B); we have re-computed the median and percentile curves.

Figure 3B directly collates the median curves obtained for each soil class using the two alternative soil type criteria. As explained in Appendix A, differences are to be expected for classes A, B, E, that include different sets of individual curves depending on the chosen criterion; soil types C, D instead, are not affected (their blue and red median curves coincide). The discrepancies observed for A, B, and E are in full agreement (as expected) with those highlighted in Appendix A (Figure 19A) and section 12 (Figure 74). In fact, the definition of class E involving Vs_{H800} < 500 m/s produces median curves (red lines) reaching lower values of spectral acceleration, in particular for soil type E; in this case, the resonance peak also moves towards lower periods.

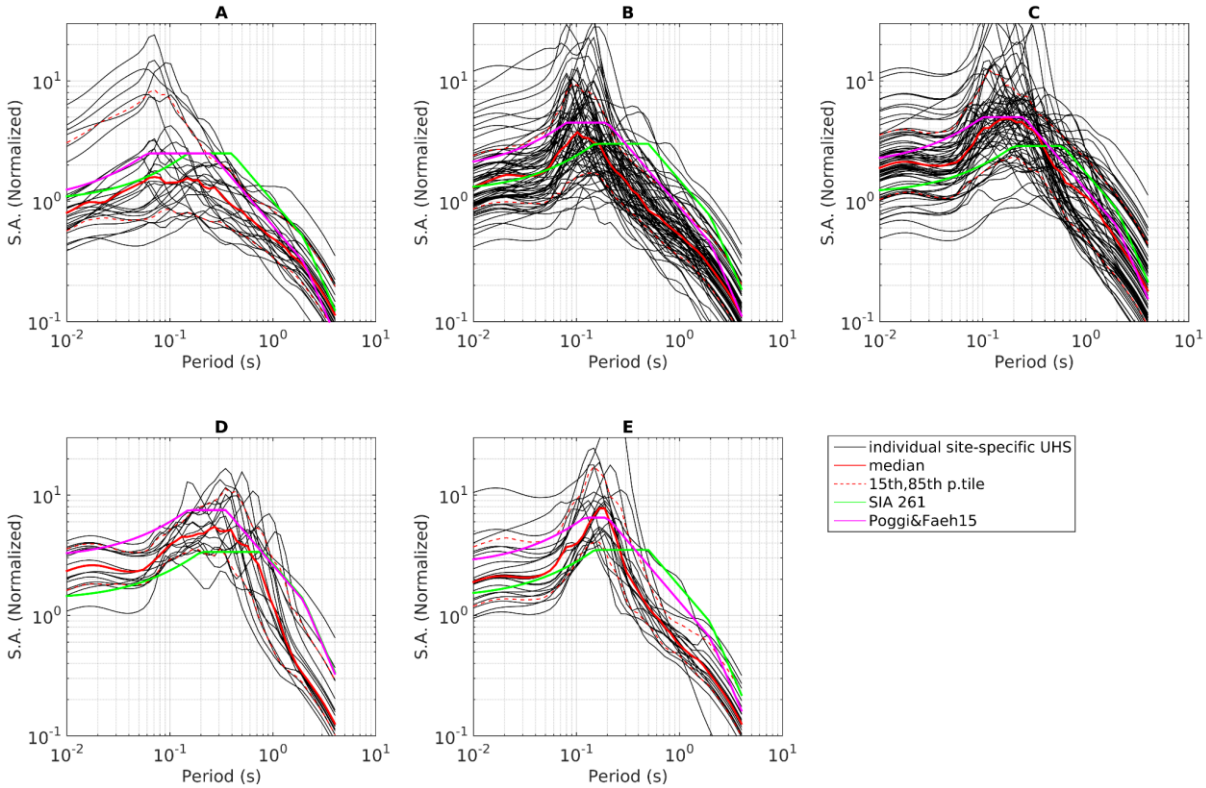

Figure 1B – Normalized (to PGA on reference rock) hazard spectra inclusive of site amplification, drawn from PF2015 database. The individual site-specific UHSs (black lines) are classified according to the soil type criterion followed in PF2015 and in the main body of this report; we re-computed the median and 15th, 85th percentile for each soil class (red lines); the SIA 261 (2014) design spectra and their amendment as per PF2015, both normalized to a_{gd}, are, also included (green and magenta line, respectively)

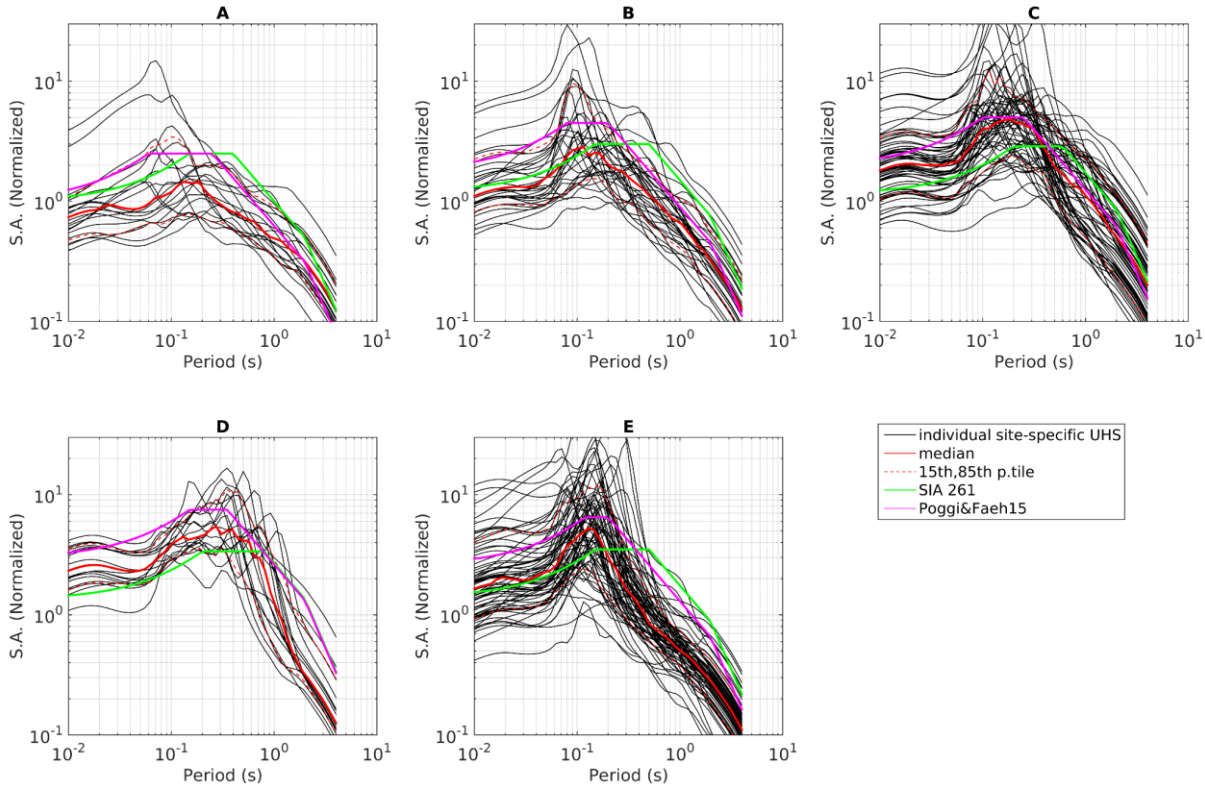

Figure 2B – Normalized (to PGA on reference rock) hazard spectra inclusive of site amplification, drawn from PF2015 database. The individual site-specific UHSs (black lines) are classified according to the soil type criterion followed in Appendix A of this report; we computed the median and 15th, 85th percentile for each soil class (red lines); the SIA 261 (2014) design spectra and their amendment as per PF2015, both normalized to a_{gd}, are also included (green and magenta line, respectively).

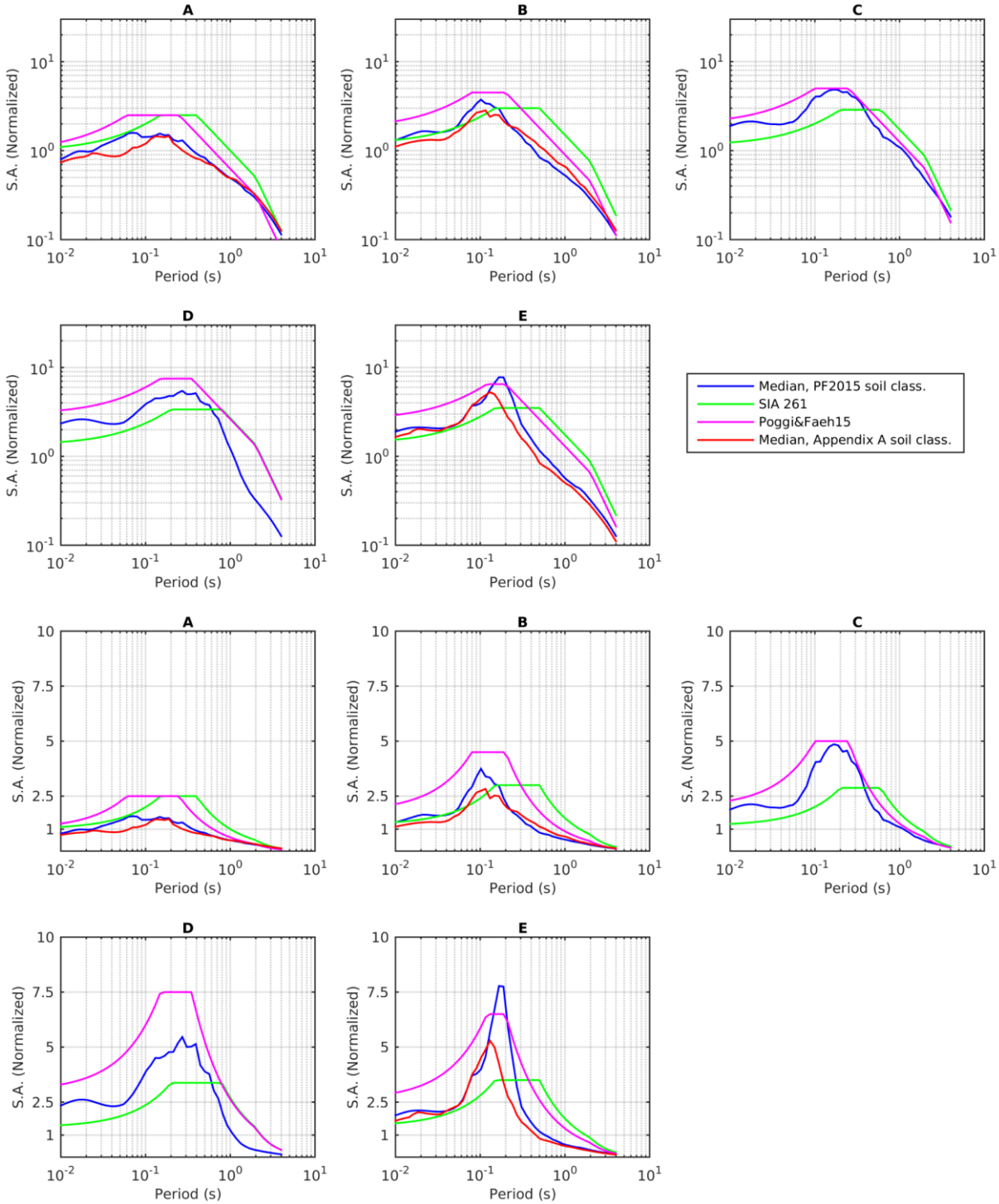

Figure 3B – Comparison between median curves of normalized site-specific UHSs drawn from PF2015, sorted according to the soil type criterion attended in PF2015 (blue lines), and to the criterion followed in Appendix A of this report (red lines). The SIA 261 (2014) design spectra and their amendment as per PF201, both normalized to a_{gd}, are also included (green and magenta line, respectively). The two upper lines display subplots with normalized S.A. axis in logarithmic scale; the two bottom lines display subplots with normalized S.A. axis in linear scale.

B.2 Comparison between normalized hazard spectra inclusive of site amplification from Poggi and Fäh's (2015) study and this work

We compare here the normalized (to PGA on reference rock) site-specific hazard spectra from Poggi and Fäh's (2015) study and their equivalent from this work. We remark that the two workflows producing the collated datasets are consistent: Fourier amplification functions for a variety of subsurface models are translated to the response spectra domain with the use of random vibration theory, then combined with uniform hazard spectra at the reference rock. We focus here on datasets that are fully comparable, i.e. the normalized hazard spectra obtained using empirically-derived amplification function (from KiK-net data) as input Fourier amplification for RVT calculations. In both cases also, the UHS on rock for Sion from SUIhaz15 (SED, 2016) is used as seismic hazard input, cautelatively representative for all Switzerland. Note that, for the purpose of a collation between analogous items, we have here removed from the PF2015 database the site-specific hazard spectra derived from Fourier amplification functions from spectral modelling detected as not reliable in this study (see section 5, Figure 13). We remind also that the selection of KiK-net sites used in PF2015 is the same named "Selection A" in this report.
Figures 4B and 5B represent the median curves from this study (black, blue, cyan lines) and their comparable counterpart from PF2015 (red lines), adopting the soil type scheme used in the main body of this report (and in PF2015, Figure 4B), and that illustrated in Appendix A (Figure 5B). In both representations, the red curves from PF2015 show a trend that is in fair agreement with that obtained in this work; in particular, we observe a marked similarity with the subset more directly corresponding (Selection A sites, site-specific UHSs derived from empirical amplification functions from spectral modelling, blue dashed lines).

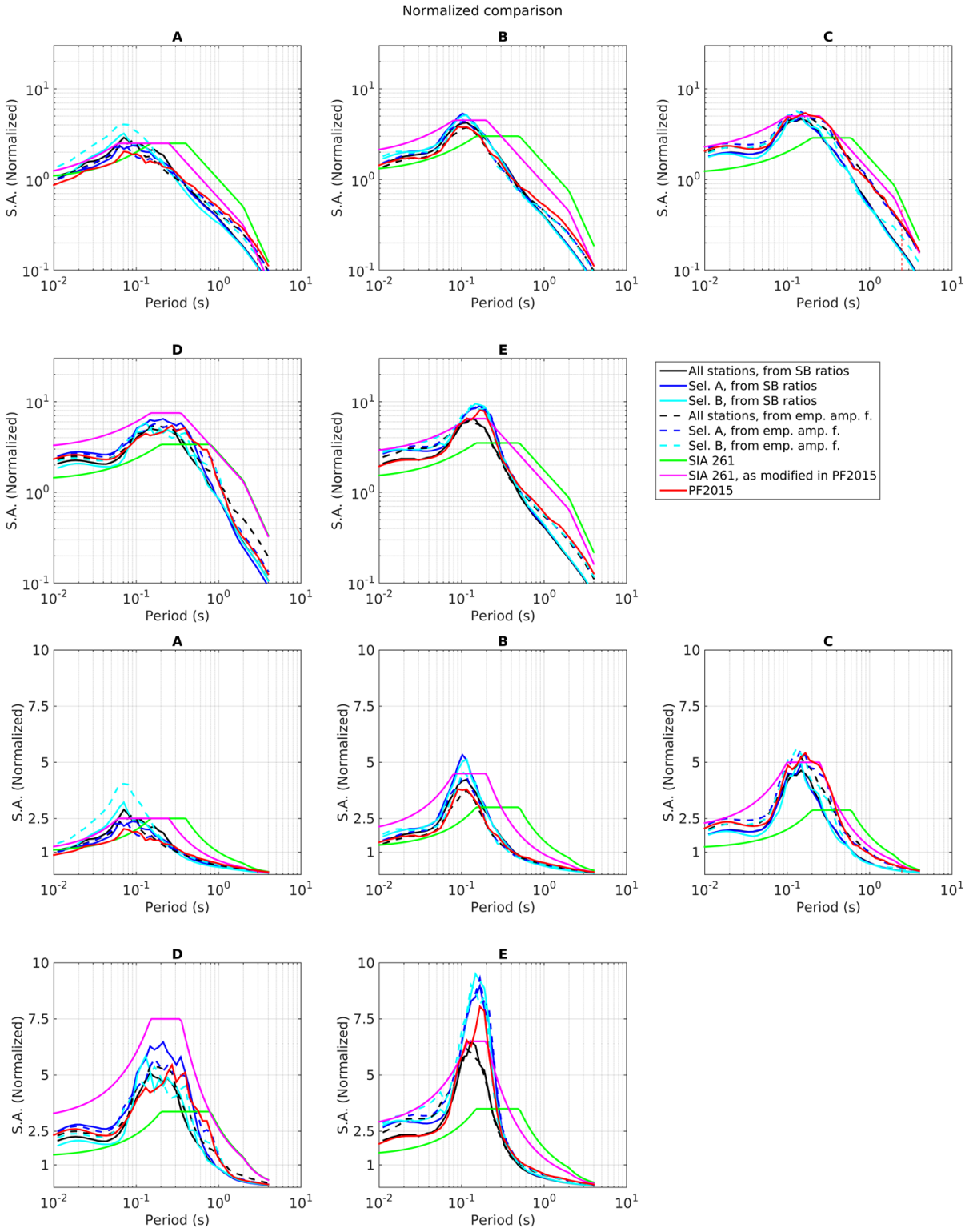

Figure 4B – Median curves of the sets of site-specific UHSs obtained in this study (blue, black and cyan lines), collated with the median curve of similarly-derived site-specific UHSs from PF2015 (red lines). The soil type classification is the one followed in PF2015 and in the main body of this report. SIA 261 normative spectra and their modifications as per PF2015 (both normalized to a_{gd}) are also displayed (green and magenta line, respectively). Top rows: subplots with normalized acceleration axis in logarithmic scale; bottom rows: subplots with normalized acceleration axis in linear scale.

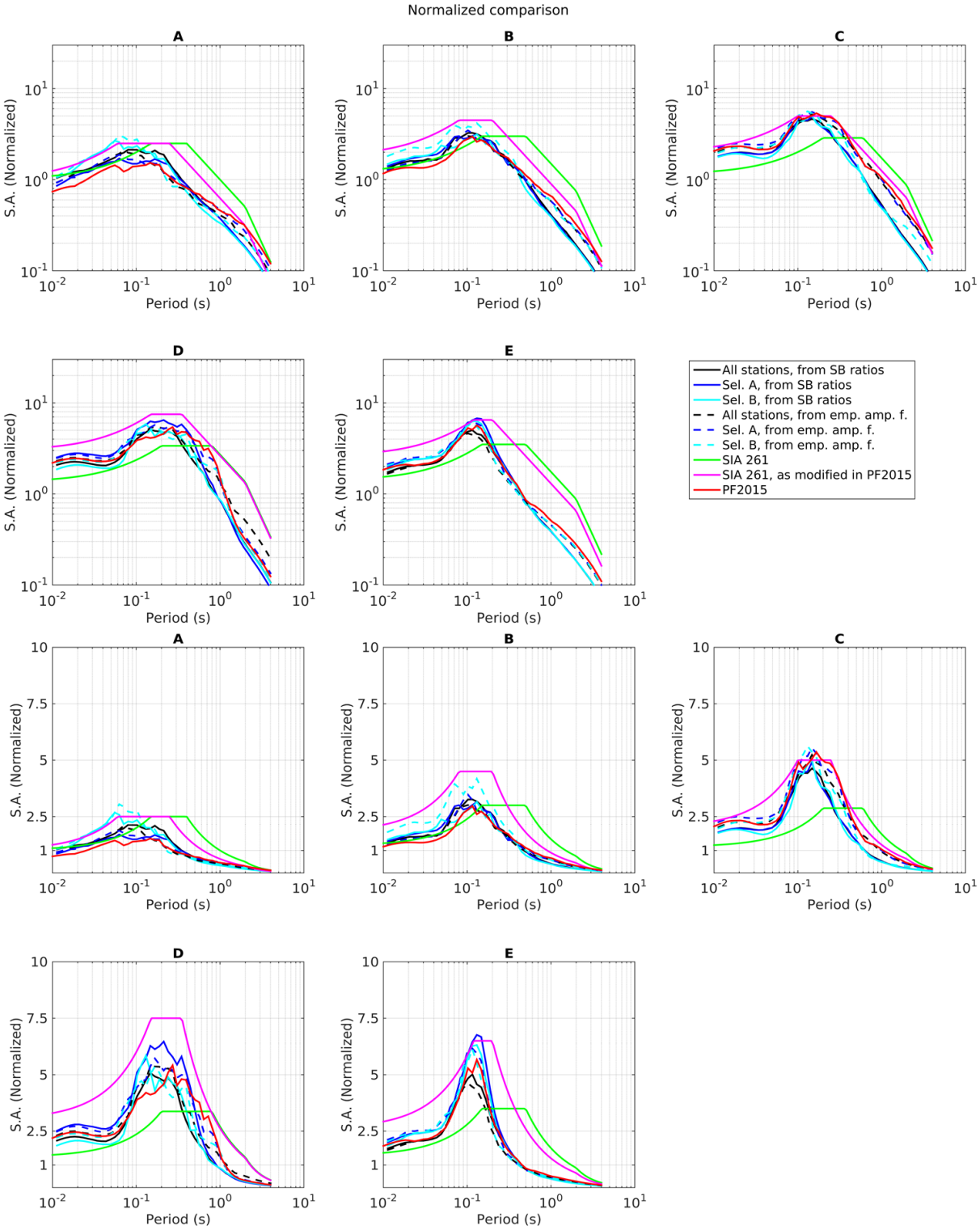

Figure 5B – Median curves of the sets of site-specific UHSs obtained in this study (blue, black and cyan lines), collated with the median curve of similarly-derived site-specific UHSs from PF2015 (red line). The soil type classification is the one illustrated in Appendix A. SIA 261 normative spectra and their modifications as per PF2015 (both normalized to a_{gd}) are also displayed (green and magenta line, respectively). Top rows: subplots with normalized acceleration axis in logarithmic scale; bottom rows: subplots with normalized acceleration axis in linear scale.